A study of Tau Leptons produced in Z° Decays

By
Julie Hart
of
Newnham College

A dissertation submitted to the University of Cambridge
for the degree of Doctor of Philosophy
December 1991

To
my parents
Tony and Mary Hart

A study of tau leptons produced in Z° Decays.

Julie Hart

Abstract

The LEP e^+e^- collider at CERN is able to test the theory of electroweak interactions by precise measurements of the properties of the Z° boson. In this thesis data from the OPAL detector are used to measure the couplings of the Z° to leptons and the results are compared with the predictions of the theory.

The τ polarization is measured using the energy spectrum of $\tau \rightarrow e\nu_\tau\bar{\nu}_e$ decays and the couplings of the Z° to the τ are extracted. The forward–backward polarization asymmetry is also measured and this is related to the couplings of the Z° to the electron. In addition, the Standard Model predicts universality of the couplings of the Z° to the three lepton generations and this allows the $\tau \rightarrow e\nu_\tau\bar{\nu}_e$ branching ratio to be predicted from measurements of the τ lifetime. The branching ratio is measured and the result compared with that expected from the τ lifetime.

During 1990, the OPAL experiment recorded about 6.4 pb^{-1} of data and these are used in this thesis to measure the $\tau \rightarrow e\nu_\tau\bar{\nu}_e$ branching ratio and the τ polarization. A brief review of electroweak theory and τ physics is followed by a description of the OPAL detector with emphasis on the fast track trigger and those components of the detector used in the τ analysis. A sample of $\tau \rightarrow e\nu_\tau\bar{\nu}_e$ events is selected from the data and these are used to measure the branching ratio and the τ polarization from which the coupling constants are extracted. The neutral current coupling constants determined from the polarization measurements are found to be consistent with expectations from the Standard Model and with measurements from other experiments.

Preface

I joined the Cambridge High Energy Physics Group in October 1988 to work on the OPAL experiment at CERN. I would like to thank the Science and Engineering Research Council for providing financial support for three years of this research. I am grateful to all members of the OPAL group in Cambridge, staff and students, for making my time here so enjoyable and for all their help during the last three years. I would particularly like to thank my supervisor, Janet Carter, for her advice and guidance, and Pat and David Ward for their helpful suggestions. Thanks also to Jan White for keeping us all supplied with coffee and 'biccies'.

Within OPAL I soon became involved with the vertex chamber and track trigger (TT). I spent from June 1989 to December 1990 in CERN and for much of that time I worked on the TT hardware. As everyone frantically prepared for the start of LEP, many people spared the time to teach me about 'online' and I would like to thank all those who helped me during that period. I am especially grateful to Colin Roach for passing on his wisdom about TT, and to John Hill and Terry Pritchard for not only teaching me about hardware and online but also for somehow maintaining a friendly and jovial atmosphere down t'pit at all times. Stan Jaroslawski and Alan Penton also deserve a mention for building and helping to commission the Track Trigger hardware.

During my stay at CERN I became involved with the τ working group and I am grateful to all those at CERN who gave me their advice and encouragement, in particular Keith Riles and Makoto Sasaki were very helpful.

On the social scene, I would like to thank all those friends both in the UK and Geneva who made the last three (and a bit) years so enjoyable. Unfortunately, there is not room to mention eveyone here so I will just say a very big thankyou to you all. I didn't ought to forget Miriam, Ruth and Ken, who I am particularly grateful to for providing a friendly atmosphere both in and out of work during my time in Cambridge.

Finally, special thanks to my family, Mum, Dad and Jane, for their love and support throughout and to Andrew for his constant love and encouragement, for all the proof–reading and for reminding me that there is life after a thesis.

Declaration

This dissertation is the result of my own work, except where explicit reference is made to the work of others, and has not been submitted for another qualification to this or any other university.

J. Hart

Contents

List of Figures

List of Tables

Chapter 1

Introduction

The Standard Model of particle physics uses gauge field theories to describe the electromagnetic, weak and strong interactions between particles. The strong interaction is described by the theory of Quantum ChromoDynamics (QCD) whilst the electromagnetic and weak interactions are unified in a single 'Electroweak' theory. This thesis is concerned with the electroweak sector of the model and its parameters. Using data collected by the OPAL experiment at LEP, some of the parameters of the electroweak model are measured, in particular the couplings of the Z^0 boson to the e and τ leptons are determined.

1.1 Standard Model

Details of the Standard Model can be found in many texts, for example [1] and [2]; here only a brief overview is given. The model contains two types of fundamental particles which are point-like and structureless. The constituents of matter are spin-$\frac{1}{2}$ fermions and these interact via exchange of spin-1 gauge bosons.

Fundamental Fermions

The known fermions can be subdivided into two classes, the quarks which interact via the strong force and the leptons which do not. In order to interact strongly the quarks must carry a colour charge and there are three 'colour' states for each quark. There are six 'flavours' of leptons and quarks and these fall into three 'families' or generations,

the second and third of which are higher mass replicas of the first.

$$\begin{aligned} \text{Leptons}: & \quad \begin{pmatrix} \nu_e \\ e^- \end{pmatrix}, \quad \begin{pmatrix} \nu_\mu \\ \mu^- \end{pmatrix}, \quad \begin{pmatrix} \nu_\tau \\ \tau^- \end{pmatrix} \\ \text{Quarks}: & \quad \begin{pmatrix} \mathrm{u} \\ \mathrm{d} \end{pmatrix}, \quad \begin{pmatrix} \mathrm{c} \\ \mathrm{s} \end{pmatrix}, \quad \begin{pmatrix} \mathrm{t} \\ \mathrm{b} \end{pmatrix} \end{aligned} \tag{1.1}$$

Recent measurements of the number of light neutrino species indicate that there are only three such fermion generations [3]. All these fermions have been observed experimentally except the ν_τ and the top (t) quark. The existence of the ν_τ is inferred from the characteristics of τ decays. Limits on the top quark mass are currently $m_t \geq 89$ GeV [4].

Gauge Bosons

Gauge field theories are derived by imposing local gauge invariance, governed by some symmetry group, on the free fermion Lagrangian. In order to realise the required invariance the Lagrangian must be modified to include interaction terms between the fermion and a new gauge field. The quanta of the gauge field introduced in this way are the spin–1 gauge bosons. Quantum ElectroDynamics (QED), which describes electromagnetic interactions between charged particles, is based on the U(1) symmetry group and the quanta of the gauge field are just the photons which couple to electric charge. Photons must be massless in order to retain the gauge invariance of the theory.

QCD is derived in an analogous way to QED but by requiring invariance under local SU(3) transformations in colour space. The application of the gauge principle leads to the introduction of 8 massless gauge bosons known as gluons which couple to the colour charge. The gluons themselves carry colour and can, therefore, self–interact. The weak force is mediated by three massive gauge bosons, the $\mathrm{W}^\pm$ and the Z°, and is described by an SU(2) symmetry in weak isospin.

1.2 Electroweak theory

Weak interactions were first observed in nuclear β decay where the continuous energy spectrum of the emitted electron led to the introduction of a weakly interacting neutral

massless particle; the neutrino. Other weak processes such as the decay of the π^- and μ^- were also observed, leading to the concept of a universal charged weak coupling. The observation of maximal parity violation in β decay showed that only left handed fermions (and right handed anti–fermions) participate in these "charged current" weak interactions. This feature of the interaction is introduced into the theory by including vector (V) and axial–vector (A) couplings in a V-A structure [1]. Fermi suggested a four–fermion point interaction to describe the weak interaction with a small coupling, G_F, to explain the low rates.

Fermi theory, however, is not renormalisable and as such is not a satisfactory theory. The solution to this problem is the unification of the electromagnetic and weak interactions into a single electroweak theory, based on $SU(2)_L \times U(1)_Y$ gauge invariance, as proposed by Glashow, Weinberg and Salaam [5]. The $SU(2)_L$ symmetry provides a triplet of gauge bosons, W^μ, which couple to weak isospin with strength g whilst the $U(1)_Y$ group gives a singlet, B^0, coupling to weak hypercharge with strength g'. These four gauge bosons are massless and the Higgs mechanism can be used to give them mass in a renormalisable way whilst introducing one more massive particle, the Higgs boson, into the theory. The mass eigenstates from the Higgs mechanism are mixtures of the original gauge bosons:

$$\begin{aligned} W^\pm &= \sqrt{\tfrac{1}{2}}\,(W^1 \mp iW^2) \\ Z^0 &= W^3 \cos\theta_W - B^0 \sin\theta_W \\ A &= W^3 \sin\theta_W + B^0 \cos\theta_W \end{aligned} \tag{1.2}$$

The mixing is described by the Weinberg angle, θ_W, which is related to the couplings by $\tan\theta_W = g'/g$, its value is not predicted by the theory but must be determined experimentally. Requiring that the photon (A) couples only to the electromagnetic current allows the electroweak couplings to be related to the electromagnetic coupling e such that $e = g\sin\theta_W$, and the fact that the photon is known to be massless results in a relationship between the masses of the weak vector bosons:

$$M_Z = \frac{M_W}{\cos\theta_W} \qquad \text{or} \qquad \sin^2\theta_W = 1 - \frac{M_W^2}{{M_Z}^2} \tag{1.3}$$

The mixing of the two symmetries in the neutral currents, as described by equation 1.2, means that the Z°, unlike the $W^\pm$, couples to both left and right handed

fermions. The couplings can be found from the electroweak Lagrangian [6] and from these the vector and axial couplings are derived:

$$\begin{aligned} a_f &= 2\mathrm{I}_3^f \\ v_f &= 2\mathrm{I}_3^f - 4\, q_f \sin^2\theta_\mathrm{W} \end{aligned} \tag{1.4}$$

where I_3^f is the third component of weak isospin and q_f is the charge of the fermion. The neutral current couplings for the first generation of fermions are given in table 1.1 [1].

Table 1.1: Couplings of the fermions to the Z°.

	I_3^f	q_f	a_f	v_f
ν	+1/2	0	+1	+1
e^-	−1/2	−1	−1	$-(1 - 4\sin^2\theta_\mathrm{W})$
u	+1/2	+2/3	+1	$(1 - \frac{8}{3}\sin^2\theta_\mathrm{W})$
d	−1/2	−1/3	−1	$-(1 - \frac{4}{3}\sin^2\theta_\mathrm{W})$

Tests of Electroweak Theory

At the cost of introducing one additional massive scalar particle, the Higgs boson, a renormalisable theory unifying the weak and electromagnetic interactions has been achieved. The theory can be described in terms of three parameters and these are usually taken to be α $(= e^2/4\pi)$, $\mathrm{G_F}$ and $\mathrm{M_Z}$ or $\sin^2\theta_\mathrm{W}$, where α and $\mathrm{G_F}$ have already been measured to high precision and the other parameter, $\mathrm{M_Z}$ or $\sin^2\theta_\mathrm{W}$, must also be determined. The model makes several predictions about experimental observables and these can be used to test the theory. Two of the most powerful predictions are the existence of the weak neutral current and the massive weak gauge bosons, the $\mathrm{W}^\pm$ and Z°.

Weak neutral currents were first observed in 1973 in the ν_μN scattering process [7]. Since then neutral currents have also been seen in other neutrino scattering processes and a fit to all such data [8] gives $\sin^2\theta_\mathrm{W} = 0.228 \pm 0.004$. The first direct observations of $\mathrm{W}^\pm$ and Z° bosons were reported by the UA1 and UA2 experiments at CERN in 1983 [9, 10, 11, 12]. The masses $\mathrm{M_W}$ and $\mathrm{M_Z}$ measured in these experiments agree well

with the predictions once higher order radiative corrections are taken into account. The measurements of M_Z from experiments at $\bar{p}p$ colliders (UA1, UA2 and CDF) are not as accurate as those now being achieved by the experiments at LEP. However, the ratio M_W/M_Z, in which many systematic errors cancel, is also measured by the hadron collider experiments and this can be combined with the LEP measurement of M_Z to give M_W. The combined result from UA2 and CDF gives $M_W = 80.13 \pm 0.22$ GeV [13] and $\sin^2\theta_W = 0.2275 \pm 0.0051$ which is in good agreement with the value determined from the neutrino–scattering experiments.

The discovery of the $W^{\pm}$ and Z^0 bosons at the Sp$\bar{p}$S provided the incentive to build an e^+e^- collider which could produce large numbers of these bosons in a very clean environment to allow more precise studies of the electroweak model. Two colliders were built, these are the SLC at Stanford, which is a linear collider, and LEP at CERN, which is a synchrotron. LEP currently operates at centre of mass energies of about 90 GeV in order to study the production and decay of Z^0 bosons.

Measurements of the Z^0 lineshape cross–sections give very precise determinations of the mass (M_Z) and width (Γ_Z) of the Z^0 and its partial decay widths to leptons and hadrons. A combination of the results from the four LEP experiments gives $M_Z = 91.175 \pm 0.021$ GeV [14]. The Z^0 resonance allows high statistics to be accumulated and these should result in the neutral couplings of the Z^0 to fermions and $\sin^2\theta_W$ being measured to greater precision than was previously possible. Within the Standard Model $\sin^2\theta_W$ depends on the masses of the top quark and Higgs boson through higher order corrections so with accurate measurements of $\sin^2\theta_W$ it is hoped to constrain these unknown masses. Also, a comparison of the values of $\sin^2\theta_W$ from different measurements at LEP and from other sources (such as ν–N scattering and the weak boson masses) constitutes an important test of the Standard Model. All results so far are in excellent agreement with the predictions of the electroweak sector of the Standard Model [14]. A direct search for the Higgs boson has been made and a mass limit of $m_H \geq 51$ GeV [15] is found at present.

In this thesis a study is made of the $\tau^+\tau^-$ final state from Z^0 decays at LEP. These events are used to determine some of the couplings of the electroweak model. In the remainder of this chapter a short overview of τ physics is given followed by a description of the quantities to be measured and how they relate to the neutral coupling constants.

1.3 τ Physics

It has already been mentioned that in the Standard Model the τ is placed in a third lepton doublet with its associated neutrino, ν_τ. The discovery of the τ was based on the observation of 64 anomalous $ee \rightarrow e\mu$ events with associated missing energy in the MARK I experiment at SPEAR [16]. The events were seen at centre of mass energies of about 4 GeV so there was initially some confusion as to whether or not they were due to charm production. More data followed [17] and confirmed that the events were due to pair production of particles with three body decays. The undetected particles carrying off missing energy were found to be νs (through elimination of all other sources). These observations were, therefore, attributed to the process:

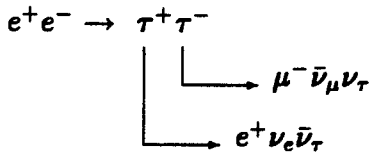

i.e. pair production of a new heavy lepton called τ, after the greek word $\tau\rho\iota\alpha$ meaning three since it was the third charged lepton to be discovered. An analysis of the energy dependence of the τ production cross–section close to threshold revealed the τ to have a mass of about 1.8 GeV and that it was indeed a spin–$\frac{1}{2}$ particle. The fact that production occurred below the threshold for charm production ruled out the possibility that the observation was in some way related to leptonic decays of charm.

Prior to the discovery of the τ, all the known fundamental fermions fitted into two generations. Thus the τ presented a puzzle which could only be resolved by postulating the third fermion generation. This assignment of the τ as a "sequential" charged lepton has immediate consequences for its properties. In particular, the τ lifetime and decays should be described by the charged weak current. Since its discovery, extensive studies of the τ have been made at e^+e^- colliders and reviews of these results can be found in references [18] and [19]. Here the main results are summarised and some remaining discrepancies are discussed.

1.3.1 Properties of τ

As mentioned above, the τ is a spin–$\frac{1}{2}$ fermion and its mass has been measured to be $1784.1^{+2.7}_{-3.6}$ MeV [6]. The mass was measured from detailed studies of the behaviour of the production cross–section near threshold, assuming the τ to be a pointlike spin–$\frac{1}{2}$ fermion. The behaviour of the production cross–section also depends on the spin of the τ and data have been found to be in good agreement with a spin assignment of $\frac{1}{2}$ but are inconsistent with the τ having a spin of 0, 1 or $\frac{3}{2}$ [20, 21]. The τ decay process is shown in figure 1.1. The nature of the τ^-–W^-–ν_τ vertex has been studied through

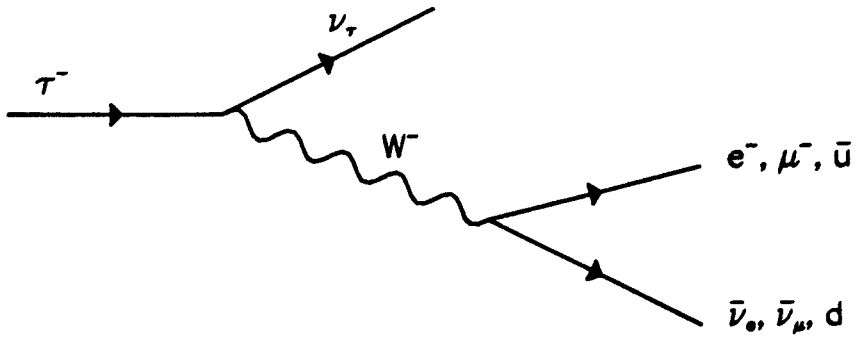

Figure 1.1: The τ decay process.

the energy spectra of the leptonic decay products of the τ which can be parameterised in terms of the Michel parameter [22], ρ. The measured value of ρ is 0.70 ± 0.06 [6] which agrees well with the predicted value of $\rho = 0.75$ assuming a V-A coupling.

The tau lifetime, τ_τ, can be measured in two ways. The first is to study the impact parameter (point of closest approach to the origin in the plane transverse to the beam) distribution of tracks from τ decays. A second method is to reconstruct the τ decay vertex for 3–prong decays and to measure the decay length. Measurements have been significantly improved by the use of high precision vertex drift chambers and the world average value of the lifetime was $\tau_\tau = (3.03 \pm 0.08).10^{-13}$ s [6] prior to the start of LEP. The LEP experiments have also measured the τ lifetime and the results are shown in table 1.2 along with an update of the world average value [23], which also includes a measurement from CLEO [24]. The measurements from the LEP experiments are statistics limited at the moment but the average LEP result is already comparable to the previous world average. With continued data taking at LEP it is expected that the

Table 1.2: Recent measurements of the τ lifetime, τ_τ taken from reference [23].

Experiment	τ_τ (10^{-13}s)
ALEPH	2.76 ± 0.17
DELPHI [25]	3.14 ± 0.25
L3 [26]	3.09 ± 0.38
OPAL [27]	3.13 ± 0.17
LEP average	2.99 ± 0.10
CLEO [24]	3.10 ± 0.17
New world average	3.03 ± 0.06

statistical errors should soon decrease. In addition, the introduction of high precision silicon vertex detectors in the LEP experiments means that the systematic errors can also be expected to decrease substantially.

As will be discussed in section 1.3.2 the measured value of τ_τ can be used to predict the $\tau \rightarrow e\nu_\tau\bar{\nu}_e$ branching ratio. In this area, however, the observed measurements show some discrepancy from those predicted. At this point it is worth noting from table 1.2 that the ALEPH measurement of τ_τ is lower than both the world average and that from the other LEP experiments. This may be simply due to a statistical fluctuation. However, ALEPH have used a new impact parameter method to measure τ_τ [23] so the observed discrepancy may be due to a bias in either the ALEPH or traditional methods. The latter possibility is interesting as it may resolve the discrepancy between the lifetime and leptonic branching ratio measurements.

There has been no direct observation of the τ neutrino, ν_τ, i.e. no observation of particles coming from interactions of ν_τs, but its existence is inferred from the kinematics of τ decays and its spin has been found to be $\frac{1}{2}$ [28]. Limits on the ν_τ mass can be made from measurements of the endpoint of the hadronic mass spectrum in multipion τ decays where the kinetic energy of the ν_τ is zero and:

$$m_{\nu_\tau} = m_\tau - m_{\text{hadrons}}$$

The best limit has been reported by ARGUS from a measurement of the $5\pi^\pm$ mass spectrum and m_{ν_τ} is found to be less than 35 MeV at 95% C.L. [29].

Our present knowledge of τ physics is based on results from e^+e^- colliders where the clean environment makes study of couplings relatively straightforward. In hadron colliders the QCD backgrounds make the observation of τs through their decays difficult. However, the importance of τs at hadron colliders has been shown by the UA1 experiment which has observed the semihadronic decay of τs from W decays. A comparison with measurements of $W \rightarrow e\bar{\nu}_e$ events gives $g_\tau/g_e = 1.01 \pm 0.09 \pm 0.05$ [30]. UA2 have performed a similar analysis and the technique is now being used by CDF.

1.3.2 Branching Ratios

The τ, unlike the other known leptons, is heavier than the π, enabling it to decay hadronically. The τ decay process is shown in figure 1.1 and there is also a Cabbibo suppressed decay to $\bar{u}s$. The quarks are not observed directly but appear as hadrons. From a simple consideration of the diagram in figure 1.1 it is possible to estimate crudely the branching ratios of the leptonic and semi-leptonic τ decays. Taking into account the colour factor of 3 for the quarks, the branching ratios for e, μ and hadrons are expected to be roughly in the proportions 1:1:3, i.e. 20%:20%:60%. The observed branching ratios are given in table 1.3. The leptonic branching ratios are reasonably close to those naively predicted. The hadronic branching ratio is modified by QCD effects and resonances which were not taken into account in the above argument.

Topological Branching Ratios

The topological, or inclusive, branching ratios are obtained by simply counting the number of charged particles in the τ decay. The measurement is straightforward, though a good understanding of tracking efficiency and conversion rates is required. The world average measured values are given in table 1.3. It has been noted by various authors (for example [31] and [32]) that the sum of the exclusive branching ratios for the 1–prong decay do not account for the measured inclusive 1–prong branching ratio. This has led to speculation about missing decay modes and provides impetus for new, more accurate measurements of all 1–prong branching ratios. Recent CELLO [33], TPC [34] and ALEPH [35] results show no discrepancy.

Table 1.3: Observed branching ratios for the most important τ decays. The data in the first column are from the Particle Data Group 1990 [6] and those in the second column are taken from reference [23] and incorporate more recent results including those from LEP.

Decay mode	Branching Ratio	
	World average	Updated value
$\tau^- \rightarrow e^- \nu_\tau \bar{\nu}_e$	17.7 ± 0.4	17.91 ± 0.24
$\tau^- \rightarrow \mu^- \nu_\tau \bar{\nu}_\mu$	17.8 ± 0.4	17.49 ± 0.24
$\tau^- \rightarrow (\text{hadron}^-)\nu_\tau +$ neutrals	50.3 ± 0.6	-
$\tau^- \rightarrow \pi^- \nu_\tau$	11.6 ± 0.6	12.0 ± 0.3
$\tau^- \rightarrow \rho^- \nu_\tau$	22.7 ± 0.8	23.0 ± 0.6
$\tau^- \rightarrow 1 - \text{prong}$	86.13 ± 0.33	85.89 ± 0.22
$\tau^- \rightarrow 3 - \text{prong}$	13.76 ± 0.32	14.02 ± 0.22
$\tau^- \rightarrow 5 - \text{prong}$	0.113 ± 0.027	0.110 ± 0.024

Leptonic Branching Ratios

By calculating the matrix element corresponding to figure 1.1, integrating over phase space and spins and assuming the masses of the ν_τ and e to be negligible, the width for the $\tau \rightarrow e\nu_\tau\bar{\nu}_e$ decay is found to be [18]:

$$\Gamma(\tau \rightarrow e\nu_\tau\bar{\nu}_e) = \frac{g_\tau g_e m_\tau^5}{192\pi^3}$$

Where g_f is the coupling constant of the fermion, f, to the W. In the Standard Model the τ and μ leptons have the same couplings to the electromagnetic and weak currents and the decay $\mu \rightarrow e\nu_\mu\bar{\nu}_e$ can be calculated in an exactly analogous way to the $\tau \rightarrow e\nu_\tau\bar{\nu}_e$ decay. This leads to the relationship:

$$\frac{\Gamma(\tau \rightarrow e\nu_\tau\bar{\nu}_e)}{\Gamma(\mu \rightarrow e\nu_\mu\bar{\nu}_e)} = \frac{g_\tau}{g_\mu}\left(\frac{m_\tau}{m_\mu}\right)^5$$

Since the width (Γ) is related to the branching ratio (BR) and the lifetime (τ) by $\Gamma = \text{BR}/\tau$, and the μ can decay only to an electron ($\text{BR}(\mu \rightarrow e\nu_\mu\bar{\nu}_e)$= 100%), this becomes:

$$\text{BR}(\tau \rightarrow e\nu_\tau\bar{\nu}_e) = \frac{g_\tau}{g_\mu}\frac{\tau_\tau}{\tau_\mu}\left(\frac{m_\tau}{m_\mu}\right)^5 \qquad (1.5)$$

which relates the $\tau \rightarrow e\nu_\tau\bar{\nu}_e$ branching ratio to the masses and lifetimes of the τ and μ. Using the current world average values for τ_τ, τ_μ, m_τ and m_μ and assuming lepton universality ($g_\mu = g_\tau$) the $\tau \rightarrow e\nu_\tau\bar{\nu}_e$ branching ratio is predicted to be $18.9 \pm 0.4\%$. The discrepancy between this and the measured value given in table 1.3 is 2.1σ. Alternatively, using the measured branching ratio, the ratio of the τ and μ couplings can be determined to be:

$$\frac{g_\tau}{g_\mu} = 0.948 \pm 0.024$$

This 2.1σ deviation from the prediction of lepton universality is not statistically significant but has been persistent and provides further incentive for making accurate measurements of the $\tau \rightarrow e\nu_\tau\bar{\nu}_e$ branching ratio.

The width of the $\tau \rightarrow \mu\nu_\tau\bar{\nu}_\mu$ decay can be calculated in an entirely analogous way to the $\tau \rightarrow e\nu_\tau\bar{\nu}_e$ decay except that the mass of the μ cannot be neglected and this leads to a phase space factor given by:

$$\frac{\mathrm{BR}(\tau \rightarrow \mu\nu_\tau\bar{\nu}_\mu)}{\mathrm{BR}(\tau \rightarrow e\nu_\tau\bar{\nu}_e)} = 0.973$$

The most recent measured values in table 1.3 give the ratio of the branching ratios to be 0.976 ± 0.019 which is in good agreement with the prediction.

Hadronic Branching Ratios

As mentioned in section 1.3.2, the τ is massive enough to have hadronic decay modes. Some of the more important branching ratios are given in table 1.3. It is possible to predict the $\tau \rightarrow \pi\nu_\tau$ branching ratio by using the $\pi \rightarrow \mu\bar{\nu_\mu}$ decay to find the strength of the W^-–$\bar{\mathrm{u}}$–d vertex. The theory predicts that

$$\frac{\mathrm{BR}(\tau \rightarrow \pi\nu)}{\mathrm{BR}(\tau \rightarrow e\nu_\tau\bar{\nu}_e)} = 0.601$$

and the experimental value of 0.62 ± 0.03 [6] is in good agreement with this. Similar calculations are possible for other hadronic decay modes and good agreement is seen between the predictions and measurements [19].

1.4 $e^+e^- \rightarrow \tau^+\tau^-$ at LEP

1.4.1 Lowest order process

The process $e^+e^- \rightarrow \tau^+\tau^-$ occurs to lowest order via photon or Z° exchange as shown in figure 1.2. These diagrams apply to production of all charged fermions except for e^+e^- where the t–channel process is also important. The cross–section predicted by the Standard Model from these diagrams is shown in figure 1.3 as a function of centre of mass energy. At low energy the QED process of photon exchange is dominant and the cross–section falls as $1/s$. At the energies achieved by LEP the resonance production of the Z° is seen. This cross–section can be calculated from the electroweak Lagrangian. At high energies ($s \gg m_\tau^2$) and for the Born level diagrams of figure 1.2 alone the cross–section is given by:

$$\frac{d\sigma}{d\Omega}(s,\cos\theta) = \frac{\alpha^2}{4s}\left\{(1+\cos^2\theta)\ F_0(s) + 2\cos\theta\ F_1(s)\right\} \tag{1.6}$$

where

$$F_0(s) = q_e^2 q_f^2 + 2v_e v_f q_e q_f \mathrm{Re}(\chi_0(s)) + (v_e^2+a_e^2)(v_f^2+a_f^2) \mid \chi_0(s) \mid^2 \tag{1.7}$$

$$F_1(s) = 2a_e a_f q_e q_f \mathrm{Re}(\chi_0(s)) + 4v_e a_e v_f a_f \mid \chi_0(s) \mid^2 \tag{1.8}$$

and,

$$\chi_0(s) = \frac{s}{s - {M_Z}^2 + iM_Z\Gamma_Z^0} \frac{1}{(4\sin\theta_W\cos\theta_W)^2}$$

is the Z° propagator. Γ_Z^0 is the lowest order expression for the total width of the Z° with summation over all possible final states, $f\bar{f}$. Γ_Z^0 is given by:

$$\Gamma_Z^0 = \sum_f N_c^f \frac{\alpha}{s} M_Z\ (v_f^2+a_f^2) \frac{1}{(4\sin\theta_W\cos\theta_W)^2} \tag{1.9}$$

The terms in equations 1.7 and 1.8 can be attributed to pure photon exchange ($q_e^2 q_f^2$), pure Z° exchange (terms in $\mid \chi_0(s) \mid^2$) and γ–Z° interference terms (terms in $\mathrm{Re}(\chi_0(s))$). Close to the Z° resonance the $\mathrm{Re}(\chi_0(s))$ disappears and the cross–section is dominated by the Z° exchange terms.

The $\cos\theta$ term in equation 1.6 means that the cross–section is asymmetric as a function of $\cos\theta$. In order to discuss this and other asymmetries more fully, the cross–section is considered before summation over spins.

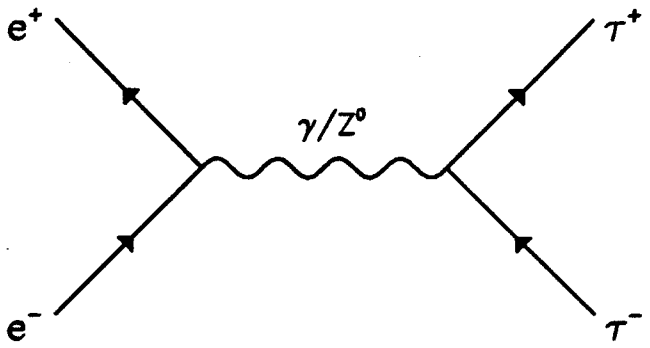

Figure 1.2: The $e^+e^- \rightarrow \tau^+\tau^-$ production process.

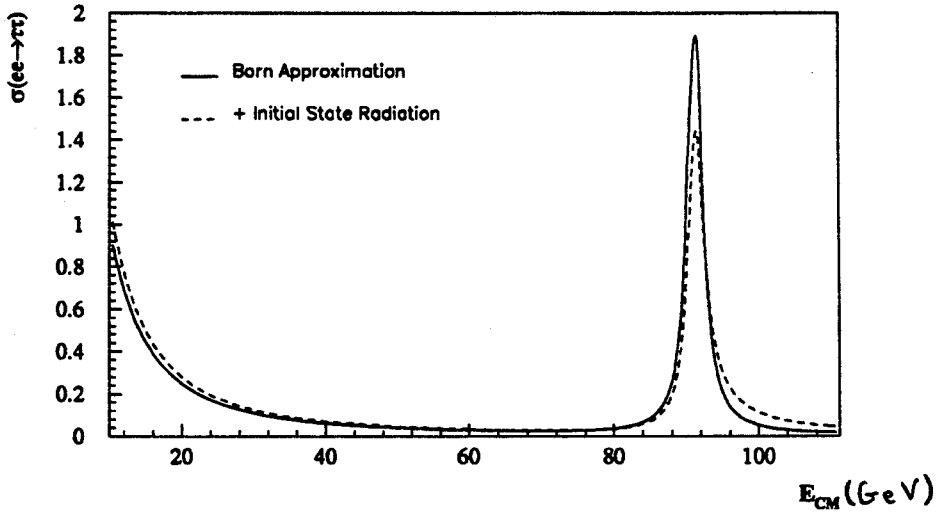

Figure 1.3: $\sigma(e^+e^- \rightarrow \tau^+\tau^-)$ as a function of E_{CM}.

1.4.2 Asymmetries

Asymmetries arise due to the chiral nature of the couplings of the leptons to the Z°. The Z° couples more strongly to left handed fermions, f_L^-, than to right handed fermions, f_R^-. If the couplings to the left and right handed fermions are written l_f and r_f, respectively, then

$$l_f = v_f - a_f, \qquad r_f = v_f + a_f \tag{1.10}$$

where v_f and a_f are the couplings defined in section 1.2. Thus the production cross-section depends on the helicity state of the initial and final state fermions. Helicity conservation means that the Z° only couples right handed fermions to left handed an-

tifermions and vice–versa at annihilation and creation vertices. This means that there are four possible spin configurations for the process $e^+e^- \rightarrow \tau^+\tau^-$, namely $e^-_L e^+_R \rightarrow \tau^-_L \tau^+_R$, $e^-_L e^+_R \rightarrow \tau^-_R \tau^+_L$, $e^-_R e^+_L \rightarrow \tau^-_L \tau^+_R$ and $e^-_R e^+_L \rightarrow \tau^-_R \tau^+_L$. Conservation of angular momentum requires that in the forward direction ($\cos\theta$=1) a left handed electron gives rise to a left handed τ so the cross–sections for $e^-_L e^+_R \rightarrow \tau^-\tau^+$ are given by:

$$\begin{aligned}
\frac{d\sigma}{d\Omega}(e^-_L e^+_R \rightarrow \tau^-_L \tau^+_R) &\propto \frac{\alpha^2}{4s}(1+\cos\theta)^2 \mid q_e q_\tau + \chi_0(s) l_e l_\tau \mid^2 \\
\frac{d\sigma}{d\Omega}(e^-_L e^+_R \rightarrow \tau^-_R \tau^+_L) &\propto \frac{\alpha^2}{4s}(1-\cos\theta)^2 \mid q_e q_\tau + \chi_0(s) l_e r_\tau \mid^2
\end{aligned} \tag{1.11}$$

where θ is the angle of production of the τ^- with respect to the direction of motion of the e^-. There are similar expressions for the other two allowed helicity states. If all four helicity states are summed and averaged then the cross–section given in equation 1.6 is recovered. If, however, only the spin states of the initial state particles are summed then the cross–section can be written as:

$$\begin{aligned}
\frac{d\sigma}{d\Omega}(s,\cos\theta;p) &= \frac{\alpha^2}{4s}\left\{(F_0(s)(1+\cos^2\theta) + F_1(s)2\cos\theta)\right. \\
&\qquad \left. + p\,(F_2(s)(1+\cos^2\theta) + F_3(s)2\cos\theta)\right\}
\end{aligned} \tag{1.12}$$

where p is the longitudinal polarization of the τ, F_0 and F_1 are given in equations 1.7 and 1.8 and F_2 and F_3 are given by:

$$F_2(s) = 2v_e a_\tau q_e q_\tau \mathrm{Re}(\chi_0(s)) + 2(v_e^2+a_e^2)v_\tau a_\tau \mid \chi_0(s) \mid^2 \tag{1.13}$$

$$F_3(s) = 2a_e v_\tau q_e q_\tau \mathrm{Re}(\chi_0(s)) + 2v_e a_e (v_\tau^2+a_\tau^2) \mid \chi_0(s) \mid^2 \tag{1.14}$$

As has already been mentioned, asymmetries arise due to the chiral nature of the couplings of the Z° to the fermions, i.e. the fact that $l_f \neq r_f$. As will be shown below the asymmetries are related to the couplings, so a measurement of the asymmetries allows the couplings to be determined. Four such asymmetries are described below. The first of these is the forward backward asymmetry, A_{FB}, which is defined as:

$$A_{FB}(s) = \frac{\sigma(\cos\theta > 0) - \sigma(\cos\theta < 0)}{\sigma(\cos\theta > 0) + \sigma(\cos\theta < 0)}$$

The $\cos\theta$ term in equation 1.6 leads to a non–zero value for A_{FB}:

$$A_{FB}(s) = \frac{3}{4}\frac{F_1}{F_0} \tag{1.15}$$

$$\sim \frac{3}{4}\frac{-2v_e a_e}{(v_e^2+a_e^2)}\frac{-2v_\tau a_\tau}{(v_\tau^2+a_\tau^2)} \tag{1.16}$$

where the expression given in terms of the couplings in equation 1.16 is only true close to the Z° peak where the real part of $\chi_0(s)$ vanishes. For ease of notation λ_i is defined as:

$$\lambda_i = \frac{-2v_i a_i}{(v_i^2 + a_i^2)}$$

where i can be e, μ, or τ. Since $\sin^2\theta_W$ has been measured to be close to 0.25, the vector coupling (given in equation 1.4) is small, therefore $\lambda_i \sim -2v_i/a_i$. Thus, a measurement of A_{FB}, which measures the product $\lambda_e\lambda_\tau$, is sensitive to the vector coupling and, as can be seen from table 1.1, can be used to determine $\sin^2\theta_W$.

A second asymmetry arising from the chiral nature of the couplings is the polarization asymmetry which is defined as:

$$P_\tau(s) = \frac{\sigma(e^+e^- \to \tau_L^-\tau_R^+) - \sigma(e^+e^- \to \tau_R^-\tau_L^+)}{\sigma(e^+e^- \to \tau_L^-\tau_R^+) + \sigma(e^+e^- \to \tau_R^-\tau_L^+)} = \frac{\sigma(p=+1) - \sigma(p=-1)}{\sigma(p=+1) + \sigma(p=-1)}$$

This is found by integrating equation 1.12 and is given by:

$$P_\tau(s) = -\frac{F_2}{F_0} \tag{1.17}$$

$$\sim \frac{-2v_\tau a_\tau}{(v_\tau^2 + a_\tau^2)} = \lambda_\tau \tag{1.18}$$

where, as in the case of A_{FB}, equation 1.18 only holds at the Z° peak. This is more sensitive to the vector coupling than A_{FB} because it is related directly to v rather than to v^2. However, it is also harder to measure. The τ polarization, P_τ, is strongly dependent on the production angle, θ, of the τ^- with respect to the e^- direction:

$$P_\tau(s, \cos\theta) = -\frac{(1+\cos^2\theta)F_2(s) + 2\cos\theta F_3(s)}{(1+\cos^2\theta)F_0(s) + 2\cos\theta F_1(s)}$$

This dependence is shown in figure 1.4 (a). A forward–backward polarization asymmetry can be defined as:

$$A_{pol}^{FB} = \frac{1}{2}(P_\tau^F - P_\tau^B) = -\frac{3}{4}\frac{F_3}{F_0} \sim \frac{3}{4}\lambda_e \tag{1.19}$$

where P_τ^F and P_τ^B are the polarization asymmetries in the forward ($\cos\theta > 0$) and backward hemispheres, respectively.

One further asymmetry, A_{LR}, can be defined:

$$A_{LR} = \frac{\sigma(e_L^-e_R^+ \to f\bar{f}) - \sigma(e_R^-e_L^+ \to f\bar{f})}{\sigma(e_L^-e_R^+ \to f\bar{f}) + \sigma(e_R^-e_L^+ \to f\bar{f})} = -\frac{F_2}{F_0}$$

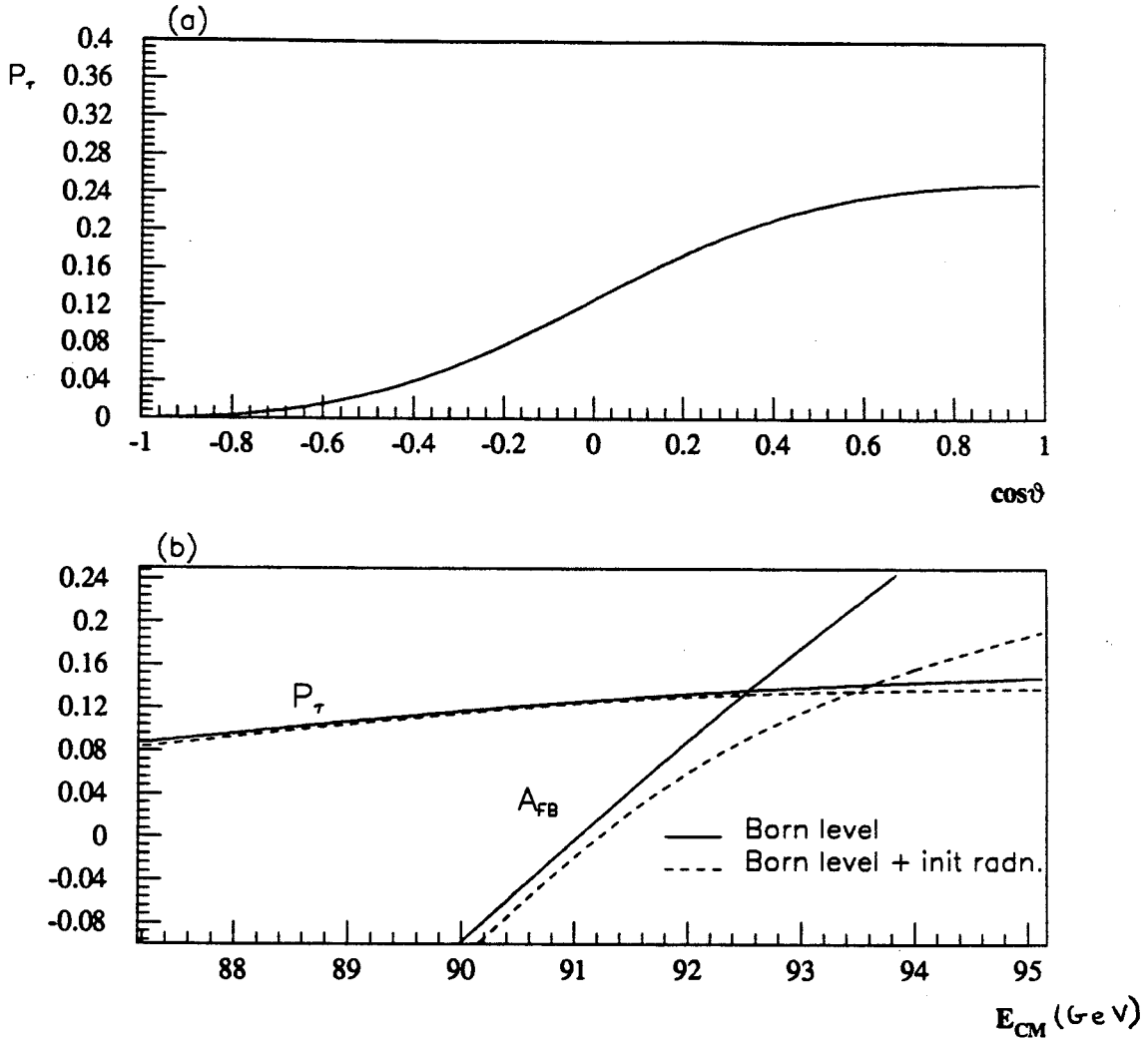

Figure 1.4: (a) P_τ as a function of cosθ. (b) P_τ and A_{FB} as functions of E_{CM}.

and at the Z° peak $A_{LR} \sim \lambda_e$. This is as sensitive to the vector couplings as P_τ and is considerably easier to measure. However, it can only be measured if polarized initial state electrons and positrons are available and this is not yet the case at LEP, although it is planned for the future.

In this thesis measurements of P_τ and A_{pol}^{FB} are described. These are used to determine the couplings of the Z° to the τ and e leptons through equations 1.18 and 1.19. A comparison of the results with predictions and other measurements is a test of the Standard Model. Also, comparison of the two sets of couplings tests the assumption of lepton universality. The polarization measurements have the advantage over measurements of the forward–backward asymmetries that they are more sensitive to the

couplings as can be seen from a comparison of equations 1.16 and 1.18. Also, as can be seen from figure 1.4 (b), the polarization asymmetry is less dependent on the centre of mass energy which means that the initial state radiation corrections are much smaller [36].

There are, of course, also some disadvantages to the polarization measurement, these arise due to the fact that the polarization of the τ is measured through the τ decay product distributions. Since this is possible for only some τ decay modes a substantial loss in statistics occurs. Also the problems of identifying the decay products lead to larger backgrounds.

1.4.3 Radiative Corrections

The expressions for the $e^+e^- \rightarrow \tau^+\tau^-$ cross–section given in equations 1.6 and 1.12 are only valid for the lowest order Born level diagram shown in figure 1.2. In higher orders the cross–sections are modified significantly by radiative corrections. Some of the diagrams which contribute to the $O(\alpha)$ corrections are shown in figure 1.5, these are usually split into two classes. The first class are the QED corrections arising from real single photons or virtual photon loops being added to the lowest order diagram, for example figures 1.5 (a), (b) and (c). The second class of corrections are non–QED, or weak, corrections and include all other diagrams such as vertex corrections, propagator corrections and box diagrams, figures 1.5 (d), (e) and (f), respectively.

The weak, or non–QED, radiative corrections occur via loops and self–interaction of the gauge fields. They have no dependence on experimental cuts and are usually small, $O(10^{-2})$. They do, however, depend on the unknown parameters in the Standard Model such as the masses of the top quark and the Higgs boson, m_t and m_H, since these particles appear in virtual loops. If precise enough measurements can be made, the radiative corrections can be measured and used to limit these unknown masses. Since new particles related to non Standard Model physics can also occur in loops the radiative corrections also give an insight into new physics. To calculate the weak radiative corrections, a renormalisation scheme must be chosen in order to deal with divergences arising from the higher order corrections. A scheme is chosen in which the non–QED corrections are small. The favoured scheme is the, so–called, 'on–shell'

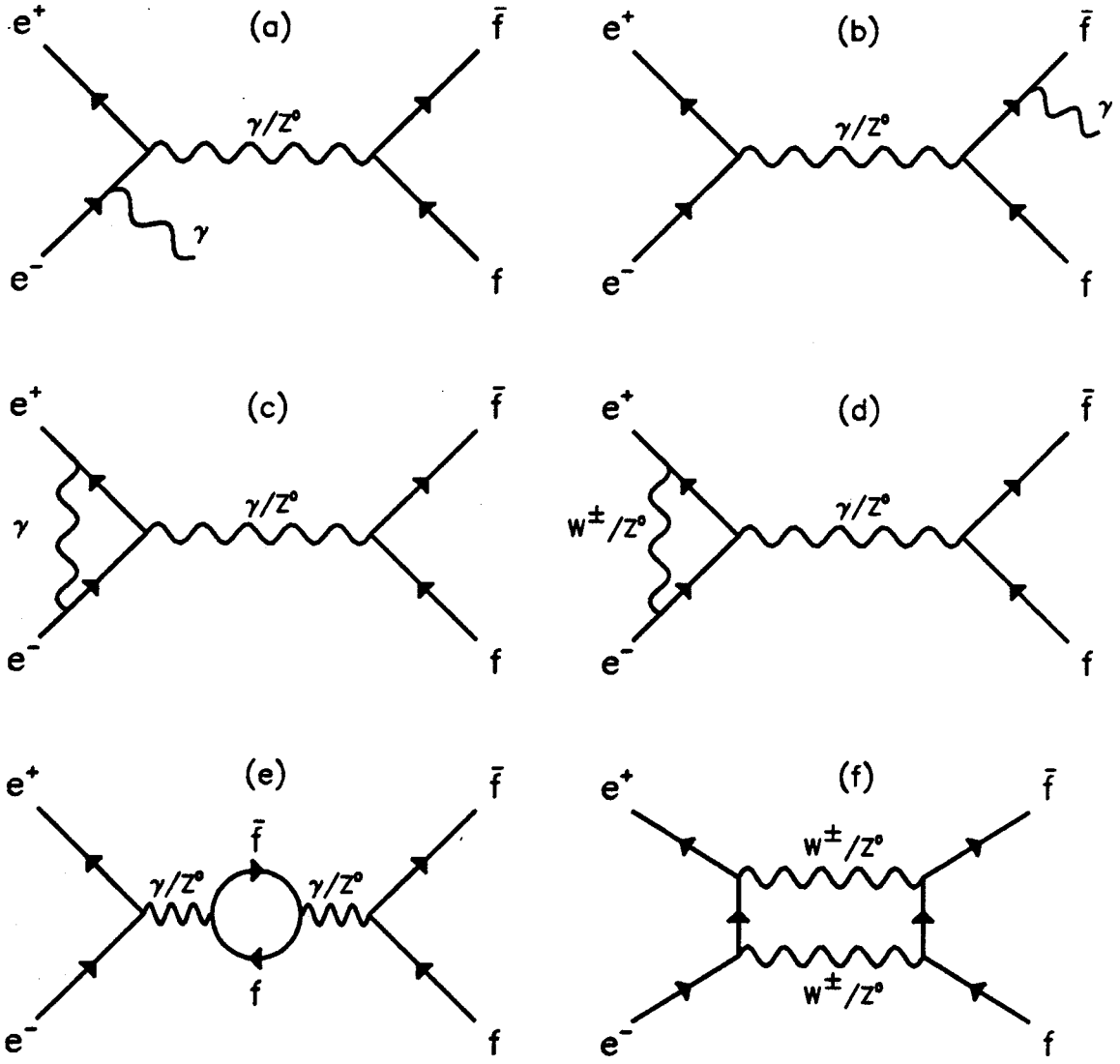

Figure 1.5: Some O(α) radiative corrections.
(a) Initial state radiation. (b) Final state radiation. (c) Vertex correction.
(d) Vertex correction. (e) Propagator correction. (f) Box diagram.

scheme in which the model is defined by the parameters α, G_F, m_Z, m_H and m_f and

$$\sin^2\theta_W = 1 - \frac{M_W^2}{{M_Z}^2}$$

This scheme has the advantage that the input parameters have a clear physical meaning and, apart from the unknowns m_H and m_t, can be precisely measured experimentally.

Close to the Z° resonance the effects of the vacuum polarization and vertex corrections can be absorbed by replacing the couplings by running couplings (the box corrections are small and non–resonant and so can be neglected). In this approximation the amplitude retains a born–like form and this is, therefore, known as the 'Improved Born Approximation'. Measurement using the Improved Born Approximation give $\sin^2\bar{\theta}_W$ which is defined as:

$$\sin^2\bar{\theta}_W = 1 - \frac{M_W^2}{\rho {M_Z}^2}$$

where the parameter ρ depends quadratically on m_t and logarithmically on m_H. Therefore, comparisons with $\sin^2\theta_W$, as determined by measurements of M_Z and M_W, probe the radiative corrections and hence m_t .

The QED corrections are not so interesting in that they do not depend on the underlying non–QED theory. They are, however, the largest contribution and as such must be well understood. Initial and final state corrections are usually treated separately and initial state bremsstrahlung has the largest effect. Initial state radiation reduces the centre of mass energy of the annihilating e^+e^- pair and thus alters the cross–section. This results in a 30% reduction in the peak cross–section and a shift of about 110 MeV, as can be seen in figure 1.3. Final state radiation gives rise to $f\bar{f}\gamma$ events where the photon may or may not be observed, depending on experimental cuts. Therefore, it is important to model such events and this can be done using Monte Carlo programs. In calculations, soft and hard bremsstrahlung are treated separately, with an artificial energy cut–off, which must be below experimentally observable photon energies, used to discriminate between them. Complete calculations of QED corrections to $O(\alpha)$ exist with leading log series to $O(\alpha^2)$ and exponentiation of soft photons to all orders.

1.4.4 Monte Carlo

In order to compare data with theoretical expectations, including radiative corrections, Monte Carlo (MC) simulations or semi-analytic calculations are used. These implement the 'well understood' theory in software to give predictions about experimental observables. Monte Carlo programs actually produce 'events' which can have cuts imposed on them just as the data do. Although this makes the MC programs slower, it is an advantage over semi-analytic calculations, for which inclusion of all but the simplest of experimental cuts is not possible. Obviously in order to measure parameters of the electroweak model to high precision the MC used must also be precise. In this thesis extensive use is made of the KORALZ [37] MC for fermion pair production in electron-positron annihilation, $e^+e^- \to f\bar{f}$. Where the fermion, f, can be any of μ, ν, u, d, s or c (and with some restrictions b) as well as τ.

KORALZ includes the effects of multiple hard QED bremsstrahlung in the initial state with terms up to leading log in $O(\alpha^2)$ and exponentiation of soft photons. Final state radiation is restricted to first order. There are no initial-final state interference effects included in the case of multiple initial state bremsstrahlung but these effects have been shown to be negligibly small [38]. $O(\alpha)$ radiative corrections from the electroweak model are also included. Longitudinal spin polarization of the electron and positron beams is possible within the program.

The MC simulates the following decays of the τ:

$$\tau \to e\nu_\tau\bar{\nu}_e \quad \tau \to \mu\nu_\tau\bar{\nu}_\mu \quad \tau \to \pi\nu_\tau \quad \tau \to \rho\nu_\tau \quad \tau \to a_1\nu_\tau$$

$$\tau \to K\nu_\tau \quad \tau \to K^*\nu_\tau \quad \tau \to 4\pi\nu_\tau \quad \tau \to 5\pi\nu_\tau \quad \tau \to 6\pi\nu_\tau$$

which constitute over 99.9% of the decay width. Spin polarization effects in the final state τ decay are fully simulated in all but the multi-pion decay modes. Single bremsstrahlung is allowed in the most important τ decays ($\tau \to e\nu_\tau\bar{\nu}_e$, $\tau \to \mu\nu_\tau\bar{\nu}_\mu$, $\tau \to \pi\nu$, $\tau \to \rho\nu_\tau$, $\tau \to K\nu$ and $\tau \to K^*\nu$) although this is in the leading log approximation only.

1.5 Outline of thesis

In summary, the electroweak theory has been very successful in describing observed phenomena. The data from LEP will allow more precise tests to be made in this area and one measurement of interest is the τ polarization. τ physics has been extensively studied at previous e^+e^- colliders but there are some discrepancies which still need to be resolved. One of the important measurements to make is the $\tau \rightarrow e\nu_\tau\bar{\nu}_e$ branching ratio. In this thesis, τ pair events from the data collected with the OPAL experiment in 1990 are used to measure the $\tau \rightarrow e\nu_\tau\bar{\nu}_e$ branching ratio. The $\tau \rightarrow e\nu_\tau\bar{\nu}_e$ events are also used to measure the τ polarization.

Before going on to discuss these measurements, descriptions of the OPAL detector and one of its main trigger components, the track trigger, are given. These are followed by a discussion of the event selection, both for $e^+e^- \rightarrow \tau^+\tau^-$ events and for the $\tau \rightarrow e\nu_\tau\bar{\nu}_e$ decays and then the measurements themselves are presented.

Chapter 2

The OPAL detector

2.1 The LEP Machine

LEP is an electron–positron collider which was designed to study physics processes in the clean environment of e^+e^- annihilation events at energies of up to 200 GeV. In its initial phase LEP operates at centre of mass energies of up to 110 GeV, producing Z° bosons. A planned second stage of the machine will almost double the beam energy by using superconducting accelerating cavities and this will allow production of W^+W^- and Z° pairs.

Bunches of electrons and positrons are accelerated around LEP, which is built in a 27 km long underground tunnel, and are collided at four points around the ring. The large radius of the machine is needed to reduce energy losses from the effects of synchrotron radiation which increase inversely with the radius of curvature. The tunnel is not quite circular and has eight curved and eight straight sections. Large multipurpose particle detectors are installed at the collision points which are in four of the straight sections, thus reducing the synchrotron radiation in the detectors. Four bunches of electrons and positrons circulate around the machine in a vacuum pipe through the centre of magnets which steer and focus the beams. The vacuum is maintained at 10^{-9} Torr when beam is in the machine and drops to 10^{-10} Torr without beam.

Particles are injected into LEP through a series of already existing CERN accelerators, see figure 2.1. The electrons and positrons are produced in a linac and are initially accelerated to energies of 660 MeV before being accumulated in a small storage ring, EPA. The particles are bunched and fed into the Proton Synchrotron, PS, where they

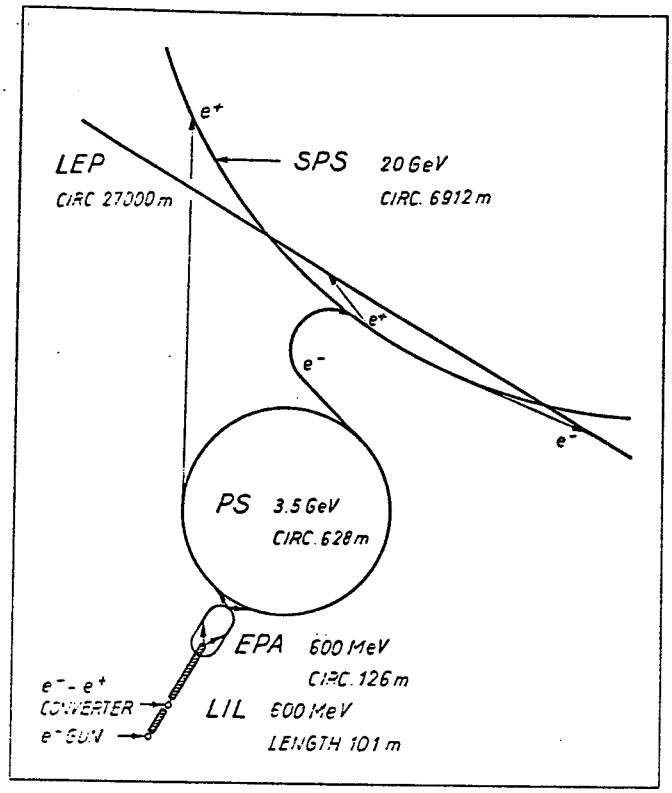

Figure 2.1: The series of accelerators used for injection of electrons and positrons into LEP.

are accelerated to 3.5 GeV before injection into the Super Proton Synchrotron, SPS. Once in the SPS the bunches are accelerated to 20 GeV and injected into LEP for final acceleration before the beams are collided in the interaction regions.

Radiofrequency (RF) accelerating cavities, positioned at two diametrically opposite points on the LEP ring, transmit energy to the beam particles in order to accelerate them and to replace the energy lost due to synchrotron radiation. There are 128 RF units, each with two cavities. The copper accelerating cavities are powered only as the particles pass and between bunches the RF power is stored in a second set of low loss cavities.

The first Z°s were seen by the LEP experiments in August 1989 and during the first running period until December that year a luminosity of 3×10^{30} cm^{-2}s^{-1} was achieved by the machine. In 1990 improvements saw the luminosity increase to $\sim 7 \times 10^{30}$ cm^{-2}s^{-1}.

2.2 OPAL – an overview

OPAL is one of the four large detectors built to take data at LEP. OPAL stands for Omni Purpose Apparatus for LEP. As the name suggests, it is an all–purpose detector designed to detect and measure all types of interacting particles produced in e^+e^- interactions at LEP. The detector covers almost the whole solid angle and consists of a number of components each designed to perform a different task within the detector. Figures 2.2 and 2.3 show the detector in cross section and from the side, illustrating the individual components (subdetectors).

The coordinate system for the detector is defined by a set of right handed axes. The z axis is along the e^- beam direction, the x axis is horizontal and points towards the centre of LEP and the y axis is vertical. A radius, r, is measured from the beam axis in the $x-y$ plane. Two angles, θ and ϕ, are also used. The polar angle, θ, is measured with respect to the z axis and the azimuthal angle, ϕ, is measured about the z axis with respect to the x axis. These coordinates are shown in figures 2.2 and 2.3.

The beampipe running through the centre of OPAL initially had a radius of 78 mm, this was reduced to 53 mm in 1991 to allow for a silicon detector to be added at the centre of the experiment[1]. The beampipe must cause as little scattering as possible to particles from the interaction point but must, at the same time, be strong enough to support the 4 bar pressure of the central tracking system. The pipe is made of carbon fibre composite epoxied onto a 0.1 mm thick aluminium tube and was made in three sections. The central section consists of a 1.3 mm layer of carbon fibre with two 5 mm thick strengthening rings, the two outer sections are made of 2 mm thick carbon fibre. The central section assembly is about 0.66% of a radiation length thick.

A central tracking detector surrounds the beampipe and provides the main tracking of charged particles in OPAL. This consists of three separate devices; the vertex chamber, the jet chamber and the z–chambers. All three are wire drift chambers but

[1]For the 1991 run a silicon detector consisting of two barrels of single sided detectors, giving $r-\phi$ coordinates close to the interaction point, was installed between two new beampipes at radii of 53 mm and 80.2 mm. The main purpose of the silicon detector is to aid secondary vertex reconstruction. The data analysed in this thesis are, however, from 1990 so the detector configuration appropriate to that period is described.

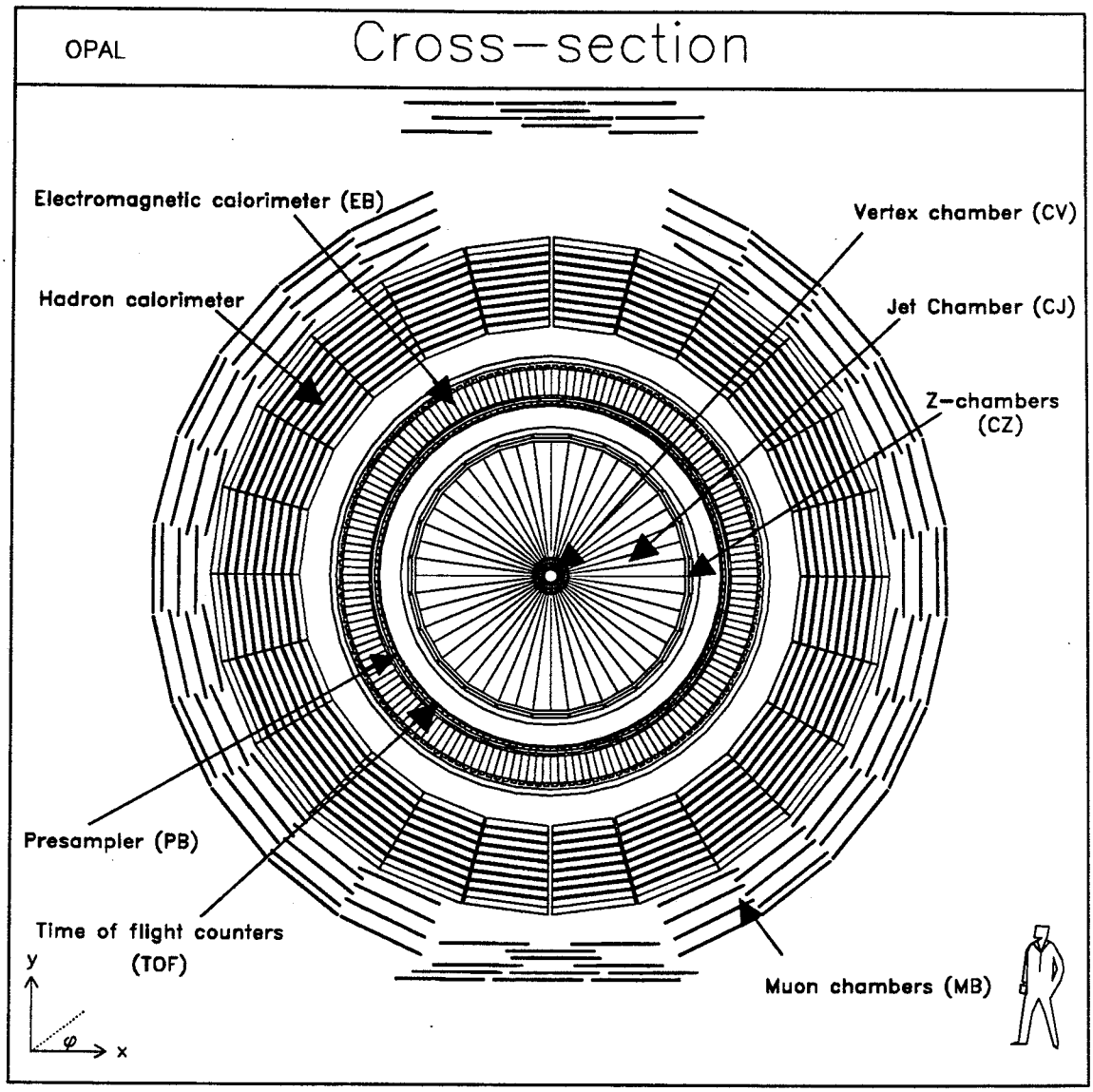

Figure 2.2: The OPAL detector in cross section, showing the individual components.

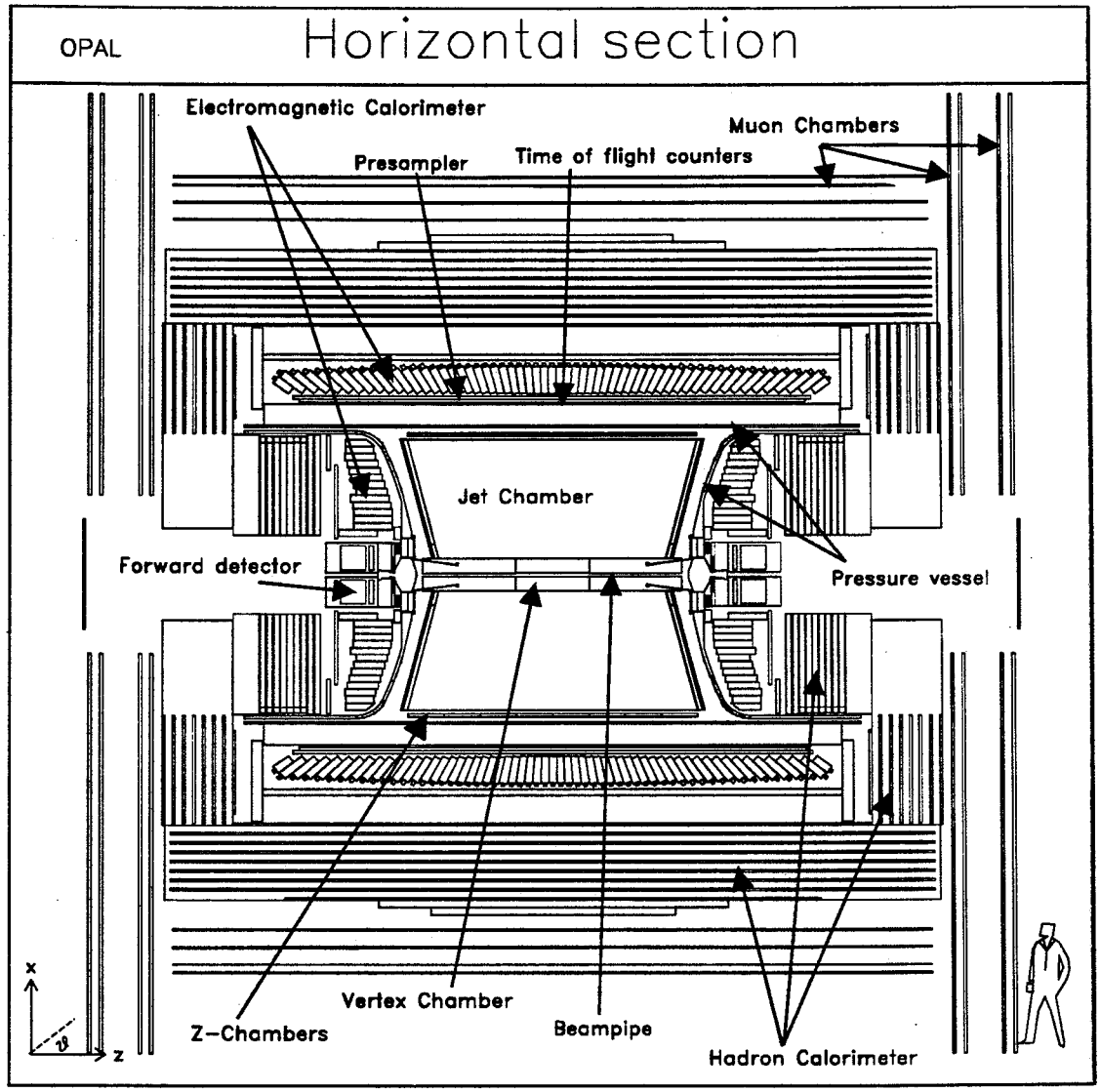

Figure 2.3: A side view of the OPAL detector.

are wired differently to perform different roles within OPAL. As well as tracking particles, the jet chamber also provides an energy loss, dE/dx, measurement for particle identification. The complete central detector operates at a pressure of 4 bar and is contained inside a cylindrical pressure vessel, closed at the ends by two bell shaped covers, as shown in figure 2.3.

The pressure vessel acts as a support for a solenoidal coil which provides an axial magnetic field within the central detector volume. The magnetic field causes charged particles to bend in the $r - \phi$ plane and the curvature of the tracks in the central detector is used to measure their momenta. The coil, like the beampipe, needs to cause as little scattering as possible to particles in the detector. To avoid excess material from support structures, the coil is self–supporting. The coil and pressure vessel together are 1.5 radiation lengths thick. A water cooled warm solenoid is used with a power consumption of about 5 MW, cooling and power were the limiting factors in the design of the magnet. A field of 0.435 T is produced within the central detector volume and this is uniform to within 0.5%. In order to achieve this uniformity and to reduce stray fields in the region outside the coil where photomultipliers are used, the coil was wound as a single unit.

A time of flight system, covering $| cos\theta | \leq 0.82$, is situated immediately outside the coil. This measures the flight time of particles from the interaction point and the information can be used for particle identification and for triggering. Beyond this an electromagnetic calorimeter measures the position and energy of electrons and photons. This calorimeter is made of 11 706 lead glass blocks and has three sections, a barrel and two endcaps. Just inside the electromagnetic calorimeter are a series of presampling devices used to improve the position and energy measurement for electromagnetic showers which start in the material before the lead glass.

Particles which traverse the electromagnetic calorimeter then encounter the 1 m thick iron return yoke of the magnet which is instrumented as a hadron calorimeter. The detector is finally surrounded by several layers of wire chambers to identify muons by measuring the position and direction of any particles which emerge from the iron.

To measure the luminosity of the colliding beams in LEP, there is a forward detector which detects and measures small angle Bhabha scattering events. This subdetector consists of two identical parts, one on each side of the detector surrounding the

beampipe, at the ends of the tracking chambers, see figure 2.3.

Electronics, for the readout and processing of the signals from the detector, are housed in 'rucksacks' and 'gondolas' which are huts situated on either side of the detector and suspended from the ceiling of the experimental hall. Typically 40 m of twisted pair or coaxial cable are used to carry the signals from the detector to the electronics in these huts. The detector is mounted on rails so that it can be moved out of the beam line to a 'garage' position. When this happens the huts move with the detector to prevent having to disconnect the cables. The detector also opens up to allow access to the central components.

Between LEP bunch crossings, which occur every 22 μs, signals from the detector are analyzed by the trigger to decide whether or not an e^+e^- interaction has occurred. If the trigger decision is negative the electronics are reset ready for the next beam-crossing and possible event. If an event is triggered then data from the front-end electronics are read out by each individual subdetector and combined at the 'event-builder'. From here the complete event, containing information from all subdetectors, is passed through a filter which classifies events into physics categories and rejects further background events. Once accepted by the filter an event is written to cartridge and stored, ready for offline reconstruction of the raw data.

The various components of the detector are described in more detail in the following sections with particular attention being given to those parts of the detector used by the track trigger and for the τ analysis described later. Further information can be found in reference [39].

2.3 Central detector

The OPAL central detector consists of three components all designed to provide tracking information for charged particles. At the centre of the detector is a high precision vertex chamber (CV), the aim of which is to measure secondary decay vertices of short lived particles. Surrounding the CV is a large volume jet chamber (CJ) which provides both good spatial resolution for tracks over almost the complete solid angle and good two track resolution for resolving individual tracks within jets. The CJ also provides a measure of the energy loss in the detector. Outside the CJ are a set of z-chambers

(CZ) which measure a precise z–coordinate for tracks and hence provide a good θ measurement which improves the mass resolution of short lived particles.

The gas used throughout the central detector is a mixture of 88.2% argon, 9.8% methane and 2.0% isobutane and is at a pressure of 4 bar. To achieve good resolution it is important to closely monitor gas properties such as drift velocity, electron attachment, etc. and to ensure that they remain constant over the long periods of running. Careful monitoring of the oxygen and water content, which affect such things, is done using a small test chamber. The central detector gas system is closed and has recirculation and purification facilities which keep the oxygen content at a level of a few ppm.

2.3.1 Vertex Chamber (CV)

The CV [40] was designed to provide accurate space point measurements on tracks close to the interaction point, it is a 1 m long cylindrical drift chamber with an outer diameter of 470 mm. The chamber is subdivided into 36 azimuthal cells, each of which has an axial part and a 'stereo' part. Each axial cell has 12 sense wires strung parallel to the beam at radii between 103 and 162 mm. The stereo cells each contain 6 sense wires inclined at an angle of $\sim 4^\circ$ to the z–axis, these lie at radii between 188 and 213 mm. The maximum drift distance within a cell is 2 cm.

The wires are strung between two 32 mm thick fibreglass endplates which are held 1 m apart by a 1.5 mm thick carbon fibre tube at the outer radius. At the inner radius, 88 mm, there is a mylar tube which provides the CV with a separate gas volume from the rest of the central detector, although in operation so far the same gas has been used throughout the central detector. The CV is supported from the endcones of the jet chamber which leaves it independent of the beampipe.

The geometry of three CV cells is shown in figure 2.4. The 12 sense wires in each axial cell form a radial plane; they are 5.3 mm apart and are interleaved with potential wires. In the stereo cells the anode wires are 5 mm apart. In both cases an anode plane is defined by the potential wires and the anode wires are staggered by ± 41 μm about it to allow the left–right ambiguity, which arises from the uncertainty about which side of the anode plane a hit originated from, to be resolved. The distance of an anode wire

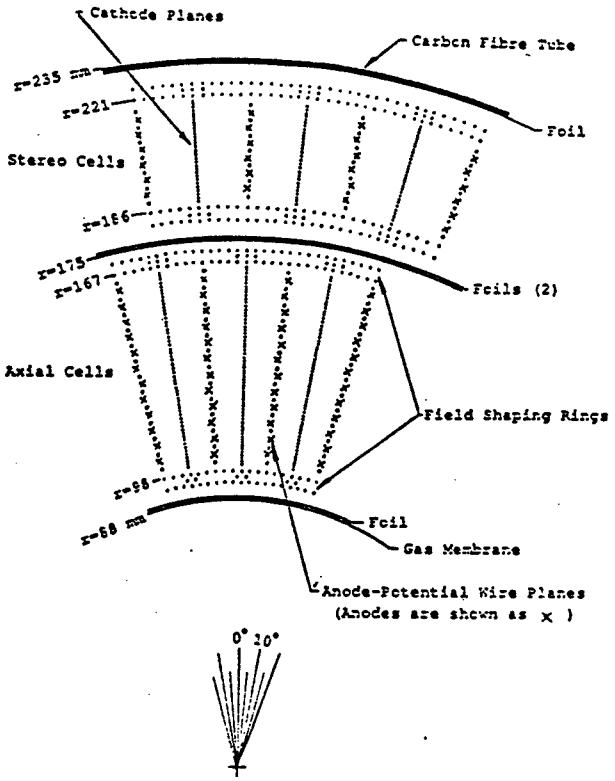

Figure 2.4: Endview of three cells of the vertex chamber, illustrating the layout of the wires.

from the anode plane may increase by up to a further 50–100 μm due to the action of electrostatic forces when the voltage is applied, this effect is known as 'bowing'. Each cathode plane is made of 125 μm Cu-Be wires spaced 1 mm apart. The position of the anode wires is known to better than ± 10 μm.

The electrostatic conditions within a cell are defined by the drift field and the anode surface field. The anode wires are at ground potential and the electric fields in each cell are determined by voltages applied to the potential wires, which determine the anode surface field, and the cathode wires, which determine the drift field. The tapered cell shape means that in order for the drift field, which is perpendicular to the anode plane, to be the same throughout the cell, the voltages on the cathode wires must increase with increasing radius. The drift field is uniform beyond about 2–3 mm from the anode wire. To ensure the same gain at each anode wire, the voltages on the potential wires are equal throughout a cell. The operating point used is a 2.5 kV/cm drift field and a 360 kV/cm anode surface field. Rings of wires and foils at the inner and outer radii of both the axial and stereo systems provide field shaping and termination, respectively.

The electronics for the readout of signals from the wires are situated both at the chamber ends and in an electronics hut. In an extension of the gas volume, at either end of the chamber, are the pre–amplifiers which provide a gain of 2.5, there is also a resistive feedback system, to compensate for crosstalk between wires, and resistor divider networks for high voltage control. After amplification and pulse shaping the signals pass down about 40 m of cable to 'converter modules' in the front–end crates, where the signals are digitized.

In the converter modules the signals from the two ends of each wire are amplified and fed to a constant fraction discriminator [41]. The signals are then combined in a mean timer so that the net time is independent of the position of the hit along the wire. The time is digitized in a 12–bit Time to Digital Converter (TDC). A 93 MHz clock, started by a beam–crossing (BX) signal, is used to clock an 8-bit counter, which provides a coarse scale with a bin width of 10.75 ns, and a 4–bit Flash Analogue to Digital Converter (FADC), which is a fine scale with a bin width of 0.67 ns. The output from the mean timer is used to start the discharging of a capacitor which is halted by the next clock pulse. The charge remaining on the capacitor is then digitized by the FADC. Up to 7 hits on each wire can be digitized.

A coarse z coordinate is obtained from the difference in the arrival times of the signals from the two ends of the wire. For the axial wires this z measurement is used by the track trigger to trigger on charged tracks from close to the interaction point in z. A more accurate z value is reconstructed offline by combining information from the stereo and axial cells. The resolution of the z digitisation is of the order of a few hundred picoseconds so the measurement is sensitive to variations in the sense wire or electronic propagation times and small cable phase variations. To monitor and correct for these effects an autocalibration procedure is used.

The resolution achieved by the chamber is about 55 μm in $r - \phi$ and about 5 cm in z. The z resolution obtained by combining the information from stereo and axial wires is about 700 μm. A 2 mm two hit resolution is achieved.

2.3.2 Jet Chamber (CJ)

The CJ [42] covers a solid angle of close to 4π, it is a large volume wire drift chamber based on principles established in the JADE experiment [43] at PETRA. The chamber is 4 m long with an outer diameter of 3.7 m and an inner one of 0.5 m. It is divided into 24 azimuthal sectors each with 159 anode wires strung axially. This gives a possible 159 space point measurements on tracks within the angular region $|\ cos\theta\ | \leq 0.79$ and at least 8 points over the complete solid angle covered by the detector, 98% of 4π. The drift distance within a cell varies from 3 cm at the inner wire to 25 cm at the outer wire. Three dimensional space points, r, ϕ and z, are measured for all hits using the wire position, the drift time and a charge division measurement, respectively. The charge division measurement uses the ratio of the charges at the two ends of the wire to determine the z coordinate of the hit whilst the sum of the two charges is used to give an energy loss measurement, dE/dx.

The wires are stretched between two conical endplates which are held apart by 24 hollow aluminium panels at the outer radius. To reduce multiple scattering, there is no inner support. The length of the wires varies from 3.2 m at the inner radius to 4 m at the outer radius. The 159 sense wires have a 10 mm spacing between radii of 255 and 1835 mm and are staggered by ± 100 μm about the anode plane to resolve left–right ambiguities. 'Bowing' can increase this distance by up to a further 70 μm at $z = 0$. The cathode planes are inclined at 7.5° to the anode planes.

The anodes are at ground potential and voltage is applied to potential wires between the anodes and to the cathode wires. As in the vertex chamber, the voltage on the cathode wires must vary with radius to provide a uniform drift field perpendicular to the anode plane, the voltage is -25 kV on the outer wires and -2.5 kV on the inner ones. Correct termination of the field at the cell boundaries is achieved by using field shaping electrodes at the outer radius and on the endcones and with a field cage of wires and foils at the inner radius. A uniform field in the cell corners is obtained by having extra inner and outer wires with a bias voltage applied. Overall there is an inhomogeneity in the field of less than 0.5% over 84% of the chamber.

Preamplifiers are mounted on the endcones to amplify the signals before they are sent down shielded twisted pair cables to 100 MHz Flash Analogue to Digital Converters

(FADCs). At the endcone there is also crosstalk compensation and pulse shaping by pole zero cancellation. The drift time and two hit resolution are improved by the high sampling frequency of the FADC [44]. Zero suppression is performed and the signals from the 80 FADC crates are sent to 40 microprocessors for further processing which includes an online pulse shape analysis, to extract the drift time and charge [45], as well as calibrations and online pattern recognition of tracks in an event.

A Nd-Yag laser is used to monitor the chamber performance. The laser can produce two sets of 24 beams at fixed positions within the chamber, the two sets are 10 mm apart. These are used to monitor the drift velocity (v_D) in the chamber and to calibrate the z measurement from charge division. Using the laser a σ_{v_D}/v_D of less than 0.1% is achieved.

The energy loss, dE/dx, of charged particles in matter is described by the Bethe–Bloch equation [6] and for a given material depends only on the particle's charge, mass and momentum. The jet chamber measures both the energy loss and the momentum of a particle and together these can be used to identify the particle. Figure 2.5 shows

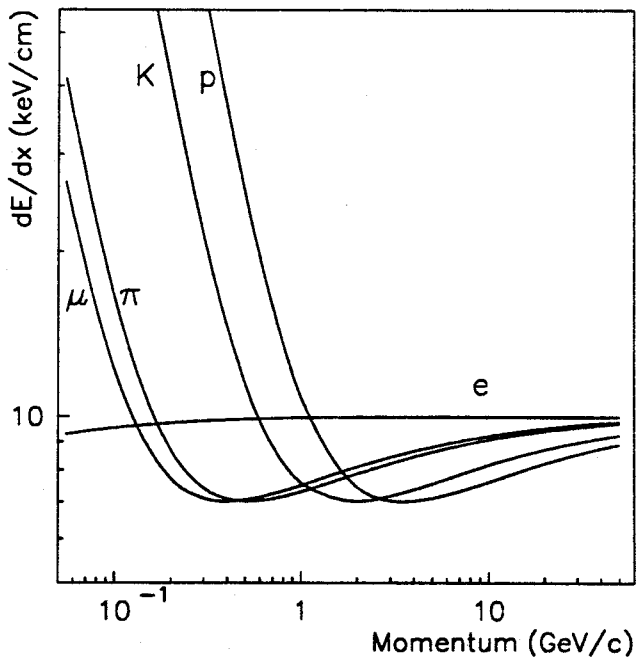

Figure 2.5: dE/dx versus momentum for different charged particles in the OPAL jet chamber.

the theoretical prediction for dE/dx as a function of momentum for different particles in the OPAL jet chamber. The dE/dx measurement can be used to identify particles with momenta below about 15 GeV. The energy loss is measured by adding the charges from the two ends of each wire. In this way up to 159 samples can be used to measure dE/dx. Plotting dE/dx for each hit on a track would give a broad spectrum with a Landau tail at high energy loss which is due to occasional hard collisions. In order to use the dE/dx measurement a truncated mean is formed and only the 70% of hits with the lowest charges are used. Corrections must be made to the measurement for the track length, the staggering of the wires, saturation, electron attachment and crosstalk. Saturation is an effect whereby the amplification of the electrons from the initial ionization produces a positive ion cloud which drifts back to the cathode and reduces the field and hence the gain for subsequent electrons. This means that the collected charge is no longer proportional to the energy loss. The effect is minimised by having a low gain.

The competing requirements of the dE/dx measurement which requires a low gain and the z measurement which favours a high gain have to be optimised in the final chamber operation. An operating point with a drift field of 890 V/cm and a gas gain of about 10^4 was chosen. The resolution achieved in the $r-\phi$ plane is about 135 μm for a drift distance of 7 cm. In z the resolution is about 6 cm. By looking at the 1/p spectra of dimuons the momentum resolution is found to be $\frac{\sigma_p}{p^2} = 1.9 \times 10^{-3}\,(\mathrm{GeV}/c)^{-1}$. The double hit resolution in the jet chamber is 2.5 mm. The dE/dx resolution is $\frac{\sigma_{dE/dx}}{dE/dx}$ =3.8% for pions in multihadron events and by using the dE/dx measurement an $e-\pi$ separation of better than 2σ is seen for particles with momenta up to 14 GeV/c.

2.3.3 Z–Chambers (CZ)

The aim of the z–chambers [46] is to provide a precise z coordinate on tracks to improve the momentum resolution, to aid pattern recognition and to improve the mass resolution of the detector for short lived particles. A z coordinate is measured from the drift time in the chambers. The chambers, together with supports for the CJ, fit between the CJ and the pressure vessel where there is less than a 10 cm gap. The chamber design was limited by the small space in which it is necessary to make several

measurements to be able to resolve ambiguities.

There are 24 z–chambers, each is 4 m long, 0.5 m wide and 59 mm thick. They form a 4 m long barrel around the CJ with a diameter of 3.85 m, covering the angular region $| cos\theta | \leq 0.77$. Each z–chamber is subdivided into eight 50×50 cm^2 cells. Anode wires are strung at the centre of each cell along the ϕ direction giving a maximum drift distance of 25 cm parallel to z. The 6 anode wires in each cell are spaced by 4 mm and have a ± 250 μm stagger about the anode plane to resolve ambiguities. The drift field within each cell is defined by field shaping electrodes spaced at 5 mm intervals around the cell. Aluminium cathode plates, with holes to allow free gas flow, separate the cells. In each cell, a grid of wires 5 mm either side of the anode plane provides separation between the drift region and the anode region. These make it possible to achieve a parallel and uniform field in the drift region right up to the grid, which is necessary if electrons are to drift for up to 25 cm in such a confined space. The signals from the wires are amplified at the wire ends and then multiplexed two to one and digitized using a FADC system.

The intrinsic resolution in z was found to be 100–200 μm, the absolute resolution of the chambers depends on the accuracy of their surveyed position and is about 350 μm. The resolution in the r-ϕ plane is about 1.5 cm from a charge division measurement.

2.4 Time of Flight Counters (TOF)

The OPAL time of flight detector consists of 160 scintillation counters which form a barrel around the outside of the magnet coil at a radius of 2.36 m. The counters are used to measure the time of flight of particles from the interaction point, this value can be used to identify particles with momenta in the range 0.6–2.5 GeV. The counters are also used to help reject cosmic rays and to provide trigger signals.

With a length of 6.84 m, the counters cover an angular range of $| cos\theta | \leq 0.82$. The counters are trapezoidal in cross section with a thickness of 45 mm and a width varying from 89 mm at the inner radius to 91 mm at the outer one. Each counter is wrapped in aluminised mylar foil and black PVC. Light is collected at both ends of the counters and is amplified by phototubes with a nominal gain of 3×10^7. The resulting signal is split into two, one third goes to a 12–bit charge integrating ADC and gives a z

measurement, the other two thirds go to a constant fraction discriminator the output from which is fed to a 11–bit TDC, with a 50 ps bin size, which gives the time of arrival of the pulse. The signals from the two ends of each counter go to a mean timer and the output is used for the trigger.

Monitoring of the counters is carried out using a laser system which simulates the passage of charged particles through the scintillator. The resolution achieved on the time of flight measurement is 250 ps for isolated electrons and 350 ps for particles in multihadron events. A z coordinate is measured using charge division and this has a resolution of 7.5 cm.

2.5 Electromagnetic calorimeter

The electromagnetic calorimeter is designed to measure the energy and position of electrons, positrons and photons with energies varying from tens of MeV to 100 GeV. It is also required that the detector has a good discriminating power between electrons and hadrons and a good two photon resolution. Lead glass was chosen for the calorimeter because it has a good intrinsic energy resolution ($\sigma_E/E \sim 5\%/\sqrt{E}$, where E is the electromagnetic energy in GeV), low noise, a linear response over a wide dynamic range, a spatial resolution of about 1 cm and good electron–hadron discrimination.

The calorimeter is built in three sections, a barrel covering $|\ cos\theta\ | \leq 0.82$ and two endcaps covering $0.81 \leq |\ cos\theta\ | \leq 0.95$. The material in front of the calorimeter amounts to about 2 radiation lengths (X_0) so most electromagnetic showers start before reaching the lead glass. To measure the position and sample the energy of such showers, presampling detectors are placed between the TOF and the lead glass in the barrel and between the pressure vessel and the lead glass in the endcap. These allow the energy measured in the lead glass to be corrected for that lost in the preceding material.

2.5.1 Electromagnetic Barrel (EB)

The barrel electromagnetic calorimeter is a cylindrical array of 9 440 lead glass blocks at a radius of 2.45 m. The blocks are arranged in an 'almost' pointing geometry so that a particle from the interaction point will shower in a single block. The pointing is

not quite exact to prevent neutral particles from disappearing down the cracks between the blocks. In fact, each block points to somewhere between $|\ z\ |$=55.5 – 157.9 mm along the beam axis and is offset by 0.574° in ϕ, which corresponds to pointing 30 mm to one side of the beam line. To achieve this geometry, it was necessary to carefully machine 16 different shapes of block. The calorimeter is segmented into 160 ϕ blocks and 59 blocks in z. The barrel is assembled in 10 half-rings, each with 80 ϕ segments and 12 blocks wide (the middle ring is only 11 blocks wide).

Each lead glass block is 37 cm long and has a cross-section of about 10×10 cm^2. For good energy resolution it is important to wholly contain the electromagnetic shower within the thickness of the calorimeter. A new heavy lead glass, SF57 [47], was used and the blocks correspond to 24.6 X_0. Another requirement for good energy resolution is that there should be as little leakage of light from each block as possible, this is achieved by polishing each block and wrapping it in a black vinyl fluoride sheet which has an aluminium coating on the inside for extra reflection. The Čerenkov light from each block is collected by a 3 inch diameter phototube via a lightguide. The phototubes can operate in magnetic fields of up to 100 Gauss due to a permaloy metal shielding, this precaution is necessary to cope with stray fields outside the solenoid. Signals from the phototubes are digitised using charge integrating FASTBUS ADCs. Each ADC takes 96 inputs and there are two sensitivities, a high and a low energy scale, which allow a high precision measurement over a wide range of energies.

Monitoring of the changes in the response of the calorimeter over the long periods of LEP running is done using a xenon flashlamp. The spectrum of the light from the flashlamp is similar to that of the Čerenkov light in the lead glass used. The light is distributed to all blocks via optical fibres. The lamp pulses at 10 Hz and produces a 20–30 GeV electron equivalent signal in the phototubes.

The calorimeter was calibrated in a SPS test beam before installation inside OPAL. The results indicate a linearity in the counters of better than 1% for electrons in the range 6–70 GeV. The response of the system was found to have a stability of 0.2% r.m.s over a period of a few days and 0.9% r.m.s over longer periods of about a year, after corrections were made using the xenon monitoring system.

2.5.2 Presampler Barrel (PB)

A cylinder of drift tubes operated in limited streamer mode make up the PB [48]. The streamer positions are detected from the charge induced on 1 cm wide cathode strips placed on both sides of the tubes. These strips are at $\pm 45°$ to the wires and are perpendicular on opposite sides of the tubes. Sixteen 6.62 m long chambers cover the angular region $|\ cos\theta\ | \leq 0.81$. Each chamber has two layers of 96 tube cells, in four extrusions, running parallel to the beam axis. The two layers are offset by half a cell with respect to each other to reduce inefficiencies at the cell walls. Each tube has a 9.6×9.6 mm^2 cross section and the tube walls are 1 mm thick. The anode wire, which runs the full length of each tube, is supported every 50 cm by a plastic bridge. A measure of the position of a hit along the wire is made using charge division. The signals from both ends of the wires and strips are amplified and multiplexed at the chamber ends and are then carried along twisted pair cables to an electronics hut where they are digitised.

In a SPS test beam the spatial resolution for single particles was found to be about 1-2 mm, depending on the angle of incidence. This degrades to about 4-6 mm for electromagnetic showers after $2X_0$ of material which corresponds to a resolution of about 2 mrad on the angle of a photon from the interaction point. In z the resolution is about 10 cm.

2.5.3 Electromagnetic Endcap (EE)

The same design requirements of good energy resolution and discriminating power apply to the electromagnetic endcap as to the barrel. Lead glass was again chosen and each endcap is a dome–shaped array of 1 132 blocks of CEREN–25 lead glass [49] which fits inside the central detector pressure bell, see figure 2.6. Due to the geometrical constraints on the endcap the pointing geometry used in the barrel was not achievable so the blocks are mounted with their axes parallel to the beam direction. Another difference from the barrel is that the EE sits within the full OPAL magnetic field, 0.435 T, for this reason specially designed single stage multipliers, Vacuum PhotoTriodes (VPTs), were used.

The cross–section of a block is 94×94 mm^2, comparable to the lateral size of an

electromagnetic shower. Each block is polished and wrapped in aluminium foil to improve reflection. A protective layer of mylar also covers each block before it is put into a brass can with 0.45 mm thick walls which acts as both an electrical screen and a mechanical support. The blocks are mounted onto a rigid backplane by way of the brass can endcap, this is the only support for each block. The front faces of the blocks follow the contours of the pressure bell, as shown in figure 2.6. To achieve this three different lengths of block were needed. Particles from the interaction point traverse at least 20.5 X_0 of lead glass.

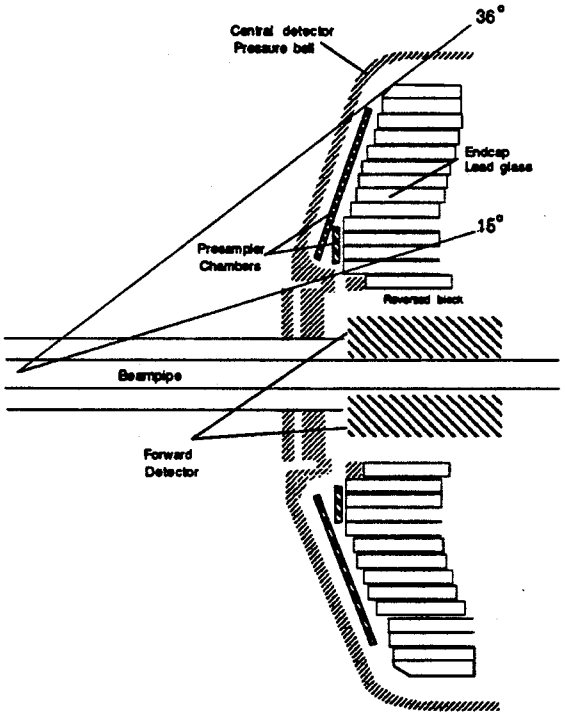

Figure 2.6: A cross section showing how the endcap electromagnetic calorimeter fits inside the central detector pressure bell. (Courtesy of S.Robins)

The VPTs are coupled to the blocks by way of an epoxy resin and give a gain of 12.3. A further signal amplification is given by a low noise amplifier close to the VPT so that the signals can travel the ~40 m to the electronics hut where they are digitised using charge integrating FASTBUS ADCs.

The endcap has two monitoring systems: a laser and a Light Emitting Diode (LED). The laser is able to pulse all blocks at once with a signal equivalent to that of a 10 GeV

electron. The LED can pulse just one or a subset of assemblies with a 20 GeV electron equivalent signal. Both systems are used to monitor the changes in gain of the detector. The laser is more accurate since its spectrum is closer to that of the Čerenkov light produced in the lead glass. The LED can also be used to check out the readout system of individual blocks since it can pulse single assemblies.

Calibration of the detector was performed in test beams before LEP started up. The tests indicated a 0.3% stability of the signals over 1–2 days and a 1.3% stability over longer periods of up to 7 months. The response is linear to about 1% for energies from 3 to 50 GeV.

2.5.4 Presampler Endcap (PE)

The presampler endcap [50] uses thin multiwire chambers to sample electromagnetic showers before the EE. Multiwire chambers were used to build the detector as they meet the needs for good energy and position resolution within the limited available space. At each end of the detector 32 chambers are arranged in 16 overlapping ϕ wedges between the central detector pressure bell and the electromagnetic endcap. The PE covers an angular range of $0.83 < |\, cos\theta \,| < 0.95$. At the outer radius this covers the area where particles from the interaction point traverse at least half an EE lead glass block. It is not possible to cover the inner radius completely but this is less important as the material in front of the calorimeter in this region corresponds to more than $4X_0$ and varies rapidly with radius so the PE is of limited use.

The trapezoidal chambers are mounted onto the front face of the electromagnetic endcap as shown in figure 2.6. There are two sizes of chambers, small ones are mounted at the inner radius, at 90° to the beam direction, and large ones are at the outside, mounted at 18° to the small chambers so as to follow the contours of the endcap lead glass. Each chamber is 6.8 mm thick and the gap for the wires is 3.2 mm, the wires are spaced by 2 mm. Readout is via cathode strips and pads on opposite sides of the chambers. Space coordinates are determined from the strips and wires whilst the best energy resolution is obtained from the pads since the summation over fewer channels allows a better signal to noise ratio to be achieved.

The chambers are operated in a saturated mode so that the pulse height is approx-

imately proportional to the number of particles in a shower. The spatial resolution achieved in a test beam was ~2-4 mm.

2.5.5 Combined performance

The performance of the electromagnetic calorimeter was studied in test beams prior to the installation within OPAL. The energy resolution of the barrel lead glass with no material in front of it was found to be $\sigma_E/E = 0.2\% + 6.3\%/\sqrt{E}$. With the addition of about $2X_0$ of material in front, the resolution is degraded by a factor of two, about half of which can be recovered using the presampler. The endcap lead glass was found to have an energy resolution of $\sigma_E/E = 5\%/\sqrt{E}$ at low energies. Using the EE and PE together gives an electron identification efficiency of 80–90% and a pion misidentification of 10^{-3} was achieved. The spatial resolution is about 11 mm for the lead glass and this is improved to about 5 mm when the presampler information is included.

2.6 Hadron Calorimeter

The hadron calorimeter, designed to measure hadronic shower energy and to track muons through the iron, is made by instrumenting the iron return yoke of the magnet. Since the electromagnetic calorimeter and the magnet coil correspond to about 1.5 interaction lengths of material, most hadronic showers start in the lead glass. Therefore, the signals from the electromagnetic and hadronic calorimeters must be combined in order to measure the hadronic energy correctly

The hadron calorimeter has five components, a barrel covering $|\ cos\theta\ | \leq 0.81$, two endcaps covering $0.81 \leq |\ cos\theta\ | \leq 0.91$ and two pole pieces covering $0.91 \leq |\ cos\theta\ | \leq 0.99$. The barrel and endcaps are instrumented with limited streamer tubes [51] and the poletip with multiwire chambers.

The barrel consists of 24 wedges, each 10.4 m long, starting at a radius of 3.39 m. Each wedge has eight 10 cm thick iron plates with 2.5 cm gaps between them, into which are fitted the streamer tube chambers. Depending on the radius, each chamber contains 7 or 8 cells. The cells have a cross section of 9×9 mm^2. The chambers in

layers 1 and 9 are 7.3 m long whilst layers 2 to 8 consist of two 5 m long chambers, the junction between these chambers is staggered from layer to layer to prevent gaps in the detector. In the endcap the iron plates are doughnut shaped and have 3.5 cm gaps between them. The endcap chambers, each with 8 wires, are formed into larger units, of 36 chambers, which cover a quarter layer. The wires in the tubes are used for monitoring purposes only and readout is via 4 mm aluminium strips and 50×50 cm^2 pads on opposite sides of the chambers. The pads are formed into 976 pointing towers within the detector with 48 ϕ bins and 21 θ bins. Signals from the pads in each tower are summed and the total charge is used to measure the hadronic energy in the tower. The strip signals are used to track particles through the calorimeter. The energy resolution, found in a SPS test beam, is about $120\%/\sqrt{E}$.

Due to constraints on the uniformity of the field within the central detector, the pole pieces have only 1 cm gaps between the iron plates. To compensate for the reduced momentum resolution of the tracking chambers at large angles the energy resolution of the poletip is increased by making the sampling frequency every 8 cm. The poletip is instrumented with multiwire chambers as used in the presampler endcap and has a resolution of about $100\%/\sqrt{E}$ at 15 GeV, though this is worse at higher energy. Some supports are needed for the structure and this leads to a degraded response in about 10% of the subdetector.

2.7 Muon Chambers

To detect charged particles which get through the iron, mostly muons with a small hadron contamination, there are layers of tracking chambers surrounding the entire detector. Over most of the solid angle, particles from the interaction point traverse 1.3 m of iron (equivalent to 7 interaction lengths for pions) which means that there is less than a 0.001 probability for a pion not to interact. Most charged particles emerging from the hadron calorimeter are muons. The muon detector has three parts, a barrel and two endcaps, which cover 93% of the solid angle with at least one layer of detector, the gaps are due to the beam pipe, magnet supports and cables. Muon identification in OPAL involves the extrapolation of tracks from the central detector through the calorimeters to the muon chambers and then requires a match in position and angle of

the track segments allowing for multiple scattering effects.

The muon barrel (MB) is made of four layers of planar drift chambers. There are 110 chambers in total; 44 on each side of the detector, 10 on the top and 12 below. Each chamber has a cross–section of 1.2 m by 90 mm and there are three different lengths of chamber so that they fit around the magnet supports. There are two drift cells per chamber, each with a sense wire running parallel to the beam. A measurement of the ϕ coordinate of a hit is made from the drift time with a resolution of about 1.5 mm. The z coordinate is measured using diagonal shaped cathode pads [52] with a 171 mm repeat distance. These give a 'fine' z measurement of the position of a hit with a resolution of about 2 mm but with an ambiguity about which pad the hit was in. This is resolved using a medium z obtained from similar pads with a repeat distance of 1710 mm. The further ambiguity is resolved using a coarse z value obtained from the pulse heights and times of arrival of the signals at the two ends of the wires.

Limited streamer tubes are used to form the muon endcap (ME) detectors [53] which cover the angular region $0.67 \leq |\ cos\theta\ | \leq 0.98$. At each end of the detector there are eight 6×6 m^2 quadrant chambers mounted in pairs perpendicular to the beam direction. The four quadrants overlap vertically but there is a gap horizontally for the beam pipe, some of which is covered by four 3×2.5 m^2 patch chambers. Each chamber has two layers 19 mm apart, one with horizontal wires and one with vertical wires. Readout of streamer positions is via 8 mm thick aluminium strips on each side of a layer, these are parallel to the wires on one side and perpendicular on the other. The spatial resolution achieved is about 1 mm from the perpendicular strips and about 3 mm from the parallel strips.

2.8 Forward Detector

By detecting small angle Bhabha scattering events the forward detector measures the LEP luminosity. The detector also helps to identify two photon events by tagging forward going electrons and positrons from these events. The forward detector consists of a number of different elements placed close to the beampipe, inside the poletip and endcap electromagnetic calorimeters, next to the central detector pressure vessel. The clean, unobstructed, acceptance of the forward detector is 47-120 mrad where the only

material traversed by particles from the interaction point is the beam pipe and a thin window (2 mm) of aluminium from the pressure vessel.

The main energy measurement of the forward detector is made using a calorimeter of lead–scintillator sandwich, the first $4X_0$ of which act as a presampler. The calorimeter has 16 ϕ segments at each end and these are built in half cylinders for easy mounting around the beampipe. The energy resolution of the calorimeter, measured from Bhabha events, is $\sigma_E/E = 18\%/\sqrt{E}$ and the spatial resolution for electron showers is 2 mm in radius and 1.5° in ϕ. Two planes of drift chambers in front of the calorimeter and proportional tube chambers between the presampler and the main calorimeter are used to measure the position of tracks hitting the calorimeter. The drift chambers measure an $r-\phi$ coordinate from the drift time with a precision of 300 μm and a z position from charges induced on pads to ± 1 mm . The tube chamber positions are known to ± 0.5 mm but individual shower positions are measured to only 3 mm due to fluctuations after the $4X_0$ of presampler.

A fine luminosity monitor consists of four pairs of 6 mm thick scintillators precisely positioned on the 45° diagonals. The gamma catcher, a lead scintillator sandwich $7X_0$ thick, covers the polar angle 142-200 mrad where a gap in calorimetric acceptance occurs due to the tubes for the jet chamber laser beams. On either side of OPAL, 7.85 m from the interaction point, are the far forward luminosity monitors. These are small lead scintillator calorimeters placed around the beampipe to detect electrons scattered between 5 and 10 mrad. Using the various components of the forward detector the luminosity was measured with a systematic error of $\pm$ 0.8%.

2.9 Online system: data acquisition, trigger and filter

The OPAL online system [54] is designed to be a multi–level system with buffering at each level. Each of the subdetectors has a VME crate, called a Local System Crate (LSC), which controls the Data Acquisition (DAQ) for that particular subdetector. Figure 2.7 shows a schematic view of the flow of data through the system. When an event is triggered each LSC reads the data from the front–end electronics and formats

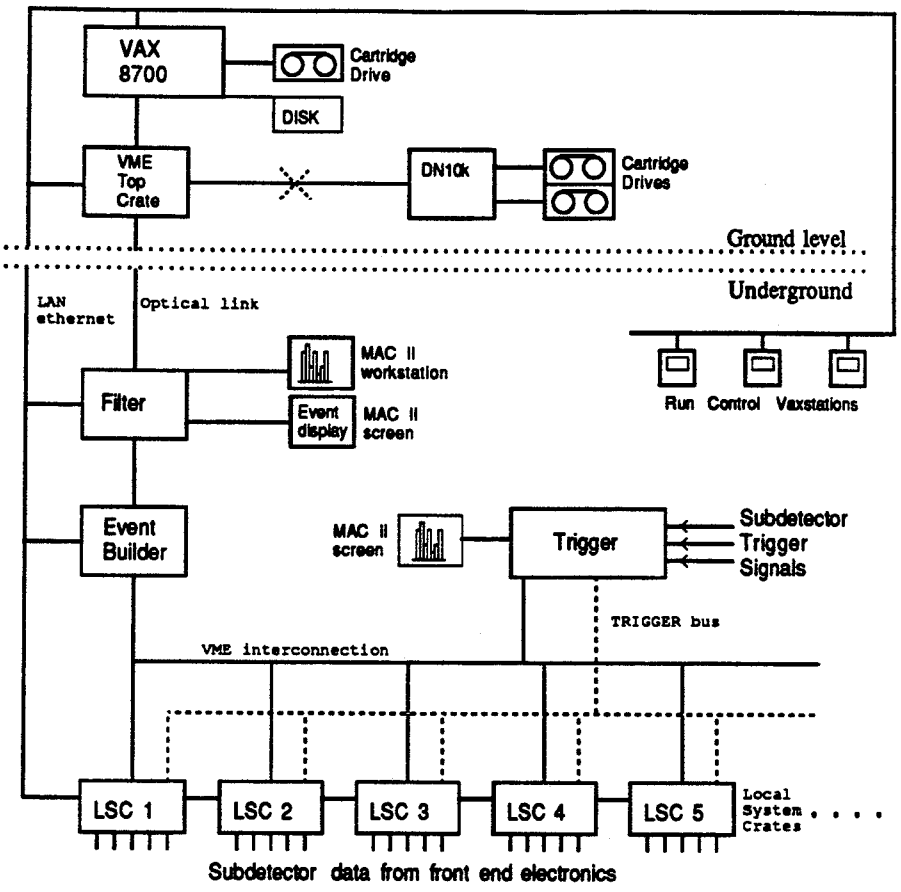

Figure 2.7: A schematic view of the OPAL online system.

it into a ZEBRA structure [55] before passing it on to the 'event builder'. In the LSC tasks such as pedestal subtraction, zero suppression, calibration and monitoring may also take place. The jet chamber LSC also performs pattern recognition of tracks in an event. The event builder controls the collection of the various subevents from each subdetector and concatenates them to produce a complete event which it buffers for use by the filter, where a fast analysis of the complete event is performed. At the filter, events are classified into physics types and background events can be rejected or downscaled. All of the electronics mentioned so far is in the underground experimental hall next to the detector. After 'filtering', however, surviving events are sent via an optical link to another VME crate on the surface, the 'top crate', before being transferred to a VAX 8700 where they are written to tape ready for reconstruction

offline. The reconstruction of events is performed on an Apollo DN10k with cartridge drives attached for reading in raw data and writing out reconstructed data. The possibility exists to send the events directly from the 'top crate' to the Apollo DN10k for 'online' reconstruction and in this case reconstructed data is written to tape.

The complete DAQ chain is controlled from a workstation in the online VAX cluster running the 'run-control' program. This allows easy control of the different parts of the DAQ chain, including the LSCs, the event builder, the filter and the trigger, from one central vaxstation in the 'control room'. The DAQ programs in each LSC can be individually controlled from this workstation thus making the inclusion and exclusion of each subdetector in a global OPAL run a simple task. The online VAX also provides many monitoring facilities and displays the status of different parts of the system, including that of LEP, each subdetector, the data flow, etc. Error messages from all parts of the chain are also displayed centrally via the VAX.

Another important aspect of running the experiment is the control of high voltages and gas levels. This task is handled by the 'slow–controls' system which has two aspects. Firstly, there is an OPAL-wide monitoring of gas flows, voltages for the electronics, temperature and humidity, etc. Seven VME crates spread throughout the electronics huts are used for this purpose. Secondly, each subdetector has a slow controls process which controls its individual gas, high voltage etc. A Macintosh computer in the control room can be used to retrieve slow control information from all over OPAL and to view this information centrally. Warning messages should anything go wrong are also displayed here. Some slow control data are written through the DAQ chain as control data.

The OPAL DAQ system operated reliably throughout the 1989 and 1990 LEP running periods during which time ~150,000 multihadronic Z^0 decays were recorded. The event size for a multihadron event was about 200 kbyte whilst other events were about 70 kbyte. With an average trigger rate of 2 Hz the readout deadtime was less than 10%. Recent upgrades to the event builder, the filter and the CJ microprocessors will enable the system to cope with the increased event rate expected as the LEP luminosity increases.

2.9.1 Trigger

At design luminosity (1.6×10^{31} cm^{-2} s^{-1}), the on resonance Z° rate at LEP is expected to be about 0.7 Hz. Bunch crossings at LEP occur every 22 μs and it is the job of the trigger to determine whether or not an e^+e^- interaction has occurred. The OPAL trigger [56] uses information from the subdetectors to make this decision and to reduce the 45 kHz beam crossing rate to a 1–5 Hz trigger rate. The aim of the trigger is to have a high efficiency for finding physics events but with a good rejection of background events from other processes which can give signals in the detector. Background events can come from cosmic rays, beam–gas and beam–wall interactions, synchrotron radiation and noise in the detector. The OPAL trigger is designed in such a way that most physics events will trigger more than one independent signal. This redundancy gives a high efficiency and allows calculation of the efficiency from the data by comparing the various triggers which fire.

Within the trigger the solid angle of the detector is divided into 6×24 overlapping $\theta\phi$ bins, called the $\theta\phi$ matrix. The angular coverage of these bins is given in table 2.1. The contributing subdetectors send trigger signals which correspond as closely as possible to the 144 bins of this matrix. In the Central Trigger Logic (CTL) the $\theta\phi$ signals from the subdetectors are combined and coincidences between them are found. Each subdetector also provides standalone triggers indicating, for example, track multiplicities and energies above threshold. Programmable Array Logic (PAL) is used in the

Table 2.1: The angular range covered by each of the bins in the $\theta\phi$ matrix.

ϕ bins		θ bins	
Bin Number	ϕ range	Bin number	$cos\theta$ range
1	0° → 30°	1	-0.980 → -0.596
2	15° → 45°	2	-0.823 → -0.213
3	30° → 60°	3	-0.596 → 0.213
.	.	4	-0.213 → 0.596
23	330° → 360°	5	0.213 → 0.823
24	345° → 15°	6	0.596 → 0.980

CTL to determine from the $\theta\phi$ and standalone signals whether to accept or reject an event.

The subdetectors which contribute to the trigger are:

Central Detector: The 'track trigger' uses hits in the vertex and jet chambers to trigger on charged tracks in the angular region $| cos\theta | \leq 0.95$. $\theta\phi$ signals which correspond to the binning used by the CTL are sent to the $\theta\phi$ matrix whenever a track is found in the appropriate bin of the matrix. Standalone signals representing track multiplicities in the whole detector and in a 'barrel' with a reduced θ range are formed. A simple hit counting is also performed in rings of wires at different radii and standalone signals are produced if the hit count in a ring is above threshold. More details of this trigger component are given in Chapter 3.

Time of flight: The time of flight detector triggers if signals from both ends of a scintillator bar are within 50 ns of each other and within 50 ns of the expected arrival time of a relativistic particle from the interaction point. $\theta\phi$ signals are provided in 24 overlapping 36° ϕ bins, there is no θ segmentation. Standalone signals are produced indicating single hits in the TOF, more than a threshold number of counters triggering, usually 2, and more than a threshold number of $\theta\phi$ bins firing, usually 7.

Electromagnetic calorimeter: Signals from groups of about 48 lead glass blocks are analogue summed in both the barrel and endcap calorimeters. This provides 200 EB and 24 EE signals which are combined to match the $\theta\phi$ binning of the CTL as closely as possible and to produce total energy sums. Two thresholds are applied to the $\theta\phi$ sums, one high (2.5 GeV) and one low (1 GeV), and signals above threshold are sent to the $\theta\phi$ matrix. Total energy sums over the whole of the barrel and each endcap are also formed and used as standalone triggers. These must have higher thresholds as they involve summing many more channels, the thresholds used are 6 GeV and 4 GeV.

Hadron calorimeter: The pad towers are used to give energy sums both for the $\theta\phi$ matrix and as standalone triggers. The signals from 12–16 towers are summed to give 92 trigger signals. Three thresholds are used to discriminate the signals.

The lowest threshold is used to provide $\theta\phi$ signals and the higher thresholds give standalone signals. The hadron calorimeter trigger was commissioned during the late part of the 1990 running period.

Muon detector: The muon barrel trigger requires three out of the four possible wire layers to fire in 15° ϕ bins. There is no θ segmentation and the ϕ bins are not overlapped. A standalone signal is provided whenever there is a muon barrel trigger, this has a high rate, about 500 Hz, because of cosmic rays and is only used in coincidence with other triggers.

In the muon endcap, groups of 64–128 strips are used to form clusters. A trigger signal is generated if two of the possible four planes have clusters above threshold which are consistent with a particle having come from the interaction point. The xy coordinates must be converted to $\theta\phi$ for use in the trigger. The ME provides 4×24 $\theta\phi$ bins approximately matched to those of the CTL, these are combined with the MB signals to form the 6×24 bins of the CTL. Standalone signals are also provided representing hits in the left or right endcaps and a signal requiring both endcaps.

Forward Detector: Signals from the FD calorimeter are used to provide energy triggers for the luminosity measurement. Coincidences are required between the left and right sides of the detector, there are also single tag triggers for triggering two photon events. Accidental triggers, where the signals from one side of the detector are delayed by a LEP bunch–crossing with respect to those from the other side, are used to measure backgrounds for the luminosity measurement.

The Central Trigger Logic (CTL) consists of a double sized VME crate containing a special 'TRIGBUS' as well as the standard VME/VSB bus. The CTL consists of a number of parts:

SIM The Standard Input Module receives up to 64 standalone signals from the sub-detectors and makes them available on the TRIGBUS.

$\theta\phi$ matrix The $\theta\phi$ matrix consists of 5 cards, one for each of the track, time of flight, electromagnetic calorimeter, hadron calorimeter and muon triggers. The signals

are received from the individual subdetectors and programmable array logic is used to combine them. $\theta\phi$ signals are produced in each of the following cases:

- If a hit is found in either the left side, the right side or the barrel of the detector.
- If more than 1 or more than 2 θ bins fire.
- If collinear, i.e. exactly back to back, $\theta\phi$ bins fire.
- If signals from different subdetectors occur in the same $\theta\phi$ bin then coincidence signals are produced. Coincidences are not considered between the electromagnetic and hadron calorimeter triggers[2].

PAM The Pattern Arrangement Module takes 120 signals, 64 from the SIM and 56 from the $\theta\phi$ matrix, and produces a trigger if certain combinations have fired. The combinations are set by way of look up tables and PALs arranged in layers. In each layer various combinations of signals can give a trigger. The final trigger decision is an OR of the output from the 8 layers[3].

If the trigger decision is negative then a reset pulse is distributed to every subdetector 6 μs before the next beam–crossing. This gives the subdetectors time to clear their electronics and reset ready for the next possible event. The signal is distributed from the Global Trigger Unit (GTU) in the CTL to a Local Trigger Unit (LTU) in each subdetector LSC via a special trigger bus. If the trigger decision is positive then the GTU sends a trigger to every LTU and the subdetectors commence readout of the front–end electronics. Further gates and resets are inhibited until all the subdetectors have read out their electronics, this is indicated in each case by the releasing of a 'BUSY' line.

The trigger rate depends on the luminosity and beam related backgrounds, it also contains a constant contribution from cosmic ray and noise events. The OPAL trigger was optimised for good efficiency for physics events whilst keeping the rate low enough

[2]Due to time constraints the original $\theta\phi$ matrix design [57] was not fully implemented in time for the startup of LEP. Although many coincidences were added later the electromagnetic–hadron coincidence is not possible with the available hardware. This coincidence would anyway only be useful for hadrons depositing energy in both calorimeters.

[3]The number of layers in the PAM has now been increased to 16 and programmable RAMs are used instead of the PALs.

that the DAQ system could cope. The average trigger rate in 1990 was 2 Hz, this peaked at 2.5 Hz at the start of a fill. The efficiency was high for all physics channels, for example, multihadron events are triggered with 100% efficiency, as are Bhabha events, other lepton pair events have a trigger efficiency of better than 99.9% and the expected trigger efficiency for events containing new particles, e.g. Higgs or supersymmetric particles, was estimated to be $> 95\%$.

2.9.2 Filter

At the filter the complete event can be analysed. The filter performs some reconstruction of each event though this is not as complex as that done offline due to time and computer resource constraints. The filter uses the information available to it to flag 'good' events from Z^0 decays and to reject background events which were accepted by the looser requirements of the trigger. During the 1989 run the filter was used to identify and flag events from Z^0 decays. Only the events selected by the filter were reconstructed offline. The selections were developed throughout the run and became quite complicated in order to select all physics channels with some redundancy.

In 1990 the aims of the filter were changed and the emphasis was placed more on rejecting obvious background events rather than selecting good events. To this end two classes of selection cuts were introduced and events were only rejected if they failed both sets of cuts. The two selection classes are:

- Global selection cuts – simple loose cuts on single subdetector quantities. These cuts are made on reconstructed quantities such as track momentum or energy in clusters in the electromagnetic calorimeter.

- Trigger validation cuts – an event passes these cuts only if one of its elemental triggers[4] is validated by simple cuts on the reconstructed data.

Once the performance of these cuts had been studied and understood, "active filtering" was introduced and events failing both sets of cuts were discarded by the filter. For each event, bits in a 'filter word' are set indicating which cuts were satisfied.

[4]An elemental trigger is a trigger signal or combination of trigger signals which is sufficient to trigger the event.

Since the 'active filtering' was only introduced late in the 1990 run, the filter code was also developed to perform a number of other tasks:

- Classification: To aid the offline reconstruction effort, the filter flags events into certain physics categories such as multihadrons, lepton pairs and luminosity events. Only events flagged as physics events by the filter were reconstructed offline.

- Monitoring: Having the complete event means that the filter can form many histograms involving more than one part of the detector. Monitoring histograms for the trigger, the filter, and for individual subdetectors are available in the control room for display on a Macintosh computer.

- Event Display: The filter produces an online event display on another Macintosh screen in the control room. This is used extensively for monitoring data quality.

2.10 Offline Software

2.10.1 ROPE

ROPE [58] is the offline software package for the Reconstruction of OPal Events. It involves turning the raw signals from hits in the detector into information about the particles in the event and their energy and momenta. The input to the program is the raw data and the output is a DST, Data Summary Tape, which contains useful physics quantities and is about 10% of the size of the original raw data.

The program is designed in a very modular way so that the code for each subprocess could be developed separately and can be run alone or as part of the whole. The various subprocesses either deal with individual subdetectors or are designed to merge the information from various subdetectors. For example, in the central detector, processes are run for CV, CJ and CZ separately to find track segments in each of the chambers then afterwards a central tracking (CT) process is run to combine the track segments into overall central detector tracks which can later be compared and matched to hits in the rest of the detector. ROPE also forms the standard framework for physics analyses within OPAL and there is a process which contains routines to allow easy access to the

DST information [59]. Details of the charged track reconstruction and cluster finding in the electromagnetic calorimeter are given in appendix A.

A program called GROPE [60] allows events to be displayed in a pictorial way. The raw hits and/or reconstructed information for each subdetector can be displayed, thus allowing the information in events to be scanned by eye.

2.10.2 OPCAL

An OPal CALibration database, OPCAL [61], is used to store calibration constants for the different subdetectors. Constants are stored with a certain validity period in terms of run and event numbers. The database is initially filled with a first pass of constants so that the reconstruction of events can be performed as data is taken. Later, after some offline analysis, better constants may be determined and these are also entered into the database and are used in subsequent reconstruction of the events.

2.10.3 GOPAL

An important part of many physics analyses is the use of Monte Carlo events to estimate efficiencies of cuts and remaining backgrounds in samples after cuts. For this purpose a good simulation of the detector is needed and for precision measurements the Monte Carlo must reproduce well those distributions on which cuts are made. The OPAL simulation program is called GOPAL [62] and uses the GEANT3 package [63] to define the geometry and material of the detector and to track particles through the detector.

The running of GOPAL occurs in a number of stages. Firstly, an initialization is performed where constants concerning the geometry of the detector, the material in the detector and tracking parameters to be used are set up. These constants can either be read from the OPAL database for a specific run or the defaults, which are realistic values, can be used. Secondly, the primary kinematics of the event to be simulated are needed. These can be produced within GOPAL by running a generator from the program or a generator can be run beforehand and GOPAL will use the '4–vector' file produced. Next the program tracks particles through the detector, this includes the simulation of physics processes such as scattering, decays and interactions. At each step control is given to the user and 'hits', containing enough information for subsequent

simulation, can be stored and the tracking of certain particles can be stopped. Finally the program digitises the hits to produce simulated data which has the same structure as the raw data coming from the detector. This simulated data is also used as the input to a trigger simulation package which predicts the trigger decision for each event. The reconstruction program, ROPE, can be run from within GOPAL and in this case the output is a DST rather than the raw data.

The full detector simulation is a time consuming process (about 450 seconds of IBM/168 units for a multihadron event) so it is desirable to have a much faster version. In GOPAL it is possible to run in a 'SMEAR' mode which uses a much simplified version of the GEANT geometry and tracking but still aims to give a reasonable representation of the detector. The SMEAR mode is about 100 times faster than the full simulation and is used for applications where large numbers of Monte Carlo events are needed with different physics parameters in order to study the effects on the data.

Chapter 3

OPAL track trigger

3.1 Introduction

Triggering at e^+e^- colliders involves selecting true e^+e^- interaction events whilst rejecting backgrounds such as cosmic rays, beam–gas and beam–wall events. OPAL uses fast information from all parts of the detector to make the decision about whether an event should be kept or discarded within the 22 μs between bunch crossings at LEP. Details of the complete trigger can be found in reference [56]. One part of the trigger is the track trigger [64] which uses information from the central tracking chambers and a simple pattern recognition to trigger on tracks from true e^+e^- interactions by requiring them to have come from close to the interaction point, which is at the centre of the detector. The track trigger is most important for detecting events where the calorimeter triggers do not fire; these are low multiplicity events where little energy is deposited in the calorimeters such as muon pair events, tau pair events and exotic events with lots of missing energy.

The design of the track trigger (TT) was constrained in a number of ways. In order for a trigger decision to be reached within the 22 μs between bunch crossings any pattern recognition used must be simple and fast and must be done in hardware. It was necessary to build a dedicated hardware processor with a high degree of parallel processing. The output event rate which can be handled by the data acquisition system puts constraints on the trigger rate. A flexible system was designed to provide a reasonable trigger rate under different possible operating conditions.

3.1.1 Principles

The OPAL track trigger uses hit information from the jet chamber (CJ) and vertex chamber (CV) to identify tracks from close to the origin of the detector, i.e. the interaction point, and thus to trigger on true e^+e^- interaction events. Since OPAL has an axial magnetic field (parallel to the beam axis), tracks bend in the $r-\phi$ plane whilst in the $r-z$ plane tracks with a transverse momentum greater than about 200 MeV (those tracks which reach the outer edge of the detector within a few sectors) follow straight line trajectories. Tracks from real e^+e^- annihilation events will emanate from the beam–crossing point, the origin of the detector, but this is not usually the case for background events such as cosmic rays, beam–wall and beam–gas events. Figure 3.1 shows how a track from the origin ($z=0$) has a constant value of θ (the angle between the track and the beam axis) along its entire length whereas for tracks not from the origin this angle varies along the track. This feature is used by the track trigger to distinguish between real and background events using a novel histogramming method.

Since a track from the origin has a constant value of θ along its length, a histogram of z/r ($=cot\theta$) values taken at different points along the track has a peak at the appropriate $cot\theta$ value. For tracks from background events the z/r value changes along the track so a similar histogram for such tracks is spread out and there is no peak. Figure 3.1 shows histograms for the two cases. To use this effect the track trigger segments the solid angle it covers into z/r and ϕ bins and forms a z/r histogram in each ϕ bin. The track trigger identifies good tracks from true e^+e^- events as peaks in the resulting z/r distributions.

The above method of finding tracks by binning and histogramming is complicated by the fact that tracks can cross bin boundaries in both θ and ϕ. In ϕ this is due to the bending of tracks by the magnetic field in the $r-\phi$ plane so that tracks can cross from one ϕ sector to another. In θ it is due to the finite z resolution of the detectors which means that even hits from good tracks can appear in adjacent z/r bins if the track is close to a bin boundary. This could mean that tracks are not found using the above method because hits from a single track can appear in more than one bin so the distributions are spread out and no peak, corresponding to a track, is observed. This problem is overcome by adding the histogram contents from adjacent bins together in

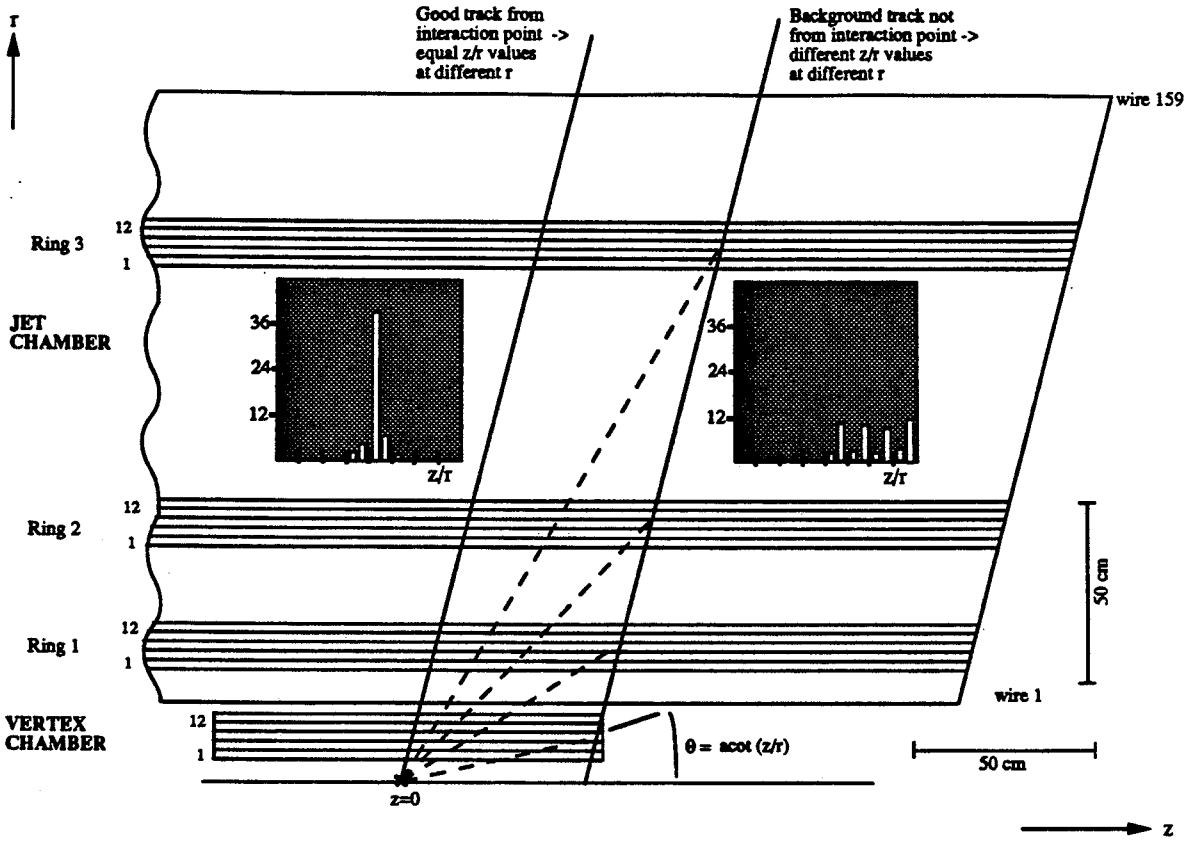

Figure 3.1: Principle of the OPAL track trigger.
A track from the origin of the detector has a constant θ value along its length but for a track from elsewhere θ varies along the track. The z/r histograms formed by histogramming hits at different points along the two tracks are shown. The hits from the good track do not all fall into one bin of the histogram due to the effects of experimental resolution.

both θ and ϕ to form overlapping bins and to ensure that all tracks from the interaction point are triggered. In θ this process is referred to as 'smearing'.

3.1.2 Implementation

The segmentation used in the OPAL track trigger is dictated by the geometry of the tracking chambers. The OPAL jet chamber (CJ) has 24 ϕ sectors so this is the natural division to use in the track trigger. In θ the segmentation is variable (with a maximum of 32 bins) and is determined by the z resolution of the detectors. To avoid missing

tracks which cross sector boundaries in ϕ the histograms from adjacent sectors are added to give 24 'overlapped bins' each covering two CJ sectors and, since the vertex chamber has 36 sectors, three CV sectors. If a track crosses more than two CJ sectors, however, it will be lost and this leads to a low momentum threshold to the track trigger efficiency which is discussed further in appendix B.1. Figure 3.2 shows a $r-\phi$ view of the chambers showing the ϕ segmentation.

It is not practical to process information from all 159 wires of the jet chamber so the track trigger uses hit data from four rings of 12 wires at different radii in the detector, these are sufficient for triggering purposes. The inner ring consists of the 12 axial wires of the vertex chamber whilst the outer three rings are in the jet chamber although the exact positioning of them is variable. The $r-z$ view of the chambers in figure 3.1 shows the four rings of wires used by the track trigger. The position of the outer ring, ring 3, determines the low momentum threshold for tracks to be efficiently triggered. Moving this ring in, therefore, reduces the threshold but also increases the beam related background so that a compromise position must be found. Placing the inner ring closer to the beam gives more information on the z position of a track where it crosses the beam axis and thus helps to reduce background.

For each of the 24 ϕ sectors the z/r values of hits in each ring are histogrammed[1]. Peaks in these histograms, which should correspond to tracks from the interaction point, are found by applying thresholds to each bin. A track flag is set for each bin in which the bin contents exceed a specified threshold. The three sets of track flags from the jet chamber (CJ) are then combined to give overall CJ decisions in each bin. This can be done in a number of ways; requiring that tracks are found in a given bin in one, two or all three rings. It is also possible to form a sum of the histograms from the three rings and to apply a separate 'sum' threshold to the resulting histogram.

Coincidences between the track flags from CV and CJ are then formed to give 32 final decision bits[2] in each ϕ sector. These coincidences are formed using a custom–built "coincidence–chip" [65]. The combination of the decisions from all sectors can

[1]In the vertex chamber up to six hits per wire are used to form the histograms and in the jet chamber all hits on the wires are used but only one entry per z/r bin is made for each wire.

[2]All 32 z/r bins are used by the hardware though the track trigger can be set up in such a way that only some of them have any physical significance.

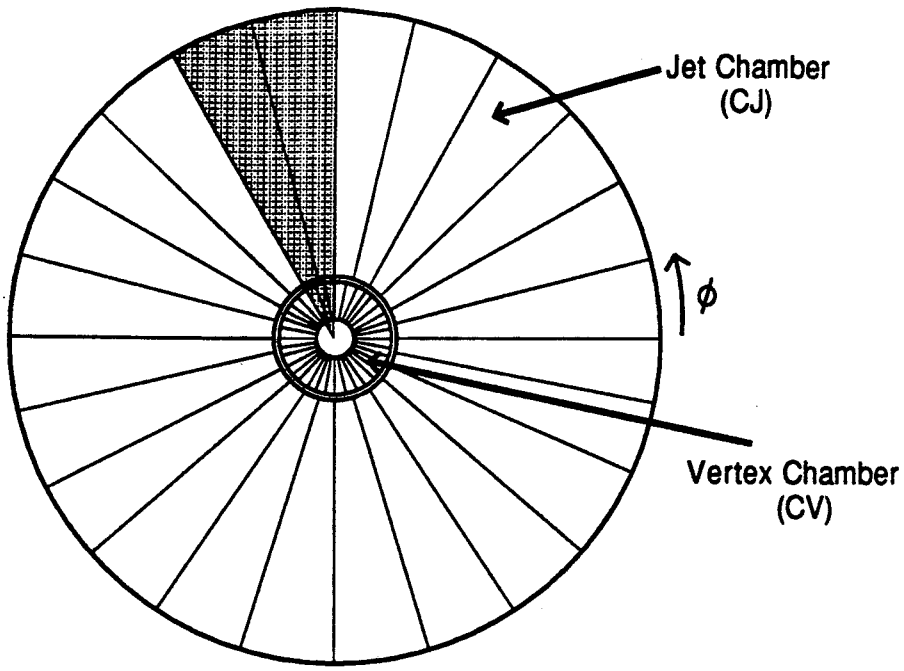

Figure 3.2: An $r-\phi$ view of the OPAL tracking chambers showing the ϕ segmentation in CV and CJ. The shaded area is one overlapped track trigger ϕ bin, covering two CJ and three CV sectors.

be viewed as a 32×24 array in θ and ϕ. This array is examined and tracks, which appear as clusters of ones in the array, are counted. Final track multiplicities of 0, $\geq$1, $\geq$2 and $\geq$3 tracks are sent to the Standard Input Module (SIM) in the Central Trigger Logic (CTL) as standalone signals. The CTL and its various components have been described in section 2.9.1. Further track multiplicities from a region of the detector with a reduced θ range, the 'barrel', are also formed and signals sent to the SIM. The barrel is defined so as to cover the same angular range as the outer CJ ring. The 32×24 $\theta\phi$ array, as well as being analysed for the multiplicity, is also reduced to the OPAL standard 6×24 array and sent to the $\theta\phi$ matrix of the CTL.

As well as counting tracks the track trigger also forms 'ring hit counts'. For each ring of wires the hits from all 24 ϕ sectors are summed to give the 'hit count'. If the hit count in a ring exceeds a certain threshold then a signal is sent to the SIM. These signals are used as a veto for a single photon trigger for which no hits are expected in the tracking chambers.

The track trigger is designed in such a way that it is very flexible which means that the setup can be varied to optimize the efficiency and background rejection depending

on the running conditions. Most of the features are programmable and can be varied by the setting of registers and/or memories, these include:

- **Positioning of CJ rings**[3] – the position of the rings in CJ should be set so as to have as high an efficiency as possible for all tracks whilst still keeping a good degree of background rejection.

- **Number of z/r bins** – this should be compatible with the z resolution of the detectors.

- **θ smear** – the smear in θ can be set to be over one, two or three adjacent bins. This feature is, however, in some respects redundant since instead of increasing the smear the number of z/r bins can be reduced.

- **Thresholds** - these should be set to give a high triggering efficiency with good background rejection.

- **Combination of the CJ track flags** – this can be used to improve the efficiency by requiring only one or two out of the three rings to trigger a track or it can be tightened up to remove more background.

- **Matching of CV and CJ track flags** – the set up of the coincidence chip controls the matching of CV and CJ track segments in z/r and thus determines the window in z around the interaction point from which tracks can trigger the TT. This is discussed in more detail in appendix B.2.

- **Barrel definition** – By defining the barrel to have a reduced θ range it is less affected than the whole detector by forward going beam–related backgrounds. Thus the track multiplicity signals have a lower rate in the barrel and can be used for standalone triggers when the equivalent signals in the whole detector are swamped by background.

- **Enabling/disabling of various parts of the track trigger** – CV and CJ can be separately enabled/disabled. Also individual rings and sectors can be turned on and off and the track trigger is still able to run.

[3]This is not an entirely programmable feature since it also involves the moving of cables.

3.2 Hardware

The track trigger hardware [66] consists of three main components. These are the CV z/r modules [67], the CJ z/r modules [68] and the track trigger processor (TTP). The track trigger processor contains track finder boards (TFBs) to do the histogramming and track finding and multiplicity boards to calculate the multiplicity of an event. The data flow through these components is as follows. The z value of each hit is determined by the CV/CJ front–end electronics and is sent to the appropriate z/r module where it is converted to a z/r value which is in turn sent to the relevant TFB. In the TFBs the hits are histogrammed and tracks are flagged as described in section 3.1.2. The track flags are sent to the multiplicity crate, where the information from all 24 sectors is combined to find an overall track multiplicity, and to the $\theta\phi$ matrix of the CTL. The following sections contain an overview of the operation of each part of the track trigger hardware. More details of the hardware registers and memories and their use can be found in reference [69].

3.2.1 CV z/r Modules

The CV z/r modules, which were built at the Rutherford Appleton Laboratory, are housed in the CV front–end crates. There is one z/r module per crate and each crate processes data from two of the 36 CV sectors, so each z/r module is effectively split into two with each half dealing with one sector. The z/r module is positioned so as to make the travel time of signals along the backplane from the converter modules, where the hit pulses are digitised, to the z/r module as short as possible.

For a hit on an axial wire in the vertex chamber, the converter module for that wire obtains a fast z value from a time difference measurement of the signals propagating to each end of the wire. This measurement is made by using the signal from one end of the wire to initiate the charging of a capacitor which is then halted by the arrival of the signal from the other end of the wire (the 'STOP' end). The signal from the 'STOP' end is delayed by 5 ns to ensure that it always arrives after the 'START' signal. The voltage across the capacitor is then proportional to the time between the two signals and, therefore, to the z value of the hit. A 6–bit Flash Analogue to

Digital Converter (FADC) is used to measure this voltage and the z value obtained is stored in a RAM. In order for the z measurement to be both precise and stable an autocalibration procedure is used. This injects pulses into alternate ends of the sense wires between beam crossings and the reference levels of the FADC are automatically adjusted.

The z/r module reads the 6–bit z values from the converter modules, making up to 6 'passes' through them. The ability to read more than one hit from each wire was introduced in case there should be background events underlying real physics events. In such a case if only one pass were performed many of the hits from the true track might be lost. In one 'pass' the z/r module makes 12 consecutive reads, one for each wire. Each individual read takes 100 ns so each pass takes 1.2 μs. The number of passes is independent of the number of hits on a wire so data are often read from the converter modules when there was no hit on a wire. In such cases the hits are flagged as 'bad' and are not histogrammed by the TTP. This flagging of 'bad' hits can be used to veto faulty wires since if a wire is vetoed then all hits from that wire are flagged as 'bad' and are not used by the track trigger.

In the z/r modules each z value is converted via a look up table (LUT) held in memory to a 5–bit z/r value which is sent to the track trigger processor. This look up table is calculated offline. In the vertex chamber the z obtained from reconstructing tracks in the stereo cells is more precise than that from the time difference measurement on the axial wires (σ_z^{stereo}= 700 μm, σ_z^{axial}= 4.5 cm) and the first is used to calibrate the latter. By extrapolating tracks found in the stereo cells back into the axial cells a plot of 'true' z against the fast z from time difference (coarse z) is made for each axial wire. An example of such a plot is shown in figure 3.3. This is fitted using a 3rd order polynomial and the constants of the fit are the 'z calibration constants' which provide a relationship between coarse and true z. More details of this procedure can be found in reference [70]. To calculate the z/r LUT the following method is used. For each coarse z value from the time difference measurement a true z is calculated using the calibration constants. This true z is converted to a z/r value, using the wire radius, and thus the z/r bin corresponding to the original coarse z value under consideration can be found. This is the value entered into the LUT.

Each z/r module also calculates a hit count or wire count for the relevant sector.

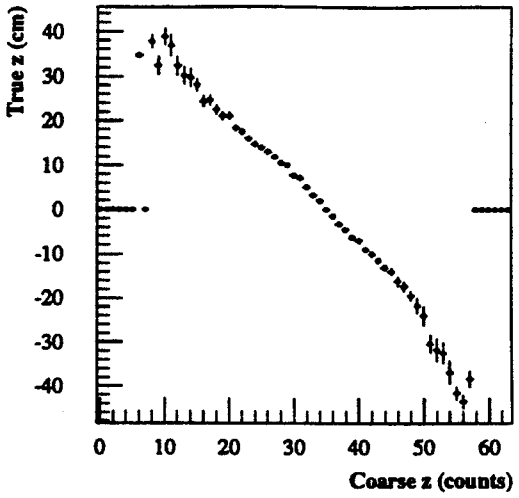

Figure 3.3: A plot of 'true' z against coarse z from time difference. This is used to calibrate the CV coarse z measurement. (Courtesy of M. Turner)

This is used by the ring hit count (RHC) part of the track trigger processor. For the first 12 reads (i.e. pass one) in addition to the z information for the first hit, the z/r module gets a 4–bit hit count from each converter module corresponding to the number of hits on that wire. The values from all 12 wires are accumulated to give both a wire count (the total number of wires hit in the sector) and a hit count (the total number of hits in the sector). Only one of these totals is passed onto the RHC board in the track trigger processor, which one is controlled by the setting of a register.

3.2.2 CJ z/r Modules

The CJ z/r modules were designed and built at the Albert Ludwigs University, Freiburg. There are 24 modules, one per ϕ sector, each one is connected to three groups of 12 adjacent wires in the corresponding sector of the CJ front–end electronics. These three groups correspond to the three rings used by the track trigger.

For each hit on a wire in one of the three rings the z/r module measures the z value by charge division. The signals from the two ends of each wire are fed into a 'multi–hit–sampler' card. The signals are amplified and summed and compared to a threshold corresponding to about 1/10 of a minimum ionizing particle. If the threshold

is exceeded then the charges from each end of the wire, q_1 and q_2, are integrated for about 200 ns. After the integration time the sum of the charges, q_1+q_2, is used as the reference point for a Flash Analogue to Digital Converter (FADC) and the charge from one end (q_1) is applied as the FADC input. In this way the FADC output corresponds to the division $\frac{q_1}{q_1+q_2}$ and gives a direct measure of the z value of the hit. This 7–bit z value is converted to a 5–bit z/r value by a look up table and this is stored in memory. A hit bit is set for each hit for which the sum of the charges q_1 and q_2 is less than that expected for 10 minimum ionizing particles. The charge from each hit is also stored in memory and is used in forming the 'charge triggers' described later.

After 5 μs, which is the maximum drift time for a hit in the outer ring, the z/r values of hits with hit bits set are sent to the track finder boards in the track trigger processor. For each ϕ sector the hits are sent down three cables, one for each ring. There is also a hit count performed in each of the three rings. If the hit count in a ring exceeds a threshold number of hits then a signal is sent directly to the SIM in the CTL.

Using the hit charges stored in memory and the sum of the charges in each ring, two other signals, the 'charge triggers', are formed. These are designed to trigger on free quarks and monopoles by identifying particles with very low and very high ionization respectively. As with the ring hit counts the signals are sent directly to the SIM in the CTL.

The look up table for the z to z/r conversion is calculated offline and uses an effective wire length which takes into account the additional apparent length of each wire due to the electronics at the end of the wire. From this the mapping of raw z value to z/r can be calculated, this process is described in detail in reference [68]. Each multi–hit–sampler (MHS) card is calibrated in two stages. To account for the fact that the gains of the CJ preamplifiers at the wire ends may not be exactly equal, a calibration is performed using a pulser system for the CJ. Using the pulser, equal charges are applied at the two ends of a wire and the gains on the MHS amplifiers are adjusted to give the same response for each end, i.e. a value of $z = 0$. The response is also equalized for all modules. Pedestals are also adjusted; using an internal pulser system, known charges are applied to the FADC inputs and the pedestals are adjusted to ensure that the response is as charge independent as possible.

3.2.3 Track Trigger Processor

The track trigger processor (TTP), designed and built at the Rutherford Appleton Laboratory, is housed in three 9U Eurocrates. The first two crates contain 24 track finder boards (one for each sector), a controller board and a fanout/ring hit count (RHC) board. The third crate contains the multiplicity modules; 12 input boards and an array board. There is also a VME crate running OS9 in the same rack which is used for control of the processor and is the Local System Crate for the track trigger data acquisition system. Figure 3.4 shows the layout of the crates and modules in the rack.

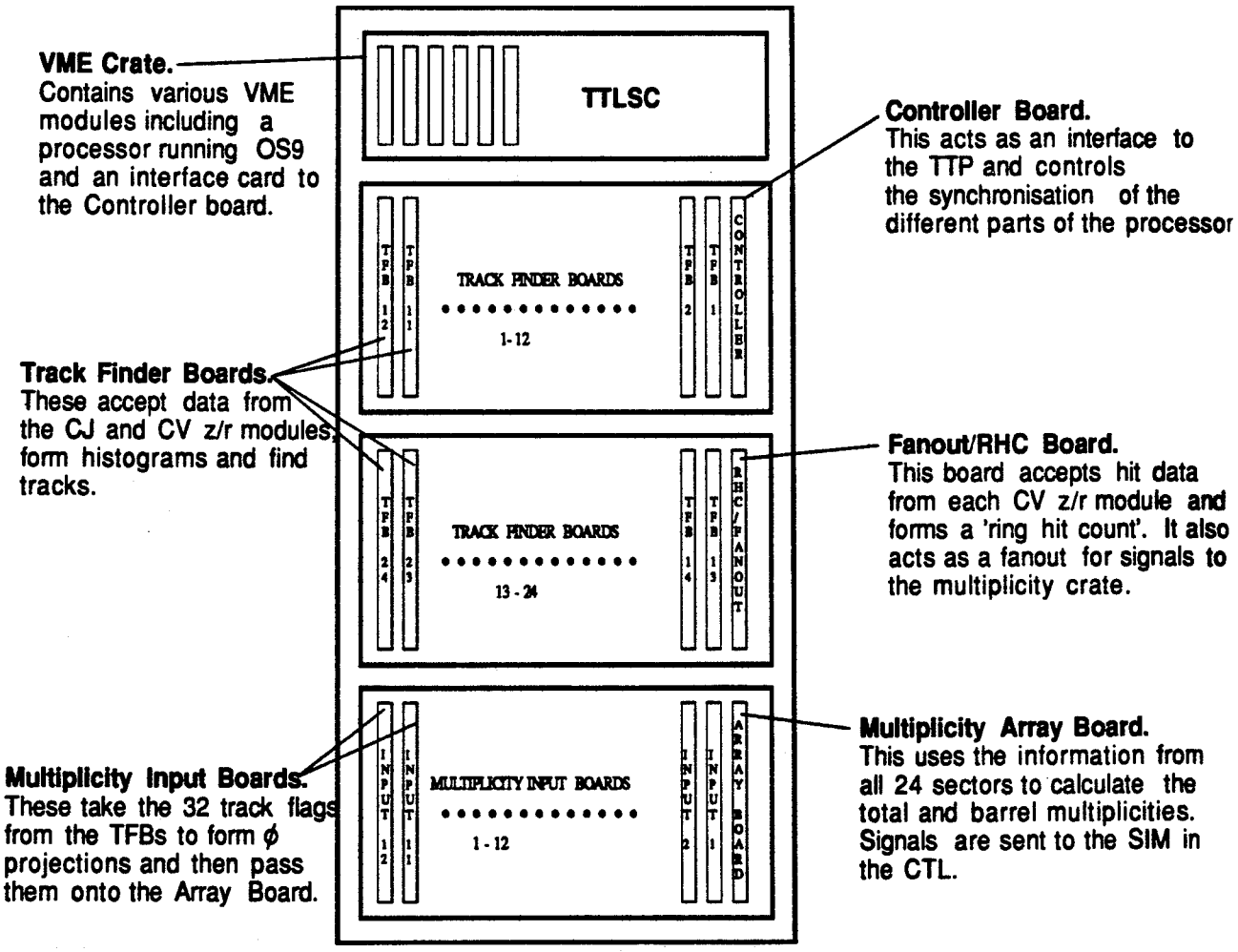

Figure 3.4: This diagram shows the positions of the various modules within the TTP rack.

3.2.3.1 Track Finder Boards

The track finder boards (TFBs) do the histogramming and track finding. Their operation is shown schematically in figure 3.5. Each TFB receives z/r data from one CJ sector and one or two CV sectors and forms z/r histograms of the hits. The number of CV sectors associated with each TFB varies from board to board because there are 36 CV sectors to match to the 24 CJ sectors. Each even numbered TFB accepts data from two CV sectors while odd numbered TFBs are connected to only one CV z/r module. The four histograms (one for CV and one for each CJ ring) are then overlapped in ϕ and smeared in θ. The ϕ overlap is done by adding histograms from adjacent track finder boards, the smearing direction is to lower ϕ, i.e. the smeared histogram in TFB

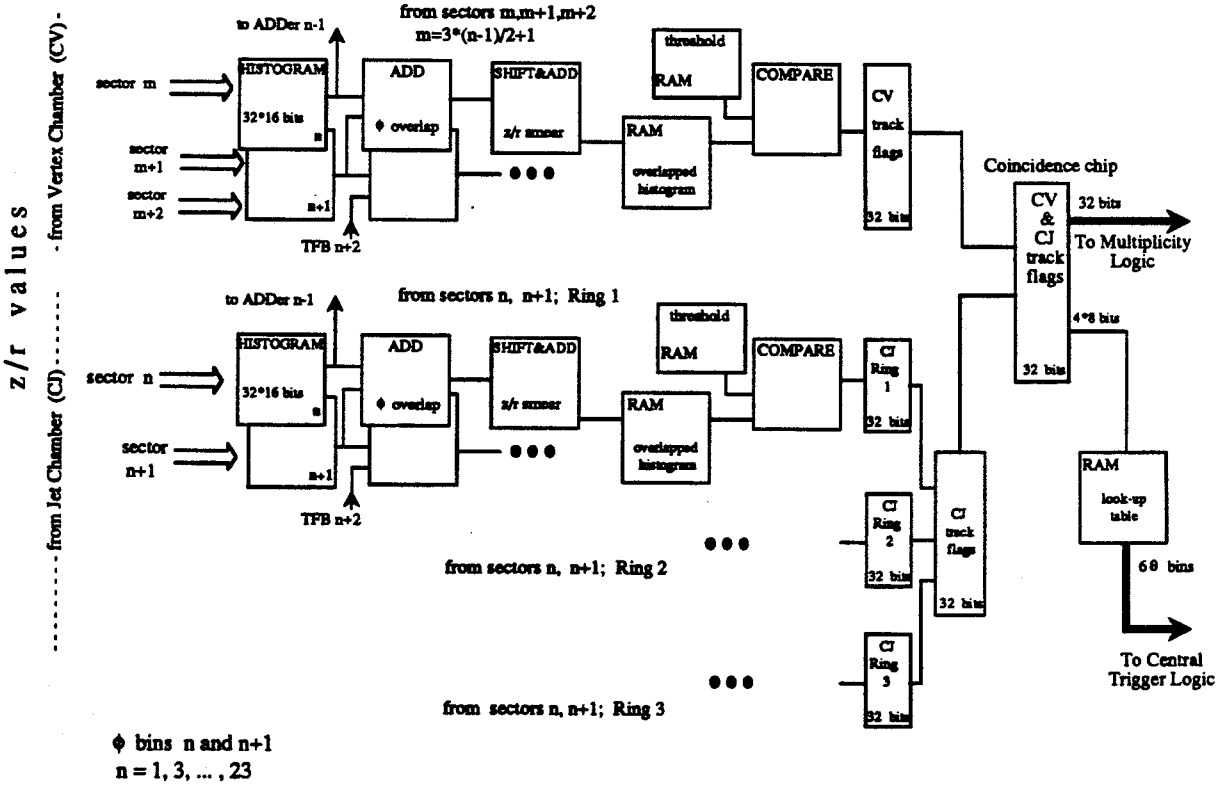

Figure 3.5: This diagram shows schematically the working of the TFB for sector n. The z/r values of hits are received from the CV and CJ z/r modules. These are histogrammed and the ϕ overlap and θ smear are performed. Track flags for CV and CJ and formed and then combined in the coincidence chip. The resulting track flags are sent to the $\theta\phi$ matrix of the CTL and to the multiplicity crate.

i is the sum of the unsmeared histograms from TFBs i and $i+1$. Since ϕ is continuous around the detector the histograms from sector 1 are added to those in sector 24. This results in 24 z/r histograms in overlapping ϕ bins. The θ smear is then done by shifting the ϕ smeared histogram and adding it to the original. Figure 3.6 shows how this works for a θ smear of 2, each smeared bin contains data from 2 unsmeared bins. The smeared histogram bin contents are then compared to preset thresholds (held in RAM) to find track segments. The track flags from the three CJ rings are combined to produce overall CJ track flags in one of the ways described in section 3.1.2

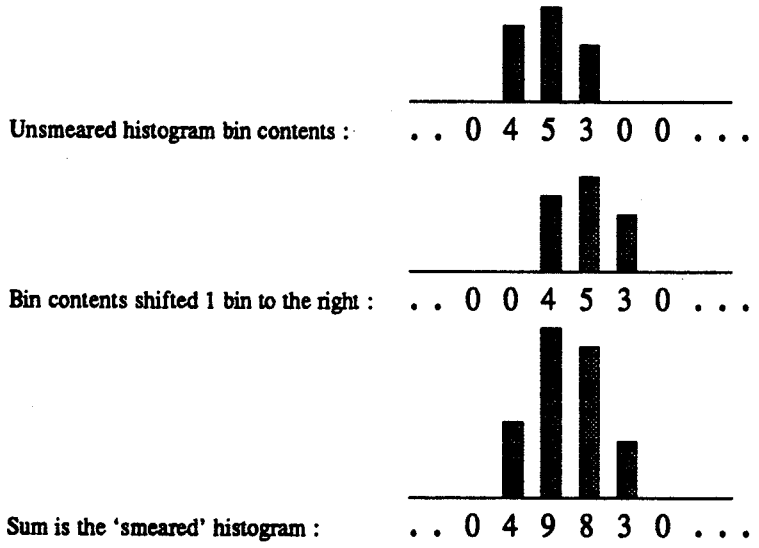

Figure 3.6: An example of how the how the θ smear in the track finder boards works.

Coincidences between the vertex and jet track flags are found using a custom–designed "coincidence chip". The coincidence chip can be viewed as a 32×32 array of ones and zeros, an example of which is shown in figure 3.7. For each CJ track flag which is set the 32 bits in the appropriate row of the array are taken. Where bits are set in this row the corresponding CV track flag is considered. Only if one of the CV track flags examined in this way is set is a final decision bit set. The final decision bit is set in the same bin as the original CJ track flag. This leads to 32 track decisions in each ϕ sector which are sent to the multiplicity crate and are also reduced to 6 bits and sent to the $\theta\phi$ matrix of the Central Trigger Logic (CTL).

The coincidence chip is usually set up with a diagonal pattern of ones (see figure 3.7).

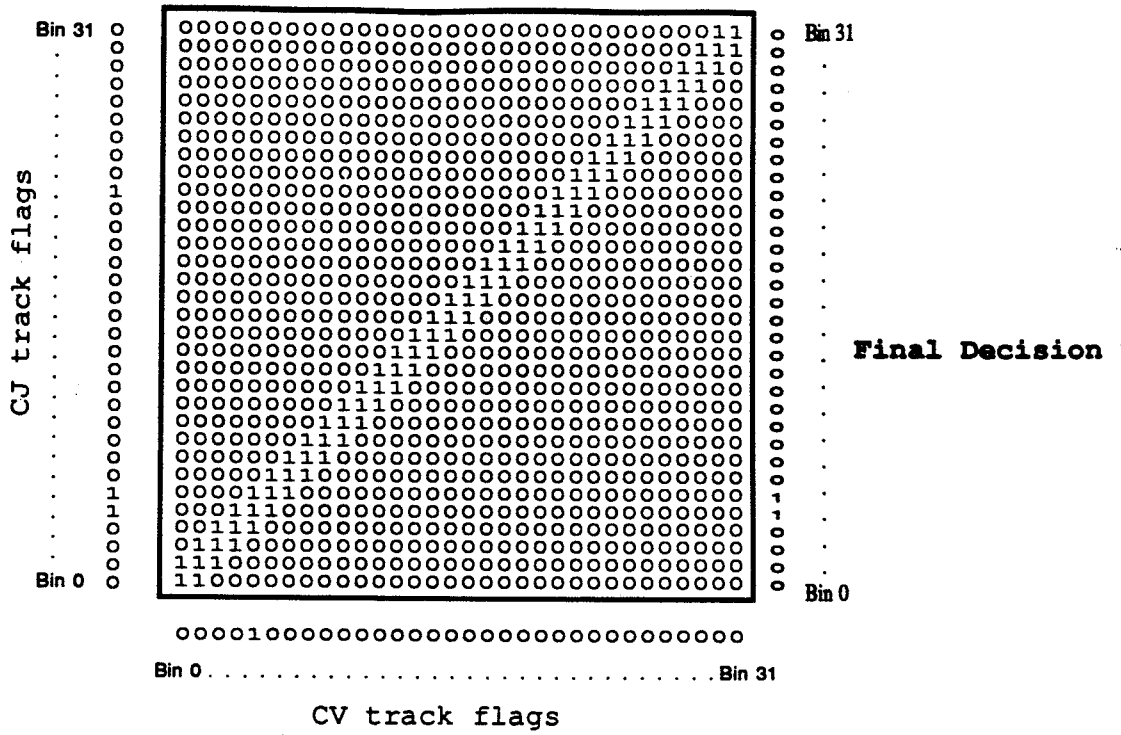

Figure 3.7: An example of the 32 × 32 array which makes up the coincidence chip and its operation. The pattern shown corresponds to a width of 1 with an offset of 0.

This pattern can be parameterized by two variables, a width and an offset. The width determines the z window around the interaction point from which tracks can originate and still be efficiently triggered. The offset can be used to allow for an inexact alignment of the CV and CJ within OPAL or in the case that the beams do not cross at the centre of the detector.

The reduction of the 32 track trigger decision bits to the 6 θ bits for the $\theta\phi$ matrix of the CTL is done by a look up table (LUT) using the following algorithm. Knowing the z/r range of the track trigger, the number of z/r bins being used and the position of the rings, the z/r range and hence the θ range of each bin can be calculated. If the decision bit in z/r bin i from the track trigger is set, then bits in all CTL bins containing the θ of i are set. This leads to rather loose associations and a single track found in the track trigger can easily fire three CTL θ bins.

In order to minimise the amount of memory space required for the above LUT, rather than using all 32 bits of the track trigger decision as an address, they are split into four groups of 8 and these 8 bits are used to address the memory. The memory

used for the LUT is actually 1024 locations long (i.e. 10 bits) and the top 2 bits of the address are used to distinguish which of the four sets of 8 decision bits are being used. The memory is used as a LUT four times and an OR of the resulting four sets of 6 bits is sent to the $\theta\phi$ matrix in the CTL.

3.2.3.2 Multiplicity crate

In the multiplicity crate there are twelve input boards, each one accepting data from two track finder boards. The information from the 24 ϕ sectors is then combined on the array board. The array board, therefore, has the whole 32×24 $\theta\phi$ array from which to find the track multiplicity. Due to the smearing which has been applied each track should appear in at least 2 θ and 2 ϕ bins, so good tracks will appear as clusters of ones in the array. The method used to find tracks is to form projections of the array onto the θ and ϕ axes, and to count clusters of ones as tracks. For the θ projection all ϕ bins with a given θ are considered, if any have a bit set then the projection bit is set for that θ bin (see figure 3.8). This leads to a 32–bit projection. A similar procedure for the ϕ projection leads to 24–bits. By looking for isolated clusters of ones in the projections it is possible to estimate the multiplicity of the event. The size of a cluster taken to correspond to one track depends on the θ smear which was applied in the track finder boards. The final multiplicity is taken as the maximum from the two projections. Two multiplicity counts are performed, one for the complete θ range and one for a reduced 'barrel' region.

The above method fails when tracks are 'shadowed' by other tracks. For example, in figure 3.8, what is clearly a 3 track event will be found to have a multiplicity of only 2 if the above method is used. To get around this problem, two additional projections are made along the left and right diagonals of the array. The largest multiplicity from the four projections is then taken as the final value. The cluster counting is complicated slightly by the fact that there is 'wraparound' in the ϕ, left diagonal and right diagonal projections, for example in the ϕ projection bin 1 and bin 24 must be considered as adjacent. This is taken into account in the algorithms used to calculate the multiplicity from each projection, further details of which can be found in references [71] and [72].

The 12 multiplicity input boards form the ϕ projection and do some bit shifting to

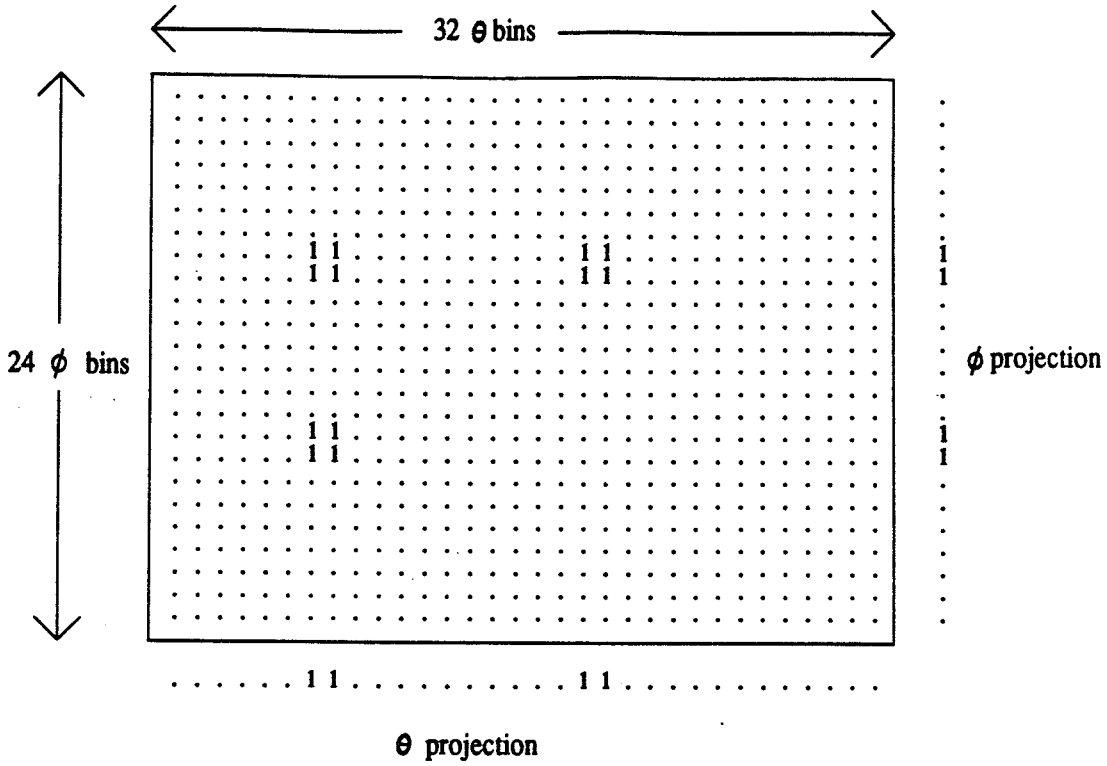

Figure 3.8: An example of a possible $\theta\phi$ array in the array board. Three tracks appear as clusters of ones. Also shown are the expected projections along the θ and ϕ axes.

make formation of the other projections on the array board a simple OR operation. In the hardware the calculation of the multiplicity is done by a look up table (LUT) for each projection. The output from each LUT is a track multiplicity of 0, $\geq 1, \geq 2$, or ≥ 3 tracks in both the full detector and the barrel part of the detector. The largest multiplicity from the four projections is sent as a standalone signal to the SIM in the Central Trigger Logic (CTL).

3.2.3.3 Ring Hit Count

Simultaneous to the track finding, the track trigger processor performs a vertex ring hit count on the ring hit count (RHC) board. The hit counts or wire counts from each individual CV z/r module are summed to give a total ring hit count which is compared to a preset threshold and a signal is sent to the SIM in the CTL if the count exceeds threshold.

The counting is done via two direct cables, each one daisy chained between 9 CV

z/r modules, i.e. 18 CV sectors, and the RHC board. A memory on the ring hit count board contains the addresses of those CV z/r modules which are connected to each cable and the hit count board uses this information to request the hit count data from each z/r board in turn. The z/r modules monitor the addresses on the cable and respond by sending their hit count data when they recognise their own address. This board also acts as a fanout for the controller to communicate with the multiplicity crate.

3.2.4 Local System Crate and TTP Controller

The VME crate at the top of the TTP rack is the Local System Crate (LSC) for the track trigger data acquisition system. It also interfaces to and controls the running of the track trigger processor (TTP). It contains a Fast Intelligent Controller (CES FIC 8320 with a Motorola 68020 processor) running OS9.

The TTP is controlled by sending instructions and data to the controller board. The instructions tell the controller to perform input/output (I/O) operations which enable reading and loading of the registers and memories within the TTP. An instruction can also force the controller into a run mode where a run cycle will be initiated by a beam-crossing ('BX') signal at the front panel of the controller.

As well as acting as an interface to the rest of the TTP for I/O the controller also controls the synchronisation of the various parts of the TTP during a run cycle. A run cycle is initiated by a 'BX' signal arriving at the front panel of the controller. The controller then waits for signals from each part of the processor to indicate completion before allowing the next phase of the processing to start. For example, the CV z/r modules must not read the hit data from the converter modules before the time difference measurement is complete and the controller makes sure that this is the case. The controller has a second input on the front panel and a signal here acts as a reset and will trigger the controller to clear all memories and prepare for the next event. During normal running the reset signal is supplied by the Central Trigger Logic.

3.3 Software

3.3.1 Online

There are two parts to the TT online software. The online test programs check the operation of the hardware, further details of these can be found in reference [73]. The data acquisition (DAQ) programs control the running and readout of the track trigger processor in global OPAL running and local test running. Both sets of programs are written in Real Time Fortran [74] and are run under the OS9 system in the track trigger LSC. Online monitoring routines are run in the trigger and filter crates, described in sections 2.9.1 and 2.9.2.

3.3.1.1 Test programs

The track trigger has many built in test features which can be used to provide set patterns of hits to the processor to test its functionality. For example, test memories are available in the CV z/r modules and by configuring the TTP correctly the information from these test memories can be used instead of the data from the front–end converter modules. These memories can be loaded with preset patterns under software control for studies of the hardware performance. There are also some so–called 'dummy run' facilities which allow the track trigger running to be done step by step rather than a complete cycle being initiated by a beam–crossing signal. These are again useful for studying the detailed workings of the hardware.

For the commissioning of the track trigger hardware many programs were written using these test features. By using known hit patterns and checking the contents of registers and memories at different stages of the TTP the hardware can be thoroughly tested. The test programs were designed to check all parts of the processor to varying degrees. They range from simple tests such as whether or not a cable is plugged in correctly or a crate powered on, to the tracking down of subtle timing problems which may cause inefficiencies. All parts of the TTP can be tested individually and the system can be tested as a whole. The programs were still of value during data taking as a frequent check that the hardware was still functioning correctly and for debugging purposes if problems were seen offline.

3.3.1.2 Data acquisition programs

In order that the working of the track trigger (TT) can be tested thoroughly offline it is desirable to store information about the decision making process within the TTP. To this end, many of the processor's registers and memories are read out on each event and the information is sent through the OPAL DAQ chain to tape. The data are also used for online monitoring of the track trigger performance as described in section 3.3.1.3. The DAQ programs must initialise the track trigger before running, control the running, synchronise with the rest of OPAL, readout the electronics and store the initialisation constants for access later. The programs are based on a standard set of software, the 'skeleton', which is used by all OPAL subdetectors to achieve uniformity throughout the detector. The 'skeleton' provides services to manage the data buffers and to control the trigger hardware in each LSC.

Originally it was not intended for the TT to be readout by the DAQ system since it is a trigger rather than a detector, and the data are used to check the functioning of the TT only. The readout of the track trigger is split into two parts, the readout of the CJ z/r modules being separate from that of the rest of the processor, the 'RAL electronics'. Since the electronics was not designed with DAQ in mind, a full readout of the RAL electronics, involving the reading of many large memories, is very time consuming. This introduces a large deadtime (about 150 ms) into the OPAL DAQ and cannot, therefore, be performed on every event (without TT the average OPAL deadtime was about 20 ms in 1990). To get around this problem the full readout is prescaled so that it is performed only every N events and in addition a short readout of only a few registers is performed every event. The short readout contains enough information to detect problems offline and to indicate their frequency, the long readout can then be used to track down the problem to a specific part of the TTP. All three types of readout (CJ, RAL short and RAL long) can be prescaled separately. It is also possible to set a flag so that readout only occurs on TT triggered events, this is useful because prescaled events are then sure to contain relevant TT information. Care must be taken, however, since this is clearly not a good way to run when trying to track down problems causing inefficiencies.

Due to the high level of programmability of the track trigger there are many 'ini-

tialisation' parameters required to set up the processor for running (see reference [73] for details). These initialisation parameters are stored in a file on the OS9 system from where at each run start they are downloaded into the hardware and are also stored in a database so that they can be retrieved by the offline programs at a later date.

In order to enable swapping between various frequently needed setups, more than one version of the initialisation file is kept available at a time and it is possible to swap between some of them from run-control. In particular, one can take CV in and out of the decision making. This is useful in case of high backgrounds when CV may not be turned on for fear of damaging the chamber. Since the track trigger is a 'required' subdetector for OPAL to take physics data it needs to be able to run even if the CV is off, so a fast changeover between modes is necessary. In fact, during the 1990 run there were few problems with turning on CV and it was always included in the TT decision making. The ability to change the set up quickly was, however, useful for testing the charge trigger which required a different z/r binning to the default.

3.3.1.3 Online monitoring

The online monitoring of the track trigger performance is done in the trigger and filter crates since at that stage of the DAQ data from all subdetectors are available making it possible to monitor efficiencies, etc. The monitoring includes:

- **Histogramming of rates of the standalone and $\theta\phi$ signals in the trigger crate.** The rates of the SIM signals are constantly monitored and this is useful for seeing if a signal suddenly dies or becomes noisy. A map of the rate of the $\theta\phi$ signals is provided as a two dimensional histogram and this is a useful tool for detecting problems affecting only one region of the track trigger. Figure 3.9 shows an example of such a histogram, the depth of shading indicates the relative rates of the signals in each bin. This histogram also supplies information about the background levels. The dark areas in θ bins 1 and 6 shows that there is more background in these bins which correspond to the 'forward' regions of the detector. It can also be seen that the background, which is due to synchrotron radiation, is concentrated in sectors 11, 12 and 13 which are on the outside of the LEP ring. The asymmetry in the distribution, bin 6 is darker than bin 1,

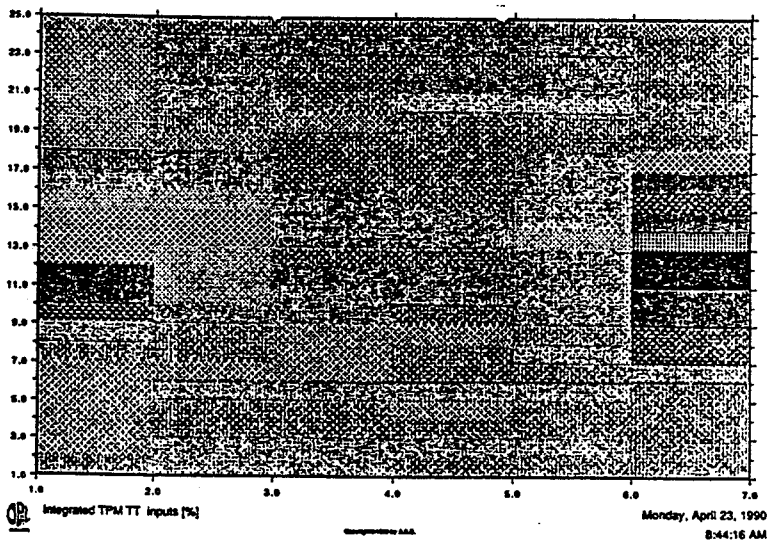

Figure 3.9: An example of the two dimensional histogram of the TT $\theta\phi$ signal rates available in the trigger crate. The depth of shading indicates the relative rates of the signals.

indicates that, in this fill, one beam (e^-) has more beam associated background than the other.

- **Checking for inconsistencies and flagging them in the filter crate.** A program running in the filter crate checks that for each TT SIM input which fires all expected other TT signals fired. For example, if 2 tracks are found in the barrel then the signal for 1 track in the barrel should also fire and those for 1 and 2 tracks in the full detector . This checking can show up problems in the multiplicity crate and faulty cables.

- **Efficiency plots for lepton pairs.** These are calculated using the filter event flagging, described in section 2.9.2, to select events and the CJ online pattern recognition results, see section 2.3.2, to define where a track was in the detector. The efficiency is plotted as a function of ϕ and $cos\theta$ and the plots allow a fast observation of any problems causing a drop in efficiency in all or part of the detector.

3.3.2 Offline

A set of routines were written to be run offline on the track trigger data [75]. These take the CV and CJ raw hit information and apply algorithms to simulate the workings of the track trigger hardware and to predict the results at all stages of the decision making process. These were used before data-taking started in 1989 to simulate the workings of the TT hardware with different setups and to decide how best to configure it (see references [71, 76, 77]). Once data taking started the routines were used to check the functioning of the track trigger. The checking program compares the true contents of the registers and memories from the TT data with the predictions from the reconstruction and gives warnings whenever inconsistencies occur. Such a facility has proved useful in finding problems and also for checking whether faults found with the hardware were in fact present in the data and causing problems.

3.4 Performance of the track trigger

3.4.1 Setup

As has already been described, there is a great deal of flexibility about the way in which the track trigger hardware is set up. This means that it is possible to tune the parameters to optimize the efficiency and background rejection for different running conditions. During initial running in 1989 the voltage on the vertex chamber was not usually turned on until some time into a fill. This was because the backgrounds were high until the LEP collimators were inserted and the beam had stabilized, which usually took some time. Being farther from the beam, CJ was less affected by the backgrounds and was usually switched on earlier than CV. To maximise the 'on time' of the track trigger, only the CJ inputs to the decision making were used. The positions of the three rings are given in table 3.1. To keep the background levels reasonable it was necessary to require at least two rings to find a track so the angular coverage of the track trigger was limited to the region covered by both CJ ring 1 and ring 2, i.e. $|\ cos\theta\ | \leq 0.9$.

In the 1990 run the LEP collimators were inserted more quickly and the stability at the beginning of a run increased so that the vertex detector was added to the decision

making in the track trigger. This meant that the 'forward' region, $0.9 \leq |\ cos\theta\ | \leq 0.95$, was then covered by two rings; CV and CJ ring 1. Therefore, the track trigger acceptance was extended to $|\ cos\theta\ | \leq 0.95$ whilst still maintaining good background rejection. Table 3.1 shows the positions and acceptances of the four rings. The other change for 1990 was that CJ ring 3 was moved closer to the beam to include another z/r bin, this increased the barrel acceptance, and hence the acceptance of the signal for ≥ 2 tracks in the barrel (TBM2), which is used as a stand alone trigger, to $|\ cos\theta\ | \leq 0.82$. Figure 3.10 is an $r - z$ view of the detector showing the position of the four rings and their relevant acceptances for the 1990 configuration.

Table 3.1: The positions of the track trigger rings for the 1989 and 1990 running periods, showing the angular coverage of each.

year	ring	wire numbers	radius (cm)	z/r bins covered	angular coverage $\lvert\ cos\theta\ \rvert \leq$
1989	CJ Ring 1	9-20	33.5-44.5	1-18	0.95
	CJ Ring 2	37-48	61.5-72.5	4-15	0.90
	CJ Ring 3	129-140	153.5-164.5	7-12	0.73
1990	CJ Ring 1	9-20	33.5-44.5	1-18	0.95
	CJ Ring 2	37-48	61.5-72.5	4-15	0.90
	CJ Ring 3	97-108	121.5-132.5	6-13	0.82
	CV	1-12	10.3-16.2	1-18	0.95

Although the hardware allows for up to 30 z/r bins (bins 0 and 31 are underflow and overflow bins) only 18 were used. This is to make the bin size compatible with the z resolution of the detectors. The vertex chamber has a z resolution of about 4.5 cm and the radius at the centre of the axial wires is 13 cm so a bin size of 0.35 in z/r corresponds to the resolution in z. The total range of the track trigger in z/r is 6.4 (this corresponds to the angular region $|\ cos\theta\ | \leq 0.95$), with a bin size of 0.35 this range covers 18 bins.

As shown in table 3.2, in 1990 the hit thresholds were set to 4 in the vertex chamber and 4, 5 and 6 in CJ rings 1, 2 and 3 respectively. In the forward direction, $|\ cos\theta\ | \geq 0.9$,

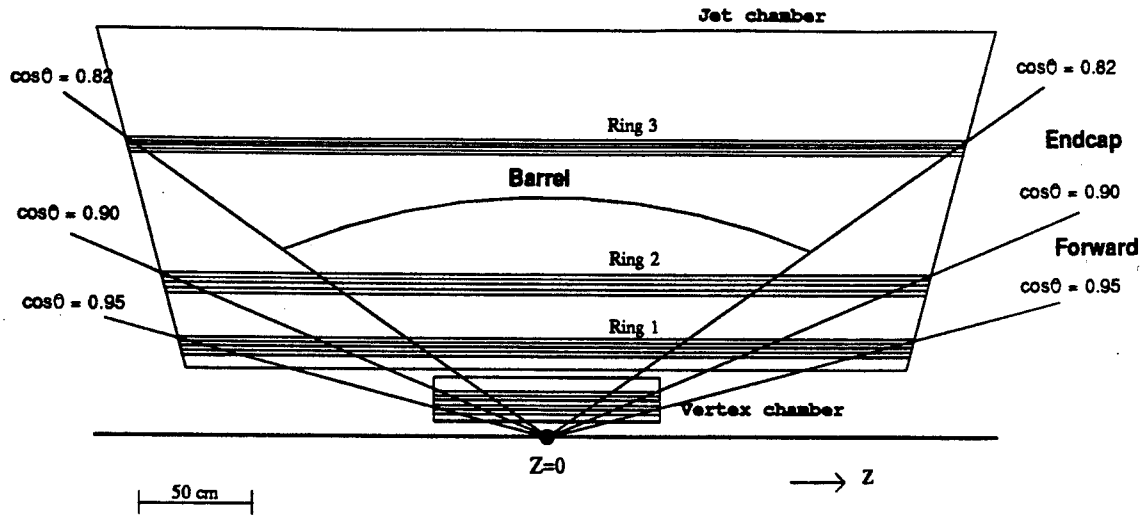

Figure 3.10: This figure shows the position of the four track trigger rings and the angular coverage of each for the 1990 setup. Since the barrel acceptance is defined to be the same as for CJ ring 3 it is $|\ cos\theta\ | \leq 0.82$. The trigger must use at least 2 rings to reduce backgrounds so the full acceptance is that of CJ ring 1 and CV, $|\ cos\theta\ | \leq 0.95$.

where only wires from the vertex chamber and first ring of the jet chamber contribute the threshold was raised to 6 in CJ ring 1 to provide better background rejection. For track finding, hits above threshold were required in all geometrically possible rings, i.e. an AND of the 3 CJ rings was required to give the overall CJ decision. This requires the setting of the thresholds to zero for regions of z/r which are outside the physical acceptance of a ring (track flags are always set in bins with a zero threshold).

The settings of the other important track trigger parameters are listed below.

- **θ smear** – the smear used is 2 in both the CV and CJ.
- **Barrel definition** – this is defined to cover the same angular region as CJ ring 3, $|\ cos\theta\ | \leq 0.82$, which corresponds to z/r bins 6-13 for the 1990 setup.
- **Coincidence chip setup** – this was set up with a width of 2 and an offset of 0 for the 1990 run, giving a z_0 window of about 16 cm around the interaction point for triggering tracks in the barrel. For most of the 1989 run the coincidence chip was not used. However, for tests including CV at the end of the run a window of 3 was used.

Table 3.2: The threshold values in the four rings of the track trigger for 1990 data taking. The bins are numbered from 0 to 31 and refer to θ smeared bins.

bins	0-1	2-4	5-6	7-13	14-15	16-18	19-31
$cos\theta$ range	underflow	-0.95 → -0.90	-0.90 → -0.81	-0.81 → 0.81	0.81 → 0.90	0.90 → 0.95	overflow
vertex	127	4	4	4	4	4	127
ring1	127	6	4	4	4	6	127
ring2	127	0	5	5	5	0	127
ring3	127	0	0	6	0	0	127

- **Four passes of CV z/r modules** – the number of read passes made by the CV z/r modules was reduced from the maximum of 6 to 4 for timing reasons. Each pass takes 1.2 μs and if more than four are made the multiplicity signals are produced too late to reach the SIM within the trigger gate and can not then be used. A Monte Carlo study indicated that this reduction in the number of passes does not affect the efficiency.

The track trigger was an active part of the OPAL trigger for almost all of the 1989 and 1990 running periods. There were few hardware faults once the trigger had been commissioned and it performed well, being an essential trigger for low multiplicity events. All data from the 1989 run was checked offline and this showed up a few minor problems which were fixed. The DAQ system had some problems in 1990 which meant that much offline checking could not take place, the online monitoring at the trigger and filter however proved sufficient for the detection of problems.

3.4.2 Performance and Efficiency

The TT signals which were used as stand alone triggers, i.e. those which were sufficient to trigger an event, were $\geq$2 tracks in the barrel, $\geq$3 tracks in the complete detector or two collinear signals in the $\theta\phi$ matrix. This last signal is formed at the CTL, rather than the track trigger, using the signals sent from the TFBs. These triggers ran at a rate of about 0.1–0.2 Hz. The main background was due to beam–wall and beam–gas

events. The efficiency of the track trigger for muon pair events was 98.5%. The main cause of inefficiency was δ–electrons which spiral along the wires in the jet chamber and destroy the charge division measurement.

In order to investigate the performance of the track trigger a sample of single isolated tracks is used. A track is considered to have triggered if the $\theta\phi$ bin to which it points is set. Since the binning of the $\theta\phi$ matrix is quite coarse (the bin sizes are given in table 2.1) the track must be well isolated to make this meaningful. Tracks are only used if there are no other tracks within 30° in ϕ.

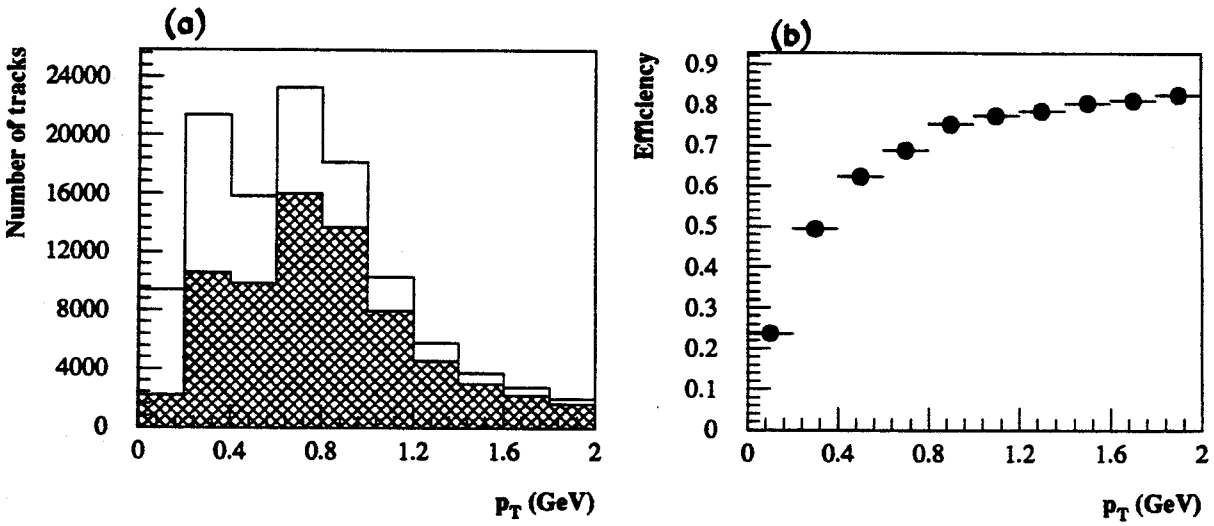

Figure 3.11: TT efficiency as a function of p_T.
(a) The open histogram shows the p_T distribution for all tracks and the shaded histogram the distribution for tracks triggered by the track trigger.
(b) Efficiency as a function of p_T.

With the given set up of the track trigger the transverse momentum (p_T) threshold is expected to be about 600 MeV in the barrel, and lower in the forward regions, see appendix B.1 for the calculation of this threshold. Figure 3.11 (a) shows the p_T distribution for all tracks and for triggered tracks (shaded). The efficiency is shown in figure 3.11 (b). As can be seen the efficiency drops off at about 600 MeV as expected, in fact the threshold is slightly higher than that calculated. The efficiency does not reach 100% because all isolated tracks were used in the plot, including those from background events.

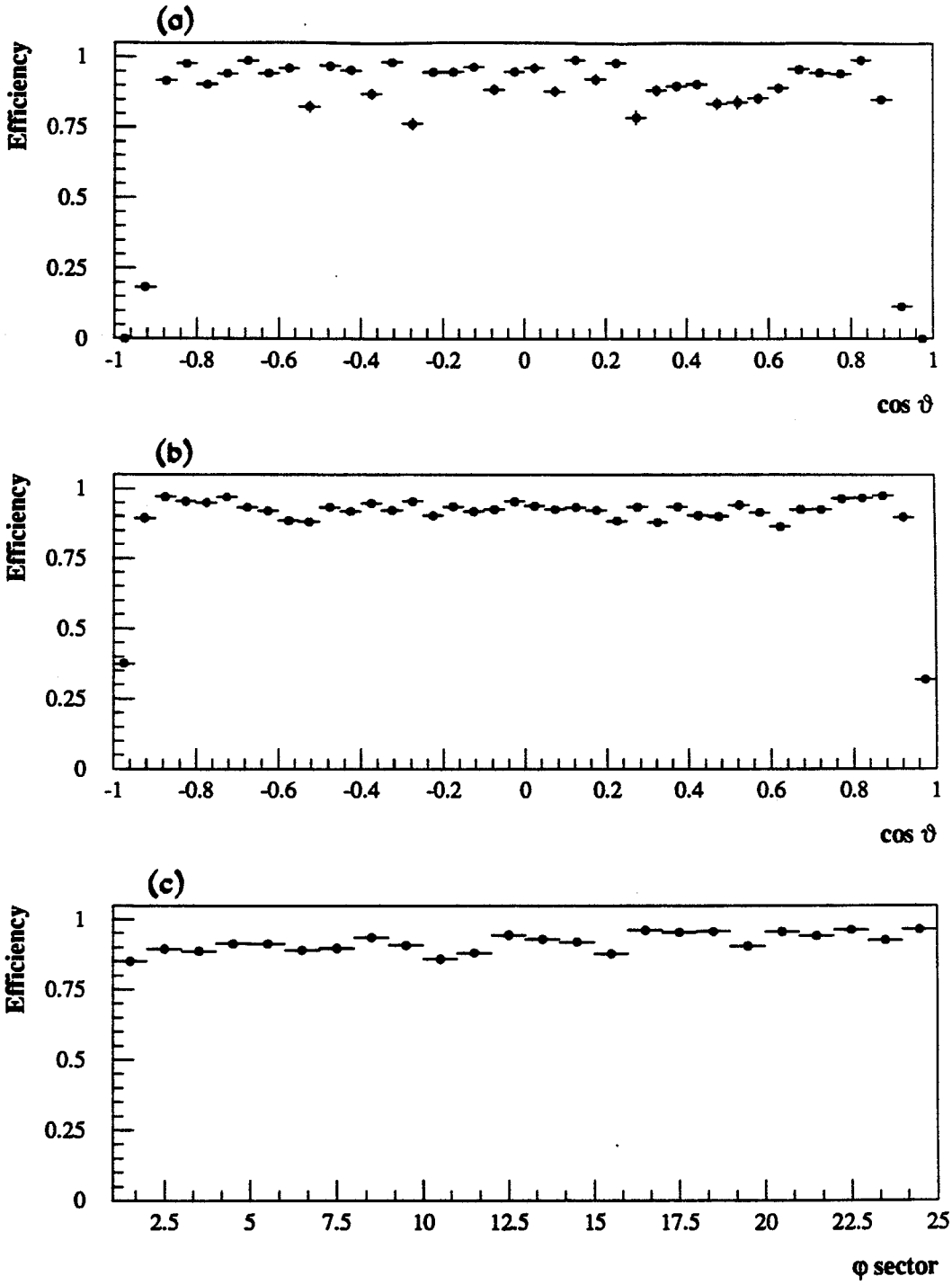

Figure 3.12: Track trigger efficiency.
The efficiency as a function of $cos\theta$ for (a) events from early 1990 before the acceptance was extended and (b) events from 1990 after the acceptance had been extended to $|\ cos\theta\ | \leq 0.95$.
(c) The track trigger efficiency versus ϕ sector.

For data taking in 1989 and the first few fills in the 1990 data taking period the track trigger acceptance was $\mid cos\theta \mid \leq 0.90$. This can be seen in figure 3.12 (a) which shows the efficiency as a function of $cos\theta$ for data from the early part of the 1990 run before the acceptance was extended. In order to choose good tracks which should fire the TT, only those tracks which originate from within 30 cm of the origin in z and have a $p_T \geq 1.0$ GeV are included in the plot. Figure 3.12 (b) shows the same plot for data from the 1990 run after the acceptance was extended to $\mid cos\theta \mid \leq 0.95$. As a function of ϕ sector the efficiency should be flat. A plot of efficiency versus sector number (figure 3.12 (c)) shows that this is not quite the case. The fluctuations are due to occasional hardware faults in individual modules.

The set up of the coincidence chip determines the z_0 window around the interaction point from which tracks can come and still be efficiently triggered, called z_{cut}. This window can be calculated (see appendix B.2) and is expected to be about 16 cm for barrel tracks with the 1990 TT setup. For the 1989 setup when only the CJ information was used by the TT, the window was larger, about 19 cm. Figure 3.13 shows plots of efficiency as a function of $\mid z_0 \mid$ for barrel tracks in the two datasets. It is clear that fewer tracks further from the origin were efficiently triggered in 1990 than in 1989, indicating the tighter vertex constraint which is applied by including CV. Due to the

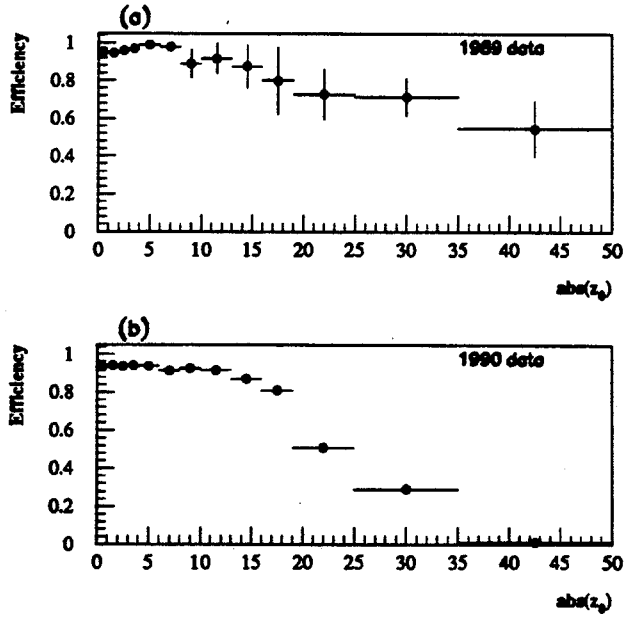

Figure 3.13: The efficiency as a function of $\mid z_0 \mid$ for (a) 1989 data and (b) 1990 data.

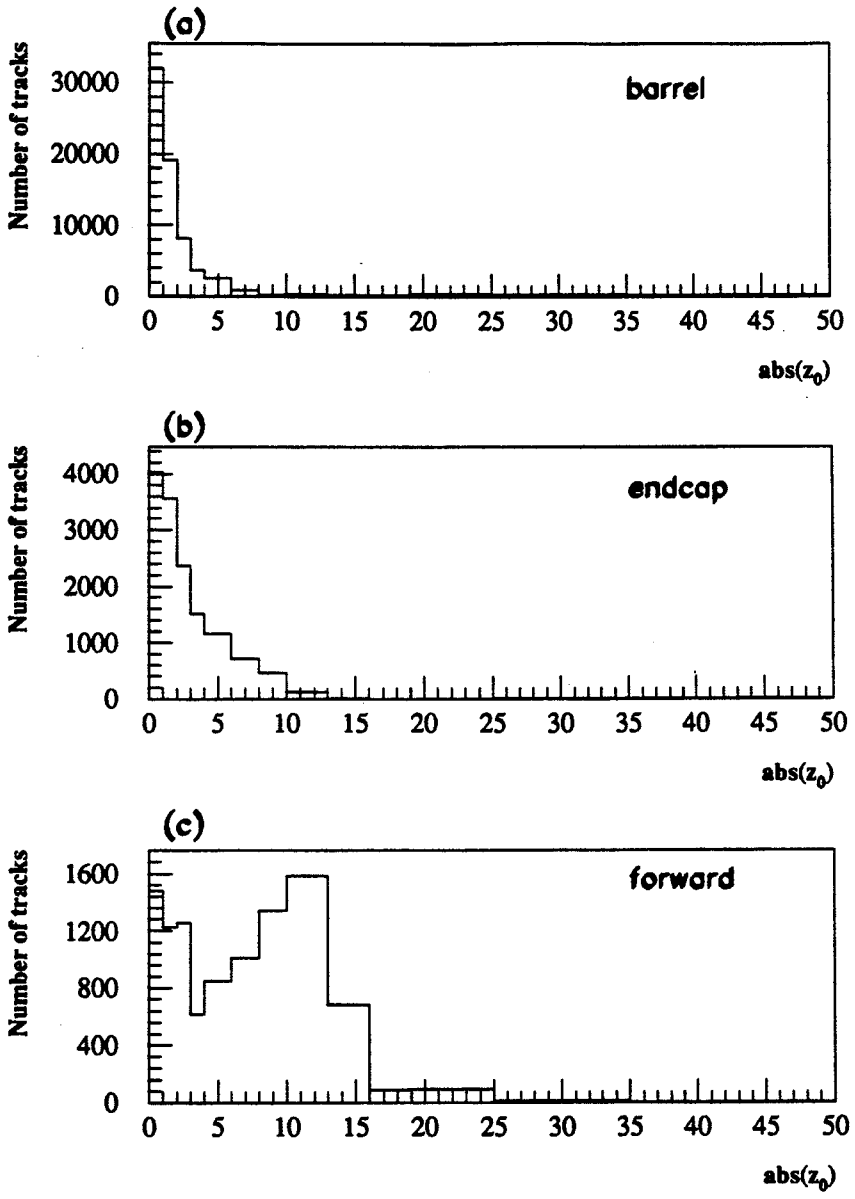

Figure 3.14: $| z_0 |$ for tracks triggering the TT in (a) the barrel region, (b) the endcap region and (c) the forward region.

z resolution of the detectors the efficiency plots do not have a well defined cutoff.

The calculations also predict that the value of z_{cut} is larger for tracks at higher $| cos\theta |$ values because there is less of a lever arm for determining the z value of a track at the beam axis when it passes through fewer rings. This can be seen in figure 3.14 which shows the $| z_0 |$ values for tracks triggering the TT in the three angular regions

defined in figure 3.10. Clearly the $|\ z_0\ |$ of the more forward going tracks is less well constrained by the track trigger and hence more background events are triggered in these regions.

Figures 3.15, 3.16, 3.17 and 3.18 are some event pictures showing events on which the track trigger does and does not trigger . Firstly, a τ pair event which TT triggered is shown in the $r-\phi$ plane, figure 3.15, and the $r-z$ plane, figure 3.16. The TBM2 trigger signal indicates two tracks found in the barrel of the detector and this is sufficient to trigger the event. Figure 3.17 is a cosmic ray event leaving two tracks in the central detector. The displacement of the tracks from the interaction point means that TT did not trigger. Finally, figure 3.18 is a beam–wall/beam–gas event which occurred outside the detector but sent tracks into the chambers. Again the fact that the tracks do not originate from the interaction point means that TT did not trigger this event.

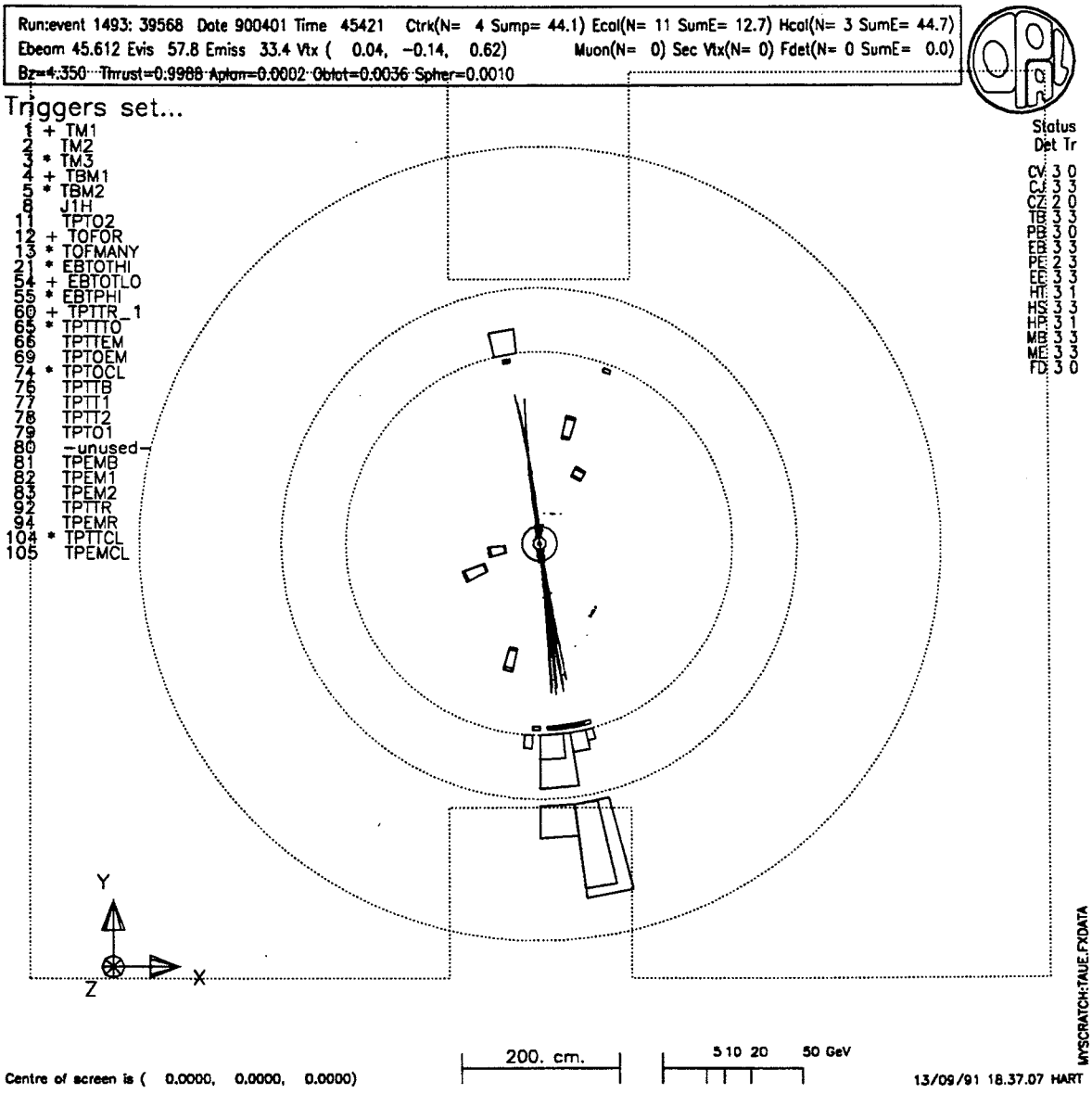

Figure 3.15: $r - \phi$ view of a τ pair event.

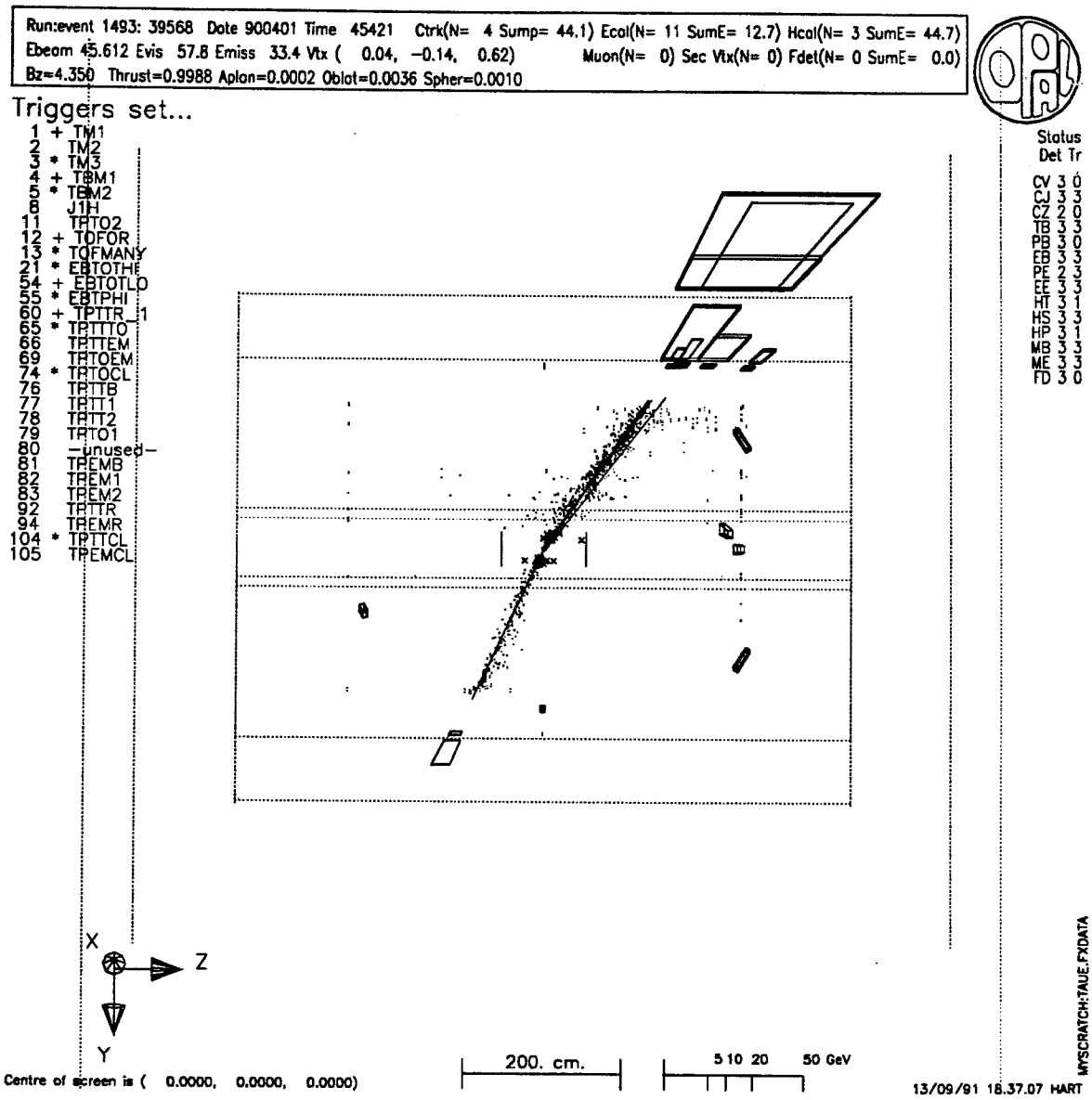

Figure 3.16: $r - z$ view of a τ pair event.

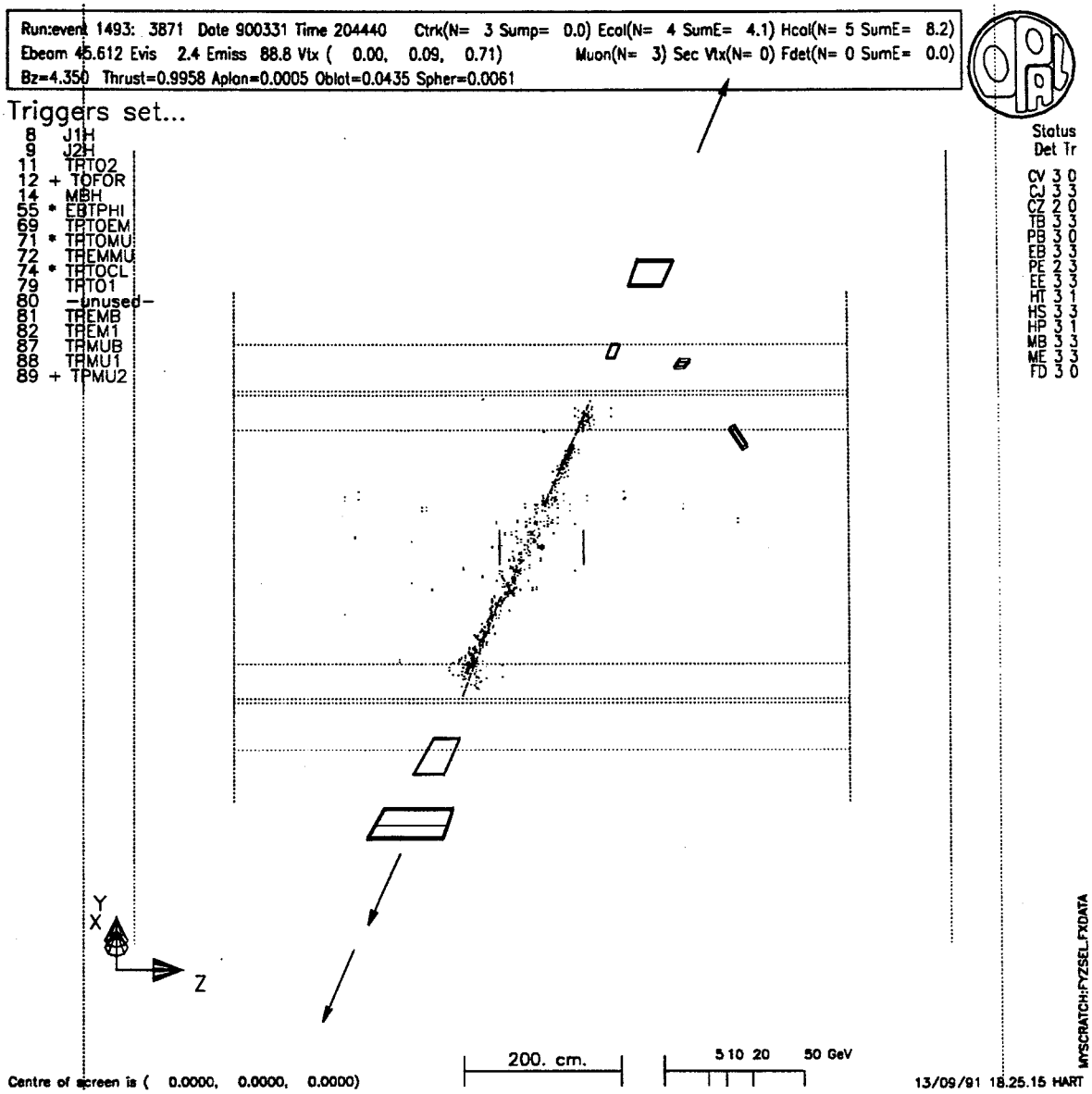

Figure 3.17: A cosmic ray event leaving tracks in the central detector.

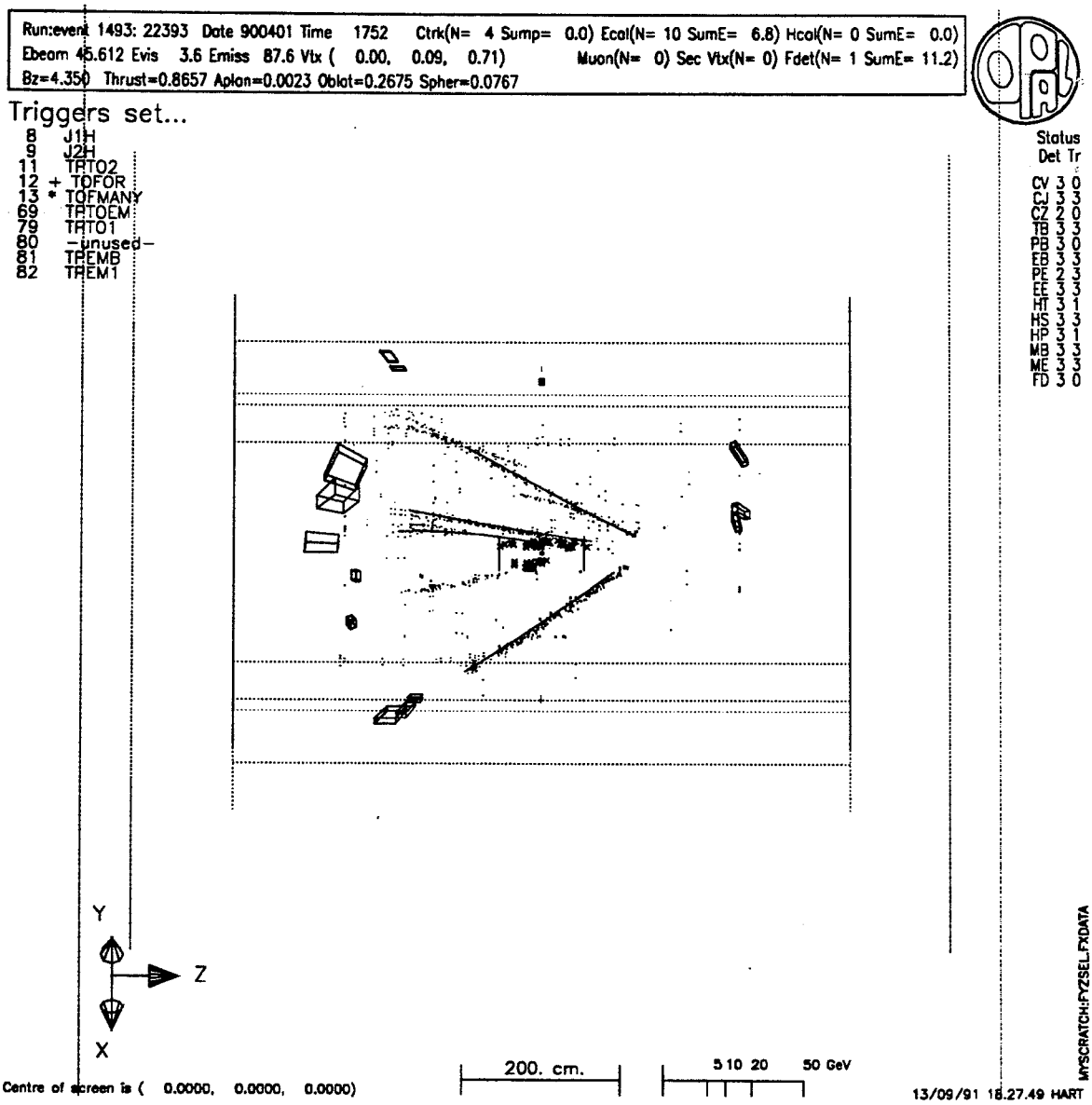

Figure 3.18: A beam–wall/beam–gas event leaving tracks in the central detector.

Chapter 4

Measurement of the $\tau \rightarrow e\nu_\tau\bar{\nu}_e$ Branching Ratio

4.1 Introduction

As has already been discussed in Chapter 1 there is interest in determining the exclusive branching ratio for the process $\tau \rightarrow e\nu_\tau\bar{\nu}_e$ in order to help resolve some long standing discrepancies in this area. In particular, much attention has been given to the disagreement between the one–prong inclusive branching ratio compared to the sum of the one–prong exclusive branching ratios and the difference between the measured $\tau \rightarrow e\nu_\tau\bar{\nu}_e$ branching ratio and that expected from the τ lifetime. Here the $\tau \rightarrow e\nu_\tau\bar{\nu}_e$ branching ratio is measured and the result is discussed with reference to these discrepancies.

The branching ratio, $\mathrm{BR}(\tau \rightarrow e\nu_\tau\bar{\nu}_e)$, is defined as:

$$\mathrm{BR}(\tau \rightarrow \mathrm{e}\nu_\tau\bar{\nu}_\mathrm{e}) = \frac{\text{Number of } \tau \rightarrow \mathrm{e}\nu_\tau\bar{\nu}_\mathrm{e} \text{ decays}}{\text{Total number of } \tau \text{ decays}}$$

This is measured by selecting a sample of $\tau \rightarrow e\nu_\tau\bar{\nu}_e$ decays from a preselected sample of τ pair events. The selected events are then corrected for background contamination and efficiency factors and the branching ratio is derived using the following expression:

$$\mathrm{BR}(\tau \rightarrow e\nu_\tau\bar{\nu}_e) = \frac{\mathrm{N}_{Cand.}^{\tau\rightarrow e\nu_\tau\bar{\nu}_e}}{\mathrm{N}_{Cand.}^{e^+e^-\rightarrow\tau^+\tau^-}} \frac{(1 - f_{bckgnd}^{non-\tau\rightarrow e\nu_\tau\bar{\nu}_e})}{(1 - f_{bckgnd}^{non-\tau})} \frac{1}{\varepsilon^{\tau\rightarrow e\nu_\tau\bar{\nu}_e}} \frac{1}{\mathrm{B}^{\tau\rightarrow e\nu_\tau\bar{\nu}_e}} \qquad (4.1)$$

where $\mathrm{N}_{Cand.}^{\tau\rightarrow e\nu_\tau\bar{\nu}_e}$ is the number of $\tau \rightarrow e\nu_\tau\bar{\nu}_e$ candidates selected, $\mathrm{N}_{Cand.}^{e^+e^-\rightarrow\tau^+\tau^-}$ is the number of preselected τ jets, $f_{bckgnd}^{non-\tau\rightarrow e\nu_\tau\bar{\nu}_e}$ is the background fraction in the $\tau \rightarrow e\nu_\tau\bar{\nu}_e$

sample with contributions from other τ decay modes and non-τ sources, $f_{bckgnd}^{non-\tau}$ is the estimated background fraction in the τ pair sample, $\varepsilon^{\tau \to e\nu_\tau\bar{\nu}_e}$ is the efficiency for selecting $\tau \to e\nu_\tau\bar{\nu}_e$ decays from the preselected τ pair events and $B^{\tau \to e\nu_\tau\bar{\nu}_e}$ is the bias towards $\tau \to e\nu_\tau\bar{\nu}_e$ decays in the preselection of the τ pair events.

In this chapter the criteria for selecting τ pair events and $\tau \to e\nu_\tau\bar{\nu}_e$ decays are described and the correction factors for backgrounds and efficiencies are determined. These are then used to measure the BR($\tau \to e\nu_\tau\bar{\nu}_e$) using the above expression. The momentum spectrum of the $\tau \to e\nu_\tau\bar{\nu}_e$ events is used in the next chapter to measure the τ polarization.

4.2 Selection of $e^+e^- \to \tau^+\tau^-$ events

In the vicinity of the Z° resonance τ pair events are characterized by two nearly back-to-back "jets" each containing one or more particles. When the τs decay, νs are produced, and, since these are undetected, this leads to a non-zero transverse momentum in the event with respect to the beam direction. It also means that the observed energy of the event is less than the centre of mass energy (E_{CM}). These features enable τ pair events to be distinguished from background events. There are four main backgrounds to the $e^+e^- \to \tau^+\tau^-$ events, these are Bhabha events, μ pair events, multihadron events and two photon events.

During the reconstruction of OPAL events, low multiplicity candidates including lepton pair, two photon, cosmic ray, beam wall and beam gas events, are flagged. These events are then stripped from the main dataset to provide a smaller more manageable set of events for developing cuts, etc. The τ pairs used for this analysis were selected from the 'Low Multiplicity' sample and the cuts used to select that sample are described below.

4.2.1 'Low Multiplicity' event selection

In order to be used in the analysis, tracks and electromagnetic calorimeter (ECAL) clusters must pass some criteria for being classified as 'good'.

Good track and cluster requirements

A 'good' track is defined as having a p_T of at least 100 MeV, $|\, d_0 \,| \leq 2$ cm, $|\, z_0 \,| \leq 50$ cm, $N_{hit}^{CJ} \geq 20$ and $r_{min} \leq 75$ cm. Here p_T is the momentum of the track transverse to the beam direction, d_0 is the distance of closest approach of the track to the beam axis, z_0 is the displacement of the track along the beam axis from the interaction point at this point of closest approach, N_{hit}^{CJ} is the number of space points measured on the track in the jet chamber and r_{min} is the radius of the first measured point on the track. Figures 4.1 (a) and (b) show the $|\, z_0 \,|$ and $|\, d_0 \,|$ distributions for all tracks in selected low multiplicity events and the cuts used to define good tracks. The cuts reject 50% of tracks in low multiplicity events and 24% of tracks in selected $e^+e^- \rightarrow \tau^+\tau^-$ events. Most of the tracks rejected by these cuts are from photon conversions, cosmic rays, etc. and are not genuine tracks from the event vertex.

A good ECAL cluster must satisfy the following requirements:

$$\begin{aligned} \text{Barrel}: &\quad E_{clus}^{raw} \geq 100 \text{ MeV} \\ \text{Endcap}: &\quad \begin{cases} E_{clus}^{raw} \geq 200 \text{ MeV} \\ N_{blck} \geq 2 \\ E_{max}^{fract} \leq 0.99 \end{cases} \end{aligned}$$

Where E_{clus}^{raw} is the raw energy of the cluster, N_{blck} is the number of lead glass blocks in the cluster and E_{max}^{fract} is the maximum fraction of the cluster energy contributed by any one block. 'Hot clusters', which are noise clusters occurring frequently for some period of the data taking, are also removed. Figure 4.1 (c) shows the raw energy versus θ distribution for all clusters in selected low multiplicity events. The large number of low energy clusters are due to noise and are removed by the 'good' cluster requirements. The noise in the endcap is at a higher energy than that in the barrel hence the higher energy cut. Figure 4.1 (d) shows the E_{clus}^{raw} distributions separately for the barrel and endcap regions and the respective cuts for good clusters. In the barrel 66% of raw clusters are rejected by these cuts, in the endcap 78% are rejected.

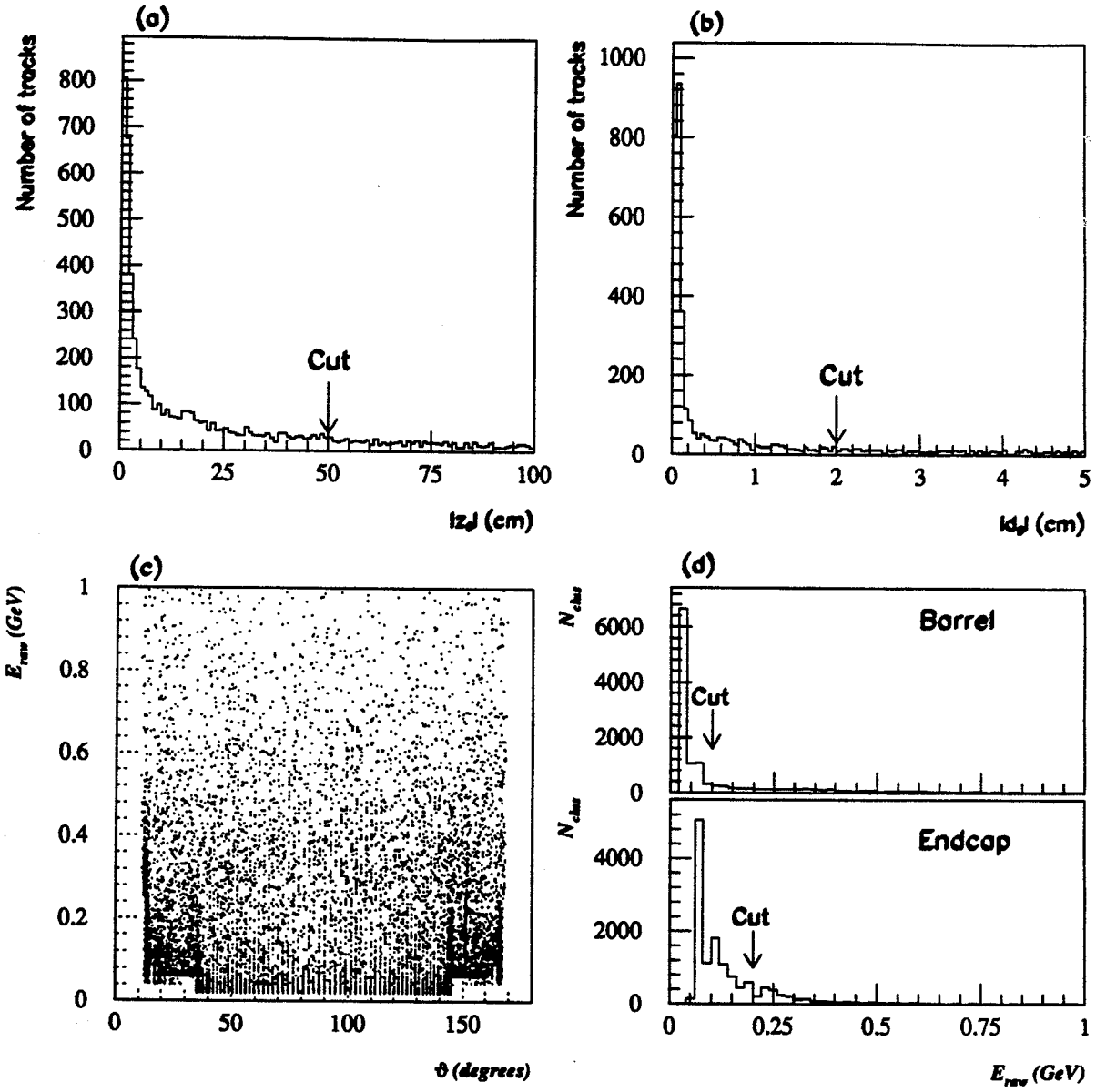

Figure 4.1: Good track and cluster requirements.
(a) $| z_0 |$ for all tracks in selected low multiplicity events.
(b) $| d_0 |$ for all tracks in selected low multiplicity events.
(c) E_{clus}^{raw} vs. θ for all electromagnetic clusters in selected low multiplicity events.
(d) E_{clus}^{raw} distributions for the barrel and endcap regions separately. The cuts for good clusters are shown.

Low Multiplicity selection

Events are preselected as low multiplicity events if they contain any of the following:

- $\geq$ 1 good charged track with $p_T \geq 0.7$ GeV, $\mid d_0 \mid \leq 1$ cm, $\mid z_0 \mid \leq 50$ cm and $N_{hit}^{trck} \geq 30$, where N_{hit}^{trck} is the number of measured points on the track in the central detector including CV, CJ and CZ.

- $\geq$ 2 good electromagnetic clusters both with $E_T \geq 6$ GeV , where E_T is the energy of the cluster.

- $\geq$ 2 good electromagnetic clusters that are back to back within 25° and one of which has $E_T \geq 2$ GeV.

In addition, a veto is made on high multiplicity events in order to remove most multihadron events. An event is rejected if:

$$N_{trck} + N_{clus} > 18$$

where N_{trck} is the number of good charged tracks and N_{clus} is the number of good electromagnetic clusters and the sum is referred to as the multiplicity. Figures 4.2 (a) and (b) show the multiplicity distributions for $e^+e^- \rightarrow \tau^+\tau^-$ and $e^+e^- \rightarrow q\bar{q}$ Monte Carlo (MC) events, respectively. It can be seen that the cut removes nearly all multihadron events, 99%, but very few τ pairs, 0.3%. Figure 4.2 (c) shows the same distribution for τ pair MC and data events. The discrepancy between data and MC at low multiplicity is due to the fact that more charged tracks are seen in the data than in the MC. This may be due to either too few gamma conversions being simulated in the MC or single tracks being split into two in the data.

The efficiency of the low multiplicity selection for τ pair events is estimated by comparing the track and calorimeter based selections and is found to be higher than 99.9%. In addition the MC predicts that 0.3% of events are rejected by the high multiplicity veto. From the 1990 OPAL data 153 501 events are selected into the 'Low multiplicity' sample by these cuts.

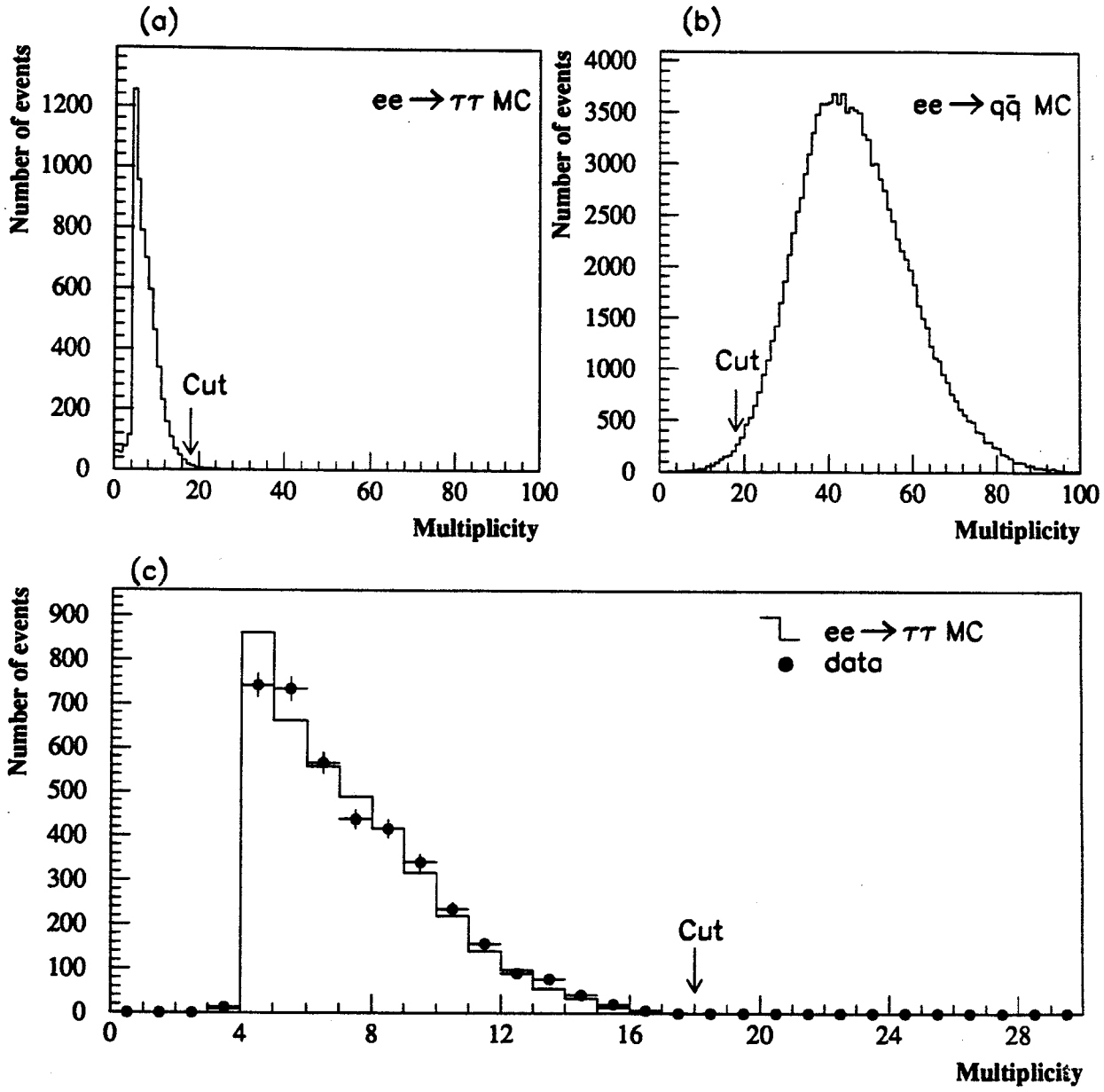

Figure 4.2: High multiplicity veto.
Multiplicity ($=N_{trck} + N_{clus}$) distributions for:
(a) $e^+e^- \rightarrow \tau^+\tau^-$ MC events after detector simulation.
(b) $e^+e^- \rightarrow q\bar{q}$ MC events after detector simulation.
(c) $e^+e^- \rightarrow \tau^+\tau^-$ events from MC and data after all τ pair selection cuts.

4.2.2 $e^+e^- \rightarrow \tau^+\tau^-$ event selection

In this section the criteria for selecting τ pair events from the 'Low Multiplicity' sample are described. The cuts used are based on 'good' tracks and 'good' electromagnetic calorimeter (ECAL) clusters as described in section 4.2.1. A comparison is made between the distributions for data and for Monte Carlo events. The Monte Carlo events include both $e^+e^- \rightarrow \tau^+\tau^-$ and expected background events and were generated using KORALZ [37] for $e^+e^- \rightarrow \tau^+\tau^-$ and $e^+e^- \rightarrow \mu^+\mu^-$ events, BABMC [78] for $e^+e^- \rightarrow e^+e^-$ events, JETSET [79] and HERWIG [80] for multihadron events and VERMAS [81] for two photon events. All of the MC samples have undergone a full detector simulation using GOPAL. In all plots the solid histograms correspond to the MC and the points to the data and the histograms are normalised to the number of selected $e^+e^- \rightarrow \tau^+\tau^-$ candidates. Data from the peak energy only is used in the plots.

To be selected as an $e^+e^- \rightarrow \tau^+\tau^-$ candidate an event must satisfy the following requirements:

- **Multiplicity cut:** To reject the remaining multihadron events, cuts are made on both the track and cluster multiplicity:

$$2 \leq N_{trck} \leq 6$$

$$N_{clus} \leq 10$$

  Where N_{trck} is the number of 'good' charged tracks in the event and N_{clus} is the number of 'good' ECAL clusters in the event. Although tracks and clusters can be 'matched', as described in appendix A.3, this is not needed for the identification of τ pair events and would only add unnecessary complexity to the cuts. Figures 4.3 (a) and (b) show the N_{trck} and N_{clus} distributions for MC and data. The solid histogram includes $e^+e^- \rightarrow \tau^+\tau^-$ and multihadron MC events and the dashed histogram only the $e^+e^- \rightarrow \tau^+\tau^-$ MC events. A small excess over the prediction of the $e^+e^- \rightarrow \tau^+\tau^-$ MC is seen in the region above the cuts due to the multihadron events.

  In the N_{trck} distribution an excess over the MC prediction is seen in the three and five track bins, there are equivalent losses in the two and four track bins but

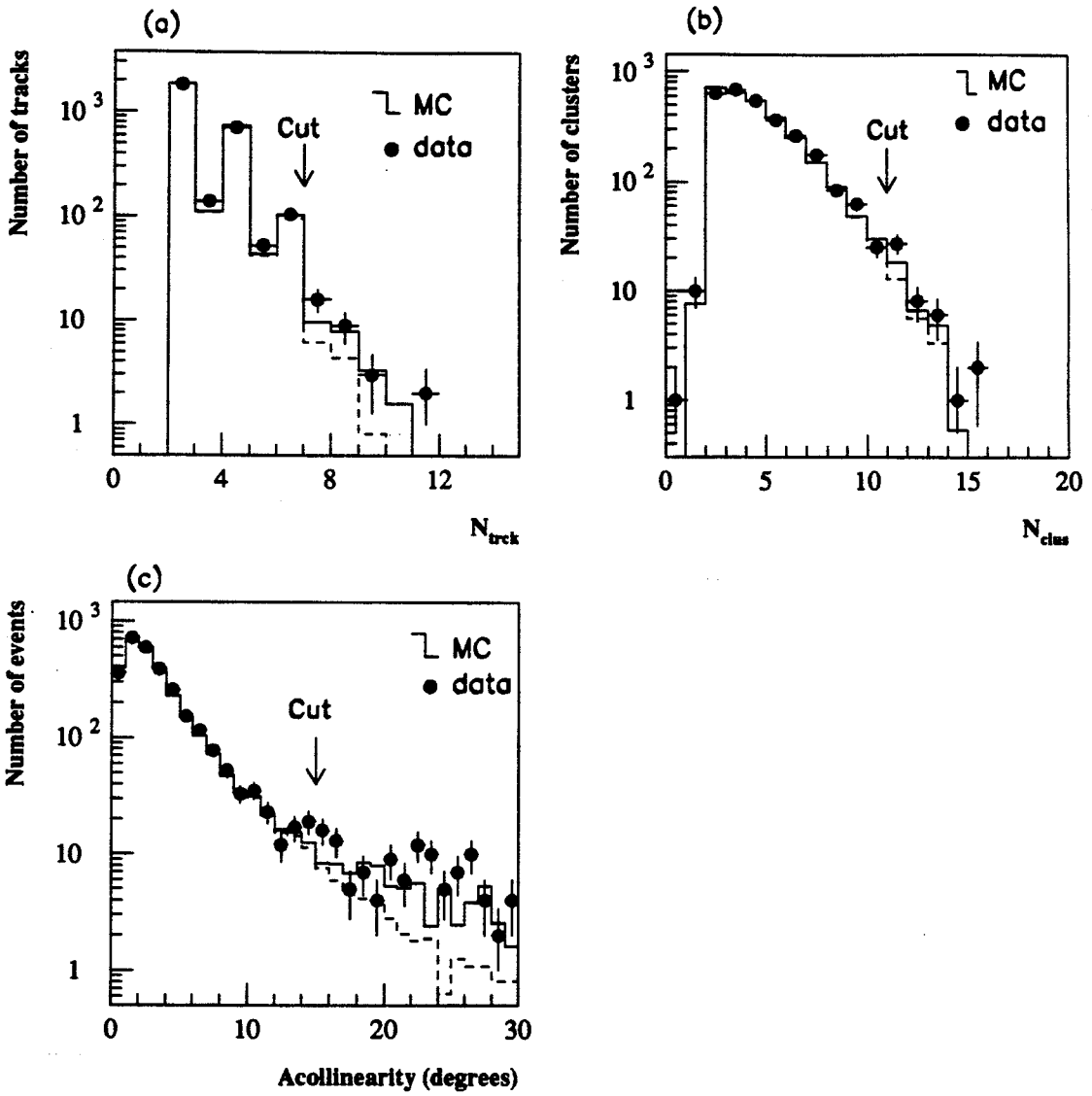

Figure 4.3: $e^+e^- \to \tau^+\tau^-$ selection cuts.
(a) N_{trck} distribution for MC events (histogram) and data (points) after all other cuts. The solid histogram contains both $e^+e^- \to \tau^+\tau^-$ and multihadron MC events, the dashed histogram is $e^+e^- \to \tau^+\tau^-$ MC events only.
(b) N_{clus} distribution for MC events and data after all other cuts. The histograms are the same as in (a)
(c) Acollinearity distribution for MC and data events after all other cuts. The solid histogram contains MC events from $e^+e^- \to \tau^+\tau^-$, $e^+e^- \to e^+e^-(\gamma)$ and two photon events and the dashed histogram is $e^+e^- \to \tau^+\tau^-$ MC only.

these cannot be seen on the scale of the plot. Possible sources of these extra tracks were discussed in section 4.2.1.

- **Cone analysis:** $e^+e^- \to \tau^+\tau^-$ events can be treated in terms of jets defined by the τ decay particles. τ pair events should have two isolated, back to back jets and a "cone analysis" is used to identify these. Both charged tracks and ECAL clusters are used and are treated as 'particles'. The highest energy particle in the event is chosen and a cone with a 35° half angle[1] is defined around it. Within this 35° cone the next highest energy particle is found and this is combined with the initial particle to define a new direction about which a new 35° cone is defined. The next highest energy particle within the new cone is then found and combined and so on until no more particles are found inside the cone. Then a new jet is started using the highest energy particle outside the first cone. The process continues until no particles are left unassociated with jets. Signals in the presampler, hadron calorimeter and muon chambers within the solid angle of a cone are associated with that jet.

  A τ pair event is required to have exactly two cones, each with at least one charged track and with an energy of at least 0.5% of E_{CM}. To ensure that the jets are back to back the acollinearity between the two cones must be less than 15° where the direction of each jet is defined by both the charged tracks and the ECAL clusters. This cut removes radiative Bhabha events and two photon events. Figure 4.3 (c) shows the acollinearity distribution for events with two charged cones for data (points) and MC (histograms). The solid histogram is the sum of $e^+e^- \to \tau^+\tau^-$, $e^+e^- \to e^+e^-(\gamma)$ and two photon MC events and the dashed histogram contains $e^+e^- \to \tau^+\tau^-$ MC events only.

- **Bhabha event rejection:** $e^+e^- \to e^+e^-$ events are characterized by two high momenta particles which each deposit close to the beam energy in the electromagnetic calorimeter. However, τ pair events are unlikely to deposit the full energy

[1] A cone half angle of 35° was chosen after a study which compared the ratio of the number of events rejected and accepted by the cone analysis in the data and the MC. The difference in this ratio between the data and the MC was found to decrease with increasing cone angle for small angles but to become stable at larger angles. The chosen value of 35° is in the stable region.

in the calorimeter because some energy is carried off by neutrinos, so cuts on the energy in the calorimeter are used to remove Bhabha events from the sample. Cuts are made on the total energy in the electromagnetic calorimeter, E^{ECAL}, and on the weighted sum of the ECAL energy and the charged track momentum, E^{WTOT}:

$$E^{ECAL} = \sum_{i=1}^{N_{clus}} E_i^{Ecal}$$

$$E^{WTOT} = \sum_{i=1}^{N_{clus}} E_i^{Ecal} + 0.3 \sum_{j=1}^{N_{trck}} p_j$$

Where the sums are over all good tracks and ECAL clusters. E^{WTOT} relies mainly on the electromagnetic shower energy since this has a better resolution than the track momentum at the high energies of Bhabha events. The factor of 0.3 in E^{WTOT} comes from an optimisation of the cut in the energy–momentum plane. An event is identified as a Bhabha if it passes both of the following cuts:

$$E^{ECAL} > 0.8\, E_{CM}$$

$$E^{WTOT} > E_{CM}$$

In the endcap, where the energy resolution is degraded due to additional material in front of the calorimeter, an extra cut is made on the total energy in an event, E^{TOT} and an event is rejected as a Bhabha if:

$$\sum_{i=1}^{N_{clus}} E_i^{Ecal} + \sum_{j=1}^{N_{trck}} p_j > E_{CM}$$

Figures 4.4 (a) and (b) show distributions of E^{WTOT}/E_{CM} versus E^{ECAL}/E_{CM} for $e^+e^- \rightarrow \tau^+\tau^-$ MC and data events, respectively, in the barrel region after all other cuts. For the $e^+e^- \rightarrow \tau^+\tau^-$ MC the scaled energy totals are both below 1., this is because the neutrinos from the τ decays carry some energy out of the event. Bhabha events are visible in the data plot clustered in the top right hand corner. The dotted lines on the plot indicate the cuts used and these are clearly effective at removing Bhabha events. Figures 4.4 (c) and (d) show the corresponding plots for the endcap region.

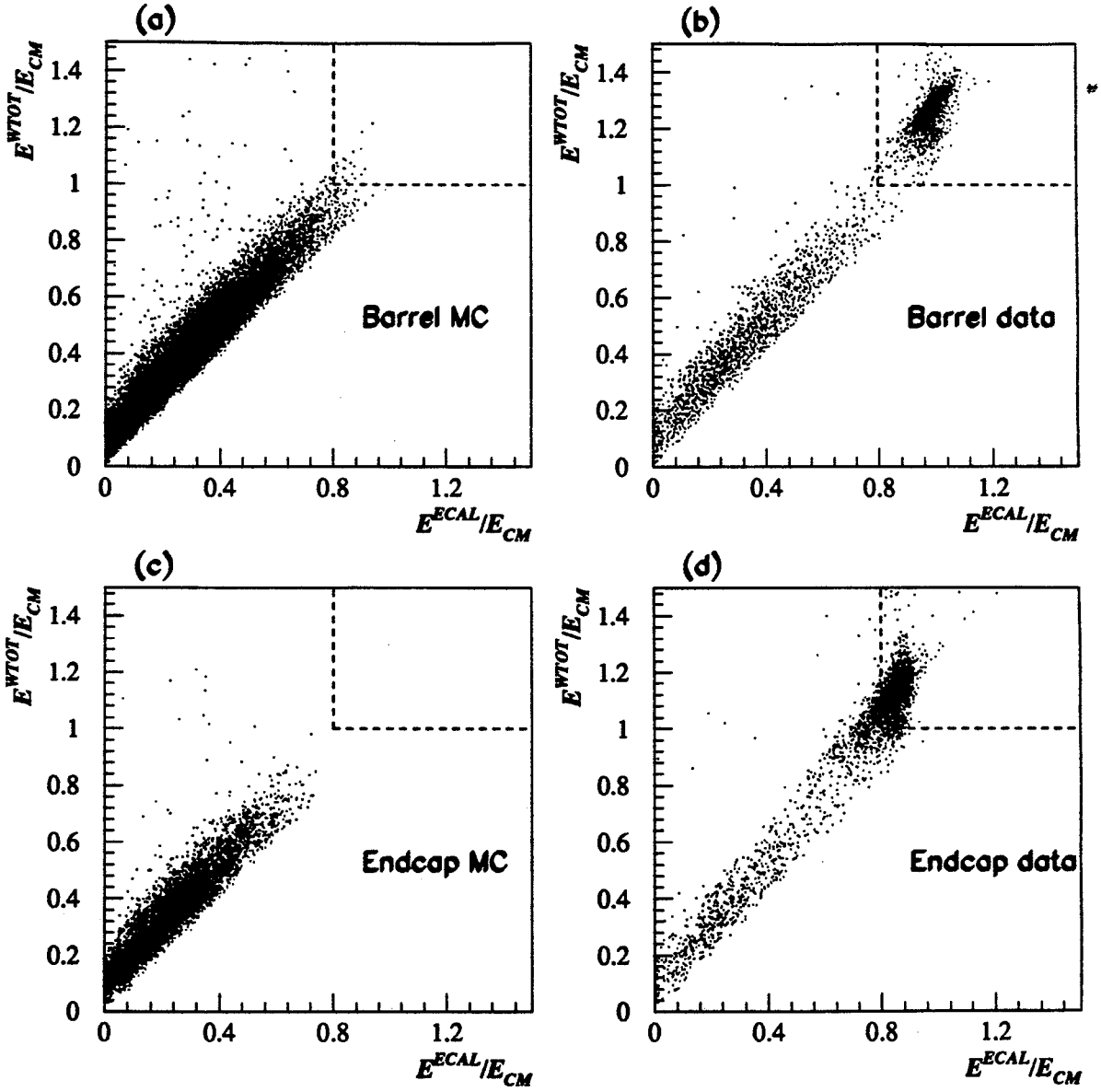

Figure 4.4: $e^+e^- \rightarrow e^+e^-$ event rejection:
E^{WTOT}/E_{CM} versus E^{ECAL}/E_{CM} after all cuts but the Bhabha rejection for:
(a) $e^+e^- \rightarrow \tau^+\tau^-$ MC events in the barrel of the detector.
(b) data events in the barrel of the detector.
(c) $e^+e^- \rightarrow \tau^+\tau^-$ MC events in the endcap.
(d) data events in the endcap.

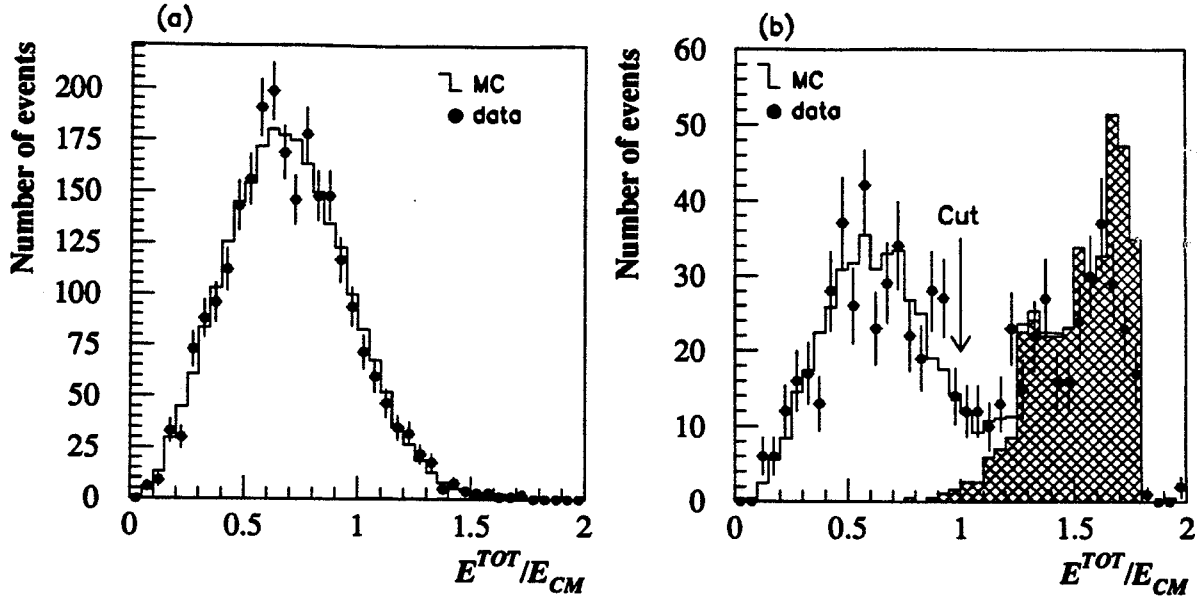

Figure 4.5: E^{TOT}/E_{CM} distributions for $e^+e^- \to \tau^+\tau^-$ MC (open histogram), $e^+e^- \to e^+e^-$ MC (shaded histogram) and data (points) events after all other cuts in (a) the barrel and (b) the endcap regions.

The raw ECAL cluster energy, uncorrected for material in front of the calorimeter, has been used in these plots. The distributions are shifted to lower energies in the endcap plots because there is more material in front of the lead glass in the endcap than in the barrel. The energy resolution is also degraded in the endcap due to the material. This makes the distinction between τ events and Bhabha events less clear, hence an additional cut on E^{TOT} is used. Using the corrected ECAL cluster energy[2] would increase the endcap energies and remove more Bhabhas with the cut shown in figure 4.4. However, the resolution is not improved and the second cut on E^{TOT} is still necessary so for simplicity the cuts on E^{ECAL} and E^{WTOT} are kept the same as in the barrel.

Figures 4.5 (a) and (b) show the E^{TOT}/E_{CM} distributions in the barrel and endcap, respectively, for $e^+e^- \to \tau^+\tau^-$ MC, $e^+e^- \to e^+e^-$ MC and data events. In the barrel the agreement between the data and MC is good and the small remaining background from Bhabha events (shaded) cannot be seen on the plot.

[2]The procedure for correcting ECAL cluster energies is described in appendix A.2.

In the endcap the data distribution has a large excess over that expected from the $e^+e^- \rightarrow \tau^+\tau^-$ MC in the region above the cut value of $E^{TOT} = E_{CM}$ due to $e^+e^- \rightarrow e^+e^-$ events not rejected by the previous cuts.

- **$e^+e^- \rightarrow \mu^+\mu^-$ rejection:** Muon pair events are identified by the presence of two high momentum tracks with associated muon signals in the hadron calorimeter (HCAL) and/or the muon chambers. An event is rejected if it has two or more muon candidates where a muon candidate is defined, as in reference [82], as a track that has more than 6 GeV momentum and has one of the following properties:

  - $\geq$2 associated signals in the 4 layers of muon chambers.
  - $\geq$4 associated signals in the HCAL, at least one of which must be in the last 3 layers of the calorimeter.
  - track momentum greater than 15 GeV but with associated ECAL energy less than 3 GeV.

  In addition it is required that the sum of the charged track energy and the energy of the largest ECAL cluster in the event is greater than 60% of E_{CM} for an event to be rejected.

- **Cosmic ray rejection:** Cuts on the vertex position of tracks and time of flight information are used to reject cosmic ray events. An event is rejected if the absolute value of the average z_0 of all tracks in the event, $\mid \overline{z_0} \mid$, is greater than 20 cm or if there is not at least one track with a $\mid d_0 \mid$ of less than 0.5 cm. Cuts on the time of flight (TOF) information are made for particles in the range $\mid cos\theta \mid \leq 0.8$. For an event to be kept it must have at least one TOF signal within 10 ns of the expected time. In addition, if all pairs of TOF signals more than 165° apart in ϕ are more than 10 ns apart in time, the event is identified as a cosmic ray and is rejected. These cuts also reject beam related background events.

  Figures 4.6 (a) and (b) show the $\mid \overline{z_0} \mid$ versus $\mid d_0 \mid_{min}$ distributions for $e^+e^- \rightarrow \tau^+\tau^-$ MC and data events after all other cuts. The good events are clustered close to the origin. A few events have large values of $\mid \overline{z_0} \mid$ and $\mid d_0 \mid_{min}$ in the data and

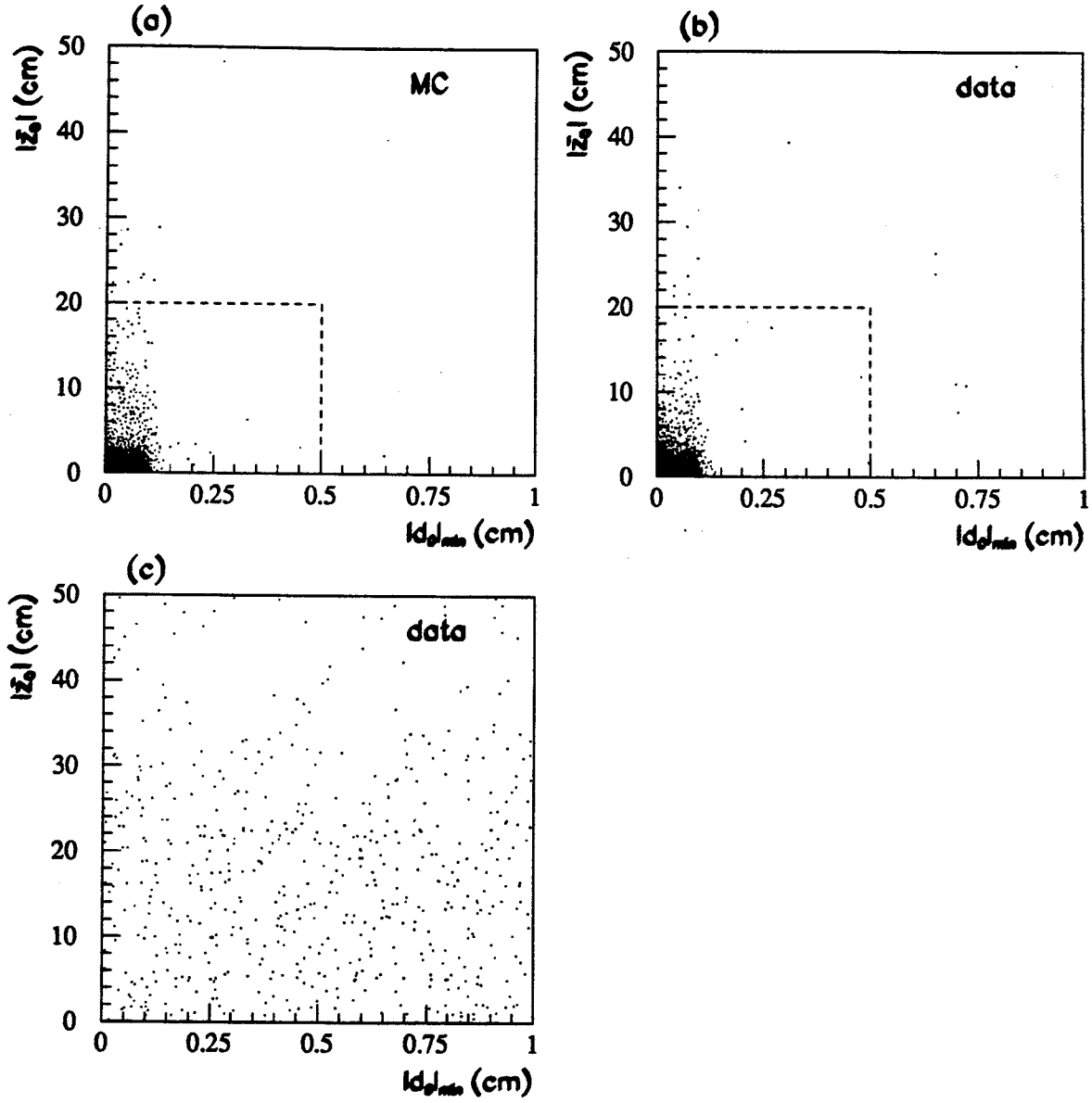

Figure 4.6: Cosmic ray rejection cuts.
$|\overline{z_0}|$ versus the minimum d_0 of tracks in the event, $|d_0|_{min}$, for
(a) $e^+e^- \rightarrow \tau^+\tau^-$ MC events after all other cuts.
(b) data events after all other cuts.
(c) data events in the region $|cos\theta| \leq 0.8$ which failed the time of flight cuts.

16 events are rejected by the cut. Figure 4.6 (c) shows the same distribution for data events in the range $|\ cos\theta\ | \leq 0.8$ which failed the time of flight cuts. There is no clustering of events around the origin in this plot which indicates that good events are not being discarded by the TOF cuts.

- **Two photon event rejection:** The main backgrounds from two photon processes come from $e^+e^- \rightarrow e^+e^-e^+e^-$ and $e^+e^- \rightarrow e^+e^-\mu^+\mu^-$ events. These events are characterised by having a low visible energy and low transverse momentum. To reject these events a cut is made on the visible energy in an event, E_{vis}, and on the transverse momentum and energy of the event. E_{vis} is defined to be the sum of the energies from the two jets where the energy of a jet is taken to be the maximum of the the track or ECAL cluster energy in that jet. An event is rejected if:

$$\begin{aligned} & E_{vis} < 0.03\ E_{CM} \\ \text{or :} \quad & E_{vis} < 0.2\ E_{CM} \\ \text{and} \quad & p_t < 2\ \text{GeV} \\ \text{and} \quad & E_t < 2\ \text{GeV} \end{aligned}$$

where p_t and E_t are the transverse momentum and energy for the tracks and the ECAL clusters in the event, respectively.

Figure 4.7 (a) shows the E_{vis} spectrum for data and MC events after all but the two photon rejection cuts. There is a large excess in the data at low energy due to two photon events. The cut on E_{vis} alone removes about 50% of the two photon events still remaining after all other cuts[3]. Figures 4.7 (b) and (c) show distributions of E_t versus p_t for both data and $e^+e^- \rightarrow \tau^+\tau^-$ MC events with $E_{vis} < 0.2\ E_{CM}$. The dashed lines indicate the cuts. The clustering in the bottom left hand corner of the data plot is due to two photon events and these are removed by the cut at 2 GeV whilst less than 1% of τ pair events are lost.

[3]a higher cut on E_{vis} was not made to avoid being inefficient for τ pair events.

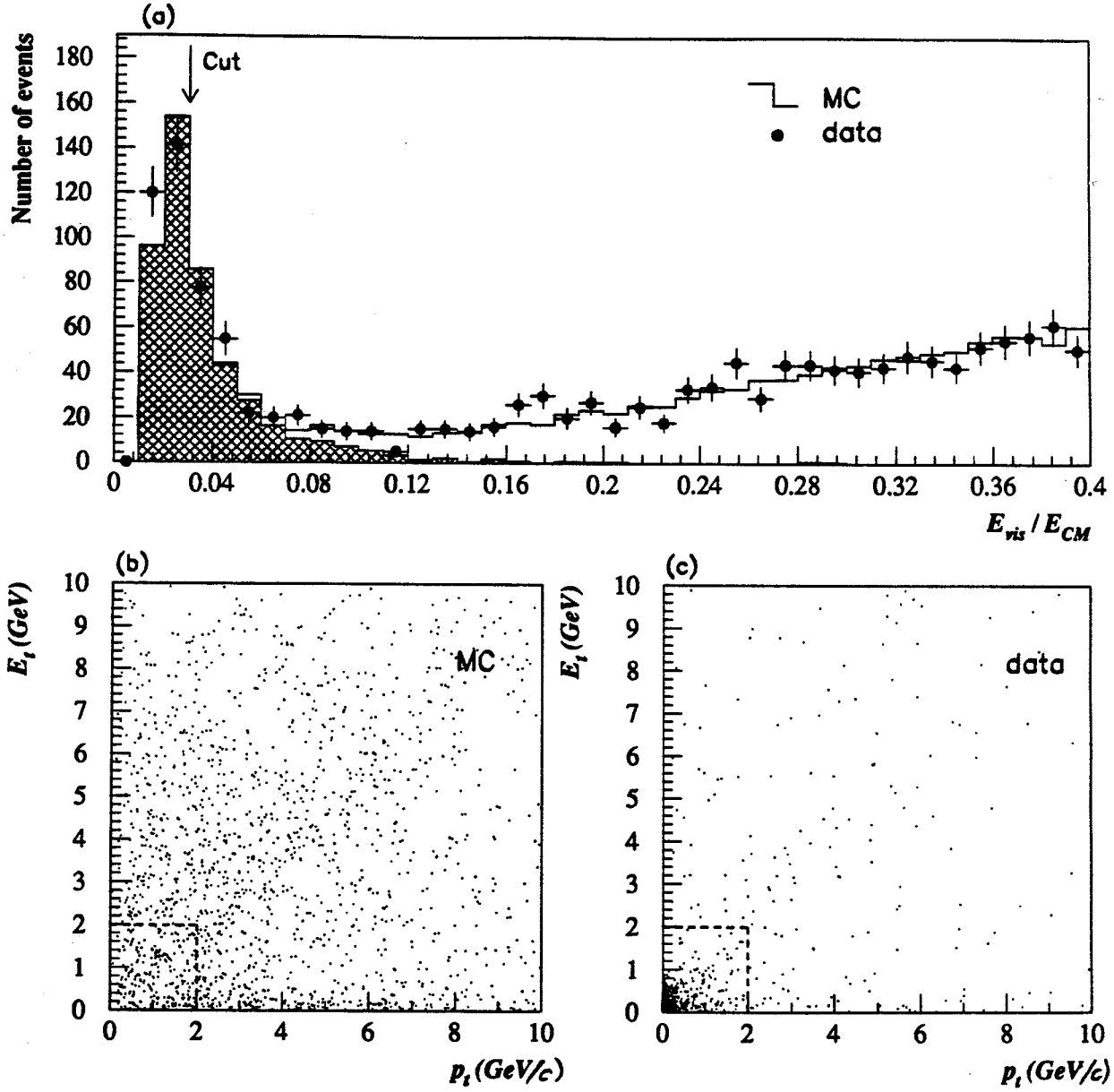

Figure 4.7: Two photon event rejection cuts.
(a) E_{vis}/E_{CM} distribution for MC (histogram) and data (points) events after all other cuts. The open histogram contains both $e^+e^- \to \tau^+\tau^-$ and two photon MC events whilst the shaded histogram contains the two photon MC events only.
(b) E_t versus p_t distribution for $e^+e^- \to \tau^+\tau^-$ MC events with $E_{vis} < 0.2E_{CM}$ after all other cuts.
(c) E_t versus p_t distribution for data events with $E_{vis} < 0.2E_{CM}$ after all other cuts.

- **Acceptance cut on $|\ cos\theta^{ave}\ |$:** To stay within the good acceptance of the calorimeter it is required that:

$$\text{Barrel}: \quad |\ cos\theta^{ave}\ | \leq 0.68$$

$$\text{Endcap}: \quad 0.82 \leq |\ cos\theta^{ave}\ | \leq 0.9$$

where $cos\theta^{ave}$ is the average $cos\theta$ of the two jets in the event:

$$cos\theta^{ave} = \frac{1}{2}\left(cos\theta(1) + cos\theta(2)\right)$$

Figure 4.8 (a) shows the $|\ cos\theta^{ave}\ |$ distribution for data and MC events after all other cuts. The open histogram includes events from all MC events and the shaded histogram contains background events only. The cut at $|\ cos\theta^{ave}\ | \leq 0.9$ is made since beyond that point the selection efficiency drops and backgrounds increase sharply. The main background at high $|\ cos\theta^{ave}\ |$ is from Bhabha events with some muon pairs and multihadrons also contributing. Figure 4.8 (b) shows the total scaled energy in ECAL clusters in the event versus $|\ cos\theta^{ave}\ |$ for selected $e^+e^- \rightarrow e^+e^-$ events. This plot shows a clear deterioration in the resolution of the calorimeter in the range where the EB and EE overlap which is due to the large amount of material in front of the calorimeter in this region. Due to this reduced resolution, events in the region $0.68 < |\ cos\theta^{ave}\ | < 0.82$ are not used.

- **Detector status cuts:** During the running of the reconstruction code, ROPE, bits are set in the header of an event to indicate the status of each subdetector. Two bits are allocated to each subdetector allowing for status values between 0 and 3, where 0 means that the status is unknown and 3 indicates that the data is good. A trigger status word is filled in a similar way, again with two bits per subdetector. In order to be considered, an event must have a status of 3 for the subdetectors used in the analysis, i.e. the tracking chambers, electromagnetic calorimeter, hadron calorimeter and presampler barrel. The trigger status must be good for the track trigger and the electromagnetic calorimeter triggers.

Applying the detector status cuts to the low multiplicity data sample leaves 131 773 events. From these 3873 events are selected as τ pairs by the cuts listed above. The fraction of events rejected at each stage is shown in table 4.1.

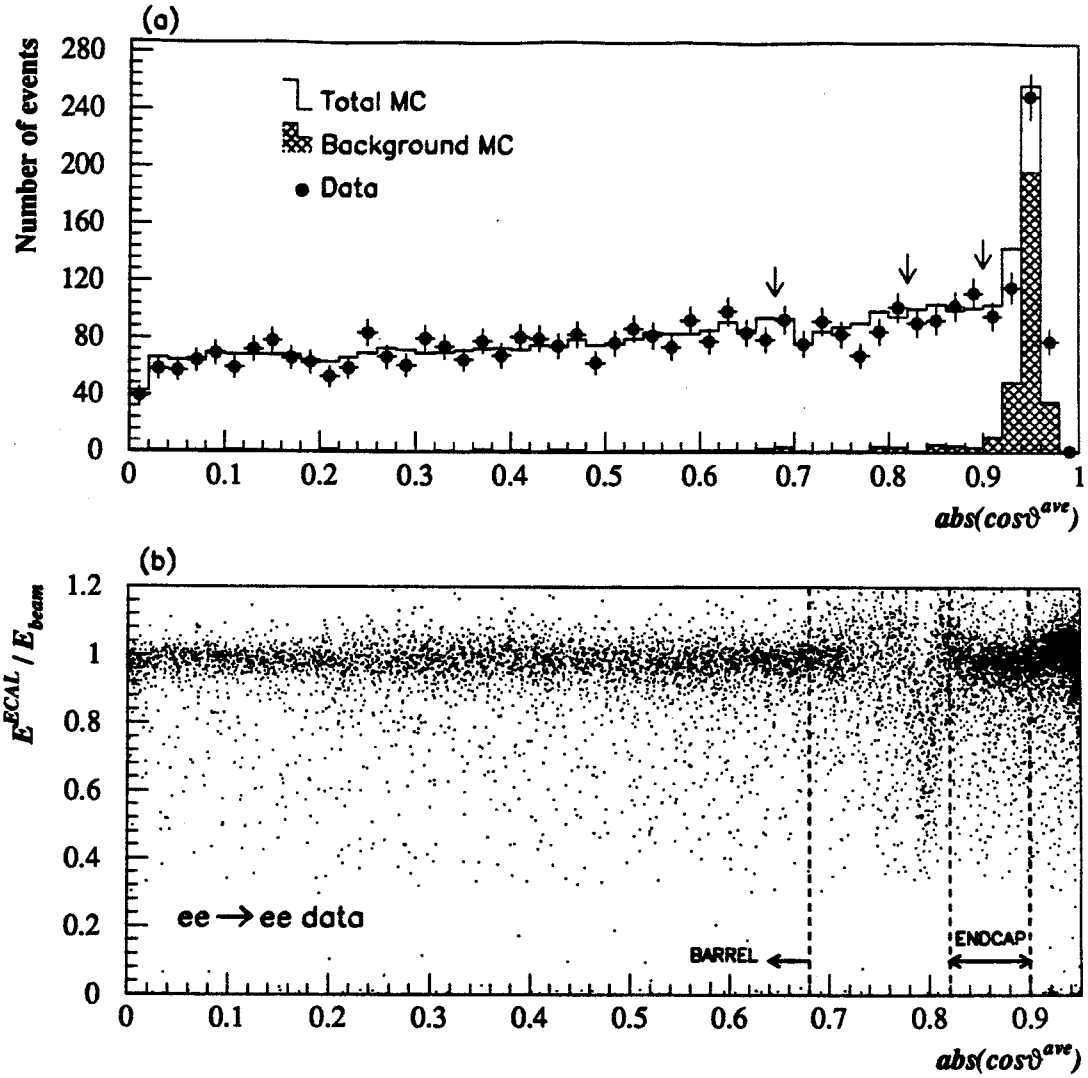

Figure 4.8: Acceptance cuts.
(a) | $cos\theta^{ave}$ | distribution for data, $e^+e^- \rightarrow \tau^+\tau^-$ MC and background MC events after all other cuts.
(b) ECAL energy (scaled to the beam energy) versus | $cos\theta^{ave}$ | for selected $e^+e^- \rightarrow e^+e^-$ events.

4.2.3 Background

The background contaminations in the τ pair sample due to the processes referred to in section 4.2.2 are estimated from MC studies using the generators listed in that section. The estimated background fractions are shown in table 4.2. Systematic checks on these numbers are carried out by comparing the distributions in the data and the MC around the region of the cuts.

Table 4.1: Fraction of events removed by successive cuts on the low multiplicity data sample.

Cut	Percentage failing cut
Track multiplicity, N_{trck}	53.7%
Cluster multiplicity, N_{ecal}	0.9%
Cone analysis	25.6%
Acollinearity angle	40.4%
Bhabha rejection	34.5%
Bhabha rejection, endcap	21.9%
Muon rejection	39.8%
Vertex constraint, $\mid \overline{z_0} \mid$	6.6%
Vertex constraint, $\mid d_0 \mid_{min}$	4.1%
Cosmic veto	3.5%
Two photon rejection	20.6%
$\mid cos\theta^{ave} \mid$	30.3%

Table 4.2: Estimated background fractions remaining in the $e^+e^- \rightarrow \tau^+\tau^-$ data sample

Background	Contamination
$e^+e^- \rightarrow e^+e^-$	$0.4 \pm 0.3\%$
$e^+e^- \rightarrow \mu^+\mu^-$	$0.6 \pm 0.3\%$
$e^+e^- \rightarrow q\bar{q}$	$0.4 \pm 0.3\%$
$e^+e^- \rightarrow e^+e^-X$	$0.2 \pm 0.2\%$
Total	$1.6 \pm 0.5\%$

Multihadron events are rejected by the cuts on the number of good tracks and ECAL clusters in an event. The estimated background fractions found using JETSET and HERWIG, $0.45 \pm 0.09\%$ and $0.42 \pm 0.12\%$ respectively, agree well. By varying the cuts around their nominal values, a systematic error of 0.2% is estimated from the excess in the data in the bins just above the cuts in figures 4.3 (a) and (b).

The systematic error on the $e^+e^- \rightarrow \mu^+\mu^-$ background in the τ pair sample is estimated by searching for μ pair events in the τ pair sample. This is done by looking at distributions containing an enhanced μ pair contribution. For example, by requiring one cone in the event to have an associated electromagnetic energy of less than 10% E_{beam} but a total energy (track momentum plus ECAL cluster energy) of greater than 60% E_{beam} such an enhanced sample can be selected. Examining events in this sample with a total energy of close to E_{CM} an excess of 8 events is seen in the data over that predicted by the MC, leading to a systematic error of 0.3%.

Bhabha events are rejected by the cuts on the energy sums of the event. By examining the number of events in the data and that predicted by the MC just above and below the cuts a systematic error of 0.3% is assigned. The systematic error on the two photon background is taken to be 100%. The contamination from cosmic ray and beam related background events is estimated by extrapolating the number of events rejected by the vertex cuts to the region under the cuts. The fraction is found to be less than 0.05% and is neglected.

4.2.4 Efficiency and Bias

Trigger and filter efficiency

The redundancy of the trigger signals within OPAL can be used to calculate the trigger efficiency from the data. For example, by selecting a control sample of events which were triggered by electromagnetic energy based triggers the efficiency for track based triggers can be found. The efficiencies for the main triggers which fire on τ pair events are given in table 4.3. Combining these independent triggers gives a total trigger efficiency of 99.9% for selected $e^+e^- \rightarrow \tau^+\tau^-$ events. This is a conservative measure of the efficiency since only triggers from single subdetectors have been considered and the triggers from coincidences between different subdetectors will increase the efficiency further. A similar study of the filter efficiency finds it to be 100% efficient for $e^+e^- \rightarrow \tau^+\tau^-$ events. Table 4.3 shows the efficiencies for the track and ECAL based filter bits.

Table 4.3: Trigger and filter efficiencies for $e^+e^- \rightarrow \tau^+\tau^-$ events. The trigger/filter for which the efficiency is being estimated is given in the first column and the second column indicates the trigger/filter used to select a control sample.

Trigger	Control sample	Efficiency
Track trigger	TOF and MUON	$94.0 \pm 0.4\%$
TOF trigger	TRACK and MUON	$85.3 \pm 0.4\%$
ECAL trigger	TRACK and TOF	$88.0 \pm 0.5\%$
Filter	**Control sample**	**Efficiency**
Track based	TOF and MUON	100.0%
ECAL based	TRACK and MUON	$99.6 \pm 0.1\%$

Selection efficiency

The efficiency of the τ pair event selection does not affect the measurements presented here but can be used as a cross check. The efficiency of the selection calculated from $e^+e^- \rightarrow \tau^+\tau^-$ MC events is $63.4 \pm 0.2\%$, where the acceptance is $69.9 \pm 0.2\%$. Using the luminosities taken at each energy point and theoretical values for the cross section from the Standard Model there should be 6248 ± 15 tau events produced, of these 3961 ± 16 would be selected which agrees with the 3873 ± 62 events found.

Selection bias

Although the efficiency of the τ pair selection is unimportant to this analysis, any biases towards $\tau \rightarrow e\nu_\tau\bar{\nu}_e$ decays over other τ decays due to the preselection need to be considered. From $e^+e^- \rightarrow \tau^+\tau^-$ MC events the bias towards $\tau \rightarrow e\nu_\tau\bar{\nu}_e$ decays due to the preselection is estimated to be 1.005 ± 0.005. This arises mainly because of the muon pair rejection cuts which do not remove $\tau \rightarrow e\nu_\tau\bar{\nu}_e$ decays.

4.3 Selection of $\tau \rightarrow e\nu_\tau\bar{\nu}_e$ candidates

From the above sample of 7746 τ jets, 7500 are within the acceptance cuts and from these $\tau \rightarrow e\nu_\tau\bar{\nu}_e$ candidates are selected. The selection cuts are described below but first it is useful to include some comments on the resolution observed in the MC compared

to that in the data and on hit associations made during the event reconstruction.

Resolution in the MC

GOPAL is a detector simulation program and needs to be tuned to give the same resolutions as observed in the data. However, since such a tuning is an iterative procedure the resolutions obtained from MC events do not exactly reproduce those from the data. Therefore, an additional smearing is applied to the momenta and energy used in the Monte Carlo. The smearing is derived from $e^+e^- \rightarrow \mu^+\mu^-$ and $e^+e^- \rightarrow e^+e^-$ events by comparing data and MC events. By fitting the E^{ECAL}/E_{CM} distribution for $e^+e^- \rightarrow e^+e^-$ events and the $1/p_T$ distribution for $e^+e^- \rightarrow \mu^+\mu^-$ events with gaussians and comparing the widths in the data and the MC the following additional smear factors were found to be needed to make the two agree:

$$\frac{\sigma_E}{E} = 3\%$$

$$\frac{\sigma_{p_T}}{p_T} = \begin{cases} 0.134\%\ p_T & \text{Barrel} \\ 0.553\%\ p_T & \text{Endcap} \end{cases}$$

These are added in quadrature to the original smearing of hits used in the MC. The corrected energy of ECAL clusters is used here.

Hit associations

The $\tau \rightarrow e\nu_\tau\bar{\nu}_e$ selection criteria use the cone analysis described in section 4.2.2 to define each τ decay as a jet. As has been mentioned previously, hits in the presampler, hadron calorimeter and muon chambers which lie within the solid angle of a cone are assigned to the appropriate jet. Associations are also made between hits in different detector components during the reconstruction of events by ROPE. The $\tau \rightarrow e\nu_\tau\bar{\nu}_e$ selection cuts use matches between charged tracks and ECAL clusters and between presampler and ECAL clusters. The criteria for these associations are described in appendix A.3.

$\tau \rightarrow e\nu_\tau\bar{\nu}_e$ selection cuts

A $\tau \rightarrow e\nu_\tau\bar{\nu}_e$ candidate jet must satisfy the following requirements:

- The number of good charged tracks assigned to the jet must be less than or equal to two. One extra track is permitted to avoid inefficiencies from conversions due

to radiation from the electron. If two tracks are assigned to the jet then the higher momentum one is taken to be the electron candidate.

- Electron identification: the momentum of the charged track, p_{trck}, and the energy of the electromagnetic calorimeter cluster associated to the track, E_{clus}, must be within the range:

$$0.7 < E_{clus}/p_{trck} < 2.$$

Figures 4.9 (a) and (b) show the E_{clus}/p_{trck} distribution for data and $e^+e^- \rightarrow \tau^+\tau^-$ MC, also shown (shaded) is the distribution for just the $\tau \rightarrow e\nu_\tau\bar{\nu}_e$ decays from the MC. The agreement between data and MC is good and the cuts remove non-$\tau \rightarrow e\nu_\tau\bar{\nu}_e$ decays.

- To reject $\tau \rightarrow \mu\nu_\tau\bar{\nu}_\mu$ and $\tau \rightarrow \pi(\mathrm{K})\nu_\tau$ decays a cut is made on the depth of penetration in the hadron calorimeter. No hits are allowed beyond the first layer of the calorimeter:

$$HCAL^{depth} \leq 1$$

The distribution of $HCAL^{depth}$ for data and MC is shown in figure 4.9 (c).

- Electrons are expected to have a narrower shower profile than hadrons in the electromagnetic calorimeter so an ECAL cluster produced by an electron should consist of only a few blocks. The shape of the ECAL cluster matched to the electron candidate track is required to be consistent with that of an electron by requiring that the minimum number of blocks containing at least 90% of the energy (N^{90}_{blck}) satisfies:

$$\text{Barrel}: \quad N^{90}_{blck} \leq 3$$

$$\text{Endcap}: \quad N^{90}_{blck} \leq 5$$

The cut is higher in the endcap because the non-pointing geometry means that a particle will inevitably traverse more than one block and thus electromagnetic showers in the endcap are spread over more lead glass blocks than those in the barrel. Figures 4.10 (a) and (b) show the N^{90}_{blck} distributions for data and MC in the barrel and endcap regions, respectively. The agreement between data and

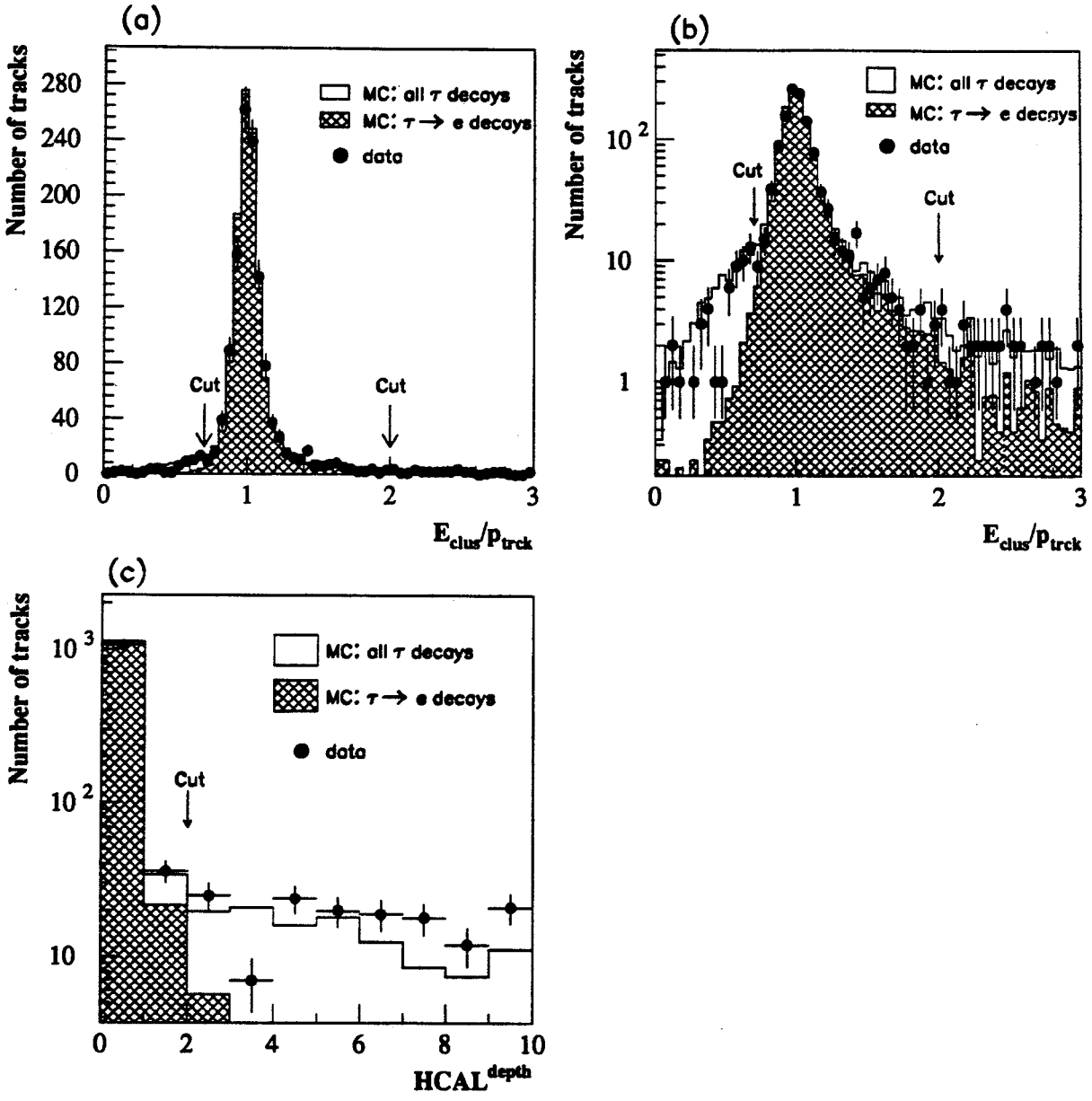

Figure 4.9: $\tau \rightarrow e\nu_\tau\bar{\nu}_e$ selection cuts.
Distributions of (a) E_{clus}/p_{trck}, (b) E_{clus}/p_{trck} with a log scale and (c) $HCAL^{depth}$. The histograms contain $e^+e^- \rightarrow \tau^+\tau^-$ MC events, all decays (open) and just $\tau \rightarrow e\nu_\tau\bar{\nu}_e$ decays (shaded), and the points are from data events. In each case the distributions are shown after all other cuts have been applied.

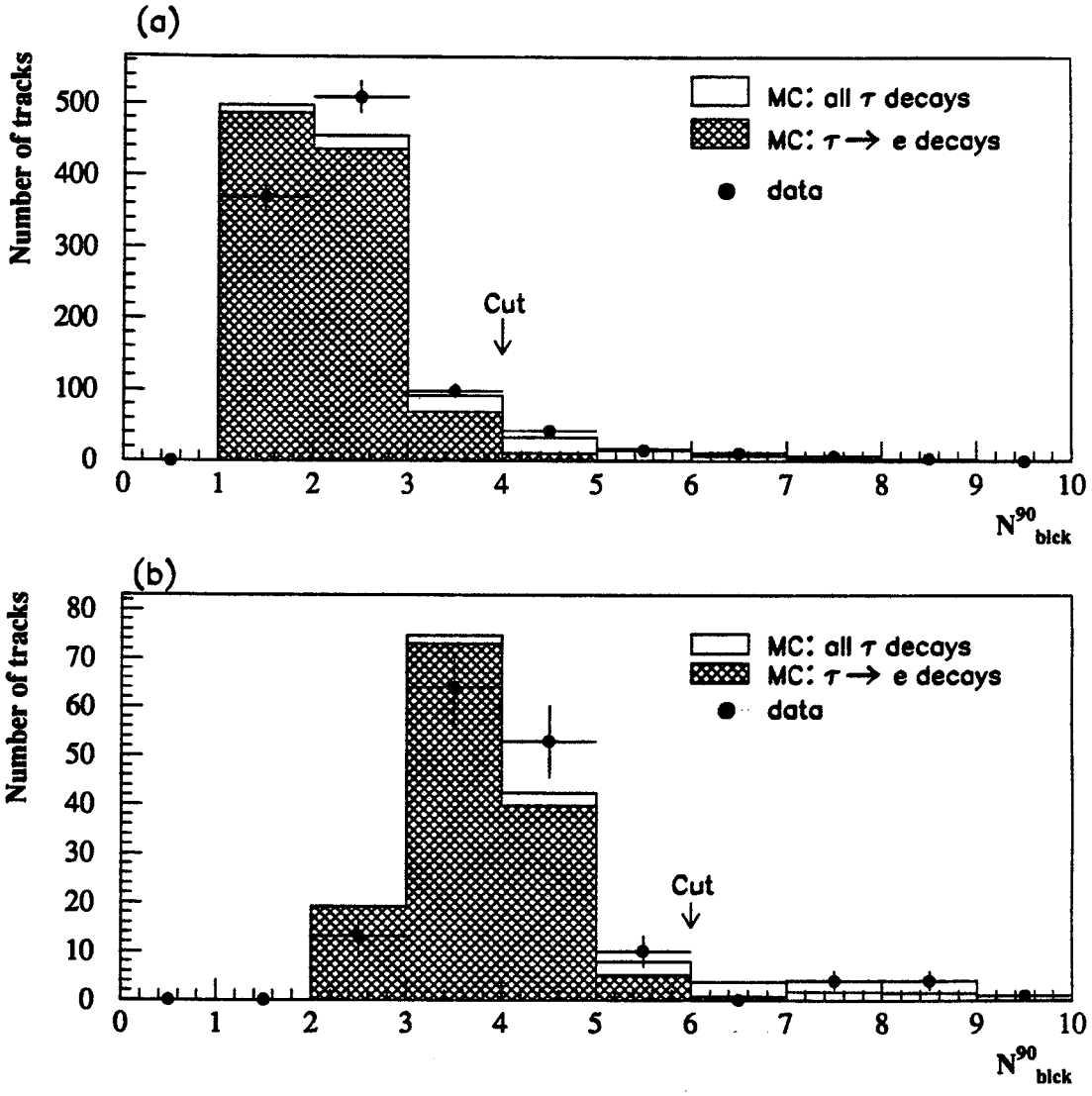

Figure 4.10: $\tau \to e\nu_\tau\bar{\nu}_e$ selection cuts.
N^{90}_{blck} distributions for $e^+e^- \to \tau^+\tau^-$ MC, all decays (open) and $\tau \to e\nu_\tau\bar{\nu}_e$ decays (shaded), and data for (a) the barrel region and (b) the endcap region.

MC is not very good at low values of N_{blck}^{90} [4], the cuts are made away from the problem areas as far as possible.

- In order to reject decays with π^0s, where $\pi^0 \rightarrow \gamma\gamma$, a cut is made on the total ECAL energy associated with the candidate cone once the energy of the cluster matched to the track has been excluded:

$$E_{else} < 0.04\ E_{beam}$$

This corresponds to a cut at about 1.8 GeV. Figure 4.11 (a) shows the E_{else}/E_{beam} distribution for data and MC.

- To remove further hadronic decays, e.g. $\tau \rightarrow \rho\nu_\tau$ with subsequent decay of the ρ, a cut is made on the difference in azimuth of the furthest presampler cluster away from the candidate track which is still within the cone:

$$\delta\phi^{max} < 5^\circ$$

To reduce the effects of noise clusters in the presampler, only presampler clusters which are associated to ECAL clusters are used. Figure 4.11 (b) shows the $\delta\phi^{max}$ distribution for data and MC in the barrel.

In the endcap region the presampler detector is less well understood and an alternative cut which uses the electromagnetic calorimeter is very effective at removing hadronic decay modes. A requirement is made that the θ direction defined by the track and by the associated ECAL cluster match well.

$$\Delta\theta^{Ecal-track} < 1^\circ$$

where θ is measured between 0° and 90°, 0° being the beam axis along $\pm z$. The cut rejects hadronic decays because of the way in which the θ value of an ECAL cluster is calculated in the endcap. The calculation assumes that the particle creating the cluster was an electron and that it started to shower at a

[4]The disagreement between data and MC for this variable was found to be due to using a gaussian function to represent the multiple scattering in the lead glass in the detector simulation program. This has since been changed to use the Moliere scattering function and there is now better agreement between data and MC.

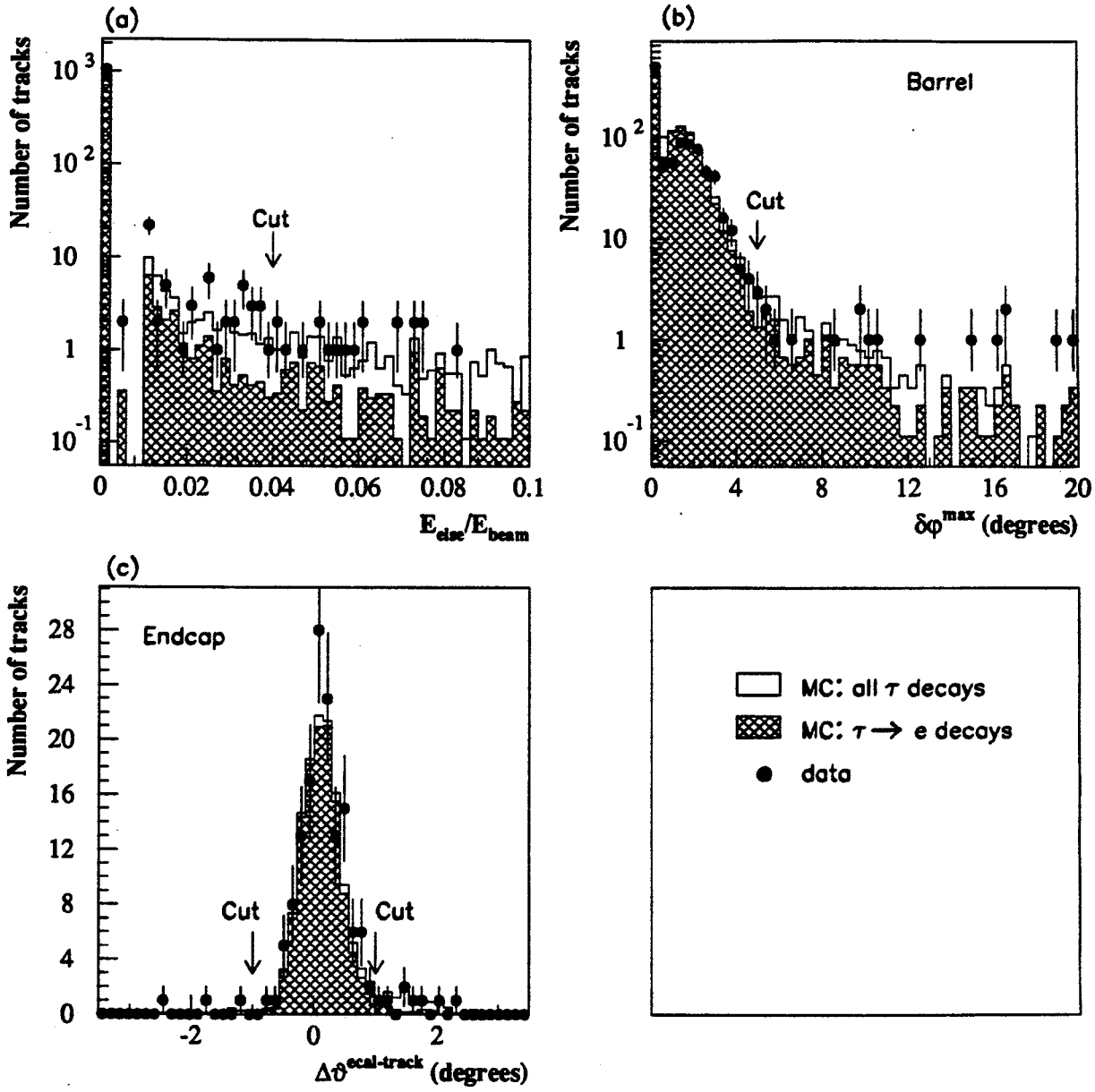

Figure 4.11: $\tau \rightarrow e\nu_\tau\bar{\nu}_e$ selection cuts.
Distributions of (a) E_{else}/E_{beam}, (b) $\delta\phi^{max}$ for barrel events and (c) $\Delta\theta^{ECAL-track}$ for endcap events. The histograms contain $e^+e^- \rightarrow \tau^+\tau^-$ MC events, all decays (open) and $\tau \rightarrow e\nu_\tau\bar{\nu}_e$ decays (shaded), and the points are the data.

certain depth in the block. Hadrons on average start to shower further into the material than electrons so the θ value is overestimated for the cluster and the $\Delta\theta^{Ecal-track}$ distribution is shifted to positive values for hadrons but centred at zero for electrons. Figure 4.11 (c) shows the $\Delta\theta^{Ecal-track}$ distribution for MC and data events in the endcap after all other cuts. There are background events at positive values of $\Delta\theta^{Ecal-track}$, as expected.

- A small residual background from $e^+e^- \rightarrow e^+e^-$ events remains in the τ pair sample after the cuts in section 4.2.2 have been applied. These are potentially a large source of background for the $\tau \rightarrow e\nu_\tau\bar{\nu}_e$ sample and to remove them a cut is made on the acoplanarity of the event. A candidate is rejected if the opposite cone contains a single track with momentum greater than $0.75E_{beam}$ and the acoplanarity between the candidate track and the opposite track, $\theta_{\rm acop}$, is less than 0.1°. Figures 4.12 (a) and (b) show acoplanarity versus the scaled momentum of the opposite track, p_{opp}/E_{beam}, distributions for $e^+e^- \rightarrow \tau^+\tau^-$ and $e^+e^- \rightarrow e^+e^-$ MC events. It can be seen that the above cut should remove most $e^+e^- \rightarrow e^+e^-$ events. Figure 4.12 (c) shows the acoplanarity distributions for candidates with one opposite track with momentum greater than $0.75E_{beam}$ for data and $e^+e^- \rightarrow \tau^+\tau^-$ MC after all other electron identification cuts. There is an excess in the first bin of the data plot due to some remaining Bhabha background, these events are removed by the cut.

- Low x: The above cuts are applied to all events with $x_e \geq 0.05$, where $x_e = E_{cone}/E_{beam}$ and E_{cone} is the sum of the energies in all ECAL clusters associated to the jet. In the region $x_e < 0.05$ electrons can be easily identified using the dE/dx information from the jet chamber and E_{clus}/p_{trck}. In order to ensure a good dE/dx measurement only tracks with more than 40 hits contributing to the measurement are used. Figure 4.13 (a) shows a surface plot of E_{clus}/p_{trck} versus dE/dx for $e^+e^- \rightarrow \tau^+\tau^-$ MC events with $x_e < 0.05$. The electrons can be seen as the peak at $E_{clus}/p_{trck} = 1.$ and $dE/dx = 10.0$ keV/cm. Figure 4.13 (b) is a scatter plot of the same distribution and again shows clearly the separation of the electrons from the other τ decays. Figure 4.13 (c) shows the distribution for the $\tau \rightarrow e\nu_\tau\bar{\nu}_e$ decays only. The equivalent plot for the data is shown in fig-

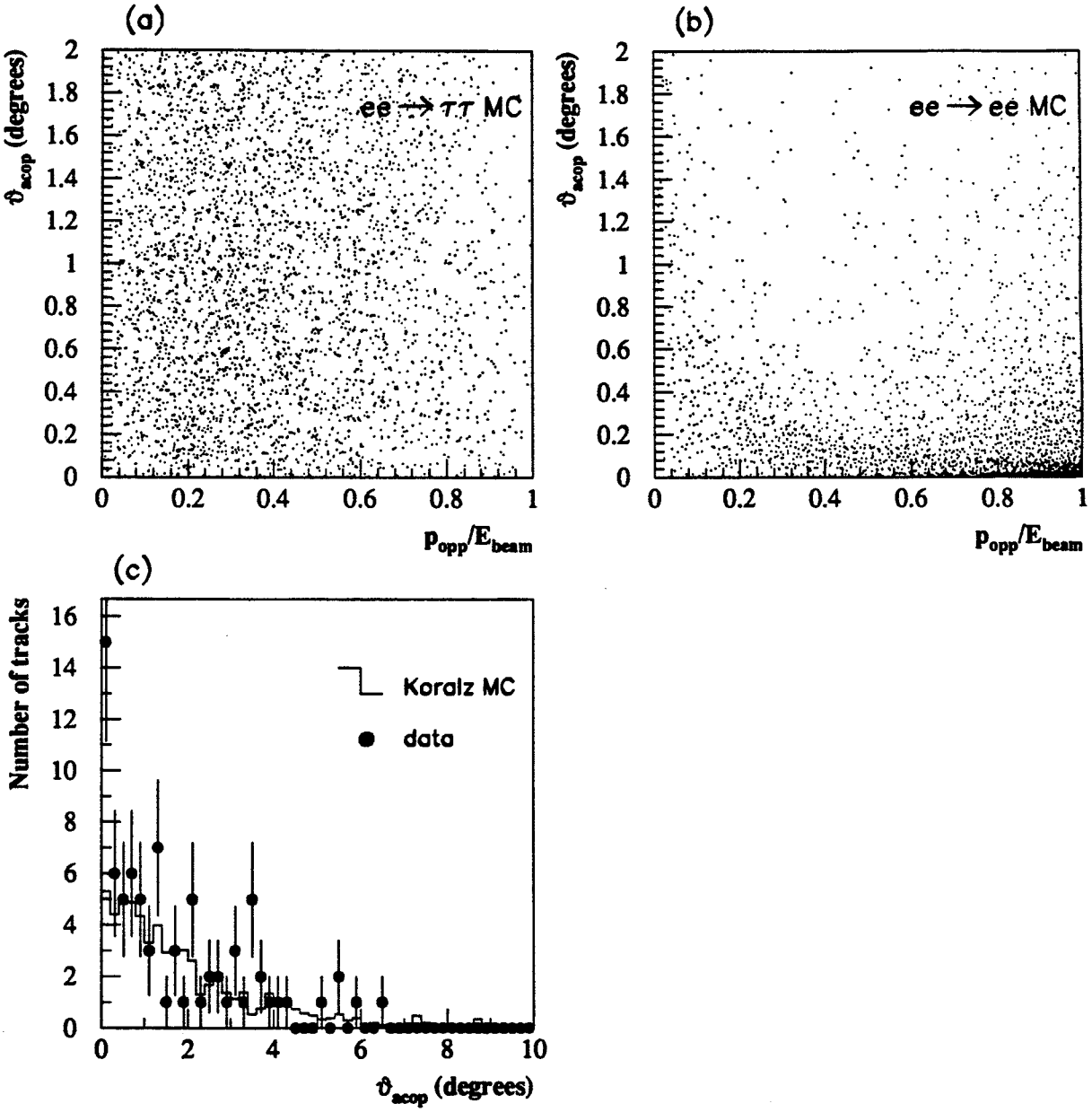

Figure 4.12: $\tau \to e\nu_\tau\bar{\nu}_e$ selection cuts: extra Bhabha rejection.
Acoplanarity (θ_{acop}) versus p_{opp}/E_{beam} for (a) $e^+e^- \to \tau^+\tau^-$ and (b) $e^+e^- \to e^+e^-$ MC events.
(c) θ_{acop} distribution for $\tau \to e\nu_\tau\bar{\nu}_e$ candidates from $e^+e^- \to \tau^+\tau^-$ MC and data which have 1 opposite track with momentum greater than $0.75E_{beam}$.

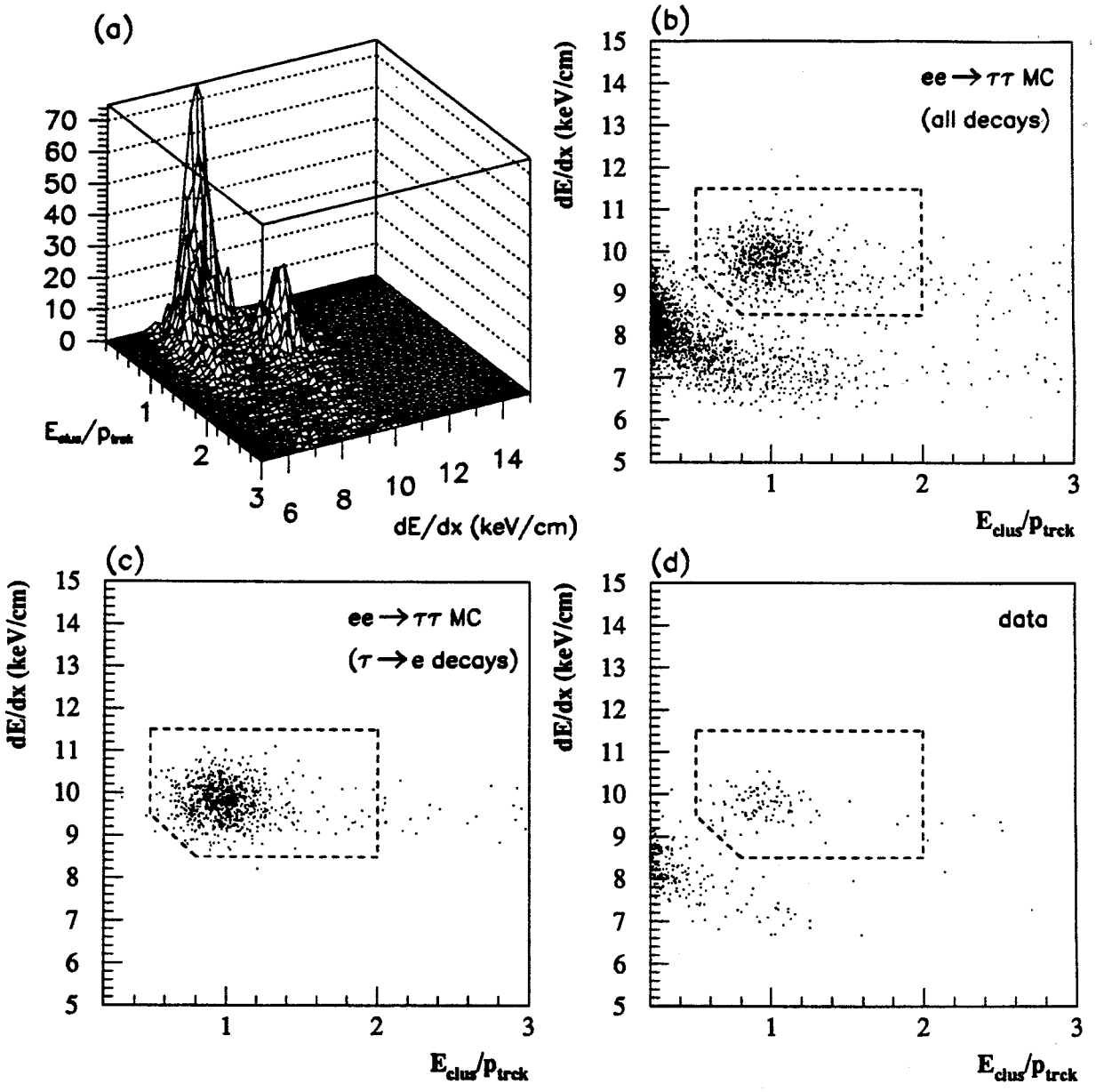

Figure 4.13: $\tau \to e\nu_\tau\bar{\nu}_e$ selection cuts, $x_e < 0.05$.
(a) Surface plot of E_{clus}/p_{trck} versus dE/dx for $e^+e^- \to \tau^+\tau^-$ MC events.
(b) Scatter plot of E_{clus}/p_{trck} versus dE/dx for $e^+e^- \to \tau^+\tau^-$ MC events.
(c) Scatter plot of E_{clus}/p_{trck} versus dE/dx for $\tau \to e\nu_\tau\bar{\nu}_e$ decays in $e^+e^- \to \tau^+\tau^-$ MC events.
(d) Scatter plot of E_{clus}/p_{trck} versus dE/dx for data.

ure 4.13 (d), the same separation of the electrons from the other decay modes is seen. A two–dimensional cut, shown by the dotted line in the plots, is made to isolate the electron decays.

After all cuts have been applied to the 7500 cones within the acceptance there are 1203 $\tau \rightarrow e\nu_\tau\bar{\nu}_e$ candidates remaining of which 1055 are in the barrel and 148 in the endcap.

4.3.1 Backgrounds

The background contamination of the $\tau \rightarrow e\nu_\tau\bar{\nu}_e$ sample is estimated using Monte Carlo events. The background fractions from other decay modes of the τ and from non–τ sources are listed in table 4.4. The total background fraction is $6.1 \pm 1.4\%$ mostly coming from hadronic decays of the τ.

Table 4.4: Background fractions from the various processes contributing to the $\tau \rightarrow e\nu_\tau\bar{\nu}_e$ background.

	Background fraction
$\tau \rightarrow \pi(\mathrm{K})\nu_\tau$	$2.3 \pm 0.1(stat) \pm 0.4(syst)\%$
$\tau \rightarrow \rho\nu_\tau$	$2.1 \pm 0.1(stat) \pm 0.7(syst)\%$
$\tau \rightarrow$ other	$0.7 \pm 0.1(stat) \pm 0.2(syst)\%$
$e^+e^- \rightarrow e^+e^-$	$0.4 \pm 0.4\%$
$e^+e^- \rightarrow e^+e^-X$	$0.6 \pm 0.6\%$
Total	$6.1 \pm 1.4\%$

Systematic errors are estimated by checking the agreement between MC and data in relevant distributions. By reversing the $HCAL^{depth}$ cut a sample of background hadronic decays can be selected. The number of hadronic τ decays selected from the data and the MC disagree by 20% and this is taken as a systematic error on this background. A second check is performed by reversing the E_{else} cut, thus accepting τ decays to ρs and to multipions. A disagreement of 30% is seen between the number of decays in the data and the MC and this is taken as a systematic error on these backgrounds.

The background contribution from the $x_e < 0.05$ region is only ~2% of the total background and a conservative 100% systematic error is assumed. The systematic errors in table 4.4 are derived from these numbers, the correlations between the systematic errors on the different decay modes are taken into account in the calculation of the error on the total background fraction.

4.3.2 Efficiency

The efficiency of the $\tau \to e\nu_\tau\bar{\nu}_e$ selection cuts is estimated from $e^+e^- \to \tau^+\tau^-$ MC events to be $88.6 \pm 0.3(stat)\%$ for $\tau \to e\nu_\tau\bar{\nu}_e$ decays in the acceptance. The plots shown to illustrate the selection cuts in section 4.3 show generally good agreement between data and MC and where there are discrepancies the cuts are loose. It is, however, useful to check the efficiency found from the MC using data. This can be done by using high statistics control samples of isolated electrons. At low energies, $x_e < 0.1$, single electrons from $e^+e^- \to e^+e^-(\gamma)$ events are used and at high energy, $x_e \simeq 1.$, electrons from Bhabha events are used.

The control samples are used to obtain correction factors to the efficiency from the $e^+e^- \to \tau^+\tau^-$ MC. This is done by comparing the efficiency of the cuts for data and MC control events and taking the ratio as the correction factor. Correction factors derived in this way are given in table 4.5. Figures 4.14 and 4.15 show distributions

Table 4.5: Efficiency correction factors derived from the electron control samples.

Acceptance	Energy	ε_{MC}	ε_{data}	Correction factor
Total	$0.05 \le x_e \le 0.1$	$94.2 \pm 0.4\%$	$88.4 \pm 0.5\%$	0.938 ± 0.007
	$0.95 \le x_e \le 1.0$	$93.7 \pm 0.4\%$	$91.6 \pm 0.5\%$	0.977 ± 0.007
Barrel	$0.05 \le x_e \le 0.1$	$94.5 \pm 0.4\%$	$88.1 \pm 0.8\%$	0.933 ± 0.009
	$0.95 \le x_e \le 1.0$	$94.6 \pm 0.4\%$	$92.5 \pm 0.5\%$	0.979 ± 0.007
Endcap	$0.05 \le x_e \le 0.1$	$92.9 \pm 1.1\%$	$88.7 \pm 0.8\%$	0.955 ± 0.014
	$0.95 \le x_e \le 1.0$	$90.2 \pm 1.1\%$	$87.9 \pm 1.2\%$	0.975 ± 0.018

for the two control samples for those variables which contribute most to the correction. For the single electrons the majority of the correction comes from disagreements in

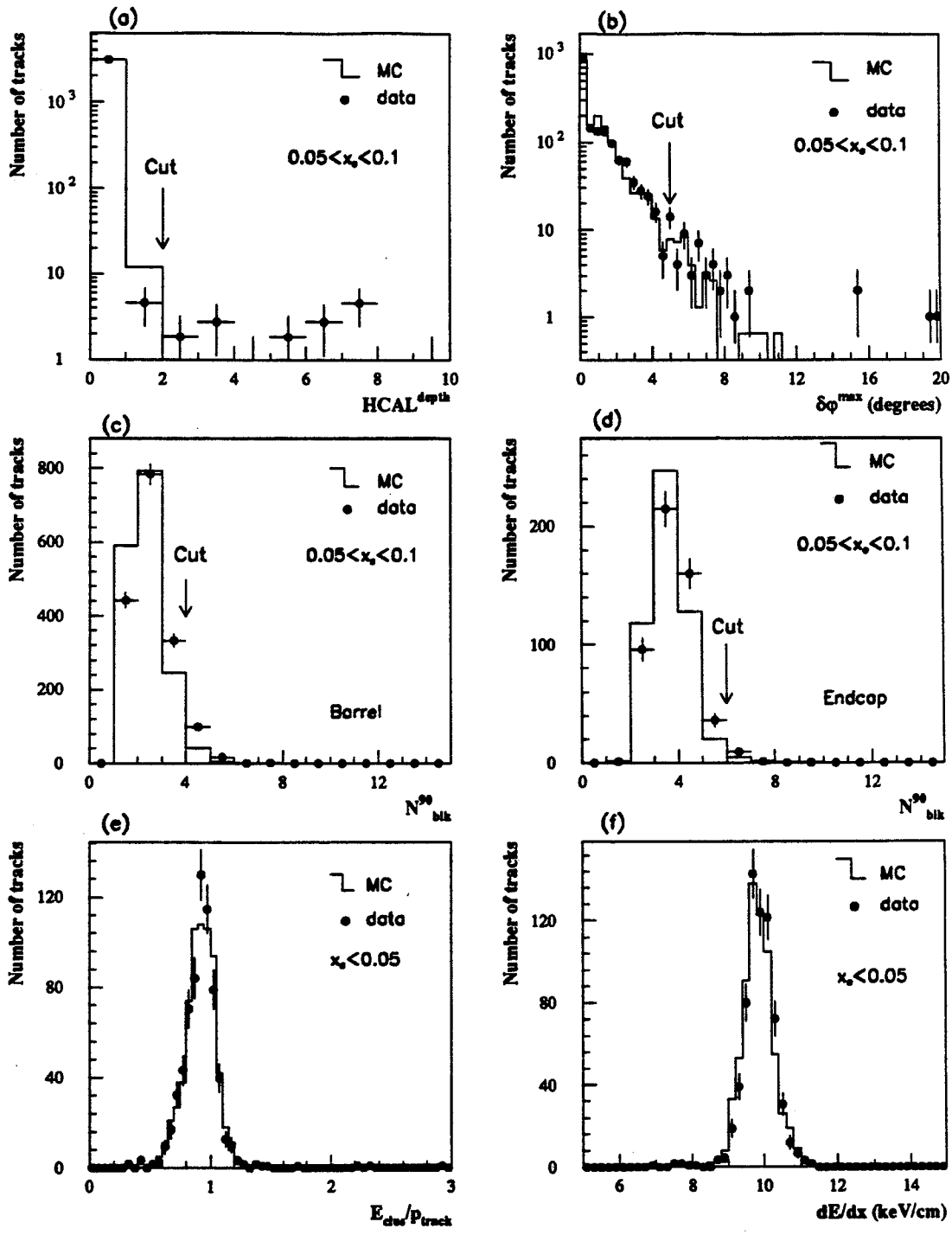

Figure 4.14: Distributions of selection variables for isolated single electrons from $e^+e^- \to e^+e^-(\gamma)$ events. The solid histogram is MC events and the points are from data. The histograms show:
(a) $HCAL^{depth}$, (b) $\delta\phi^{max}$, (c) N^{90}_{blck} for barrel events and (d) N^{90}_{blck} for endcap events, for electrons in the energy range $0.05 \leq x_e < 0.1$.
(e) E_{clus}/p_{track} and (f) dE/dx for electrons with $x_e < 0.05$

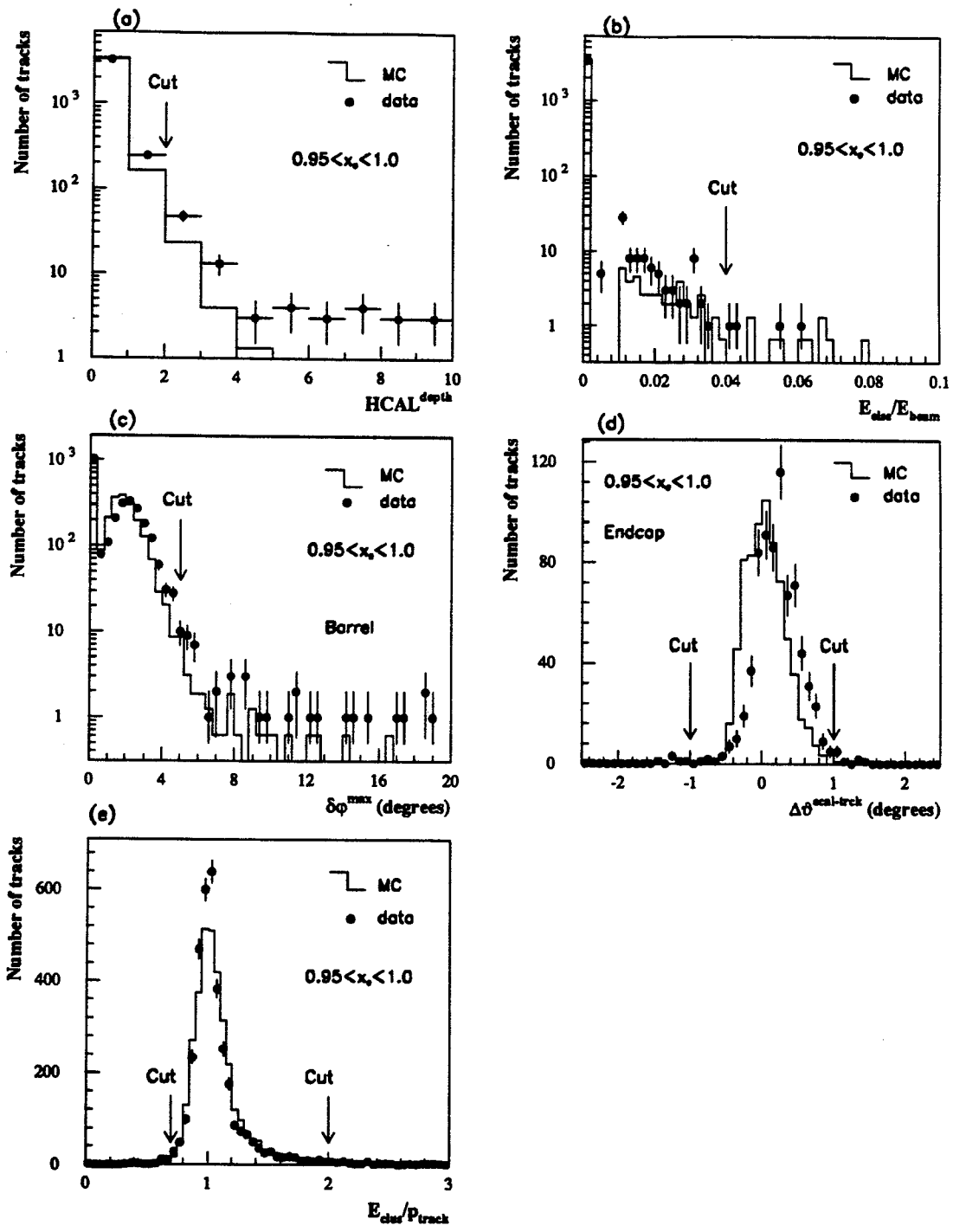

Figure 4.15: Distributions of selection variables for isolated single electrons from $e^+e^- \to e^+e^-$ events with $0.95 \leq x_e < 1.$. The solid histograms come from MC events and the points are from data. The histograms show:
(a) $HCAL^{depth}$, (b) E_{else}, (c) $\delta\phi^{max}$ for barrel events, (d) $\Delta\theta^{ECAL-track}$ for endcap events and (e) E_{clus}/p_{track}.

the $HCAL^{depth}$ and the N^{90}_{blck} distributions. For the low energy region, $x_e < 0.05$, no correction is applied. The data and MC distributions for E_{clus}/p_{trck} and dE/dx, figures 4.14 (e) and (f) respectively, agree well in this region and the calculated correction factor, 0.995 ± 0.006, is consistent with unity. For electrons from Bhabha events the correction arises mainly due to discrepancies in the $HCAL^{depth}$, $\delta\phi^{max}$ and E_{else}/E_{beam} distributions. The $\Delta\theta^{Ecal-track}$ distribution is also shown for events in the endcap. A shift is seen to higher values in the data which is due to problems with track reconstruction, these are worse for higher energy tracks so the discrepancy is not so obvious in the τ data.

The control samples give correction factors at both high and low energies. To derive an overall correction factor a straight line extrapolation is performed between the two extremes to find correction factors at intermediate energies. Each is weighted according to the observed $\tau \rightarrow e\nu_\tau\bar{\nu}_e$ energy spectrum and an average value found. The overall correction factors and the corrected efficiencies are given in table 4.6 for the total acceptance and for the barrel and endcap regions separately. The errors on the correction factors come from the statistics of the control samples and from considering the change in the correction factor when the extrapolation procedure is varied.

Table 4.6: Corrected efficiencies.

Acceptance	Raw efficiency	Correction factor	Corrected efficiency
Total	$88.6 \pm 0.3\%$	0.954 ± 0.008	$84.5 \pm 0.8\%$
Barrel	$88.9 \pm 0.3\%$	0.952 ± 0.010	$84.6 \pm 1.1\%$
Endcap	$86.4 \pm 0.9\%$	0.964 ± 0.014	$83.3 \pm 1.5\%$

A further cross check of the efficiency is made using the good electron–hadron discriminating power of dE/dx in the low momentum region to check the number of electrons rejected by the cuts. Figure 4.16 shows the dE/dx distribution for events in the range $x_e > 0.05$ and $x < 0.1$ (where $x = p_{track}/E_{beam}$) which failed the electron identification cuts. By looking at those events with $dE/dx > 9.4$ keV/cm the number of electrons failing the cuts can be estimated. This is found to be $4.2 \pm 0.6\%$ of the total number of selected electron candidates and is in good agreement with the $4.0 \pm 0.2\%$ predicted by the MC.

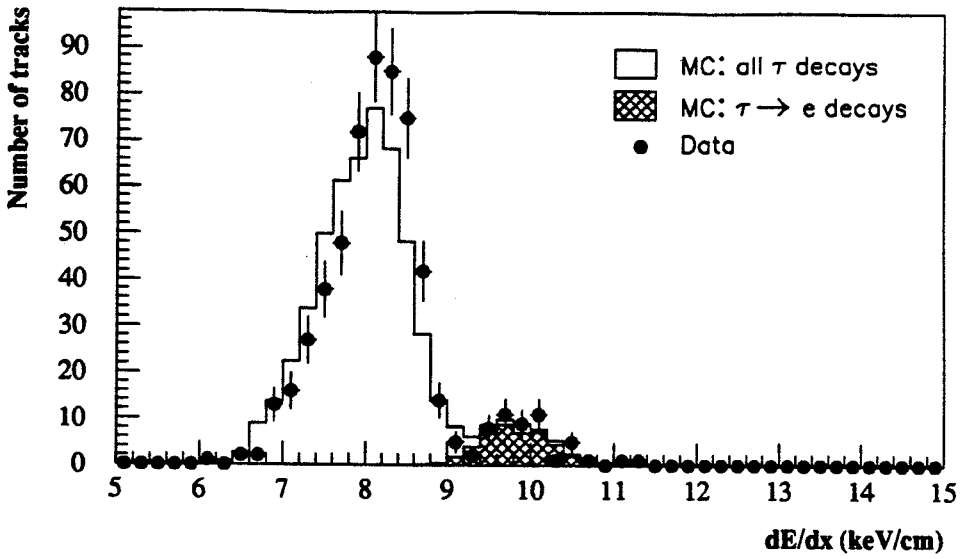

Figure 4.16: dE/dx for data and MC for events failing the electron selection and with $x_e > 0.05$ and $x < 0.1$

4.4 $\tau \rightarrow e\nu_\tau\bar{\nu}_e$ Branching Ratio

Using the selected data, the branching ratio for $\tau \rightarrow e\nu_\tau\bar{\nu}_e$ is calculated using equation 4.1. The numbers used in the calculation and the result are given in table 4.7 for the total sample and for the barrel and endcap regions separately. With the current statistics the inclusion of the data from the endcap does not influence the measurement. Although only about 10% of the statistics are in the endcap this region is a useful cross check since different cuts are used to select the data and different systematic errors are involved. As a cross check on the final result the number of events with two identified electrons is counted and found to be 88. This agrees with the 91 ± 6 events predicted from the measured branching ratio, efficiency and backgrounds.

The measured value for the BR($\tau \rightarrow e\nu_\tau\bar{\nu}_e$) of $18.0 \pm 0.5 \pm 0.3\%$ agrees very well with the 1990 Particle Data Group world average value of $17.9 \pm 0.4\%$ [6] and with recent results from other experiments, some of which are shown in table 4.8. An updated value of the world average including all these measurements is BR($\tau \rightarrow e\nu_\tau\bar{\nu}_e$) $= 17.93 \pm 0.24\%$.

Since the result presented here agrees with the previous world average value it offers no evidence that the 'missing–decay' mode problem discussed in section 1.3.2 could be due to a previous mismeasurement of the $\tau \rightarrow e\nu_\tau\bar{\nu}_e$ branching ratio.

Table 4.7: Numbers used in the calculation of the BR($\tau \to e\nu_\tau\bar{\nu}_e$)

	Total	Barrel	Endcap
$N_{Cand.}^{e^+e^- \to \tau^+\tau^-}$	7500	6590	910
$N_{Cand.}^{\tau \to e\nu_\tau\bar{\nu}_e}$	1203	1055	148
$f_{bckgnd}^{non-\tau \to e\nu_\tau\bar{\nu}_e}$	$6.1 \pm 1.4\%$	$5.5 \pm 1.4\%$	$8.1 \pm 2.5\%$
$f_{bckgnd}^{non-\tau}$	$1.6 \pm 0.5\%$	$1.3 \pm 0.5\%$	$3.9 \pm 1.3\%$
$\varepsilon_{corr.}^{\tau \to e\nu_\tau\bar{\nu}_e}$	$84.5 \pm 0.8\%$	$84.6 \pm 0.9\%$	$83.3 \pm 1.5\%$
$B^{\tau \to e\nu_\tau\bar{\nu}_e}$	1.005 ± 0.005	1.006 ± 0.006	0.995 ± 0.021
BR($\tau \to e\nu_\tau\bar{\nu}_e$)	$18.0 \pm 0.5 \pm 0.3\%$	$18.0 \pm 0.5 \pm 0.3\%$	$18.8 \pm 1.6 \pm 0.8\%$

Table 4.8: Recent measurements of BR($\tau \to e\nu_\tau\bar{\nu}_e$) from other experiments.

Experiment	BR($\tau \to e\nu_\tau\bar{\nu}_e$)
ALEPH [23]	$18.0 \pm 0.4 \pm 0.4\%$
L3 [26]	$17.7 \pm 0.7 \pm 0.6\%$
ARGUS [83]	$17.3 \pm 0.4 \pm 0.5\%$
CLEO [24]	$19.0 \pm 0.4 \pm 0.7\%$

Using the $\tau \to e\nu_\tau\bar{\nu}_e$ branching ratio presented here and the OPAL result for the $\tau \to \mu\nu_\tau\bar{\nu}_\mu$ branching ratio, $16.8 \pm 0.5 \pm 0.4\%$ [84], a measurement of the ratio of the electron and muon charged couplings can be made:

$$\frac{g_\mu}{g_e} = \frac{\text{BR}(\tau \to e\nu_\tau\bar{\nu}_e)}{\text{BR}(\tau \to \mu\nu_\tau\bar{\nu}_\mu)} \times 0.973 = 1.042 \pm 0.052$$

where the 0.973 factor is due to the difference in phase space for the $\tau \to \mu\nu_\tau\bar{\nu}_\mu$ decay. This is consistent with the assumption of lepton universality which predicts the same couplings for all leptons. This result is shown in table 4.9 along with the equivalent value found using the updated world average branching ratios, this also agrees well with the prediction of lepton universality.

Table 4.9: Charged coupling ratios derived from the BR($\tau \to e\nu_\tau\bar{\nu}_e$) measurement. The first column shows values derived using the measurement presented in this thesis. In the second column this is combined with results from other experiments to form a new world average.

	OPAL	Updated World average
BR($\tau \to e\nu_\tau\bar{\nu}_e$) (%)	$18.0 \pm 0.5 \pm 0.3$	17.93 ± 0.24
BR($\tau \to \mu\nu_\tau\bar{\nu}_\mu$) (%)	$16.8 \pm 0.5 \pm 0.4$ [84]	17.49 ± 0.24 [23]
g_μ/g_e	1.042 ± 0.052	0.997 ± 0.024
g_τ/g_e	0.951 ± 0.036	0.948 ± 0.023

Assuming lepton universality and using the world average values for the lifetimes and masses of the τ and μ:

	Lifetime	Mass
μ	$(2.19703 \pm 0.00004) \times 10^{-6}$s	105.658387 ± 0.000034 MeV
τ	$(3.03 \pm 0.06) \times 10^{-13}$s	$1784.1 \pm^{2.7}_{3.6}$ MeV

where the value of τ_τ has been updated to include recent LEP results as in section 1.3.1, equation 1.5 predicts a value of $18.9 \pm 0.4\%$ for the $\tau \to e\nu_\tau\bar{\nu}_e$ branching ratio. The measurement from the analysis presented in this thesis is within 1.3σ of this prediction. Alternatively, using the measured branching ratio the ratio of the fermi couplings for the μ and the τ can be determined to be $g_\tau/g_\mu = 0.951 \pm 0.036$. The difference between this and the prediction of lepton universality is not statistically significant and does not, therefore, either confirm or contradict the previously observed discrepancy.

Combining the measurement presented here with others to form a new world average gives $g_\tau/g_\mu = 0.948 \pm 0.023$ which is 2.3σ from the prediction of lepton universality. This is still not a large statistical effect but there has been much speculation about the cause of such a disagreement. Possible explanations are statistical fluctuations or biases in the measurements of τ_τ, the branching ratios or m_τ. The ALEPH lifetime measurement discussed in section 1.3.1 may or may not be relevant here. Also, the measurement of the mass is dominated by a single result from the DELCO experiment at SPEAR [20], clearly further measurements of the mass are important. One other

explanation is mixing between ν_τ and a fourth generation heavy neutrino [85].

The major errors on g_τ/g_μ come from the $\tau \rightarrow e\nu_\tau\bar{\nu}_e$ branching ratio (1.3%) and the τ lifetime measurement (2%) with a contribution also from the τ mass (1%). The branching ratio and lifetime measurements should both improve considerably with the increase in statistics expected from LEP in the next few years and this should clarify the question of whether or not there is a real discrepancy.

Chapter 5

Measurement of τ polarization

5.1 Introduction

As was discussed in Chapter 1, the measurement of the τ polarization, P_τ, can be used to extract the axial (a_τ) and vector (v_τ) couplings of the τ to the Z°. The polarization asymmetry averaged over the complete solid angle at energies close to the Z° peak is given in the Improved Born Approximation (neglecting small corrections) by:

$$P_\tau \simeq \frac{-2(v_\tau/a_\tau)}{1+(v_\tau/a_\tau)^2}$$

The polarization varies strongly with $\cos\theta$, the production angle of the τ^- with respect to the e^-, with a stronger polarization in the forward direction. This leads to a forward–backward polarization asymmetry, A_{pol}^{FB}, which is related to the couplings of the electron to the Z° by:

$$A_{pol}^{FB} \simeq -\frac{3}{4}\frac{2(v_e/a_e)}{(1+(v_e/a_e)^2)} \tag{5.1}$$

Therefore, by comparing the couplings derived from measurements of P_τ and A_{pol}^{FB} the validity of the assumption of lepton universality can be checked. The expression for A_{pol}^{FB} given in equation 5.1 is found by integrating over the full solid angle. In an experiment where events are observed within some $\cos\theta$ range, say [-c,c], the measured forward–backward polarization asymmetry is given by:

$$A_{pol}^{FB}(c) \simeq -\frac{3c}{(3+c^2)}\,\frac{2(v_e/a_e)}{(1+(v_e/a_e)^2)} \tag{5.2}$$

The τ polarization is measured from the energy spectra of the τ decay products. In the τ rest frame the τ polarization, which is an asymmetry in the number of left and

right handed τs produced, leads to an asymmetry in the angular distribution of the τ decay product. When the system is boosted to the laboratory frame this leads to an energy distribution of the τ decay product which depends on the degree of polarization of the τ. This is seen most easily in the two–body decay $\tau \rightarrow \pi\nu_\tau$ which is illustrated in figure 5.1 in the rest frame of the τ. Since the ν_τ is left handed and the π has spin zero,

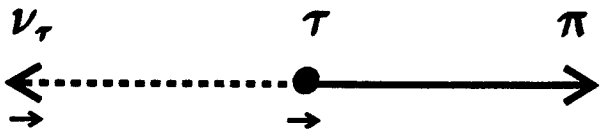

Figure 5.1: A $\tau \rightarrow \pi\nu_\tau$ decay in the τ rest frame.

the ν_τ must be emitted in the direction opposite to that of the τ spin and, therefore, the π is emitted along the direction of the τ spin. The τ polarization means that the π angular distribution is asymmetric in the τ rest frame and is given by [86]:

$$\frac{\mathrm{d}\sigma}{\mathrm{d}\cos\theta} \propto 1 + \mathrm{P}_\tau \cos\theta$$

where θ is the angle between the direction of flight of the π and the τ spin and P_τ is the τ polarization. In the τ rest frame the energy (E_π) and momenta (p_π) of the pion are given by:

$$E_\pi = \frac{m_\tau^2 + m_\pi^2}{2m_\tau}, \qquad p_\pi = \frac{m_\tau^2 - m_\pi^2}{2m_\tau}$$

When the system is boosted to the laboratory frame the energy of the pion, E_π^*, is given by:

$$E_\pi^* = \gamma(E_\pi + \beta p_\pi \cos\theta) \tag{5.3}$$

where, assuming $E_\tau = E_{beam}$:

$$\beta \simeq \frac{p_\tau}{E_{beam}} \quad \text{and} \quad \gamma \simeq \frac{E_{beam}}{m_\tau}$$

Neglecting the pion mass and defining $x_\pi = E_\pi^*/E_{beam}$ equation 5.3 gives:

$$\cos\theta = 2x_\pi - 1$$

So the angular distribution in the tau rest frame leads to an energy distribution for the pion in the laboratory frame given by:

$$\frac{1}{N}\frac{dN}{dx_\pi} = 1 + P_\tau(2x_\pi - 1)$$

Figure 5.2 (a) shows this expected pion energy spectra for polarization values of 0, 1 and -1. It can be seen that by measuring the slope of the observed pion momentum spectrum the polarization can be found.

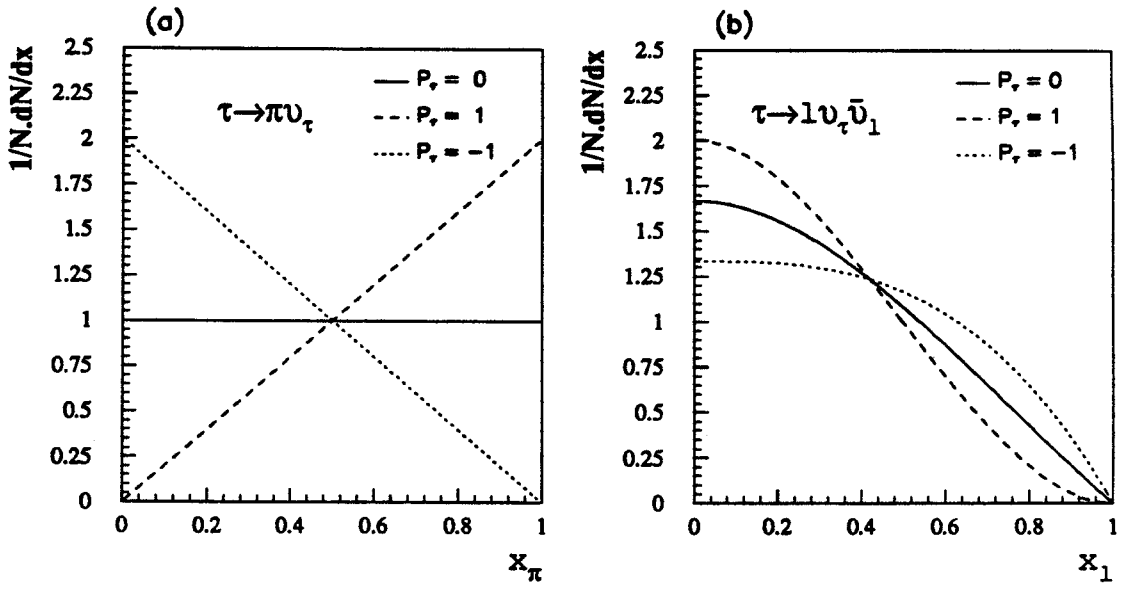

Figure 5.2: Expected energy spectra for (a) πs and (b) leptons from τ decays with P_τ= 0, 1 and -1.

Similar mechanisms to those described above also distort the spectra of other τ decay products. For the three body leptonic decay of the τ, the kinematics are more complicated and the energy spectrum of the charged leptons is given by the following expression [87]:

$$\frac{1}{N}\frac{dN}{dx_l} = \frac{1}{3}(5 - 9x_l^2 + 4x_l^3) + \frac{1}{3}P_\tau(1 - 9x_l^2 + 8x_l^3) \qquad (5.4)$$

where x_l is the energy of the lepton normalized to the beam energy. This distribution is shown in figure 5.2 (b) for values of P_τ = 0, 1 and -1.

The τ polarization can, therefore, be found by fitting the above formulae to the observed τ decay product energy spectrum for the parameter P_τ. In addition, by fitting the spectrum in the forward ($\cos\theta > 0$) and backward hemispheres separately A_{pol}^{FB} can be measured. In this chapter the results for P_τ and A_{pol}^{FB} using the $\tau \rightarrow e\nu_\tau\bar{\nu}_e$ decays selected as described in Chapter 4 are presented. From figure 5.2 it can be seen that the three body decay of the $\tau \rightarrow e\nu_\tau\bar{\nu}_e$ channel has less discriminating power for the polarization than the π channel. However, the $\tau \rightarrow e\nu_\tau\bar{\nu}_e$ channel is still useful since it has a higher branching ratio and selection efficiency which means that higher statistics are available.

The predicted spectra shown in figure 5.2 can be modified due to the effects of radiation, detector resolutions and selection cuts. Therefore, the measured energy spectra must be corrected for these effects before a fit for P_τ can be made. Corrections are made to the observed spectrum for four effects which are listed below and are described in more detail in section 5.2.

Background and efficiency

The measured spectrum must be corrected for the effects of background contamination, both from non–τ events and from other τ decays, and for any energy dependence of the selection efficiency.

Detector resolution

Due to the resolution of the detector, the measured energy of a particle is not necessarily equal to its true energy. This introduces a smearing of the true energy distribution. A matrix 'unfolding' technique is used to take into account this smearing. A two dimensional matrix is used to transform the measured energy spectrum into the underlying 'true' energy spectrum.

Radiative effects

Both initial and final state radiation can affect the observed electron spectrum. For initial state radiation this is due to two effects. The first is a direct effect whereby the radiation of a photon from the incoming electron or positron means that the centre of mass energy, E_{CM}, is reduced and this affects the polarization through its weak dependence on E_{CM}. A second, indirect, effect occurs due to the fact that the energy of

the produced τs and therefore also the energy of the electron is reduced, thus modifying the observed energy spectrum of the electron. The energy is lowered by the effects of radiation thus mimicking a positive polarization. Final state radiation from the τ has only an indirect effect. Bremsstrahlung from the electron also modifies the observed spectrum, and therefore affects the polarization measurement, and in fact, as will be seen later, this is the largest effect.

τ pair preselection cuts

Biases in the observed energy spectrum of the electron can be introduced by the τ pair preselection cuts. For example, cuts to reject Bhabha events are more likely to remove high energy $\tau \rightarrow e\nu_\tau\bar{\nu}_e$ decays than low energy ones, thus biasing the spectrum towards lower energies and affecting the polarization measurement.

Bremsstrahlung from the τ decay and from the electron mean that there are large radiative corrections to the momentum spectrum of the electron which shift the measured spectrum to lower values than predicted and thus increase the measured polarization. In order to reduce this problem, since the radiation is generally collinear with the electron's direction of motion, the normalised energy of an electron candidate, x_e, is defined by using the energy observed in the electromagnetic calorimeter rather than the momentum of the charged track. In addition, the smearing effects of the detector resolution are less for the electromagnetic energy than the track momentum over most of the energy range. The energy is taken to be that within the 35° cone used to define the τ jet:

$$x_e = \sum_{i=1}^{Nclus} E_i^{clus} / E_{beam}$$

where the summation is over all electromagnetic clusters assigned to the candidate cone.

The corrections listed above are applied to the observed electron energy spectrum using the following expression:

$$N_i^{corr} = C_i^{bias}\, C_i^{rad/E_{CM}} \sum_j A_{ij} \frac{1}{\epsilon_j^{corr}} N_j^{meas} (1 - f_j^{bckgnd}) \qquad (5.5)$$

where N_j^{meas} is the number of candidates in measured energy bin j and N_i^{corr} is the corrected number of candidates in 'true' energy bin i. f_j^{bckgnd} and ϵ_j^{corr} are, respectively,

the estimated background contamination and selection efficiency in measured energy bin j. A_{ij} is the matrix used to transform measured energy into true energy, $C_i^{rad/E_{CM}}$ and C_i^{bias} are correction factors for the effects of radiation, centre of mass energy and preselection bias in true energy bin i.

5.2 Corrections

The correction factors for backgrounds, selection efficiency, detector resolution and preselection bias are derived using Monte Carlo (MC) $e^+e^- \rightarrow \tau^+\tau^-$ events with full detector simulation. A sample of 50 000 events generated with KORALZ were used for this purpose.

5.2.1 Background and efficiency corrections

Background contaminations (f_j^{bckgnd}) and selection efficiencies (ε_j) were estimated in sections 4.3.1 and 4.3.2, respectively, using the 50 000 $e^+e^- \rightarrow \tau^+\tau^-$ MC events with full detector simulation. In figure 5.3 these corrections are shown as functions of x_e. The mismeasurement of the momenta of forward going tracks at high energies in the endcap leads to the inefficiency at high x_e due to the E_{clus}/p_{trck} cut used to identify electrons. The total corrections for the data from the barrel and endcap together are found by combining the individual distributions weighted by the relative statistics in each sample and, since the statistics in the endcap are only ~15% of those in the barrel, the drop in efficiency at high x_e is not seen. The correction factors (C^ε) derived in section 4.3.2 to account for the differences seen between the efficiency in the MC and that in the data in the single electron and Bhabha control samples are used to correct the raw efficiency shown in figure 5.3. This leads to a corrected efficiency, $\varepsilon_j^{corr} = C^\varepsilon \varepsilon_j$, for each bin which is then used to correct the data.

The corrections for background and efficiency are given in table 5.1 for the barrel and endcap separately. The second column of the table gives the observed number of events in each energy bin and the last column shows these after the corrections have been made. The corrections for non–τ background contaminations are derived from MC samples of Bhabha and two–photon events. Typically only one or two such

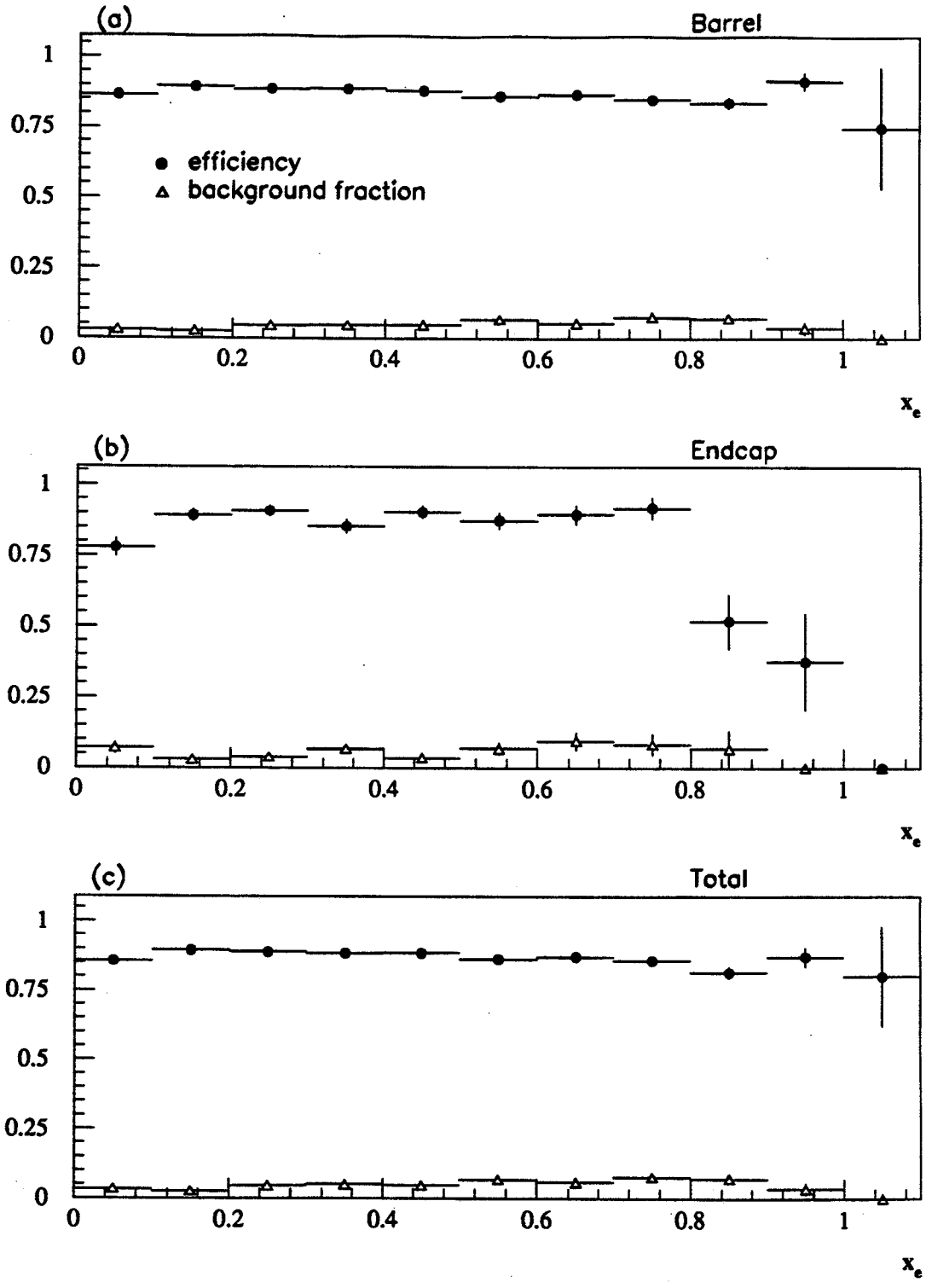

Figure 5.3: Background fractions (f_j^{bckgnd}) and selection efficiencies (ϵ_j) for the $\tau \to e\nu_\tau\bar{\nu}_e$ sample. The values are calculated from $e^+e^- \to \tau^+\tau^-$ MC events with full detector simulation.

Table 5.1: Background and efficiency corrections for the barrel and the endcap. The data are shown before and after correction. The corrections for background contamination are split into those from non–τ events and those from other τ decays. The raw efficiency from the $e^+e^- \to \tau^+\tau^-$ MC (ε_j) is given along with the corrections (C^ε) for observed differences between data and MC. Errors on the τ backgrounds and efficiency corrections are those due to MC statistics.

x_j	Raw data (Barrel) (N_j^{meas})	Background contamination (f_j^{bckgnd})		Efficiency (ε_j) (%)	Efficiency correction (C^ε)	Corrected data
		non–τ (events)	τ (%)			
0.0–0.1	160 ± 12.6	1.98	3.04 ± 0.48	88.67 ± 0.85	0.964 ± 0.009	179.2 ± 14.1
0.1–0.2	158 ± 12.6	0.99	2.58 ± 0.41	90.76 ± 0.72	0.937 ± 0.009	179.9 ± 14.3
0.2–0.3	176 ± 13.3	0.99	4.65 ± 0.55	89.86 ± 0.77	0.942 ± 0.009	197.1 ± 14.9
0.3–0.4	149 ± 12.2	0.00	4.79 ± 0.58	89.78 ± 0.80	0.947 ± 0.009	166.9 ± 13.7
0.4–0.5	123 ± 11.1	0.00	4.85 ± 0.63	89.15 ± 0.88	0.952 ± 0.009	137.9 ± 12.4
0.5–0.6	115 ± 10.7	0.00	6.79 ± 0.81	87.36 ± 1.04	0.957 ± 0.009	128.2 ± 11.9
0.6–0.7	78 ± 8.8	0.00	5.48 ± 0.80	87.24 ± 1.13	0.962 ± 0.010	87.8 ± 9.9
0.7–0.8	51 ± 7.1	1.40	7.71 ± 1.16	86.44 ± 1.44	0.967 ± 0.010	54.8 ± 7.7
0.8–0.9	31 ± 5.6	0.70	7.26 ± 1.49	84.64 ± 1.98	0.973 ± 0.007	34.1 ± 6.1
0.9–1.0	13 ± 3.6	1.40	3.70 ± 2.10	91.76 ± 2.98	0.979 ± 0.007	12.4 ± 3.4
1.0–1.1	1 ± 1.0	0.00	0.00	75.00 ± 21.6	0.979 ± 0.007	1.4 ± 1.4

x_j	Raw data (Endcap) (N_j^{meas})	Background contamination (f_j^{bckgnd})		Efficiency (ε_j) (%)	Efficiency correction (C^ε)	Corrected data
		non–τ (events)	τ (%)			
0.0–0.1	19 ± 4.3	0.4	6.94 ± 2.12	77.91 ± 3.16	0.983 ± 0.009	22.6 ± 5.1
0.1–0.2	27 ± 5.2	0.4	2.93 ± 1.18	89.24 ± 2.07	0.957 ± 0.009	30.2 ± 5.8
0.2–0.3	23 ± 4.8	0.4	3.72 ± 1.29	90.79 ± 1.91	0.959 ± 0.009	25.0 ± 5.2
0.3–0.4	19 ± 4.3	0.0	6.60 ± 1.70	85.34 ± 2.32	0.961 ± 0.009	21.6 ± 4.9
0.4–0.5	30 ± 5.5	0.0	3.43 ± 1.37	90.37 ± 2.16	0.963 ± 0.010	33.3 ± 6.1
0.5–0.6	16 ± 4.0	1.4	6.72 ± 2.16	87.41 ± 2.77	0.966 ± 0.010	16.1 ± 4.0
0.6–0.7	7 ± 2.6	0.0	9.41 ± 3.17	89.53 ± 3.30	0.968 ± 0.010	7.3 ± 2.7
0.7–0.8	3 ± 1.7	0.0	8.16 ± 3.91	91.84 ± 3.91	0.970 ± 0.011	3.1 ± 1.8
0.8–0.9	3 ± 1.7	0.0	6.67 ± 6.44	51.85 ± 9.61	0.972 ± 0.012	5.6 ± 3.2
0.9–1.0	1 ± 1.0	0.0	0.0	37.5 ± 17.1	0.975 ± 0.018	2.7 ± 2.7
1.0–1.1	0	0.0	0.0	–	–	0.0

events pass the selection cuts in a given energy bin and these are scaled to the correct luminosity to give the numbers in the table. The errors given for the background contamination from other τ decay modes and for the efficiency corrections are those due to MC statistics.

5.2.2 Unfolding of the detector resolution

In order to correct the measured energy distribution for detector resolution effects a matrix unfolding technique is used. For MC events a plot of the observed energy of a particle versus its true energy (which is available from the MC information) is used to derive a matrix:

$$A_{ij} = \frac{N_{ij}}{N_j}$$

where N_{ij} is the number of events observed in energy bin j which originated from true energy bin i and N_j is the total number of events in observed energy bin j. Thus, the matrix element A_{ij} is the probability that a particle in observed energy bin j originated from true energy bin i. The matrix was calculated from the $e^+e^- \rightarrow \tau^+\tau^-$ MC events generated using KORALZ with full detector simulation and using those $\tau \rightarrow e\nu_\tau\bar{\nu}_e$ jets which passed the τ pair preselection.

Figures 5.4 (a) and (b) show the two dimensional distributions derived using the energy of the ECAL cluster associated with a candidate track and the energy of the candidate cone, respectively. It can be seen that by using the cone energy, and thereby including bremsstrahlung photons in the energy, a better correlation between the observed and true energies is achieved. The matrix derived from the distribution shown in figure 5.4 (b) is shown in table 5.2

The matrix derived in this way depends not only on the detector resolution but also on the original MC energy distribution. This means that the procedure is only reliable if the MC distribution is close to the 'true' distribution. Figure 5.5 shows a comparison of the observed energy spectra in the data and the MC after the efficiency and background corrections have been applied and shows good agreement between data and MC. The histograms are normalised to the number of τs passing the preselection cuts.

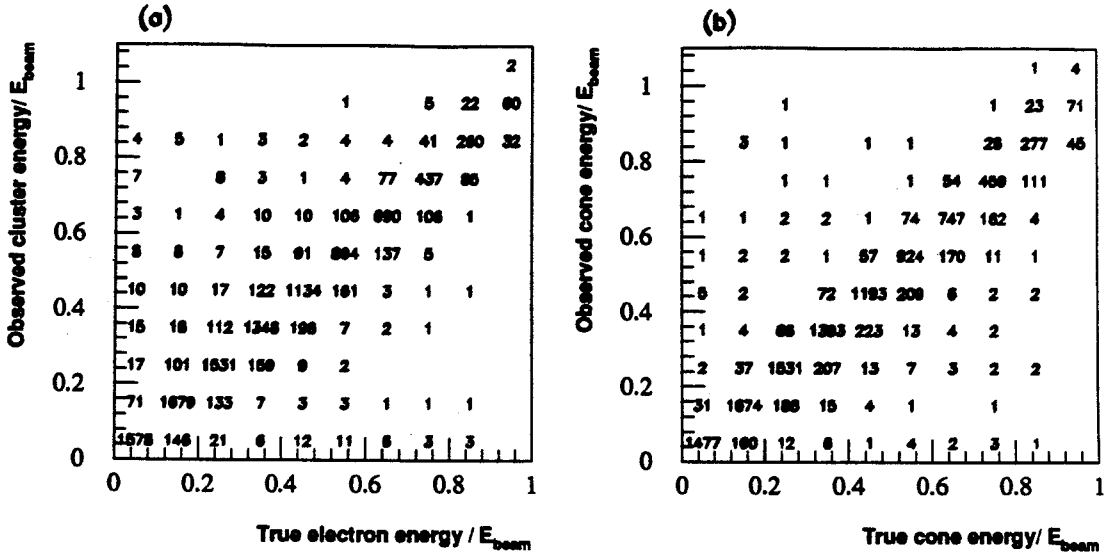

Figure 5.4: Distributions of observed energy versus true energy used to derive the unfolding matrix. The energy is normalized to the beam energy and is defined as:
(a) Energy of the electromagnetic cluster associated to the candidate track versus the true energy of the electron.
(b) Energy in all electromagnetic clusters in a cone of half angle 35° around the candidate track versus energy of the electron plus any photons within a 35° cone around the electron.

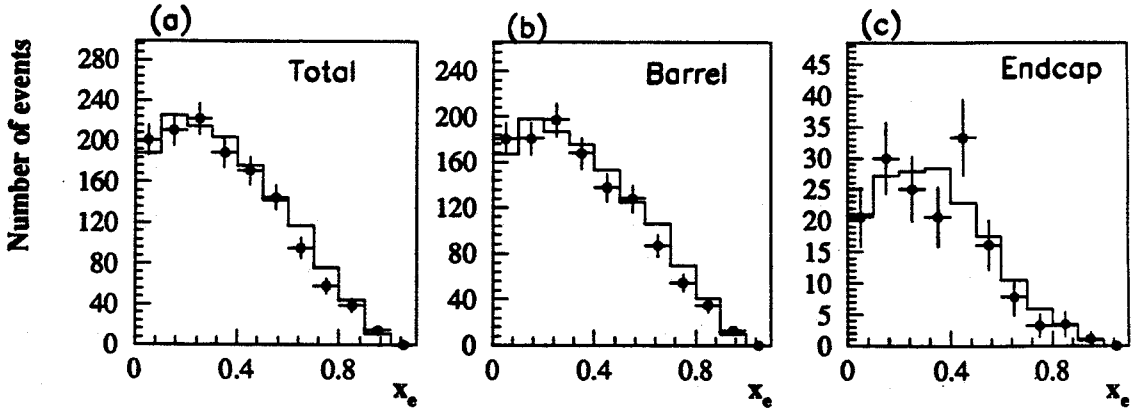

Figure 5.5: Electron energy spectra corrected for background and efficiency from data (points) and MC (solid histogram).

Table 5.2: Matrix used to correct the data for the effects of detector resolution.

True energy bin (x_i)	Observed energy bins (x_j)										
	.0–.1	.1–.2	.2–.3	.3–.4	.4–.5	.5–.6	.6–.7	.7–.8	.8–.9	.9–1.	1.–1.1
0.0–0.1	0.887	0.016	0.001	0.001	0.003	0.001	0.001	0.000	0.000	0.000	0.000
0.1–0.2	0.096	0.875	0.020	0.002	0.001	0.002	0.001	0.000	0.008	0.000	0.000
0.2–0.3	0.007	0.098	0.849	0.039	0.000	0.002	0.002	0.002	0.003	0.010	0.000
0.3–0.4	0.004	0.008	0.115	0.816	0.048	0.001	0.002	0.002	0.000	0.000	0.000
0.4–0.5	0.001	0.002	0.007	0.131	0.800	0.049	0.001	0.000	0.003	0.000	0.000
0.5–0.6	0.002	0.000	0.004	0.008	0.140	0.790	0.074	0.002	0.003	0.000	0.000
0.6–0.7	0.001	0.000	0.002	0.002	0.004	0.145	0.751	0.086	0.000	0.000	0.000
0.7–0.8	0.002	0.000	0.001	0.001	0.001	0.009	0.163	0.732	0.079	0.010	0.000
0.8–0.9	0.001	0.000	0.001	0.000	0.001	0.001	0.004	0.177	0.778	0.240	0.200
0.9–1.0	0.000	0.000	0.000	0.000	0.000	0.000	0.000	0.000	0.126	0.740	0.800

5.2.3 Radiative corrections

To illustrate the effects of radiation on the observed electron spectrum, figure 5.6 (a) shows the expected energy spectrum for electrons from τ decays at the Born level and including various sorts of radiation. For convenience the plots are produced using the $O(\alpha)$ semi-analytic program CALASY [88] which calculates the expected energy spectra for τ decay products. The program allows the inclusion of radiation in the initial and final states and from the decay product. Comparisons with the KORALZ ($O(\alpha^2)$) MC have shown reasonable agreement between the two programs [89]. The solid line shows the Born level prediction for the electron spectrum. Initial state radiation has a very small effect on the spectrum and the curve including only this effect is indistinguishable from the Born level curve. The effects of final state radiation and radiation from the electron are significant, particularly at low energy.

Figure 5.6 (b) shows the dependence of P_τ on the centre of mass energy, E_{CM}. The dependence is weak and the corrections for this effect are small. The dashed line illustrates once again that the effects of initial state radiation are small.

Correction factors for the effects of radiation and centre of mass energy were derived from two high statistics Monte Carlo samples generated using KORALZ but with no

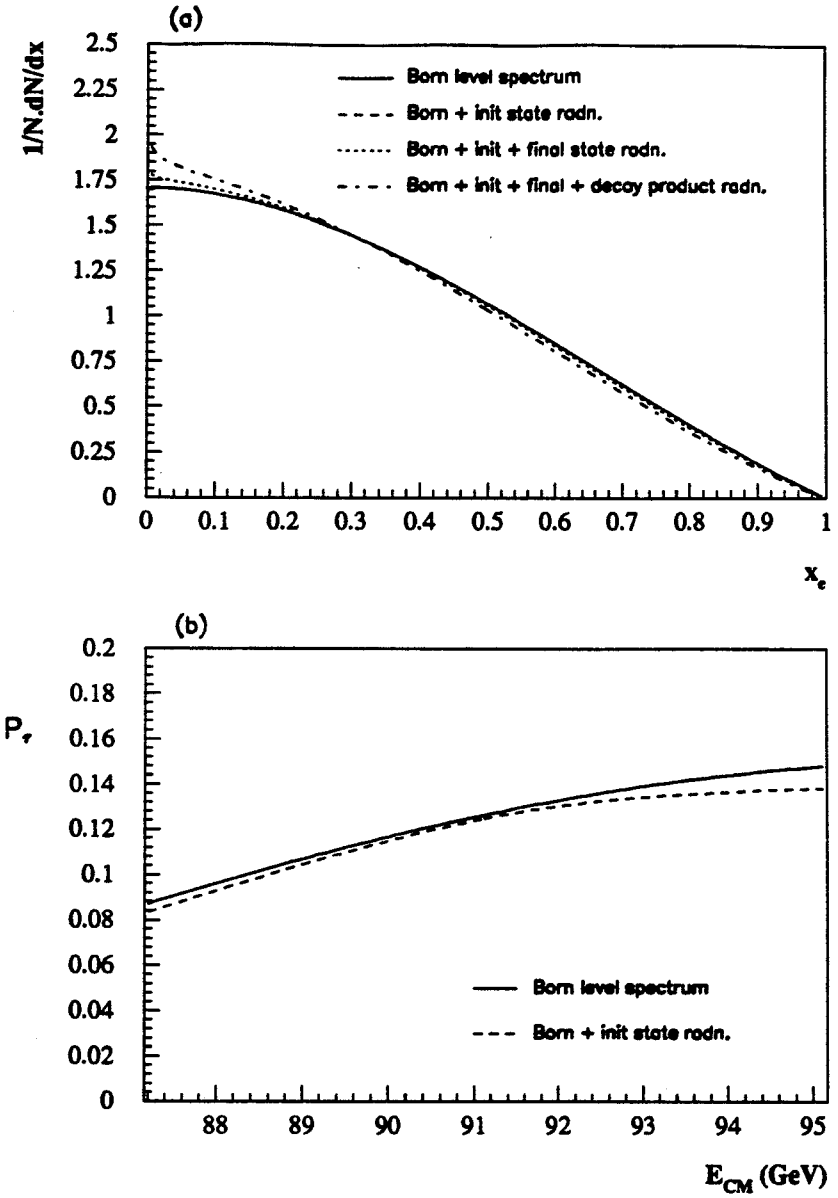

Figure 5.6: (a) Electron energy spectra with different radiative effects included. (b) P_τ as a function of centre of mass energy.

detector simulation. The first sample was generated at the Z° pole with no initial state, final state or decay product radiation. The second sample included full radiation effects and events were generated at seven centre of mass energies in ratios determined by the luminosity taken by OPAL at each energy point in 1990. The correction factors ($C^{rad/E_{CM}}$) are calculated as the ratio of the normalized energy spectra from the two samples.

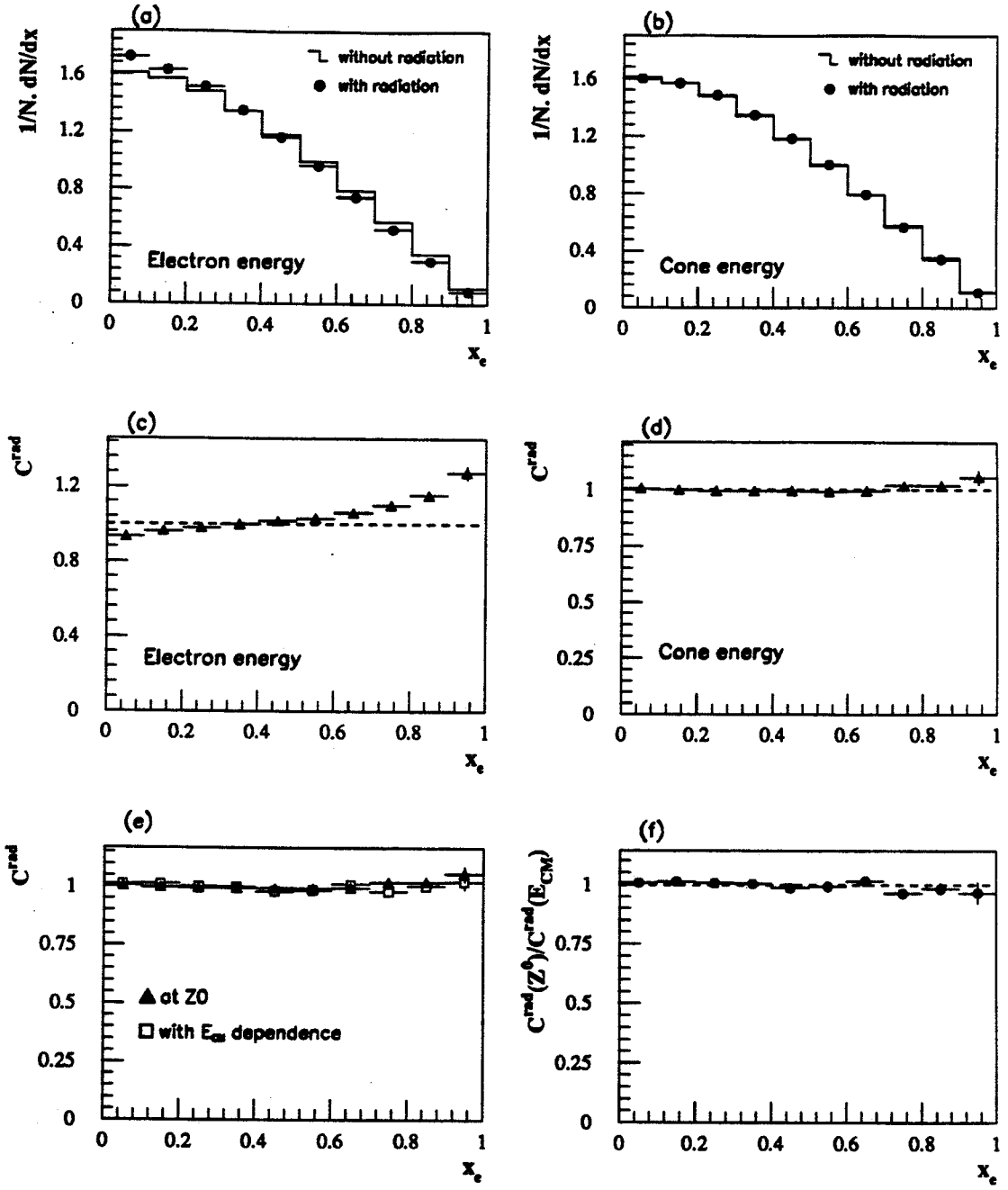

Figure 5.7: Radiation corrections.
(a) and (b): Energy spectra for Monte Carlo events generated with and without radiation in the event. The energy in (a) is the energy of the emerging electron and that in (b) is the energy of the emerging electron plus that of any photons within a 35° cone.
(c) and (d): Radiation corrections derived using the electron energy and the electron energy plus that of nearby photons respectively. The horizontal dashed line at 1.0 is to guide the eye.
(e) Correction factors derived with and without including the effects of E_{CM}.
(f) Ratio of correction factors in (e).

Figures 5.7 (a) and (b) show the normalised electron energy spectra for events generated with and without radiation where the energy is defined in (a) as the energy of the electron and in (b) as the energy of the electron plus nearby photons. The effect of radiation on the spectrum expected from figure 5.6 can be seen in figure 5.7 (a) where the spectrum including radiation has been shifted to lower energies. Figure 5.7 (b) shows that by adding the energies of photons close to the electron, i.e. by using the cone energy, the effect of radiation on the spectrum is significantly reduced. Figures 5.7 (c) and (d) show the correction factors in the two cases. The horizontal dashed lines on the plots are to illustrate a correction factor of 1.0. The correction factors shown in figure 5.7 (d) are used to correct the data and are given in table 5.3, the errors are statistical.

To illustrate that the dependence on E_{CM} is indeed small, figure 5.7 (e) shows the correction factors from figure 5.7 (d) along with those which would be found if no account was taken of the E_{CM} distribution in the data. Figure 5.7 (f) shows the ratio of the two sets of corrections in figure 5.7 (e), as can be seen the effect of the variation in E_{CM} is small.

5.2.4 Preselection Bias corrections

Finally corrections are applied to account for biases in the energy spectrum arising from the τ pair preselection cuts. This effect is corrected for by using bin-by-bin correction factors. The factors were calculated from the $e^+e^- \rightarrow \tau^+\tau^-$ MC sample of events after full detector simulation. The corrections (C^{bias}) are calculated as the ratio of the normalized true energy distribution for $\tau \rightarrow e\nu_\tau\bar{\nu}_e$ decays before preselection to that after preselection. Figure 5.8 (a) shows the normalised energy spectra for $\tau \rightarrow e\nu_\tau\bar{\nu}_e$ decays in the barrel of the detector both before and after preselection. Figure 5.8 (b) shows the bias factors calculated from the ratio of the two spectra. Figures 5.8 (c) and (d) show the same distributions for the endcap data. In the barrel the largest bias occurs at low energy and is due to the the cuts which remove two–photon events and the acollinearity cut. In the endcap the large bias at high energies is due to the tight cuts needed to remove Bhabha events in this region, however since the statistics in the endcap are much smaller than in the barrel this has little effect on the total correction

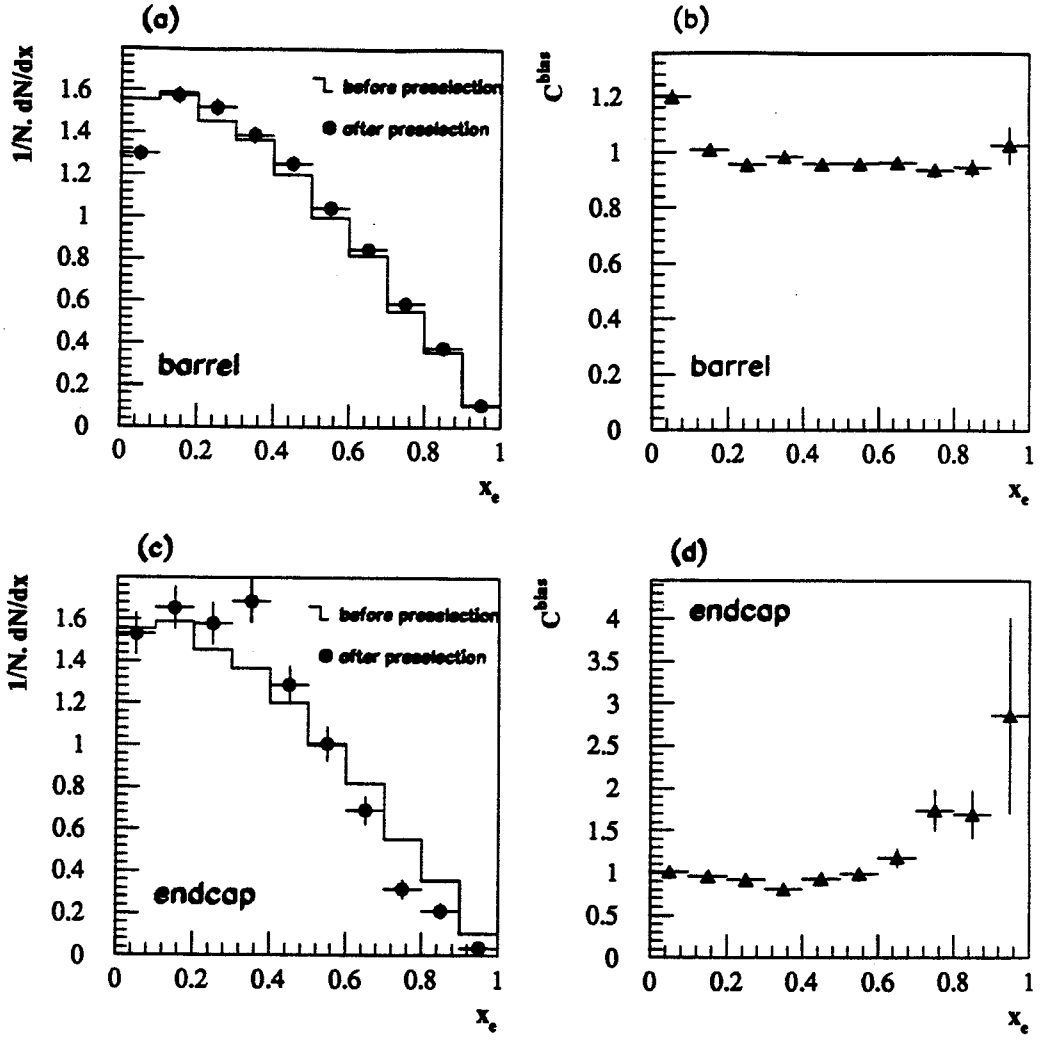

Figure 5.8: Preselection bias corrections:
(a): Normalized energy distribution for barrel $\tau \rightarrow e\nu_\tau\bar{\nu}_e$ events before and after preselection.
(b): Bias factors derived from (a).
(c) and (d): same as (a) and (b) but for the endcap data.

factors which are given in table 5.3. The errors on the corrections in the table are statistical.

Table 5.3: Data and corrections.
The data from the barrel and endcap in table 5.1 have been summed and are given in the second column. The same data after unfolding for detector resolution effects are given in column three. Corrections for radiation and biases are shown along with the final corrected data. In the final column the same data are given after being normalized. The errors on the final data are due to the statistics of the data only.

x_i	Data corr. for ϵ_j^{corr} and f_j^{bckgnd}	Unfolded data	Radiation correction ($C_i^{rad/E_{CM}}$)	Bias correction (C_i^{bias})	Final data (N_i^{corr})	Normalized data (z_i)
0.0–0.1	201.8 ± 15.2	182.9	1.0057 ± 0.0067	1.2356 ± 0.0171	227.3 ± 17.0	1.69 ± 0.13
0.1–0.2	210.1 ± 15.4	209.4	1.0035 ± 0.0068	1.0000 ± 0.0079	210.1 ± 15.5	1.56 ± 0.11
0.2–0.3	222.1 ± 15.8	218.9	0.9999 ± 0.0070	0.9463 ± 0.0057	207.1 ± 14.9	1.53 ± 0.11
0.3–0.4	188.5 ± 14.5	190.5	0.9971 ± 0.0073	0.9473 ± 0.0059	179.9 ± 13.8	1.33 ± 0.10
0.4–0.5	171.2 ± 13.8	170.8	0.9793 ± 0.0076	0.9427 ± 0.0060	157.7 ± 12.7	1.17 ± 0.09
0.5–0.6	144.3 ± 12.5	148.3	0.9958 ± 0.0085	0.9452 ± 0.0068	139.6 ± 12.2	1.03 ± 0.09
0.6–0.7	95.1 ± 10.3	99.2	1.0160 ± 0.0097	0.9666 ± 0.0090	97.4 ± 10.2	0.72 ± 0.07
0.7–0.8	57.9 ± 7.9	63.8	0.9929 ± 0.0111	0.9847 ± 0.0123	62.4 ± 8.1	0.46 ± 0.06
0.8–0.9	39.7 ± 6.9	46.4	1.0157 ± 0.0148	1.0428 ± 0.0199	49.1 ± 8.6	0.36 ± 0.06
0.9–1.0	15.1 ± 4.3	18.0	1.0454 ± 0.0266	1.0629 ± 0.0410	20.0 ± 5.1	0.15 ± 0.04
1.0–1.1	1.4 ± 1.4	-	-	-	-	-

5.3 Fitting

The data are unfolded and corrected using equation 5.5 and the correction factors derived in section 5.2. The correction factors and the corrected data (N_i^{corr}) are shown in table 5.3. The energy distribution after all the corrections have been applied is normalized such that the normalised bin contents, z_i, are given by:

$$z_i = \frac{N_i^{corr}}{\sum_j N_j^{corr} \Delta x_i}$$

where Δx_i is the width of energy bin i and N_i^{corr} is the number of events in true energy bin i after all the corrections have been applied. The z_i are given in table 5.3. The Born level formula for the electron energy distribution given in equation 5.4 is then fitted to the z_i using a χ^2 minimisation fit. The χ^2 is defined as :

$$\chi^2 = \sum_i \sum_j y_i^T V_{ij}^{-1} y_j$$

where y_i is the difference between z_i, the measured value in bin i, and $\Phi(P, x_e)$, the value predicted from the Born formula for a polarization of P at an energy fraction x_e:

$$y_i = z_i - \Phi(P, x_e)$$

The error matrix, V_{ij}, is defined as:

$$V_{ij} = F_i F_j \sum_{k,l} A_{ik}^T S_{kl} A_{lj}$$

where A is the unfolding matrix and S is the covariance matrix for the statistical errors on the data. The factors F_i are the total corrections applied for radiation and preselection effects, i.e. $F_i = C_i^{rad/E_{CM}}\ C_i^{bias}$. The χ^2 is minimised using the MINUIT [90] package of routines to extract the τ polarization, P_τ.

5.3.1 Systematic Errors

The systematic errors on the fitted values of the polarization are found by varying the corrections applied in section 5.2. The data are then re–corrected with the new corrections and refitted. The change in the fitted value of the polarization due to such a procedure is taken as the systematic error.

To estimate the systematic error due to the efficiency and background corrections given in table 5.1 the selection cuts for the $\tau \rightarrow e\nu_\tau\bar{\nu}_e$ sample (described in section 4.3) are varied. Each cut is varied within values which are reasonable given the resolution of the cut parameter. After varying each cut in both the data and the MC, the backgrounds and efficiencies are recalculated and then the data are corrected using these new values before being refitted. The range of variation of each cut and the observed change in the fitted value of P_τ due to the variation are given in table 5.4. For the cuts on $\cos\theta$ in the endcap region the variation of the cut is not symmetric because, as can be seen from figure 4.8 (b), the endcap acceptance cuts are at the limit of the well understood part of the detector. To extend the acceptance would not make sense and, therefore, in the calculation of the systematic errors the acceptance is reduced

Table 5.4: Systematic errors on the measurement of P_τ due to the selection cuts described in section 4.3. For each cut the nominal cut value is given along with the variation of the cut used to estimate the systematic error. The changes in the fitted value of P_τ due to the variations are given. In the cases where different cuts are used in the barrel and the endcap these are listed separately.

Selection variable	Nominal cut		Variation in cut	Change in P_τ		
				Total	Barrel	Endcap
E_{clus}/p_{track}	low:	0.7	0.6 → 0.8	0.02	0.01	0.06
	high:	2.0	1.6 → 2.4	0.04	0.03	0.05
HC^{depth}		1	0 → 4	0.03	0.03	0.01
N^{90}_{blck}	barrel:	3	2 → 5	0.03	0.02	0.14
	endcap:	5	4 → 7			
E_{else}		0.04	0.025 → 0.055	0.02	0.01	0.03
$\delta\phi^{max}$	(barrel)	5.	3.8 → 6.4	0.01	0.01	
$\Delta\theta^{Ecal-track}$	(endcap)	1.	0.88 → 1.20	0.01		0.08
dE/dx, E/p, low x_e		–	–	0.01	0.01	0.17
$cos\theta$	barrel:	0.68	0.65 → 0.71	0.03	0.03	
	endcap:	0.82	0.820 → 0.835	0.02		0.24
		0.90	0.885 → 0.900	0.01		0.07
Total				0.08	0.06	0.35

only. The total systematic error due to the background and efficiency corrections is taken as the sum in quadrature of the errors for each cut.

The corrections to the efficiency (C^e) which were derived from the comparison between MC and data control samples are varied by $\pm 1\sigma$ and the correction procedure is repeated. The change in the polarization value when the data are refitted is shown in table 5.5.

As mentioned in section 5.2.2, the unfolding matrix (A_{ij}) depends not only on the detector resolution but also on the energy spectrum in the MC and hence on the value of P_τ in the MC. To account for this effect the polarization in the MC is artificially changed by $\pm 50\%$ from its nominal value of -0.16 and the unfolding matrix

Table 5.5: Systematic errors on the measurement of P_τ due to the unfolding and correction procedures.

Source of error	Change in P_τ		
	Total	Barrel	Endcap
Efficiency corrections (C^ϵ)	0.01	0.01	0.02
Unfolding procedure (A_{ij})	0.01	0.01	0.04
Radiative corrections ($C^{rad/E_{CM}}$)	0.01	0.01	0.04
Pres. Bias corrections (C^{bias})	0.01	0.02	0.10
Total	0.03	0.03	0.12

Table 5.6: Fitted values of $< P_\tau >$ for MC events

	Total	Barrel	Endcap
P_τ	-0.18 ± 0.05	-0.17 ± 0.05	-0.20 ± 0.15

is recalculated. The polarization is changed by varying the number of τs with positive and negative helicities in the sample. The change in the fitted polarization value observed when the new matrices are used is taken as the systematic error and is given in table 5.5.

The correction procedure was performed after varying the radiative correction factors ($C^{rad/E_{CM}}$) by $\pm 1\sigma$ and the change in the fitted value of P_τ is taken as a systematic error due to these corrections. These changes are shown in table 5.5. The systematic error due to the preselection bias corrections (C^{bias}) is calculated in the same way, again the values are given in table 5.5.

The total systematic error due to the unfolding and correction procedure is the sum in quadrature of the values in table 5.5.

As a check on the method used to correct and fit the data, the same procedure is applied to the observed MC spectrum after all cuts. The results of the fits after correcting the spectra in exactly the same way as the data are given in table 5.6, and are in good agreement with the value of -0.16 used in the Monte Carlo generation.

The statistical errors on these fits are taken as additional systematic errors on P_τ due to MC statistics. The systematic effects already discussed will include some effects due to MC statistics. However, since it is unknown how much the MC statistics contribute to the previous errors they are included explicitly here to be conservative. The final systematic error on the fitted value of P_τ is taken as the sum in quadrature of the total errors given in tables 5.4, 5.5 and 5.6.

5.4 Results of fits

A fit is made to the corrected and normalized data, z_i, from table 5.3 using the procedure described in section 5.3. The data and fitted curve are shown in figure 5.9 (a) for the complete data sample. The correction procedure is repeated for the forward and backward hemispheres separately and the fits redone, the resulting spectra and fits are shown in figures 5.9 (b) and (c). The polarization values obtained from the fits are given in table 5.7 along with the values for the barrel and endcap separately. There are insufficient statistics in the endcap to perform the fits for the separate hemispheres. The first error on the fitted values is statistical and the second systematic, where the calculation of the systematic errors has been described in section 5.3.1. The good χ^2 values indicate the quality of the fits.

Table 5.7: Fitted values of P_τ

	Total	Barrel	Endcap
P_τ	$0.04 \pm 0.13 \pm 0.09$	$0.03 \pm 0.13 \pm 0.08$	$0.23 \pm 0.41 \pm 0.40$
	$(\chi^2/d.o.f = 8.2/9)$	$(\chi^2/d.o.f = 6.3/9)$	$(\chi^2/d.o.f = 6.7/9\ )$
P_τ^F	$0.001 \pm 0.18 \pm 0.09$	$-0.02 \pm 0.18 \pm 0.08$	-
	$(\chi^2/d.o.f = 9.6/9)$	$(\chi^2/d.o.f = 7.8/9)$	
P_τ^B	$0.20 \pm 0.17 \pm 0.09$	$0.16 \pm 0.18 \pm 0.08$	-
	$(\chi^2/d.o.f = 2.3/9)$	$(\chi^2/d.o.f = 2.8/9)$	
A_{pol}^{FB}	-0.10 ± 0.14	-0.09 ± 0.14	-
$A_{pol}^{FB}(corr)$	-0.12 ± 0.17	-0.11 ± 0.18	-

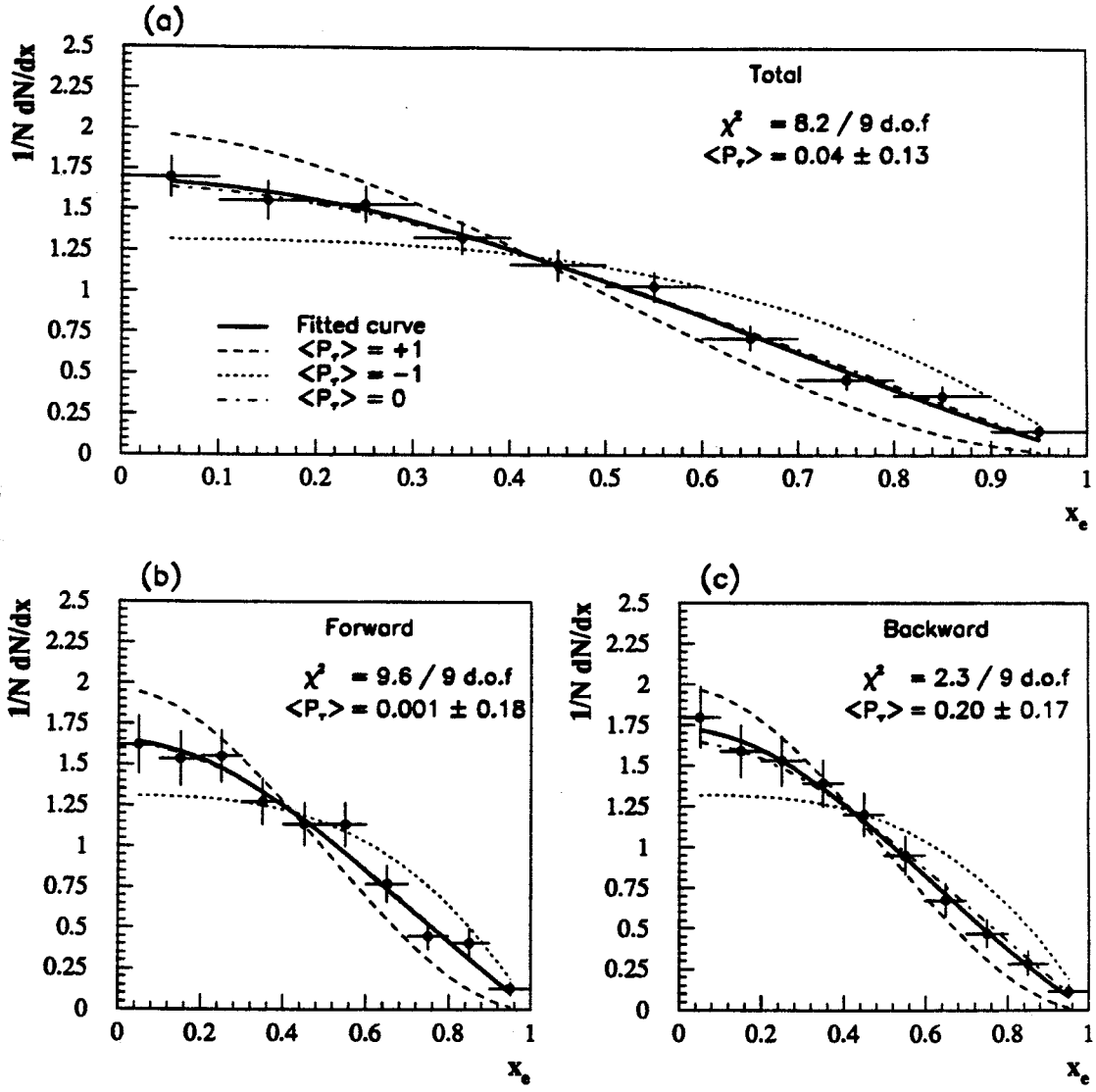

Figure 5.9: Fit to the electron energy spectrum to determine $< P_\tau >$.

Using the polarization values found in the forward and backward hemispheres, P_τ^F and P_τ^B, the forward–backward polarization asymmetry is calculated using:

$$A_{pol}^{FB} = \frac{1}{2}(P_\tau^F - P_\tau^B)$$

and the values are given in table 5.7. This, however, depends on the angular acceptance of the τ events and to calculate couplings it has to be corrected as indicated by equation 5.2 in section 5.1. Correcting for the angular acceptance:

$$|\, cos\theta \,| \leq 0.68 \quad \text{and} \quad 0.82 \leq |\, cos\theta \,| \leq 0.90$$

gives the $A_{pol}^{FB}(corr)$ values in table 5.7.

5.5 Standard Model Couplings

The mean τ polarization is related to the vector and axial couplings of the τ to the Z° by the relationship:

$$P_\tau \simeq \frac{-2(v_\tau/a_\tau)}{1+(v_\tau/a_\tau)^2}$$

Since from other measurements [82] it is known that $v_\tau \ll a_\tau$, this reduces to:

$$P_\tau \simeq -2\,(v_\tau/a_\tau) = -2\,(1-4\sin^2\bar{\theta}_W)$$

where $\bar{\theta}_W$ is the effective electroweak mixing angle in the Improved Born Approximation. The above measurement of $P_\tau = 0.04 \pm 0.13 \pm 0.09$, therefore, gives:

$$v_\tau/a_\tau = -0.02 \pm 0.08 \quad \text{and} \quad \sin^2\bar{\theta}_W = 0.255 \pm 0.020 \qquad (5.6)$$

Using the measured value of the partial width for $Z^\circ \rightarrow \tau\tau$, $\Gamma_{\tau\tau} = 82.7 \pm 1.9$ MeV [82], which is related to the couplings by:

$$\Gamma_{\tau\tau} = \frac{G_F M_Z^3}{24\sqrt{2}\pi}(v_\tau^2 + a_\tau^2)$$

v_τ and a_τ can be found separately:

$$\begin{aligned} v_\tau &= 0.02 \pm 0.04 \\ a_\tau &= -0.998 \pm 0.016 \end{aligned}$$

The value of a_τ is consistent with the Standard Model expectation of $a_\tau \sim -1$ and $\sin^2\bar{\theta}_W$ value determined from v_τ agrees with other OPAL measurements from the forward–backward charge asymmetries [82]. The forward–backward polarization asymmetry is related to the couplings of the electron to the Z° by:

$$A_{pol}^{FB}(corr) \simeq -2(v_e/a_e) = -2(1 - 4\sin^2\bar{\theta}_W)$$

and the measurement in table 5.7 gives:

$$v_e/a_e = 0.06 \pm 0.08 \quad \text{and} \quad \sin^2\bar{\theta}_W = 0.235 \pm 0.020 \tag{5.7}$$

The measurements of v_τ/a_τ and v_e/a_e, from equations 5.6 and 5.7, are in agreement within the quoted errors as expected from lepton universality.

Table 5.8 shows the values of P_τ measured by other LEP experiments [23]. The results presented here for the $\tau \to e\nu_\tau\bar{\nu}_e$ channel are in agreement with measurements for this decay channel by other experiments, within the quoted errors. The measurement of A_{pol}^{FB} for the $\tau \to e\nu_\tau\bar{\nu}_e$ channel is consistent with the values obtained for the $\tau \to \mu\nu_\tau\bar{\nu}_\mu$ and $\tau \to \pi(K)\nu_\tau$ channels from OPAL.

Table 5.9 shows results for the τ polarization asymmetries from lower energy experiments and the couplings extracted from these measurements. It can be seen that the results presented here are much more precise than these previous measurements. In reference [95] a fit is made to all non–LEP measurements of $\sigma_{\tau\tau}$ and A_{FB} for the coupling constants of the Z° to the τ. The results given for a fit to 102 such measurements are:

$$v_\tau = -0.18\pm^{0.50}_{0.56}, \qquad v_\tau/a_\tau = 0.186 \pm 0.579$$

Again it can be seen that the LEP results have improved on the precision of such measurements significantly.

The couplings of the Z° to leptons can also be extracted from measurements of forward backward asymmetries, A_{FB}, at LEP. In this case fits give $(v_l/a_l)^2$ so the relative signs of the couplings are not determined. The OPAL results from fits to the cross section and A_{FB} measurements for the e^+e^-, $\mu^+\mu^-$ and $\tau^+\tau^-$ channels combined [82] give:

$$v_l/a_l = \pm 0.048 \pm 0.029$$

Table 5.8: Measurements of P_τ and the coupling constants from other LEP analyses.

Experiment	Channel	$< P_\tau >$	v_τ/a_τ	A_{pol}^{FB}
ALEPH [91]	$\tau \to e\nu_\tau\bar{\nu}_e$	$-0.36 \pm 0.17 \pm 0.06$		
	$\tau \to \mu\nu_\tau\bar{\nu}_\mu$	$-0.19 \pm 0.13 \pm 0.06$		
	$\tau \to \pi(\mathrm{K})\nu_\tau$	$-0.13 \pm 0.06 \pm 0.04$		
	$\tau \to \rho\nu_\tau$	$-0.12 \pm 0.05 \pm 0.05$		
	$\tau \to a_1\nu_\tau$	$-0.15 \pm 0.15 \pm 0.07$		
	Average	-0.152 ± 0.045	0.076 ± 0.023	
DELPHI [23]	$\tau \to e\nu_\tau\bar{\nu}_e$	$-0.10 \pm 0.20 \pm 0.09$		
	$\tau \to \mu\nu_\tau\bar{\nu}_\mu$	$-0.09 \pm 0.19 \pm 0.10$		
	$\tau \to \pi(\mathrm{K})\nu_\tau$	$-0.28 \pm 0.10 \pm 0.08$		
	$\tau \to \rho\nu_\tau$	$-0.17 \pm 0.08 \pm 0.08$		
	Average	-0.176 ± 0.076	0.088 ± 0.038	
L3 [23]	$\tau \to e\nu_\tau\bar{\nu}_e$	$-0.19 \pm 0.16 \pm 0.06$		
	$\tau \to \mu\nu_\tau\bar{\nu}_\mu$	$-0.07 \pm 0.14 \pm 0.06$		
	Average	-0.12 ± 0.12	0.06 ± 0.06	
OPAL [84], other measurements	$\tau \to \mu\nu_\tau\bar{\nu}_\mu$	$-0.17 \pm 0.16 \pm 0.10$		-0.08 ± 0.22
	$\tau \to \pi(\mathrm{K})\nu_\tau$	$-0.08 \pm 0.10 \pm 0.07$		-0.34 ± 0.16
	Average	-0.11 ± 0.10	0.05 ± 0.05	-0.25 ± 0.13

Table 5.9: Measurements of the τ polarization and the derived values of v_τ at lower energy experiments.

Experiment	Measurement	v_τ
CELLO [92]	A_{pol}^{FB}	-0.1 ± 2.8
MAC [93]	P_τ and A_{pol}^{FB}	$(-1.04 \pm 1.24) \times (1 \pm 0.011)$
AMY [94]	P_τ and A_{pol}^{FB}	-0.954 ± 0.712

The results in equations 5.6 and 5.7 are consistent with this. At the moment the forward–backward asymmetry measurement gives a more precise determination of the couplings but does not give the relative signs of the vector and axial couplings, whereas the polarization measurement should. In fact, combining the LEP polarization measurements gives:

$$v_\tau/a_\tau = 0.067 \pm 0.017$$

determining that v_τ and a_τ have the same sign with better than 99.9% CL.

The errors on the polarization measurements are currently too large to constrain m_t. However, by combining the τ polarization results with those from the lineshape and forward backward asymmetries for the leptonic and hadronic Z° decays for all LEP experiments a limit of $m_t = 150^{+29+20}_{-34-22}$ GeV [14] can be determined, where the second set of errors are due to varying m_H between 50 GeV and 1000 GeV. With the additional data expected from LEP in the next few years, the measurements of electroweak parameters from P_τ should improve significantly.

Chapter 6

Conclusions and Outlook

In this thesis 1203 $\tau \rightarrow e\nu_\tau\bar{\nu}_e$ events have been identified in the 6.4 pb^{-1} of data recorded with the OPAL detector in 1990. These events have been used to measure the $\tau \rightarrow e\nu_\tau\bar{\nu}_e$ branching ratio and the τ polarization. The measurement of the branching ratio is:

$$\text{BR}(\tau \rightarrow e\nu_\tau\bar{\nu}_e) = 18.0 \pm 0.5 \pm 0.3\%$$

If this is compared to the OPAL measurement of the $\tau \rightarrow \mu\nu_\tau\bar{\nu}_\mu$ branching ratio of $16.8 \pm 0.6\%$ [84], the ratio of the weak charged couplings for the e and μ is found to be $g_\mu/g_e = 1.042 \pm 0.052$ Combining these OPAL results with other recent measurements to form a new world average gives $g_\mu/g_e = 0.997 \pm 0.017$. Both of these results are consistent with lepton universality.

A comparison of the measured $\tau \rightarrow e\nu_\tau\bar{\nu}_e$ branching ratio with the world average τ lifetime measurement gives the ratio $g_\tau/g_\mu = 0.951 \pm 0.036$ and again combining with measurements from other experiments to form a new world average $\tau \rightarrow e\nu_\tau\bar{\nu}_e$ branching ratio gives $g_\tau/g_\mu = 0.948 \pm 0.023$. Although this is not a large statistical effect, the fact that these ratios do not agree with the predictions of lepton universality means that this previously observed discrepancy has not yet been resolved. The dominant errors in this ratio are from the branching ratio and τ lifetime measurements, both of which can be expected to improve with increased statistics at LEP. Since the measurement of the $\tau \rightarrow e\nu_\tau\bar{\nu}_e$ branching ratio presented here agrees with previous measurements it offers no explanation of the "missing decay modes" problem.

Measurements of the τ polarization and polarization forward–backward asymmetry

from an analysis of the $\tau \rightarrow e\nu_\tau\bar{\nu}_e$ momentum spectrum give:

$$\begin{aligned} P_\tau &= 0.04 \pm 0.13 \pm 0.09 \\ A_{pol}^{FB}(corr) &= -0.12 \pm 0.17 \end{aligned}$$

and

$$\begin{aligned} v_\tau/a_\tau &= -0.02 \pm 0.08 \qquad & v_e/a_e &= 0.06 \pm 0.08 \\ \sin^2\bar{\theta}_W &= 0.255 \pm 0.020 \qquad & \sin^2\bar{\theta}_W &= 0.235 \pm 0.020 \end{aligned}$$

These measurement are still insufficiently precise to constrain the relative signs of the vector and axial-vector couplings. However, they are consistent with those from other LEP experiments and other decay modes and together these determine the ratio v_τ/a_τ to be positive to better than 99.9% CL. Also, the results for the neutral current couplings agree with those from measurements of A_{FB} and from lower energy experiments and already the errors are smaller than those on non-LEP τ polarization measurements.

With the LEP experiments continuing to record more data the statistical errors on the τ polarization measurements will decrease. The systematic errors should also decrease as the detectors become better understood and increased MC statistics allow more detailed studies of systematic effects. This should allow more precise measurements of the polarization asymmetries and hence more stringent tests of the electroweak model. In reference [36] an analysis of 3.10^6 Z°s is considered and errors of 0.01 statistical and 0.006 systematic are predicted for the measurement of P_τ. This will allow $\sin^2\bar{\theta}_W$ to be measured to ± 0.0014, giving more than a factor 10 improvement on the current measurement and more accuracy than measurements from A_{FB} with similar statistics.

Appendix A

Event Reconstruction

In the identification of τ pair events and $\tau \rightarrow e\nu_\tau\bar{\nu}_e$ decays extensive use is made of reconstructed charged tracks and electromagnetic clusters. Here, a short description of the algorithms used to form these quantities from the raw data is given. In addition, the requirements for matching tracks and clusters and for matching presampler and calorimeter clusters are described.

A.1 Track reconstruction

The axial magnetic field in OPAL means that the trajectories of charged particles bend in the $r-\phi$ plane. These particles are tracked in OPAL using hits from the Central Tracking Detectors (CT). Track segments are found in each of the tracking chambers, CV, CJ and CZ separately and are merged together at a later stage to form a CT track. A CT track is formed from a CJ track by matching CV and CZ track segments to it and the final track parameters are formed by considering all the hits assigned to the track. Since a CJ track forms the basis for a CT track the pattern recognition algorithm used to form such tracks is described below. More details of these procedures can be found in references [96] and [97].

Within each of the 24 CJ ϕ sectors a search is made, starting at the outside wire, for three hits on consecutive wires to form an initial triplet. In order to form such a triplet the hits must lie on a straight line within some tolerance values which allow for low p_T tracks. The left–right ambiguities are resolved using the staggered wires. This first triplet is used to start a circular track in the $r-\phi$ plane which is extrapolated both up

and down the sector to other wires. Hits are collected onto the track if they lie within some road (typically $\sim 5\sigma$) of the extrapolated track position. Only one hit per wire is collected. The track parameters used in the extrapolation are updated as more hits are assigned to the track. The collection of hits stops once all wires have been searched or if there is a gap of N (~ 3) wires with no matching hits or if the χ^2 of the track gets too large. Once a track has been formed the hits assigned to it are stored and removed from the list of usable hits in that sector. Further iterations of the procedure are performed using the remaining hits. The parameters of the pattern recognition algorithm can be changed at each iteration to find successively lower momentum tracks.

Once all sectors have been completed, tracks which cross sector boundaries are merged together and the track parameters are determined using all hits assigned to a track.

z-refit

In order to improve the θ measurement of tracks a 'z-refit' can be performed in which tracks are constrained to have come from the primary vertex of the event. The constraint is applied in z at the point of closest approach of the track to the vertex in the $r-\phi$ plane and takes into account the errors on the vertex position and the track parameters. In the endcap, an additional constraint can be applied using the 'endpoint' of the track. The 'endpoint' is derived from the last wire hit in the jet chamber. Using the geometry of the endcone the z position of this hit can be found and used to constrain the track. The endpoint constraint is important for the $\Delta\theta^{Ecal-track}$ cut, see section 4.3, which separates electrons and hadrons in the endcap.

A.2 Electromagnetic cluster finding

In order to reduce the effects of noise fluctuations on the energy sums formed from the electromagnetic calorimeter, clusters of contiguous blocks with energy above some threshold are formed. The signal in each lead glass blocks is first calibrated to give an energy in GeV. In the electromagnetic endcap (EE) calorimeter clusters are formed by searching for an 'initiator' block with an energy above 60 MeV. Once such a block is found its eight neighbours are considered and those with an energy of greater than

40 MeV are included in the cluster and their energy added to that of the initiator. The next nearest neighbours are then considered and so on until all blocks surrounding the cluster have an energy below 40 MeV. This results in a coarse cluster and the remaining blocks are searched for more initiators.

Each coarse cluster is examined in more detail to see if it can be split into fine clusters. This is done by looking for peaks in the shower profile of the cluster. Finally, all single block clusters of more than 5 GeV are discarded as being due to noise. Clusters are formed in the barrel calorimeter in a similar way but using lower energy thresholds.

Corrections

For each cluster, the energies of the individual blocks are used to calculate the energy (E) and position (θ, ϕ) of the cluster. These are the 'raw' values and corrections can be made to them for the effects of the material in front of the calorimeter. The corrections are calculated using MC events containing single electrons of known energy. The electrons are propagated through the detector using GOPAL, the full detector simulation program, which includes the material in front of the calorimeter.

In the endcap the energy correction factor is a function of the θ value of the cluster. The calculation of the θ value of a cluster depends on the assumed depth of the electromagnetic shower in each block. The depth is taken to be that for an electron and depends on the energy deposited in the cluster. This inter–dependence between the energy and angle, θ, means that the correction procedure must go through a number of iterations for the endcap.

Since the calculation of the θ value of a cluster in the endcap is made assuming the particle was an electron, for other particles such as muons or hadrons it is wrong. This feature is used in the selection of $\tau \rightarrow e\nu_\tau\bar{\nu}_e$ events in the endcap to separate electrons from hadrons, see section 4.3.

A.3 Matching

Particles travelling through the detector usually leave signals in a number of different subdetector components. For particle identification it is important to match the signals

in the different components and then to assign them to have come from a single particle. The results of two such matching procedures are used in the τ analysis (the matching of electromagnetic (ECAL) clusters to charged tracks and the matching of presampler clusters to electromagnetic ones) and are described below.

Track–cluster matching

Central detector tracks are extrapolated to the outer detectors where hits within a certain 'road' of the track are matched to the track. The extrapolation uses the detector geometry in the GOPAL program to simulate the effects of energy loss and multiple scattering and matches are made in both θ and ϕ. An electromagnetic cluster is matched to a track if it is within $\Delta\theta$ and $\Delta\phi$ of the extrapolation where these parameters are different for the barrel and endcap:

	$\Delta\theta$(mrad)	$\Delta\phi$(mrad)
Barrel	150	80
Endcap	50	50

Presampler–ECAL matching

Associations are also made between clusters in the presampler detectors and ECAL clusters wherever possible. For the barrel this is done by considering each electromagnetic barrel (EB) cluster in turn. For each block in the cluster a minimum and maximum θ and ϕ are calculated, any presampler barrel cluster with a position within these limits is matched to the EB cluster. In the endcap the θ and ϕ of a presampler cluster are used to extrapolate its position into the electromagnetic calorimeter (EE) and any blocks hit by the extrapolation are noted. The presampler cluster is matched to any EE clusters containing one or more of these blocks.

For the selection of τ pair events it is not necessary to use the matching of subdetectors since sufficient separation from background events can be seen using simple single subdetector quantities. For the selection of the τ decay products, however, the matched quantities are very useful.

Appendix B

Calculations for TT

B.1 Low momentum threshold

Charged tracks are bent in the $r-\phi$ plane due to OPAL's axial magnetic field. Low momentum tracks may be bent out of a sector before reaching the outer radius of the jet chamber (CJ). This is important for the track trigger since only tracks which cross the first and last rings within two CJ sectors will be triggered. The angle, ϕ, through which a particle with a transverse momentum p_T is bent in traversing a radial distance r is given by:

$$\phi = 0.3 \times \frac{Bqr}{p_T}$$

where B is in Tesla, q is the electron charge, r is in m and p_T in GeV/c.Figure 3.2 shows the $r-\phi$ segmentation of the tracking chambers and the coverage of a track trigger sector. For convenience, the figure is reproduced here as figure B.1.

As can be seen from the figure, a trigger sector covers an angular range of $\pi/12$ so for a track to cross a complete sector between radii r_1 and r_2 the transverse momentum must be less than:

$$p_T = 0.3 \times \frac{12B(r_2 - r_1)}{\pi}$$

This is, therefore, the threshold p_T for a track to trigger the track trigger, p_T^{thresh}. The magnetic field, B, is 0.435 T.

For the track trigger to fire, a track had to be 'seen' in all rings through which it should have passed. So in the barrel where tracks must reach CJ ring 3 the threshold is expected to be higher than in the endcap and forward regions where the particles

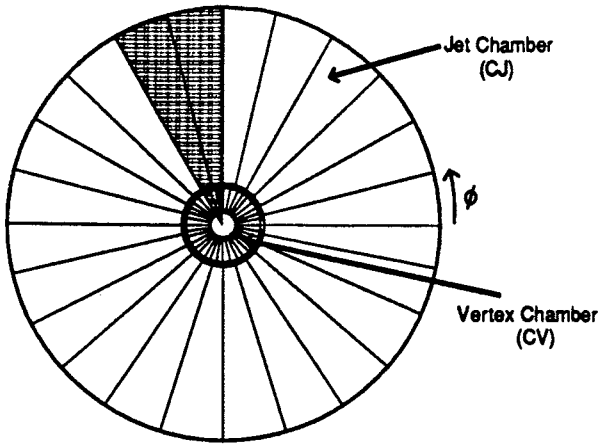

Figure B.1: An $r-\phi$ view of the OPAL tracking chambers showing the ϕ segmentation in CV and CJ. The shaded area is one overlapped track trigger ϕ bin, covering two CJ and three CV sectors.

only have to reach rings 2 and 1, respectively. The wire positions for the rings used by the track trigger are given in table 3.1 and the thresholds for various setups of the track trigger and angular ranges are given in table B.1

Table B.1: p_T threshold for TT to trigger for various setups and angular ranges.

year	setup	region	r_2/cm	r_1/cm	p_T^{thresh}/MeV
1989	CJ only	barrel	160	40	590
	CJ only	endcap	68	40	140
1989	CJ and CV	barrel	160	13.2	730
	CJ and CV	endcap	68	13.2	270
	CJ and CV	barrel	128	13.2	570
1990	CJ and CV	endcap	68	13.2	270
	CJ and CV	forward	40	13.2	130

B.2 z cutoff

The window in z around the interaction point from which tracks can originate and still efficiently trigger the track trigger can be calculated by considering the construction shown in figure B.2

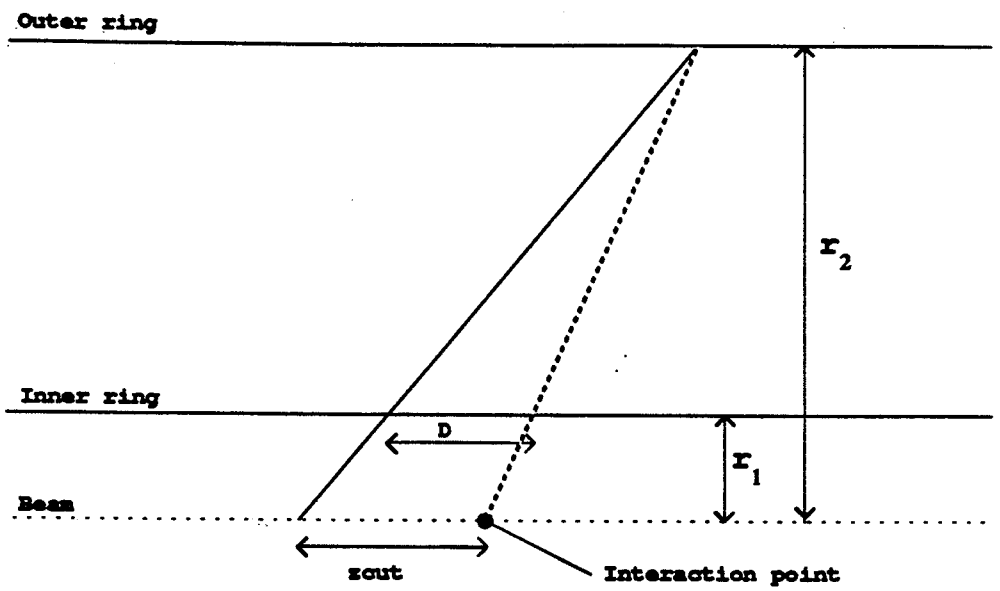

Figure B.2: Construction to calculate the z cutoff for TT operation.

From similar triangles the cutoff, z_{cut}, is given by the expression:

$$z_{cut} = \frac{Dr_2}{(r_2 - r_1)}$$

where r_1 and r_2 are the radii of the inner and outer rings through which a track is required to pass. The distance D is the maximum offset of a track segment in the inner ring from its nominal position if the track had come from the interaction point. This is given by:

$$D = W_{z/r} \times R_{inn} \times N_{bin}$$

where $W_{z/r}$ is the z/r bin width, R_{inn} is the radius of the inner ring and N_{bin} is the number of bins by which a track in the inner ring can be offset from one in the outer ring and still be found by the track trigger.

Table B.2: z_{cut} values for various TT setups and angular ranges.

year	setup	region	r_2/cm	r_1/cm	D/cm	z_{cut} / cm
1989	CJ only	barrel	160	40	14.2	19.0
	CJ only	endcap	68	40	14.2	34.5
1989	CJ and CV	barrel	160	13.2	18.8	20.5
	CJ and CV	endcap	68	13.2	18.8	23.3
1990	CJ and CV	barrel	128	13.2	14.1	15.7
	CJ and CV	endcap	68	13.2	14.1	17.5
	CJ and CV	forward	40	13.2	14.1	21.0

The values of z_{cut} for various setups of the track trigger and angular regions are given in table B.2. For the 1989 run only information from CJ was used, the θ smearing allowed for an offset of one z/r bin between the inner and outer rings. One z/r bin in the inner ring corresponds to a z distance of 14.2 cm. This means that the z cutoff is 18.9 cm. When CV was included for tests at the end of the 1989 run a wide window, IWIN, of three bins was used in the coincidence chip. Each CV bin covers a z distance of 4.7 cm. A track flag in CV can be offset by IWIN+1 bins from one in CJ and still trigger the TT so $D = 4 \times 4.7 = 18.8$ cm. This gives a z cutoff of 20.7 cm. With the closer CJ rings of 1990 and a coincidence window of only two bins the expected cutoff was reduced to 15.6 cm. In the forward direction where only one or two CJ rings need to be reached the cutoff is larger. Reducing the window on the coincidence chip would decrease the z cutoff further.

References

[1] F. Halzen and A.D. Martin. 'Quarks and Leptons: An Introductory Course in Modern Particle Physics', John Wiley and Sons Inc., 1988.

[2] I.J.R. Aitchinson and A.J.G. Hey. 'Gauge Theories in Particle Physics', Adam Hilger, 1989.

[3] F. Dydak. 'Results from LEP and SLC'. Proceedings of the 25th International High Energy Physics Conference, Singapore, September 1990.

[4] M.A. Parker. 'Status of Searches for the Top Quark'. Proceedings of the 25th International High Energy Physics Conference, Singapore, September 1990.

[5] S. Weinberg. 'Conceptual Foundations of the Unified Theory of Weak and Electromagnetic Interactions',
A. Salaam. 'Gauge Unification of Fundamental Forces',
S.L. Glashow. 'Towards a Unified Theory: Threads in a Tapestry'.
The 1979 Nobel Lectures. Rev. Mod. Phys. 52 (1980) 515.

[6] Particle Data Group, M.Aguilar–Benitez *et al.* 'Review of Particle Properties', Phys. Lett. B239 (1990) 1.

[7] F. Hasert *et al.* 'Observation of Neutrino–Like Interactions without Muon or Electron in the Gargamarelle Neutrino Experiment'. Phys. Lett. B46 (1973) 138.

[8] G. Costa *et al.* 'Neutral Currents Within and Beyond the Standard Model'. Nucl. Phys. B297 (1987) 244.

[9] UA1 Collaboration, G. Arnison *et al.* 'Experimental Observation of Isolated Large Transverse Energy Electrons with Associated Missing Energy at

$\sqrt{s}$ =540 GeV'. Phys. Lett. B122 (1983) 103.

[10] UA2 Collaboration, M. Banner *et al.* 'Observation of Single Isolated Electrons of High Transverse Momentum in Events with Missing Transverse Energy at the CERN $\bar{p}p$ Collider'. Phys. Lett. B122 (1983) 476.

[11] UA1 Collaboration, G. Arnison *et al.* 'Experimental Observation of Lepton Pairs of Invariant Mass around 95 GeV/c^2 at the CERN SPS Collider'. Phys. Lett. B126 (1983) 398.

[12] UA2 Collaboration, P. Bagnaia *et al.* 'Evidence for $Z^\circ \rightarrow e^+e^-$ at the CERN $\bar{p}p$ Collider'. Phys. Lett. B129 (1983) 130.

[13] J. Ellis. 'Status of the Electroweak Interaction'. To appear in Proceedings of the Joint International Lepton–Photon Symposium and Europhysics Conference on High Energy Physics, Geneva, July 1991.

[14] J.R. Carter. 'Precision Tests of the Standard Model at LEP'. To appear in Proceedings of the Joint International Lepton–Photon Symposium and Europhysics Conference on High Energy Physics, Geneva, July 1991.

[15] M. Davier. 'Searches for New Particles at LEP'. To appear in Proceedings of the Joint International Lepton–Photon Symposium and Europhysics Conference on High Energy Physics, Geneva, July 1991.

[16] M.L. Perl *et al.* 'Evidence for Anomalous Lepton Production in e^+e^- Annihilation', Phys. Rev. Lett. 35 (1975) 1489.

[17] M.L. Perl *et al.* 'Properties of Anomalous $e\mu$ Events Produced in e^+e^- Annihilation', Phys. Lett. B63 (1976) 466.

[18] B.C. Barish and R. Stroynowski. 'The Physics of the τ Lepton'. Physics Reports 157 (1988) 1.

[19] C. Kiesling. 'τ Physics'. In 'High Energy Electron–Positron Physics', Edited by A.Ali and P.Söding, World Scientific Advanced Series on Directions in High Energy Physics, Volume 1, 1988.

[20] DELCO Collaboration, W. Bacino *et al.* 'Measurement of the Threshold Behaviour of $\tau^+\tau^-$ Production in e^+e^- Annihilation'. Phys. Rev. Lett. 41 (1978) 13.

[21] DASP Collaboration, R. Brandelik *et al.* 'Measurements of Tau Decay Modes and a Precise Determination of the Mass'. Phys. Lett. B73 (1978) 109.

[22] L. Michel. 'Interaction Between Four Half–Spin Particles and the Decay of the μ–meson'. Proc. Phys. Soc. A63 (1950) 514; A63 (1950) 1371.

[23] K. Riles. 'Review of Tau Physics at LEP'. To appear in Proceedings of Division of Particles and Fields, American Physical Society Conference, Vancouver, August 1991.

[24] CLEO Collaboration, A.J. Weinstein.'Recent Results on taus from CLEO'. To appear in Proceedings of Division of Particles and Fields, American Physical Society Conference, Vancouver, August 1991.

[25] DELPHI Collaboration, P. Abreu *et al.* 'A Measurement of the Lifetime of the Tau Lepton'. CERN–PPE/91-115. Submitted to Phys.Lett. B.

[26] L3 Collaboration, B. Adeva *et al.* 'Decay Properties of Tau Leptons Measured at the Z° Resonance'. Phys. Lett. B265 (1991) 451.

[27] OPAL Collaboration, P.D. Acton *et al.* 'Measurement of the Tau Lepton Lifetime'. CERN–PPE/91-164. Submitted to Phys. Lett. B.

[28] W. Alles. 'Spin of the τ–Lepton and its Neutrino from Decay Branching Ratios'. Lettere al Nuovo Cimento 25 (1979) 404.

[29] ARGUS Collaboration, H. Albrecht *et al.* 'An Improved Upper Limit on the ν_τ Mass from the Decay $\tau^- \rightarrow \pi^-\pi^-\pi^-\pi^+\pi^+\nu_\tau$'. Phys. Lett. B202 (1988) 149.

[30] UA1 Collaboration, C. Albajar *et al.* 'Events with Large Missing Transverse Energy at the CERN Collider: I. W$\rightarrow \tau\nu$ Decay and Test of τ-μ-e Universality at $Q^2 = m_W^2$'. Phys. Lett. B185 (1987) 233.

[31] T.N. Truong. 'Hadronic τ decay, pion radiative decay and pion polarizability'. Phys. Rev. D30 (1984) 1509.

[32] F.J. Gilman and S.H. Rhie. 'Calculation of Exclusive Decay Modes of the Tau'. Phys. Rev. D31 (1985) 1066.

[33] CELLO Collaboration, H.J. Behrend *et al.* 'Exclusive τ Decays with the CELLO Detector at PETRA'. Z. Phys. C46 (1990) 537.

[34] TPC Collaboration, H. Aihara *et al.* 'Measurement of τ Branching Ratios'. Phys. Rev. D35 (1987) 1553.

[35] Z. Zhang. 'τ Branching Ratios (ALEPH)', To appear in Proceedings of the Workshop on Tau Lepton Physics, Orsay, September 1990.

[36] S. Jadach and Z. Was. 'The Tau Polarization Measurement'. In 'Z physics at LEP 1. Volume 1: Standard Physics'. Editors G.Altarelli, R.Kleiss and C.Verzegnassi. CERN Yellow Report. CERN-89-08

[37] S. Jadach, B.F.L. Ward and Z. Was. 'The Monte Carlo program KORALZ, version 3.8, for the Lepton or Quark Pair Production at LEP/SLC Energies'. CERN–TH–5994/91. Submitted to Comp. Phys. Comm.

[38] S. Jadach *et al.* 'QCD and QED Corrections to the Longitudinal Polarization Asymmetry'. Z. Phys. C38 (1988) 609.

[39] OPAL Collaboration, K. Ahmet *et al.* 'The OPAL Detector at LEP', Nucl. Inst. Meth. A305 (1991) 275.

[40] J.R. Carter *et al.* 'The OPAL Vertex Drift Chamber'. Nucl. Inst. Meth. A286 (1990) 99.

[41] D.J. White. 'Second Coordinate Measurement in Drift Chambers by Time Difference'. RAL–89–123.

[42] H.M. Fischer *et al.* 'The OPAL Jet Chamber'. Nucl. Inst. Meth. A283 (1989) 492.

[43] H. Drumm *et al.* 'Experience with the Jet Chamber of the JADE Experiment at PETRA'. Nucl. Inst. Meth. A176 (1980) 333.

[44] P. Bock *et al.* 'Drift Chamber Readout with Flash ADCs'.
Nucl. Inst. Meth. A242 (1986) 237.

[45] D. Schaile *et al.* 'A Simultaneous Hit Finding and Timing Method for Pulse Shape Analysis of Drift Chamber Signals'. Nucl. Inst. Meth. A242 (1986) 247

[46] H. Mes *et al.* 'Design and Tests of the Z-Coordinate Drift Chamber System for the OPAL Central Detector at LEP'. Nucl. Inst. Meth. A265 (1988) 445.

[47] SF57 lead glass from Schott Glaswerke, Hattenbergstrasse 10, D–6500 Mainz 1, West Germany.

[48] A.N. Ji–Gang *et al.* 'Influence of Gas Mixture and Primary Ionization on the Performance of Limited Streamer Mode Tubes'. Nucl. Inst. Meth. A267 (1988) 386.

[49] M.Z. Akrawy *et al.* 'Development Studies for the OPAL Endcap Electromagnetic Calorimeter using Vacuum Phototriode Instrumented Lead Glass'.
Nucl. Inst. Meth. A290 (1990) 76.

[50] C. Beard *et al.* 'Thin, High Gain Wire Chambers for Electromagnetic Presampling in OPAL'. Nucl. Inst. Meth. A286 (1990) 117.

[51] G. Artusi *et al.* 'Limited Streamer Tubes for the OPAL Hadron Calorimeter'. Nucl. Inst. Meth. A279 (1989) 523.

[52] J. Allison *et al.* 'The Diamond Shaped Cathode Pads of the OPAL Muon Barrel Drift Chambers'. Paper Contributed to 2nd London Conference on Position Sensitive Detectors, London, September 1990. Submitted to Nucl. Inst. Meth.

[53] G.T.J. Arnison *et al.* 'Production and Testing of Limited Streamer Tubes for the Endcap Muon Subdetector of OPAL'. Nucl. Inst. Meth. A294 (1990) 431.

[54] S. Wotton. 'A Data Acquisition and Experimental Control System for the OPAL Experiment at the CERN LEP Collider.' Proceedings of the 2nd International Conference on Advanced Technology and Particle Physics, Como, 1990.

[55] 'ZEBRA Data Structure Management System', CERN Computer Centre Library.

[56] M. Arignon *et al.* 'The Trigger System of the OPAL Experiment at LEP', CERN-PPE/91-32, Submitted to Nucl. Inst. Meth.

[57] K.W. Bell *et al.* 'OPAL Hardware Trigger'. OPAL Note 14/Trigger/024, September 1987.

[58] S. Weisz *et al.* 'ROPE Users' Guide. Latest Revisions for ROPE401'. OPAL Offline Software Documentation, November 1991.

[59] A. Buijs. 'The OPAL DST (OD) Processor in ROPE, Version 3.12'. OPAL Offline Software Documentation, September 1991.

[60] D.R. Ward. 'A GROPE Primer, latest revisions for GR115'. OPAL Offline Software Documentation, July 1991.

[61] R. Cranfield *et al.* 'OPCAL User Guide - OC504'. OPAL Note OPAL/OFFL/36/0003, March 1991.

[62] D.R.Ward. 'A GOPAL Primer, latest revisions for GOPAL126', OPAL Offline Software Documentation, July 1991.

[63] R. Brun *et al.* 'GEANT3 Users' Guide'. CERN/DD/EE/84-1.

[64] A.A. Carter *et al.* 'A Fast Track Trigger Processor for the OPAL Detector at LEP'. Nucl. Inst. Meth. A250 (1986) 503.

[65] M.J. French and F. Slorach. '32-bit Coincidence Array A.S.I.C'. Trieste Conference on 'Digital Microelectronics in Particle Physics', 1988.

[66] M. Bramhall *et al.* 'A Fast Track Trigger Processor for the OPAL Experiment at LEP, CERN'. IEEE Transactions on Nuclear Science, Vol. 36, No. 1, 380, February 1989.

[67] M. Bramhall. 'OPAL Track Trigger Processor Z/R Converter Module'. OPAL TT Group Internal Note, August 1988.

[68] R. Humbert. 'Calibration of the OPAL Track Trigger', Diploma Thesis, Freiburg 1990.

[69] J. Hart. 'TT Register Set Explained'. OPAL TT Group Internal Note, March 1991.

[70] M.F. Turner. 'Tests of QCD at the Z° Resonance'. Ph.D. Thesis in preparation.

[71] C.M. Roach. 'Tau Pairs from Z° Decays at the LEP collider'. Ph.D. Thesis, University of Cambridge, November 1990. RALT-111

[72] C.M. Roach. 'Performance of Various Multiplicity Algorithms'. OPAL Note 14/Trigger/0131, March 1988.

[73] J. Hart. 'TT Online Programs'. OPAL TT Group Internal Note, March 1990.

[74] H. von der Schmidt. 'RTK/68K Real Time Fortran 77 for 68K Processors'. Physikalisches Institut Universität Heidelberg, March 1990.

[75] C.M. Roach. 'TT Offline Software'. OPAL TT Group Internal Note, March 1990.

[76] C.M. Roach. 'Simulation of OPAL's Track Trigger'. OPAL Note 14/Trigger/0130, March 1988.

[77] C.M. Roach. 'Killing Beampipe Showers with the Track Trigger'. OPAL Note 14/Trigger/0132, March 1989.

[78] M. Bohm *et al.* 'Radiative Corrections to Bhabha Scattering at High Energies (I). Virtual and Soft Photon Corrections'. Nucl. Phys. B304 (1988) 687.
F.A. Berends *et al.* 'Radiative Corrections to Bhabha Scattering at High Energies (II). Hard photon Corrections and Monte carlo Treatment'.
Nucl. Phys. B304 (1988) 712.

[79] T. Sjostrand. Comp. Phys. Comm. 39 (1986) 347.
T. Sjostrand and M. Bengtsson. Comp. Phys. Comm. 39 (1987) 367.

[80] G. Marchesini and B.R. Webber. 'Monte Carlo Simulation of General Hard Processes with Coherent QCD Radiation'. Nucl. Phys. B310 (1988) 461.

[81] R. Bhattacharya and J. Smith. 'Two-photon production processes at high energy. I'. Phys. Rev D15 (1977) 3267.

J. Smith, J.A.M Vermasseren and G. Gramer Jr. 'Two–photon production processes at high energy. II'. Phys. Rev D15 (1977) 3280.

[82] G. Alexander *et al.* 'Measurement of the Z° Line Shape Parameters and the Electroweak Couplings of Charged Leptons'. Z. Phys. C52 (1991) 175.

[83] H. Albrecht *et al.* 'Measurement of Exclusive One–Prong and Inclusive Three–Prong Branching Ratios of the τ Lepton'. DESY 91-084, July 1991.

[84] OPAL Collaboration, G. Alexander *et al.* 'Measurement of the Branching Ratios and τ polarization from $\tau \to e\nu\bar{\nu}$, $\tau \to \mu\nu\bar{\nu}$ and $\tau \to \pi(K)\nu$ Decays at LEP', Phys. Lett. B266 (1991) 201.

[85] X. Li and E. Ma. 'Gauge Model of Generation Nonuniversality'. Phys. Rev. Lett. 47 (1981) 1788.

[86] Y. Tsai. 'Decay Correlations of Heavy Leptons in $e^+ + e^- \to l^+ + l^-$'. Phys. Rev. D4 (1971) 2821.

[87] G. Goggi. 'Study of Heavy–Lepton Polarization in e^+e^- Annihilations at the Z° Pole'. Proceedings of the LEP Summer Study, Volume 2, Les Houches and CERN, September 1978. CERN 79–01.

[88] S. Jadach and Z. Was. 'CALASY, CALculator of ASYymmetries'. In 'Z Physics at LEP 1, Volume 3: Event Generators and Software'. Editors G.Altarelli, R.Kleiss and C.Verzegnassi. CERN Yellow Report. CERN-89-08.

[89] Editors G.Altarelli, R.Kleiss and C.Verzegnassi. 'Z Physics at LEP 1, Volume 3: Event Generators and Software'. CERN Yellow Report. CERN-89-08.

[90] F. James and M. Roos. 'MINUIT Function Minimization and Error Analysis'. CERN Computer Centre Library, December 1989.

[91] ALEPH Collaboration, D. Decamp *et al.* 'Measurement of the Polarization of τ Leptons Produced in Z Decays'. Phys. Lett. B265 (1991) 430.

[92] CELLO Collaboration, H.J. Behrend *et al.* 'τ Branching Ratios and Polarization Limits in e^+e^- Interactions at $\sqrt{s} = 34$ GeV'. Phys. Lett. B127 (1983) 270.

[93] MAC Collaboration, W.T. Ford *et al.* 'Measurement of the Polarization of τ Leptons in e^+e^- Annihilation at $\sqrt{s} = 29$ GeV'. Phys. Rev. D36 (1987) 1971.

[94] AMY Collaboration, M.H. Lee *et al.* 'Measurement of the Polarization of τ–Leptons from $e^+e^- \rightarrow \tau^+\tau^-$ at $\sqrt{s} = 57$ GeV'. Proceedings of 25th International High Energy Physics Conference, Singapore, September 1990. KEK 90–70.

[95] S.Odaka. 'Neutral–current Properties of Tau Leptons at PEP/PETRA/TRISTAN'. Talk given at the Workshop on Tau Lepton Physics, Orsay, September 1990. KEK 90–164.

[96] 'The CT Processor for ROPE, Version 3.02'. OPAL Offline Software Documentation, April 1991.

[97] M.Hansroul. 'CJ Primer (Version 7.20)'. OPAL Offline Software Documentation, April 1991.